

The Pennsylvania State University
The Graduate School
Intercollege Graduate Program in Materials Science and Engineering

**DEVELOPMENT OF A KNOWLEDGE BASE OF Ti-ALLOYS
FROM FIRST-PRINCIPLES AND THERMODYNAMIC
MODELING**

A Dissertation in
Materials Science and Engineering
by
Cassie Marker

© 2017 Cassie Marker

Submitted in Partial Fulfillment
of the Requirements
for the Degree of

Doctor of Philosophy

August 2017

The dissertation of Cassie Marker was reviewed and approved* by the following:

Zi-Kui Liu

Professor of Materials Science and Engineering

Dissertation Advisor

Chair of Committee

Allison Beese

Assistant Professor of Materials Science and Engineering

Kristen Fichthorn

Merrell Fenskey Professor of Chemical Engineering and Professor of Physics

Michael Manley

Senior Researcher, Oak Ridge National Laboratory, Materials Science & Technology Division

Special Member

Susan Sinnott

Head of the Department and Professor of Materials Science and Engineering

*Signatures are on file in the Graduate School.

Abstract

An aging population with an active lifestyle requires the development of better load-bearing implants, which have high levels of biocompatibility and a low elastic modulus. Titanium alloys, in the body centered cubic phase, are great implant candidates, due to their mechanical properties and biocompatibility. The present work aims at investigating the thermodynamic and elastic properties of bcc Ti-alloys, using the integrated first-principles based on Density Functional Theory (DFT) and the CALculation of PHase Diagrams (CALPHAD) method. The use of integrated first-principles calculations based on DFT and CALPHAD modeling has greatly reduced the need for trial and error metallurgy, which is ineffective and costly. The phase stability of Ti-alloys has been shown to greatly affect their elastic properties. Traditionally, CALPHAD modeling has been used to predict the equilibrium phase formation, but in the case of Ti-alloys, predicting the formation of two metastable phases ω and α'' is of great importance as these phases also drastically effect the elastic properties. To build a knowledge base of Ti-alloys, for biomedical load-bearing implants, the Ti-Mo-Nb-Sn-Ta-Zr system was studied because of the biocompatibility and the bcc stabilizing effects of some of the elements.

With the focus on bcc Ti-rich alloys, a database of thermodynamic descriptions of each phase for the pure elements, binary and Ti-rich ternary alloys was developed in the present work. Previous thermodynamic descriptions for the pure elements were adopted from the widely used SGTE database for global compatibility. The previous binary and ternary models from the literature were evaluated for accuracy and new thermodynamic descriptions were developed when necessary. The models were evaluated using available experimental data, as well as the enthalpy of formation of the bcc phase obtained from first-principles calculations based on DFT. The thermodynamic descriptions were combined into a database ensuring that the sublattice models are compatible with each other.

For subsystems, such as the Sn-Ta system, where no thermodynamic description had been evaluated and minimal experimental data was available, first-principles calculations based on DFT were used. The Sn-Ta system has two intermetallic phases, TaSn_2 and Ta_3Sn , with three solution phases: bcc, body centered tetragonal (bct) and diamond. First-principles calculations were completed on the intermetallic and solution phases. Special quasirandom structures (SQS) were used to obtain information about the solution phases across the entire composition range. The Debye-Grüneisen approach, as well as the quasiharmonic phonon method, were used to obtain the finite-temperature data. Results from the first-principles calculations and experiments were used to complete the thermodynamic description. The resulting phase diagram reproduced the first-principles calculations and experimental data accurately.

In order to determine the effect of alloying on the elastic properties, first-principles calculations based on DFT were systematically done on the pure elements, five Ti-X binary systems and Ti-X-Y ternary systems ($X \neq Y = \text{Mo, Nb, Sn, Ta, Zr}$) in the bcc phase. The first-principles calculations predicted the single crystal elastic stiffness constants c_{ij} 's. Correspondingly, the polycrystalline aggregate properties were also estimated from the c_{ij} 's, including bulk modulus B , shear modulus G and Young's modulus E . The calculated results showed good agreement with experimental results. The CALPHAD method was then adapted to assist in the database development of the elastic properties as a function of composition. On average, the database predicted the elastic properties of higher order Ti-alloys within 5 GPa of the experimental results.

Finally, the formation of the metastable phases, ω and α'' was studied in the Ti-Ta and Ti-Nb systems. The formation energy of these phases, calculated from first-principles at 0 K, showed that the phases have similar formation energies to the bcc and hcp phases. Inelastic neutron scattering was completed on four different Ti-Nb compositions to study the entropy of the phases as well as the transformations occurring when the phases form and the phase fractions. Ongoing work is being done to use the experimental information to introduce thermodynamic descriptions for these two phases in the Ti-Nb system in order to be able to predict the formation and phase fractions. DFT based first-principles were used to predict the effect these phases have on the elastic properties and a rule of mixtures was used to determine the elastic properties of multi-phase alloys. The results were compared with experiments and showed that if the ongoing modeling can predict the phase fraction, the elastic database can accurately predict the elastic properties of the ω and α'' phases.

This thesis provides a knowledge base of the thermodynamic and elastic properties of Ti-alloys from computational thermodynamics. The databases created will impact research activities on Ti-alloys and specifically efforts focused on Ti-alloys for biomedical applications.

Table of Contents

List of Figures	x
List of Tables	xix
Acknowledgments	xxiii
Chapter 1	
Introduction	1
1.1 Motivation	1
1.2 Overview	2
1.2.1 Equilibrium Phases	2
1.2.2 Metastable Phases	3
Chapter 2	
Methodology	9
2.1 First-Principles Calculations	9
2.1.1 Density Functional Theory at 0 K	11
2.1.2 Finite-temperature thermodynamics	12
2.1.3 Elastic stiffness coefficients	14
2.1.4 Special quasirandom structures (SQS)	16
2.1.5 First-principles calculation error/difference	16
2.2 CALPHAD method	17
2.2.1 Solution phases	17
2.2.2 Stoichiometric compounds	18
2.2.3 Elastic Properties	19
2.3 Experimental	20
2.3.1 Ti-Nb sample preparation	20
2.3.2 Neutron Scattering	20
2.3.2.1 ARCS	20
2.3.2.2 Data Analysis	21

Chapter 3	
Ti-Mo-Nb-Sn-Ta-Zr Thermodynamic Database	23
3.1 Introduction	23
3.2 Computational details	24
3.3 Sn binaries and ternaries	25
3.4 Pure element calculation results	25
3.5 Enthalpy of formation of bcc phase from first-principles	26
3.6 Thermodynamic modeling of the ten binary systems	27
3.6.1 Mo-Nb, Mo-Ta, Nb-Ta	27
3.6.2 Mo-Zr, Nb-Zr and Ta-Zr	28
3.6.3 Ti-Mo	29
3.6.4 Ti-Nb	30
3.6.5 Ti-Ta	31
3.6.6 Ti-Zr	31
3.7 Thermodynamic modeling of six Ti-containing ternary systems	32
3.7.1 Ti-Mo-Nb	32
3.7.2 Ti-Mo-Ta	33
3.7.3 Ti-Mo-Zr	34
3.7.4 Ti-Nb-Ta	34
3.7.5 Ti-Nb-Zr	35
3.7.6 Ti-Ta-Zr	36
3.8 Conclusion	36
Chapter 4	
Thermodynamic modeling of the Sn-Ta system	62
4.1 Introduction	62
4.2 Literature Review	63
4.3 Modeling and Calculations	64
4.4 Results and discussion	65
4.4.1 First-principles	65
4.4.2 CALPHAD	67
4.5 Conclusion	69
Chapter 5	
Effects of alloying elements on the elastic properties of bcc Ti-X alloys	85
5.1 Introduction	85
5.2 Modeling and Calculations	85
5.3 Results and discussion	87
5.3.1 Evaluation of calculation settings	87

5.3.2	Calculations of elastic coefficients in Ti-X binary systems	87
5.3.3	Extrapolation to ternary and higher ordered systems	91
5.4	Conclusion	92
Chapter 6		
Effects of alloying elements on the elastic properties of bcc ternary and higher ordered Ti-alloys		113
6.1	Introduction	113
6.2	Modeling and Calculations	114
6.3	Results and discussion	115
6.3.1	Elastic calculation results	115
6.3.2	Extrapolation to higher ordered systems	121
6.4	Conclusion	122
Chapter 7		
Metastable phase study in the Ti-Ta and Ti-Nb systems		145
7.1	Introduction	145
7.2	Modeling and Calculations	146
7.3	Results and discussion	147
7.3.1	Elastic properties	147
7.3.2	First-principles calculations at 0 K	149
7.3.3	Neutron scattering results	150
7.3.3.1	Phonon density of states at 300 K	150
7.3.3.2	Diffraction patterns at 300 K	151
7.4	Conclusion	152
Chapter 8		
Conclusions and Future Work		178
8.1	Conclusions	178
8.2	Future Work	182
Appendix A		
Ti-Mo-Nb-Ta-Zr Database		184
Appendix B		
Sn-Ta Database		201
Appendix C		
Calculation and Fitting Details		209

Appendix D	
Ti Elastic Database	213
Appendix E	
Pycalphad script	220
Appendix F	
Ti-Nb Experimental Elastic Data	230
Bibliography	234

List of Figures

1.1	Comparison of first-principles calculations [1, 2] and experimental measurements of the Young's moduli of Ti-Ta alloys [3–5]. From 0.10 to 0.35 x(Ta) the calculations and experimentally determined E do not match up due to the formation of two metastable phases ω and α''	7
1.2	Comparison of the present first-principles calculations and experimental measurements of the Young's moduli of Ti-Nb alloys [6–10]. From 0.10 to 0.30 x(Nb) the calculations and experimentally determined E do not match up due to the formation of two metastable phases ω and α''	8
3.1	Previously modeled thermodynamic descriptions of the Mo-Nb (a) [11], Mo-Ta (b) [11] and Nb-Ta (c) [11] binary systems in comparison with available liquidus and solidus phase boundary experimental data to ensure accuracy (as detailed in [11]).	46
3.2	Previously modeled thermodynamic description of the Mo-Zr [12] system is plotted with phase boundary, reaction, single phase and two phase experimental data. The previously modeled Nb-Zr [13, 14] system is plotted with solidus, hcp solvus and bcc solvus experimental data. The previously modeled Ta-Zr [15] system is plotted with single-phase, two-phase, phase boundary and solidus experimental data (detailed in the mentioned references).	47
3.3	Previously modeled thermodynamic description of the Ti-Mo system versus available phase boundary and solidus experimental data to ensure accuracy [16, 17] (a), and enthalpy of formation of the bcc phase predicted by the previous thermodynamic modeling (solid line) at 300 K versus the present first-principles calculations (circles) at 0 K and compared with the enthalpy of formation of the bcc phase obtained from experiments (square) [18] (b).	48

3.4 Previously modeled thermodynamic description of the Ti-Nb system versus available phase boundary and solidus experimental data to ensure accuracy [19–21][20,48] (a), and enthalpy of formation of the bcc phase predicted by the previous thermodynamic modeling (solid line) at 300 K versus the present first-principles calculations (circles) at 0 K compared with the enthalpy of formation of the bcc phase obtained from experiments (square) [18] (b).	49
3.5 Previously modeled thermodynamic description of the Ti-Ta system versus available phase boundary and solidus experimental data to ensure accuracy [16, 22] (a), and enthalpy of formation of the bcc phase predicted by the previous thermodynamic modeling (solid line) at 300 K versus the present first-principles calculations (circles) at 0 K (b).	50
3.6 Previously modeled thermodynamic description of the Ti-Zr system versus available phase boundary and solidus experimental data to ensure accuracy [21] (a), and enthalpy of formation of the bcc phase predicted by the previous thermodynamic modeling (solid line) at 300 K versus the present first-principles calculations (circles) at 0 K (b).	51
3.7 Binary interpolation of the isothermal section of the Ti-Mo-Nb system plotted at 873 K (a), and enthalpy of formation of the bcc phase predicted by the binary interpolation of the thermodynamic modeling (solid line) at 300 K versus the present first-principles calculations (circles) at 0 K (b).	52
3.8 Binary interpolation of the isothermal section of the Ti-Mo-Ta system plotted at 873 K (a), and enthalpy of formation of the bcc phase predicted by the previous thermodynamic modeling (solid line) at 300 K and the ternary assessed thermodynamic modeling (red dotted line) versus the present first-principles calculations (circles) at 0 K (b).	53
3.9 Ternary assessed isothermal section of the Ti-Mo-Ta system plotted at 873 K (a), and zoomed in ternary assessed isothermal section at 873 K (b) with the phase boundary and two-phase region experimental data [23] to ensure accuracy of the ternary assessment.	54
3.10 The assessed ternary isothermal section of the Ti-Mo-Zr system plotted at 1273 K compared with experimental phase boundary data [24,25] (a), and enthalpy of formation of the bcc phase predicted by the previous thermodynamic modeling (solid line) at 300 K versus the present first-principles calculations (circles) at 0 K (b).	55

3.11	Binary interpolation of the isothermal section of the Ti-Nb-Ta system plotted at 673 K compared with experimental phase boundary data [26] (a), and binary interpolation of the isothermal section of the Ti-Nb-Ta system plotted at 823 K compared with experimental phase boundary data [26] (b).	56
3.12	Enthalpy of formation of the bcc phase predicted by the previous thermodynamic modeling (solid line) at 300 K and the ternary assessed thermodynamic modeling (red dotted line) versus the present first-principles calculations (circles) at 0 K.	57
3.13	Ternary assessed isothermal section of the Ti-Nb-Ta system plotted at 673 K compared with experimental phase boundary data [26] to ensure accuracy of the ternary assessment (a), and ternary assessed isothermal section at 823 K compared with experimental phase boundary data [26] to ensure accuracy of the ternary assessment (b).	58
3.14	Binary interpolation of the isothermal section of the Ti-Nb-Zr system plotted at 843 K compared with experimental phase boundary and two-phase region data [27] (a), and enthalpy of formation of the bcc phase predicted by the previous thermodynamic modeling (solid line) at 300 K versus the present first-principles calculations (circles) at 0 K (b).	59
3.15	Binary interpolation of the isothermal section of the Ti-Ta-Zr system plotted at 1273 K compared with experimental phase boundary data [28,29] (a), and binary interpolation of the isothermal section of the Ti-Ta-Zr system plotted at 1773 K compared with experimental single phase and two-phase region data [28,29] (b).	60
3.16	Enthalpy of formation of the bcc phase predicted by the previous thermodynamic modeling (solid line) at 300 K versus the present first-principles calculations (circles) at 0 K.	61
4.1	Calculated phonon dispersion curve of bcc-Ta, compared with neutron diffraction experiments (\circ) [30] along with the phonon DOS.	74
4.2	Calculated phonon dispersion curve of bct-Sn on the left and phonon DOS on the right. The open squares (\square) are the LO and TO modes from Raman [31] and the filled squares the theoretical prediction of the LO and TO modes at the M point [31].	75
4.3	Calculated phonon dispersion curve for $TaSn_2$ at 0 K and the phonon DOS.	76
4.4	Calculated phonon dispersion curve of Ta_3Sn at 0 K on the left and the phonon DOS on the right.	77

4.5	Comparison of the enthalpy and entropy of bcc-Ta from the Debye model (solid line) and the quasiharmonic phonon calculations (red dotted line) to the SGTE data (blue dashed line) [32].	78
4.6	Comparison of the enthalpy and entropy of bct-Sn from the Debye model (solid line) and the quasiharmonic phonon calculations (red dotted line) to the SGTE data (blue dashed line) [32].	79
4.7	Heat capacity, enthalpy and entropy of TaSn_2 using the Debye model (solid line) and the quasiharmonic phonon calculation (red dotted line) from first-principles calculations, compared with those from the current CALPHAD modeling (blue dashed line).	80
4.8	Heat capacity, enthalpy and entropy of Ta_3Sn using the Debye model (solid line) and the quasiharmonic phonon calculation (red dotted line) compared with those from the current CALPHAD modeling (blue dashed line).	81
4.9	Enthalpy of formation of the bcc phase of the Sn-Ta system as a function of composition at 298 K and ambient pressure from the current CALPHAD modeling (solid line) and from the first-principles calculations at 0 K (dots), showing asymmetric behavior. This was compared with data of the Nb-Sn system from Toffolon et al. [33] (dashed red line) which was modeled using experimental data, showing similar asymmetric behavior.	82
4.10	Calculated Sn-Ta phase diagram using the present thermodynamic description.	83
4.11	Enthalpy of mixing of the liquid phase as a function of composition at 298 K and ambient pressure in the Sn-Ta system.	84
5.1	Elastic stiffness coefficients of the bcc Ti-Ta binary system calculated with the PW91 and PBE exchange correction functions, respectively.	102
5.2	Elastic stiffness coefficients for the bcc Ti-Mo binary system calculated with strains, ± 0.01 , ± 0.013 and ± 0.07 , respectively, showing comparable results.	103
5.3	Calculated \overline{C}_{11} values (circles) plotted with their errors as well as the linear combination of the pure element (red dashed line) and the present modeling (black dashed line) for five Ti-X binary systems ($X = \text{Mo, Nb, Ta, Sn, Zr}$). Ti-Mo, Ti-Nb, and Ti-Ta alloys are compared with previous calculations from Ikehata et al. [2].	104

5.4	Calculated \bar{C}_{12} values (circles) plotted with their errors as well as the linear combination of the pure element (red dashed line) and the present modeling (black dashed line) for five Ti-X binary systems ($X = \text{Mo, Nb, Ta, Sn, Zr}$). Ti-Mo, Ti-Nb, and Ti-Ta alloys are compared with previous calculations from Ikehata et al. [2].	105
5.5	Calculated \bar{C}_{44} values (circles) plotted with their errors as well as the linear combination of the pure element (red dashed line) and the present modeling (black dashed line) for five Ti-X binary systems ($X = \text{Mo, Nb, Ta, Sn, Zr}$). Ti-Mo, Ti-Nb, and Ti-Ta alloys are compared with previous calculations from Ikehata et al. [2].	106
5.6	Young's modulus E of the Ti-X binary systems. The present calculations are plotted as the filled circles with the error bars. The dotted purple line is the Voigt upper Young's modulus bound, the gold dot dashed line is the lower Reuss Young's modulus bound and the black line is the Hill Young's modulus average. The experimental values [1–5, 7, 8, 34–36] are also included for comparison.	107
5.7	Young's moduli mapped as a function of composition from bcc Ti to bcc X ($X = \text{Mo, Nb, Sn, Ta, Zr}$).	108
5.8	Calculated \bar{C}_{11} - \bar{C}_{12} values (circles) plotted with the present modeling (solid lines) for five Ti-X binary systems ($X = \text{Mo, Nb, Ta, Sn, Zr}$). The \bar{C}_{11} - \bar{C}_{12} shows the stability of the bcc phase. When the \bar{C}_{11} - \bar{C}_{12} value is negative the bcc phase is not stable in the corresponding composition ranges.	109
5.9	Bulk moduli B of the Ti-X binary systems. The present calculations are plotted as the filled circles with the error bars. The dotted purple line is the Voigt upper bulk modulus bound, the gold dot dashed line is the lower Reuss bulk modulus bound and the black line is the bulk modulus from the Hill approach.	110
5.10	Shear moduli G of the Ti-X binary systems. The present calculations are plotted as the filled circles with the error bars. The dotted purple line is the Voigt upper shear modulus bound, the gold dot dashed line is the lower Reuss shear modulus bound and the black line is the shear modulus from the Hill approach.	111

- 5.11 Young's moduli values of multicomponent bcc Ti alloys measured experimentally plotted against the predicted Young's moduli from the pure elements and binary interaction parameters with the black diagonal line showing the exact correlation between the experimental and calculated values. Error in the experiments and the bounds from Reuss and Voigt approximations are plotted as the vertical and horizontal error bars, respectively. The variance in the first-principles calculations from Eq.2.18-Eq.2.20 was averaged and plotted as the grey region. More information on the alloys is in Table 5.6 [37–39]. 112
- 6.1 \overline{C}_{11} values (circles) from the current first-principles calculations plotted with their errors as well as the current modeling with (black solid line) and without ternary interaction parameters (red dashed line) for five of the Ti-X-Y binary systems from a 50-50 mixture of the alloying elements $X_{0.5}Y_{0.5}$ to Ti ($X \neq Y = Mo, Nb, Ta, Sn, Zr$). 129
- 6.2 \overline{C}_{11} values (circles) from the current first-principles calculations plotted with their errors as well as the current modeling with (black solid line) and without ternary interaction parameters (red dashed line) for five of the Ti-X-Y binary systems from a 50-50 mixture of the alloying elements $X_{0.5}Y_{0.5}$ to Ti ($X \neq Y = Mo, Nb, Ta, Sn, Zr$). 130
- 6.3 \overline{C}_{12} values (circles) from the current first-principles calculations plotted with their errors as well as the current modeling with (black solid line) and without ternary interaction parameters (red dashed line) for five of the Ti-X-Y binary systems from a 50-50 mixture of the alloying elements $X_{0.5}Y_{0.5}$ to Ti ($X \neq Y = Mo, Nb, Ta, Sn, Zr$). 131
- 6.4 \overline{C}_{12} values (circles) from the current first-principles calculations plotted with their errors as well as the current modeling with (black solid line) and without ternary interaction parameters (red dashed line) for five of the Ti-X-Y binary systems from a 50-50 mixture of the alloying elements $X_{0.5}Y_{0.5}$ to Ti ($X \neq Y = Mo, Nb, Ta, Sn, Zr$). 132
- 6.5 \overline{C}_{44} values (circles) from the current first-principles calculations plotted with their errors as well as the current modeling with (black solid line) and without ternary interaction parameters (red dashed line) for five of the Ti-X-Y binary systems from a 50-50 mixture of the alloying elements $X_{0.5}Y_{0.5}$ to Ti ($X \neq Y = Mo, Nb, Ta, Sn, Zr$). 133
- 6.6 \overline{C}_{44} values (circles) from the current first-principles calculations plotted with their errors as well as the current modeling with (black solid line) and without ternary interaction parameters (red dashed line) for five of the Ti-X-Y binary systems from a 50-50 mixture of the alloying elements $X_{0.5}Y_{0.5}$ to Ti ($X \neq Y = Mo, Nb, Ta, Sn, Zr$). 134

6.7	\overline{C}_{11} - \overline{C}_{12} values (symbols) from the current first-principles calculations plotted with the current modeling (lines) plotted from a 50-50 mixture of the alloying elements X and Y to Ti ($X \neq Y = Mo, Nb, Ta, Sn, Zr$). The \overline{C}_{11} - \overline{C}_{12} shows the stability of the bcc phase, when the value is negative the bcc phase is not stable in the corresponding composition ranges.	135
6.8	Young's modulus of five Ti-X-Y ternary systems plotted from a 50-50 mixture of the alloying elements to Ti in the bcc phase. The present calculations are plotted as filled circles with the error bars. The red dotted line is without the ternary interaction parameters. The dotted purple line is the Voigt upper Young's modulus bound, the gold dot dashed line is the lower Reuss Young's modulus bound and the black line is the Hill Young's modulus average. Experimental values are included for comparison [38–41].	136
6.9	Young's modulus of five Ti-X-Y ternary systems plotted from a 50-50 mixture of the alloying elements to Ti in the bcc phase. The present calculations are plotted as filled circles with the error bars. The red dotted line is without the ternary interaction parameters. The dotted purple line is the Voigt upper Young's modulus bound, the gold dot dashed line is the lower Reuss Young's modulus bound and the black line is the Hill Young's modulus average. Experimental values are included for comparison [38–41].	137
6.10	Young's modulus in GPa mapped as a function of composition for the Ti-Mo-Nb, Ti-Mo-Sn, Ti-Mo-Ta, Ti-Mo-Zr and Ti-Nb-Sn alloy systems using pycalphad [42].	138
6.11	Young's modulus in GPa mapped as a function of composition for the Ti-Mo-Nb, Ti-Mo-Sn, Ti-Mo-Ta, Ti-Mo-Zr and Ti-Nb-Sn alloy systems using pycalphad [42].	139
6.12	Bulk modulus in GPa mapped as a function of composition for the Ti-Mo-Nb, Ti-Mo-Sn, Ti-Mo-Ta, Ti-Mo-Zr and Ti-Nb-Sn alloy systems using pycalphad [42].	140
6.13	Bulk modulus in GPa mapped as a function of composition for the Ti-Nb-Ta, Ti-Nb-Zr, Ti-Sn-Ta, Ti-Sn-Zr and Ti-Ta-Zr alloy systems using pycalphad [42].	141
6.14	Shear modulus in GPa mapped as a function of composition for the Ti-Mo-Nb, Ti-Mo-Sn, Ti-Mo-Ta, Ti-Mo-Zr and Ti-Nb-Sn alloy systems using pycalphad [42].	142
6.15	Shear modulus in GPa mapped as a function of composition for the Ti-Nb-Ta, Ti-Nb-Zr, Ti-Sn-Ta, Ti-Sn-Zr and Ti-Ta-Zr alloy systems using pycalphad [42].	143

6.16	E of multicomponent bcc Ti alloys predicted from the database compared with measured experimental results. Vertical error bars plotted are from the variation in experimental data for given multi-component alloys, and horizontal error bars Voigt-Reuss bounds from the DFT-based first-principles. The grey region refers to the error introduced from the elastic stiffness coefficients in the first-principles calculations. More information on the alloys is Table 6.4 [37–39].	144
7.1	Calculated c_{11} , c_{12} , c_{13} , c_{22} , and c_{23} values (circles) plotted with the linear combination of the pure elements (red dashed line) and the present modeling (black solid line) for five of the elastic stiffness coefficients of Ti-Nb in the α'' phase.	160
7.2	Calculated c_{33} , c_{44} , c_{55} , and c_{66} values (circles) plotted with the linear combination of the pure elements (red dashed line) and the present modeling (black solid line) for four of the elastic stiffness coefficients of Ti-Nb in the α'' phase.	161
7.3	Calculated c_{11} , c_{12} , c_{13} , c_{33} , and c_{44} values (circles) plotted with the linear combination of the pure elements (red dashed line) and the present modeling (black solid line) for the elastic stiffness coefficients of Ti-Nb in the ω phase.	162
7.4	Calculated c_{11} , c_{12} , c_{13} , c_{33} , and c_{44} values (circles) plotted with the linear combination of the pure elements (red dashed line) and the present modeling (black solid line) for the elastic stiffness coefficients of Ti-Nb in the hcp phase.	163
7.5	Elastic properties of the bcc, hcp, ω , α'' phases in the Ti-Nb system calculated from first-principles based on DFT are plotted as symbols. The CALPHAD fittings are plotted as the dashed lines. The figure is plotted from pure Ti to pure Nb.	164
7.6	Formation energies of the bcc, hcp, ω , α'' phases in the Ti-Nb system are plotted from pure Ti to pure Nb.	165
7.7	Formation energies of the bcc, hcp, ω , α'' phases in the Ti-Ta system are plotted from pure Ti to pure Ta.	166
7.8	Martensitic transformation temperature is plotted versus the Ti-Nb composition.	167
7.9	Phonon density of states for the Ti-Nb alloy at 20 at. % Nb. The dashed line represents the slow cooled sample while the solid line represents the quenched sample.	168

7.10 Phonon density of states for the Ti-Nb alloy at 18 at. % Nb. The dashed line represents the slow cooled sample while the solid line represents the quenched sample.	169
7.11 Phonon density of states for the Ti-Nb alloy at 12 at. % Nb. The dashed line represents the slow cooled sample while the solid line represents the quenched sample.	170
7.12 Phonon density of states for the Ti-Nb alloy at 10 at. % Nb. The dashed line represents the slow cooled sample while the solid line represents the quenched sample.	171
7.13 Entropy difference between the Ti-Nb alloys with the same alloy composition as a function of temperature.	172
7.14 Diffraction pattern of the Ti-Nb alloy at 20 at. % Nb. The dashed line represents the slow cooled sample while the solid line represents the quenched sample.	173
7.15 Diffraction pattern of the Ti-Nb alloy at 18 at. % Nb. The dashed line represents the slow cooled sample while the solid line represents the quenched sample.	174
7.16 Diffraction pattern of the Ti-Nb alloy at 12 at. % Nb. The dashed line represents the slow cooled sample while the solid line represents the quenched sample.	175
7.17 Diffraction pattern of the Ti-Nb alloy at 10 at. % Nb. The dashed line represents the slow cooled sample while the solid line represents the quenched sample.	176
7.18 Ti-Nb phase diagram with the hcp suspended, shows the formation of the ω and bcc phase as well as the phase fractions.	177

List of Tables

1.1	Young's moduli of common implant materials compared with the Young's modulus of bone [43].	6
3.1	Equilibrium properties energy E_0 , bulk modulus B and the lattice parameters from the first-principles calculations for each pure elements in their SER state. The presently calculated results are also compared with available experimental data and previously calculated results.	38
3.2	First-principles results at 0 K for the enthalpy of formation (H_{Form}) of the bcc phase for different mole fractions (x) of alloying element X in the Ti-X binary systems (X = Mo, Nb, Ta, Zr).	39
3.3	First-principles results at 0 K for the enthalpy of formation (H_{Form}) of the bcc phase for different mole fractions (x) of Ti in the Ti-X-Y ternary systems (X ≠ Y = Mo, Nb, Ta, Zr).	40
3.4	Modelled binary and ternary thermodynamic parameters for the Ti-Mo-Nb-Ta-Zr system. The thermodynamic description of pure elements is not included. The pure element functions, such as GFCCTI, describe the Gibbs energy (G) of the phase (fcc) for the element (Ti) were adopted from the SGTE database [32] are listed in the Supplementary TDB (thermodynamic database) file (appendix A).	41
3.4	Modelled binary and ternary thermodynamic parameters for the Ti-Mo-Nb-Ta-Zr system. The thermodynamic description of pure elements is not included. The pure element functions, such as GFCCTI, describe the Gibbs energy (G) of the phase (fcc) for the element (Ti) were adopted from the SGTE database [32] are listed in the Supplementary TDB (thermodynamic database) file (appendix A).	42

3.4	Modelled binary and ternary thermodynamic parameters for the Ti-Mo-Nb-Ta-Zr system. The thermodynamic description of pure elements is not included. The pure element functions, such as GFCCTI, describe the Gibbs energy (G) of the phase (fcc) for the element (Ti) were adopted from the SGTE database [32] are listed in the Supplementary TDB (thermodynamic database) file (appendix A).	43
3.4	Modelled binary and ternary thermodynamic parameters for the Ti-Mo-Nb-Ta-Zr system. The thermodynamic description of pure elements is not included. The pure element functions, such as GFCCTI, describe the Gibbs energy (G) of the phase (fcc) for the element (Ti) were adopted from the SGTE database [32] are listed in the Supplementary TDB (thermodynamic database) file (appendix A).	44
3.4	Modelled binary and ternary thermodynamic parameters for the Ti-Mo-Nb-Ta-Zr system. The thermodynamic description of pure elements is not included. The pure element functions, such as GFCCTI, describe the Gibbs energy (G) of the phase (fcc) for the element (Ti) were adopted from the SGTE database [32] are listed in the Supplementary TDB (thermodynamic database) file (appendix A).	45
4.1	Lattice parameters from first-principles calculations compared with experimental values.	70
4.2	Equilibrium volume V_0 , bulk modulus B , and the first derivative of bulk modulus with respect to pressure B' , from fitted equilibrium properties from the EOS at 0 K compared to experimental work and previous DFT studies.	71
4.3	Elastic stiffness coefficients and elastic properties predicted using the Hill approach and the scaling factors used in the Debye model, calculated from the Poisson ratio, see Eq. 2.12. To ensure the accuracy of the calculated scaling factor, the bulk modulus (B_{cij}) calculated from the elastic coefficients was compared to the B_{EOS} calculated from the EOS fitting Eq. 2.6.	72
4.4	Modeled parameters in SI units in the present work for the phases in the Sn-Ta binary system. These parameters were incorporated with the SGTE data for the pure elements [32].	73

5.1	Calculated pure element elastic stiffness coefficients and the bulk modulus B (in GPa) by X-C functional of PBE are compared with the previous first-principles calculations (FP) by X-C functional PW91 and experiments (Expt). Sv, pv and d referring to the s, p, and d states being treated as valance, respectively.	94
5.2	Evaluated interaction parameters L_0 and L_1 using the R-K polynomial Eq. 2.32 for the elastic stiffness coefficients for the Ti-X binary systems.	95
5.3	First-principles calculations of the elastic stiffness coefficients \bar{C}_{11} , \bar{C}_{12} , and \bar{C}_{44} for different atomic percent compositions of the bcc Ti-X binary systems at 0 K.	96
5.3	First-principles calculations of the elastic stiffness coefficients \bar{C}_{11} , \bar{C}_{12} , and \bar{C}_{44} for different atomic percent compositions of the bcc Ti-X binary systems at 0 K.	97
5.4	First-principles calculations of the bulk modulus B , shear modulus G , and Young's modulus E in GPa for different atomic percent compositions of the bcc Ti-X binary systems at 0 K. As well as experimental data for the Young's modulus obtained at 300 K by the reference stated.	98
5.4	First-principles calculations of the bulk modulus B , shear modulus G , and Young's modulus E in GPa for different atomic percent compositions of the bcc Ti-X binary systems at 0 K. As well as experimental data for the Young's modulus obtained at 300 K by the reference stated.	99
5.5	Compositions of the binary alloys that fall in the target E range compared to the bcc phase stability can predict the alloy compositions where the E is close to bone and the bcc phase is stable and those compositions can be targeted.	100
5.6	Predicted Young's moduli (in GPa) of higher order alloys in the bcc phase compared to experimental values found with both the weight percent and atomic percent listed.	101
6.1	First-principles calculations of the elastic stiffness coefficients for different atomic percent compositions of the bcc Ti-X-Y ternary systems at 0 K.	123
6.1	First-principles calculations of the elastic stiffness coefficients for different atomic percent compositions of the bcc Ti-X-Y ternary systems at 0 K.	124

6.2	First-principles calculations of the bulk modulus B , shear modulus G , and Young's modulus E in GPa for different atomic percent compositions of the bcc Ti-X-Y ternary systems at 0 K as well as experimental data obtained for the Young's modulus at 300 K by the references stated.	125
6.2	First-principles calculations of the bulk modulus B , shear modulus G , and Young's modulus E in GPa for different atomic percent compositions of the bcc Ti-X-Y ternary systems at 0 K as well as experimental data obtained for the Young's modulus at 300 K by the references stated.	126
6.3	Evaluated interactions parameters (L_2 , Eq. 2.24) for the elastic stiffness coefficients of the Ti-containing ternary alloys.	127
6.4	Predicted Young's moduli (E) (in GPa) of higher order alloys using the binary and ternary interaction parameters in the bcc phase compared to the predicted Young's moduli (E_{BIN}) using just the binary interaction parameters and the experimental values found with both the weight percent and atomic percent listed.	128
7.1	Evaluated interaction parameters L_0 and L_1 , using Eq. 2.32, for the elastic stiffness coefficients of the hcp, α'' and ω phases in the Ti-Nb systems.	154
7.2	Results of the first-principles calculations of the elastic stiffness coefficients in GPa for different atomic percent compositions in the α'' , bcc, hcp, and ω phases in the Ti-Nb system at 0 K.	155
7.2	Results of the first-principles calculations of the elastic stiffness coefficients in GPa for different atomic percent compositions in the α'' , bcc, hcp, and ω phases in the Ti-Nb system at 0 K.	156
7.3	Phase fractions and experimentally determined E (averaged from the data in appendix F [6, 8, 8, 9]) compared with the predicted E using the rule of mixtures and interaction parameters in Table 7.1 for the Ti-Nb system. The * denotes the estimated phase fractions as opposed to the experimentally determined phase fractions with no *.	157
7.4	Phase fractions determined from the diffraction patterns for the Ti-Nb alloys.	158
7.5	Phase fractions determined from the diffraction patterns and the current phase diagram modeling for the bcc and ω phase in the Ti-Nb system.	159

Acknowledgments

The completion of graduate school and this dissertation could not have been possible without the support from many people that I would like to thank now.

First off I would like to thank my PhD advisor Dr. Zi-Kui Liu. I am so grateful to him for his guidance and support throughout my graduate school career. He opened the doors for many wonderful opportunities and I learned more than I thought was imaginable. On top of that he continued to push me and help me try and learn new things. His constant positive attitude and outlook on life has been inspirational to be me and I will continue to benefit from this for the rest of my life.

I want to thank the Penn State Materials Science and Engineering Department. There have been multiple staff, faculty, and external advisory board members who have helped me, mentored me and opened the door to new opportunities. I would like to specifically thank my committee members Dr. Allison Beese, Dr. Kristen Fichthorn, Dr. Michael Manley and Dr. Susan Sinnott for their time, constructive criticism and advice throughout this journey.

I want to thank Dr. Ji-Cheng Zhao, Dr. Michael Manley, and Dr. Yong Du. Each of you gave me the opportunity to learn new things and expand my PhD experience through collaborations, and allowing me to visit your labs.

I want to express my deepest thanks to my family. I am lucky to have multiple family members who support and love me including my parents Shannon and Peter, my siblings Kaitlyn, Andy and Colin, my grandparents Stella and Jerry, my nieces, and my cousins the Halfmann's and the Cheney's. There were many ups and downs in my educational pursuit and you were each there for me in multiple different ways and I am very grateful.

I would also like to thank the members of the Phases Research Lab past and present. It was an honor to get to work with so many wonderful people and to connect with previous members. I learned a lot from each of you and formed many lasting friendships amongst the group. Listing all of the members that positively impacted my life would take up too much space but I wanted to thank the members who served as mentors to me and helped me get my footing, Dr. Shun-Li Shang,

Dr. Richard Otis, Dr. Greta Lindwall, and Dr. Xuan Liu. Additionally, I would like to thank the members who collaborated and helped me with my research, Dr. Yong-Jie Hu, Dr. Bi-Cheng Zhou, Austin Ross, Hongyeun Kim, Pinwen Guan, and Brandon Bocklund.

Lastly, I want to thank all of my friends at Penn State, my significant other Tobias Frueh, and all of my CALPHAD friends. While there are many people here to name, I would like to especially thank Carl Arvhult, Chris Rotella, Dan Schulman, Ethan Kahn, Florian Tang, Lyndsey Denis, Nathan Smith, Tessa Davey, Timothy Lichtenstein, and Timothy Pillsbury. Without all of you in my life I do not know what I would do. Graduate school can be difficult but with you guys I enjoyed it every step of the way. I found a family here with all of you and became part of a group of misfit toys, nomad chemistry and a cohort. You taught me new things, explored new places with me, and served as constant support. I will never be able to express how thankful I am to have you all in my life and how fondly I will look back at all of the things we did during this time. I am truly looking forward to all of our future adventures.

Dedication

For my papa, Dr. Jerry Cash. Thank you for inspiring me to get my PhD, helping me improve my writing and listening to me talk about my research. I am so fortunate to have such a wonderful and inspiring grandpa. I love you

Chapter 1

Introduction

1.1 Motivation

Titanium (Ti) and its alloys have been used in biomedical applications for many years because of their biocompatibility and corrosion resistance properties [43]. In recent years, there has been an increasing interest in developing better materials for load-bearing implants, due to the increase in total knee and hip replacements. Krutz et al. [44] predicted that the total number of hip and knee replacements would increase by 174% and 673%, respectively, from 2005 to 2030, leading to 572,000 hip and 3.48 million knee procedures in the United States in 2030. Two of the driving factors for this situation involve the increasing number of younger individuals requiring replacements and the fact that the average life of these implants is only about 7-12 years [45]. These factors contribute significantly to the necessity for better implant materials. The primary considerations for biomedical implants, such as load-bearing knee and hip implants, are biocompatibility, corrosion resistance, fatigue strength, and Young's modulus (E) [43]. In previous years, the most common implants for these applications have been Ti-6Al-4V, stainless steels, and MoCoCr alloys [40, 46]. However, there have been issues with these materials, such as cytotoxicity that has been observed with alloys containing aluminum and vanadium [47]. Another important impediment concerning the common implant materials is stress shielding, which can lead to implant failure. Stress shielding occurs when the E of the implant is higher than that of bone. Due to the difference in Young's moduli, load applications to the joint result in the implant material absorbing all of the stress and causing the bone surrounding the implant to

atrophy, which leads to a loss in bone density, and can result in implant loosening and failure [43]. Table 1.1 summarizes the comparison of the Young's moduli of common implant materials (> 100 GPa) to bone (10-40 GPa) [43] and shows the extreme elasticity mismatch between the various materials. Using computational thermodynamics to develop a knowledge base of Ti and its alloys is an extremely useful tool in overcoming these challenges.

This work focused on investigating the thermodynamic and elastic properties of the biocompatible Ti-Mo-Nb-Sn-Ta-Zr system. The thermodynamic and elastic properties were calculated using first-principles calculations based on Density Functional Theory (DFT). The parametrization of the properties was completed using the CALPHAD modeling approach. A new computational methodology to predict the metastable phase formation was presented and verified by neutron scattering experiments. The culmination of this work provides a fundamental understanding of the thermodynamics and elastic properties for the Ti-Mo-Nb-Sn-Ta-Zr system.

1.2 Overview

1.2.1 Equilibrium Phases

The phase stability of Ti alloys has been shown to greatly affect the mechanical properties of these materials, so predicting and understanding this aspect of a Ti alloy will greatly impact its effectiveness as a biomedical implant. Titanium is stable in the α (hexagonal close packed, hcp) phase (space group $P6_3/mmc$) under standard temperature and pressure. However, at temperatures above 1155 K, Ti is stable in the β (body centered cubic, bcc) phase (space group $Im\bar{3}m$). The bcc phase can also be stabilized by alloying, and such bcc Ti alloys have received much attention because of their low E values. Ti in the hcp phase has a E of 105 GPa while, Ti-6Al-4V which is a two-phase mixture of hcp and bcc has an E of 110 and the Ti-35Nb-5Ta-7Zr alloy in the bcc phase has a E of 55 GPa which is more comparable to that of bone (10-40 GPa) [43, 48–51]. Other alloys such as Ti-13Nb-13Zr, Ti-35Nb-5Ta-7Zr-0.4O, Ti-29Nb-Ta-Zr, and Ti-25Nb-Ta-Zr, which are all bcc alloys, have a E of between 57 and 71 GPa [37, 43, 52]. With phase stability playing an important role in the alloy selection for load-bearing implants,

it is important to study how to stabilize the bcc phase at low temperature (<1155 K). Mo, Nb and Ta were all chosen to be studied because they are biocompatible elements and strong β -stabilizers, while Zr is a biocompatible weak β -stabilizer individually but strong stabilizer when in combination with other elements, such as Mo, Nb, and Ta [43]. In conjunction with their biocompatibility, studies have shown Mo, Nb, Ta and Zr have excellent corrosion resistance and no allergy problems [52]. Recently, Sn has also been studied for use in Ti-alloys, due to its low cost [40] and in small concentrations, Sn does not affect the biocompatibility of the alloy.

While many bcc Ti-alloys have been shown to have a E more closely matching that of bone, in some cases a bcc Ti-alloy can miss the mark and not have a E that comes close to matching bone. Such an example is Ti-16Nb-13Ta-4Mo which has E of 110 GPa [38]. So, while understanding the thermodynamics of the system will help to target the bcc phase, also being able to predict the elastic properties before attempting to develop alloys for biomedical implants will reduce the need for trial and error and narrow the scope of alloys being selected for experimental investigation. Therefore, the present study focused on determining the effects of alloying Ti with Mo, Nb, Sn, Ta and Zr on the thermodynamic and elastic properties. The integrated first-principles calculations based on DFT and the CALPHAD approach was used to evaluate previous models and new models for the binary and ternary alloys in the Ti-Mo-Nb-Sn-Ta-Zr system to build a completed database describing the thermodynamic and elastic properties of the system.

1.2.2 Metastable Phases

The completed thermodynamic database predicts the formation of the equilibrium phases, hcp and bcc. Based on the predictions, alloys that are in the bcc phase can be targeted and their elastic properties predicted. However, Ti and its alloys can form two metastable phases, α'' and ω . α'' is an orthorhombic martensitic phase (space group Cmcm). The martensitic transformation is displacive [53, 54]. Thermodynamically the martensitic transformation is first-order and initiated by supercooling. An applied stress can also contribute to the driving force for a martensitic transformation. Kinetically the martensitic transformation propagates in an athermal manner. The ω phase is a metastable hexagonal phase (space group P6/mmm) of Ti that has lattice parameters closely matching that of bcc Ti. The

ω phase has been seen to form athermally when Ti is alloyed with β stabilizing elements such as Mo, Nb and Ta. It has been shown that different cooling techniques of alloys at certain compositions in the Ti-Mo, Ti-Nb and Ti-Ta systems cause either the α'' phase or the ω phase to form with a matrix of untransformed bcc phase. Quenching the samples leads to the formation of α'' , while slow cooling the samples leads to the formation of ω phase. The formation of these phases causes variations to the predicted elastic properties as seen in Figure 1.1 and 1.2, where the closed symbols represent the calculated E and the open symbols represent the experimentally determined E from the literature. The calculations and experiments agree well on the Ti-rich and Ta or Nb-rich sides but in the 0.10 to 0.35 x(Ta) and 0.10 to 0.30 x(Nb) regions, the experiments show a higher E than predicted by calculations. This is due to the formation of α'' and ω . While the formation of the metastable phases greatly effects the properties of the Ti-alloys, there is no current way to predict their formation.

In this dissertation, the modeling of these phases and the effect on the elastic properties was studied for the Ti-Nb and Ti-Ta systems. Initially, the elastic properties the α'' , ω , bcc and hcp phases were calculated for the Ti-Nb system. Using experimentally determined phase fractions, the rule of mixtures was then used to predict the Young's modulus of Ti-Nb alloys from the literature to validate the accuracy of the database. The focus then changed to studying and modeling the thermodynamic properties of these phases. The formation energy of the four phases at 0 K was calculated for multiple different structures across the entire Ti-Nb and Ti-Ta composition range. The finite temperature properties were then studied. Inelastic neutron scattering experiments were then completed to study the phonon DOS and phase fractions of four different Ti-Nb compositions.

This completed thesis consists of the following main tasks:

1. The thermodynamics of the Ti-Mo-Nb-Sn-Ta-Zr system was investigated using first-principles calculations based on DFT and the CALPHAD method.
 - (a) Previous binary models were evaluated with the available experimental data as well as the calculated enthalpy of formation of the bcc phase
 - (b) The thermodynamic description of the Sn-Ta binary alloy was modeled
 - (c) The thermodynamic descriptions of the Ti-containing ternary alloys were modeled
2. The elastic properties of the Ti-Mo-Nb-Sn-Ta-Zr system in the bcc phase were systematically calculated using first-principles calculations based on DFT. The results were used to obtain interaction parameters, following the CALPHAD method, to predict the elastic properties as a function of composition.
3. The metastable phase formation in Ti alloys was investigated by first-principles calculations and experiments carried out for the Ti-Nb and Ti-Ta systems
 - (a) The elastic properties of the Ti-Nb system in the hcp, bcc, ω and α'' were predicted using first-principles calculations and compared to experimentally determined elastic properties
 - (b) The thermodynamic properties, phase fractions and improved modeling of the α'' , ω , hcp, and bcc phases were studied for the Ti-Nb and Ti-Ta systems using DFT-based first-principles calculations and is still in progress.
 - (c) The phonon density of states and phase fractions were studied for the Ti-Nb system at four different compositions using inelastic neutron scattering.

Table 1.1: Young's moduli of common implant materials compared with the Young's modulus of bone [43].

Alloy	Young's Modulus (GPa)
Bone	10-40
cp-Ti*	105
Ti-6Al-4V	110
Stainless Steel	200
CoCrMo	200-230

*cp-commercially pure titanium

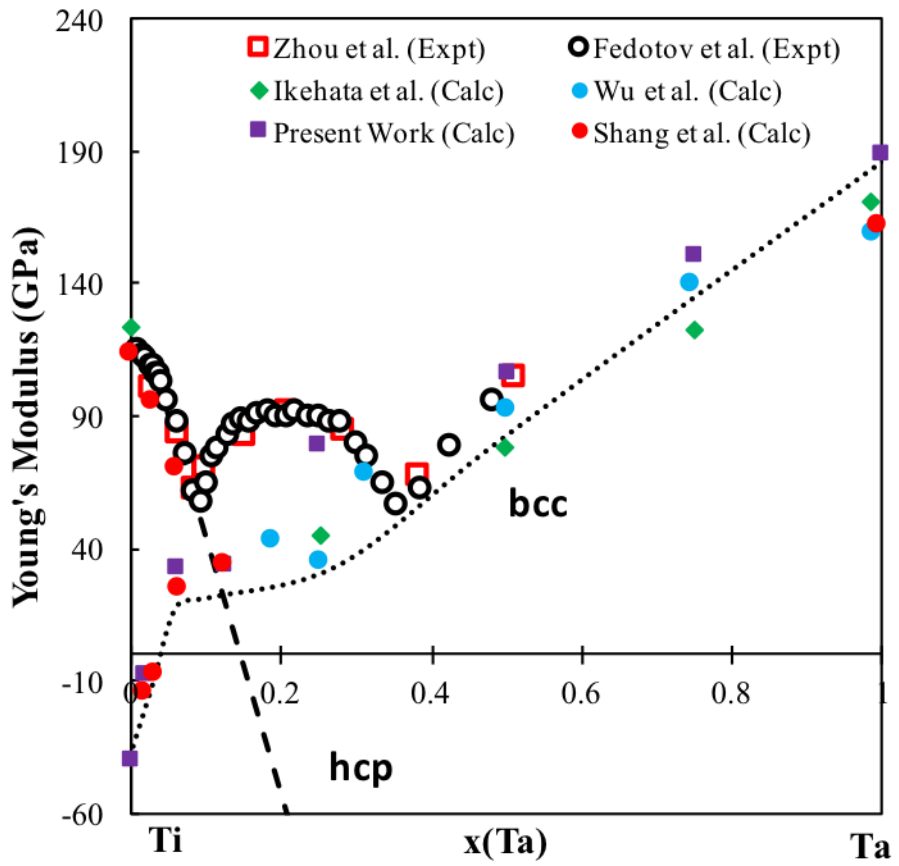


Figure 1.1: Comparison of first-principles calculations [1, 2] and experimental measurements of the Young's moduli of Ti-Ta alloys [3–5]. From 0.10 to 0.35 $x(\text{Ta})$ the calculations and experimentally determined E do not match up due to the formation of two metastable phases ω and α''

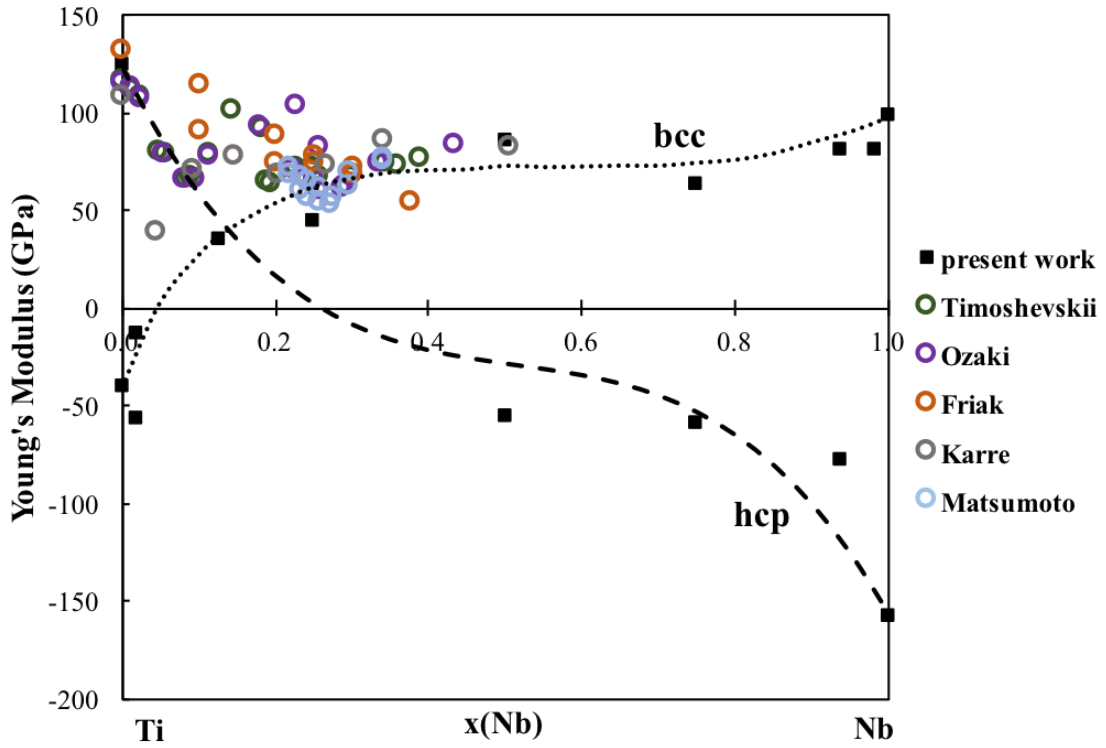


Figure 1.2: Comparison of the present first-principles calculations and experimental measurements of the Young's moduli of Ti-Nb alloys [6–10]. From 0.10 to 0.30 $x(\text{Nb})$ the calculations and experimentally determined E do not match up due to the formation of two metastable phases ω and α''

Chapter 2

Methodology

2.1 First-Principles Calculations

In this dissertation, the ground state energy structures, thermodynamic properties and mechanical properties of Ti and Ti-alloys were calculated using first-principles based on Density Functional Theory. The first-principles refers to the calculations originating from "first-principles", meaning that the inputs were the atomic coordinates and atomic numbers. The first-principles method computes the interactions between atoms in a periodic supercell. This was determined using quantum mechanical electronic theory that is based on the electronic charge density and does not rely on any empirical data. This section provides a description of the DFT methodology.

Schrödinger's time-independent non-relativistic equation is a solution to the many-body problem of calculating the interactions of positively charged nuclei and negatively charged electrons. The Schrödinger equation is:

$$\left[\sum_{i=1}^N \left(-\frac{\hbar^2}{2m} \nabla_i^2 + V_{ext}(r_i) \right) + \sum_{i < j} U(r_i, r_j) \right] \Psi = E_s \Psi \quad (2.1)$$

where the first bracketed part represents the Hamiltonian (\hat{H}), Ψ describes the wave function of electrons, and E_s describes the energy of the system. The \hat{H} of the system is described by three parts, the first part represents the kinetic energy with N being the total number of electrons in the system, \hbar being Planck's constant and m the mass of an electron. The second term V_{ext} is the external potential and U is the potential of the electron-electron repulsion.

Eq. 2.1 can be solved for Ψ assuming the nuclei-nuclei interactions can be neglected due to the Born-Oppenheimer approximation. The Born-Oppenheimer approximation allows the assumption that the motion of the nuclei on the electronic timescale can be ignored, due to the mass difference, with the nuclei being $\sim 10^3$ to 10^5 larger than electrons. However, even with this approximation solving Eq. 2.1 is difficult due to the electron-electron Columb interactions making the electronic motion correlated and the fact that the many-body problem results in too many variables because there are $3N$ degrees of freedom.

Hohenberg-Kohn formulated two theorems to simplify this problem [55]. The first theorem states that the external potential is a unique functional of the electron density. The second theorem states that the density that minimizes the total energy is the exact ground state density and thus the ground state is obtained variationally. With these theorems, Kohn-Sham proved that the problem can be solved as if the electrons are not interacting and still obtain the density as if they were, by [56]:

$$\left[-\frac{\hbar^2}{2m} \nabla^2 + V_{ext}(r) + V_{Hartree}(r) + V_{XC}(r) \right] \phi_1(r) = \epsilon_i \psi_i(r) \quad (2.2)$$

where $V_{ext}(r)$ describes the electron-nuclei interaction similar as in Eq. 2.1 and is expressed by:

$$V_{ext} = -e^2 \sum_a \frac{Z_a}{|r_i - R_a|} \quad (2.3)$$

where r_i represents the position of electron i and R_a represents the position of nucleus a with a charge valance of Z_a . The electron-electron interactions are represented by $V_{Hartree}$:

$$V_{Hartree}(r) = e^2 \int \frac{\rho(r)}{|r - r_j|} d^3r \quad (2.4)$$

where r and r_j represent the electrons and $\rho(r)$ is described by:

$$\rho(r) = \sum_i^N |\psi_i(r)|^2 \quad (2.5)$$

The final term, V_{xc} , is the exchange correlation potential that is described in terms of an exchange-correlation energy. While there is no exact solution to the exchange-correlation (X-C) energy available, there are multiple different approximations.

Each approximation is done to account for different things. In the present work, the generalized gradient approximation by Perdew and Wang (PW91) [57] and the generalized gradient approximation by Perdew, Burke and Ernzerhoff (PBE) [58] were used. The generalized gradient approximation improves the total energies and atomization energies compared to other methods such as the local density approximation [59] but can over-correct for the expansion and softening of bonds. The generalized gradient approximation (GGA) is favored for inhomogeneous densities. Based on previous research by Perdew et al. [58], GGA's are considered to be adequate approximations for calculating metals. The PW91 X-C functional was designed to satisfy as many exact conditions as possible and thus has some issues. Perdew introduced the PBE X-C functional as an improvement to PW91 to satisfy less exact conditions and only looked at the ones that were energetically significant for metals. The use of PW91 vs PBE was compared for the elastic results of the Ti-Ta system. The results are discussed in detail in chapter 5 and based on the results the PBE X-C functional was chosen in the present thesis work. By implementing the theorems and the Kohn-Sham equation, the energy of the system can thus be calculated.

2.1.1 Density Functional Theory at 0 K

The ground state energy at 0 K without the contribution of zero-point vibrational energy was calculated by using the equation of states (EOS) fitting for the relationship between the energy and volume of the structure. The EOS fitting was achieved through an energy-volume ($E_0 - V$) curve of 5 or more relaxed volumes and using the four-parameter Birch-Murnaghan (BM4) EOS [60]:

$$E_0(V) = a + bV^{-\frac{2}{3}} + cV^{-\frac{4}{3}} + dV^{-2} \quad (2.6)$$

where a , b , c and d are fitting parameters. From this equation, the equilibrium properties of a structure can be obtained such as, volume V_0 , ground state energy E_0 , bulk modulus B , and first derivative with respect to pressure B' .

From the ground state energies, the enthalpy of formation at 0 K was calculated by:

$$H_{Form} = H_{X_s Y_r} - (sH_X^{SER} + rH_Y^{SER}) \quad (2.7)$$

where $H_{X_s Y_r}$ is the enthalpy of a specific structure at a specific composition ($X_s Y_r$) and s and r are the mole fractions of elements X and Y , respectively. H_X^{SER} and H_Y^{SER} are the enthalpies of the pure elements X and Y in their standard element reference (SER) at standard temperature and pressure. The SER states of the pure elements are hcp Ti, bcc Mo, bcc Nb, bct Sn, bcc Ta, and hcp Zr. The formation energy can be calculated the same way using the energy values instead of enthalpy. The valance configuration for each element was selected based on the Vienna Ab-initio Software Package (VASP) recommendations [61]. The p electrons were treated as valance electrons for the Mo and Ta, the d electrons were treated as valance electrons for Sn and the s electrons were treated as valance electrons for Ti, Nb, and Zr [61, 62].

2.1.2 Finite-temperature thermodynamics

The Helmholtz energy, $F(V, T)$, was calculated, as a function of temperature T and volume V using first-principles based on DFT:

$$F(V, T) = E_0(V) + F_{vib}(V, T) + F_{T-el}(V, T) \quad (2.8)$$

where E_0 is the static contribution at 0 K calculated from Eq. 2.6, F_{vib} is the temperature-dependent vibrational contribution, and F_{T-el} is the thermal electronic contribution. At ambient pressure, the Helmholtz energy of the system is equal to the Gibbs energy, which is used in the CALPHAD modeling. The vibrational contribution was obtained through the phonon quasiharmonic supercell (phonon approach) or the Debye-Grüneisen method (Debye). The phonon approach is a more accurate approach than the Debye model but it is also more computationally expensive. In the present work, both the phonon and Debye models are used in different sections. The vibrational contribution obtained through phonon calculations of at least five different volumes is expressed by [63]:

$$F_{vib}(V, T) = k_b T \int_0^\infty \ln \left[2 \sinh \frac{\hbar \varrho}{2k_B T} \right] g(\varrho) d\varrho \quad (2.9)$$

where $g(\varrho)$ is the phonon density of states as a function of phonon frequency ϱ at volume V . ϱ is normally expressed in the literature as ω , however, due to the extensive discussion of the ω phase in this work the phonon frequency is expressed

as ϱ to avoid confusion. In addition, the Debye model is used to estimate the vibrational contribution by [60]:

$$F_{vib}(V, T) = \frac{9}{8}k_b\theta_D(V) + k_B T \left[3\ln\left(1 - e^{-\frac{\theta_D}{T}}\right) - D\left(\frac{\theta_D}{T}\right) \right] \quad (2.10)$$

where θ_D is the Debye temperature, T is the temperature, and $D\left(\frac{\theta_D}{T}\right)$ is the Debye function. θ_D is calculated through:

$$\theta_D = s \frac{(6\pi^2)^{\frac{1}{3}}\hbar}{k_B} V_0^{\frac{1}{6}} \left(\frac{B}{M}\right)^{\frac{1}{2}} \left(\frac{V_0}{V}\right)^{\gamma} \quad (2.11)$$

where s is the Debye temperature scaling factor, γ is the Grüneisen parameter determined by the pressure derivative of the bulk modulus (B'), B is the bulk modulus, M is the atomic mass, and V_0 is the equilibrium volume. Here the V_0 , B , and B' are estimated from the EOS fitting using Eq. 2.6. The Debye temperature scaling factor was determined by Moruzzi et al. [64] to be 0.617 for nonmagnetic metals. However, this value has been shown to be less accurate for all materials. Liu et al. [65] extensively studied the Debye scaling factor and how to calculate the scaling factor based on the Poisson's ratio of a material. The methodology by Liu et al. [65] was used for the present work to calculate the scaling factor:

$$s(\nu) = 3^{\frac{5}{6}} \left[4\sqrt{2} \left(\frac{1+\nu}{1-\nu}\right)^{\frac{3}{2}} + \left(\frac{1+\nu}{1-\nu}\right)^{\frac{-1}{3}} \right] \quad (2.12)$$

where ν is the Poisson's ratio, which can be calculated from the elastic stiffness coefficients. The calculations are discussed below.

The thermal electronic contribution is based on the electronic density of states and calculated with the Fermi-Dirac statistics [60, 66]:

$$F_{T-el} = E_{T-el} - TS_{T-el} \quad (2.13)$$

The E_{T-el} and S_{T-el} represent the energy and entropy of the thermal electron excitations, respectively. The E_{T-el} is expressed by:

$$E_{T-el}(V, T) = \int n(\epsilon, V) f(\epsilon, T) \epsilon d\epsilon - \int^{\epsilon_f} n(\epsilon) \epsilon d\epsilon \quad (2.14)$$

and the entropy S_{T-el} is expressed by:

$$S_{T-el}(V, T) = -k_B \int n(\epsilon, V) [ln f(\epsilon, T) + (1 - f(\epsilon, T)) ln(1 - f(\epsilon, T))] d\epsilon \quad (2.15)$$

where $n(\epsilon, V)$ is the electronic density of states (DOS) at energy ϵ , $f(\epsilon, T)$ is the Fermi-Dirac distribution, ϵ_f is the Fermi energy level and k_B is Boltzmann's constant. The Fermi-Dirac distribution $f(\epsilon, T)$ is expressed by:

$$f(\epsilon, T) = \left[\exp \left(\frac{\epsilon - \mu}{k_B T} \right) + 1 \right]^{-1} \quad (2.16)$$

where μ is the chemical potential of the electrons.

2.1.3 Elastic stiffness coefficients

The single crystal elastic stiffness coefficients (c_{ij} 's) were calculated from the ground state energy structure using a stress-strain method developed by Shang et al. [67]. With this method, a set of independent strains $\varepsilon = (\varepsilon_1, \varepsilon_2, \varepsilon_3, \varepsilon_4, \varepsilon_5, \varepsilon_6)$ were imposed on the crystal lattice, where $\varepsilon_1, \varepsilon_2$, and ε_3 are the normal strains, $\varepsilon_4, \varepsilon_5$, and ε_6 are the shear strains, generating a set of stresses $\sigma = (\sigma_1, \sigma_2, \sigma_3, \sigma_4, \sigma_5, \sigma_6)$. Hooke's law is then used to calculate the elastic stiffness coefficients:

$$\begin{pmatrix} c_{11} & c_{12} & c_{13} & 0 & 0 & 0 \\ c_{12} & c_{22} & c_{23} & 0 & 0 & 0 \\ c_{13} & c_{23} & c_{33} & 0 & 0 & 0 \\ 0 & 0 & 0 & c_{44} & 0 & 0 \\ 0 & 0 & 0 & 0 & c_{55} & 0 \\ 0 & 0 & 0 & 0 & 0 & c_{66} \end{pmatrix} = \begin{pmatrix} \varepsilon_{1,1} & \varepsilon_{1,n} \\ \varepsilon_{2,1} & \varepsilon_{2,n} \\ \varepsilon_{3,1} & \dots & \varepsilon_{3,n} \\ \varepsilon_{4,1} & \varepsilon_{4,n} \\ \varepsilon_{5,1} & \varepsilon_{5,n} \\ \varepsilon_{6,1} & \varepsilon_{6,n} \end{pmatrix}^{-1} \begin{pmatrix} \sigma_{1,1} & \sigma_{1,n} \\ \sigma_{2,1} & \sigma_{2,n} \\ \sigma_{3,1} & \dots & \sigma_{3,n} \\ \sigma_{4,1} & \sigma_{4,n} \\ \sigma_{5,1} & \sigma_{5,n} \\ \sigma_{6,1} & \sigma_{6,n} \end{pmatrix} \quad (2.17)$$

where "-1" represents the pseudo-inverse. Due to symmetry, the bcc structure has only three independent elastic stiffness coefficients. However, with a lack of bcc stability for some of the calculations, all of the elastic stiffness coefficients were calculated and the average \bar{C}_{11} , \bar{C}_{12} and \bar{C}_{44} values were used:

$$\bar{C}_{11} = \frac{(c_{11} + c_{22} + c_{33})}{3} \quad (2.18)$$

$$\bar{C}_{12} = \frac{(c_{12} + c_{13} + c_{23})}{3} \quad (2.19)$$

$$\bar{C}_{44} = \frac{(c_{44} + c_{55} + c_{66})}{3} \quad (2.20)$$

This case is for the unstable bcc elastic calculations to mimic the behavior of a cubic structure. The largest variance between the similar elastic stiffness coefficients, when calculating the average, was used to show the deviation from the bcc symmetry in the calculations, shown as error bars. The stable bcc structures show no variance and thus no error bars. To examine the effects of different strain on the elastic properties, three groups of non-zero strain magnitudes, ± 0.01 , ± 0.03 , and ± 0.07 , were tested and the results are discussed in chapter 5. After testing, the ± 0.01 was used for all the calculations. The polycrystalline elastic properties including bulk (B), shear (G), and Young's (E) modulus were calculated from the elastic stiffness coefficients, based on the Voigt-Reuss-Hill approach [68]. The Voigt gives the upper elastic bound due to the assumption of constant strain in all grains, the Reuss gives the lower elastic bound due to the assumption of constant stress in all grains, and the Hill approach is the average of Voigt and Reuss and is closer to real values [69, 70]. The Hill approach is hence what is listed in the results section. The Voigt and Reuss bounds were also plotted in the figures to give the bounds of the moduli values.

In order to fully investigate the effects of the alloying elements on the Ti-alloys, the mechanical stability of the bcc phase was studied. The mechanical stability is given by Born's criteria for a cubic crystal [71, 72]:

$$\bar{C}_{11} - |\bar{C}_{12}| > 0 \quad (2.21)$$

$$\bar{C}_{11} + 2\bar{C}_{12} > 0 \quad (2.22)$$

$$\bar{C}_{44} > 0 \quad (2.23)$$

Based on Born's criteria, when $\bar{C}_{11} - \bar{C}_{12}$ becomes negative then the phase, bcc in this case, loses its mechanical stability and thus $\bar{C}_{11} - \bar{C}_{12}$ is plotted in the results section.

2.1.4 Special quasirandom structures (SQS)

To calculate the energies, enthalpies of formation and elastic properties across the entire binary and ternary composition range, varying compositions of special quasirandom structures (SQS) were used. The SQS are small supercells used to mimic randomly substituted structures in terms of correlation functions. The binary and ternary bcc SQS, used in the present work, were previously generated by Jiang et al. [73, 74]. The relaxation of these SQS structures is complicated because local atomic relaxations can cause the structure to lose the desired lattice symmetry which is far from the original bcc lattice. To preserve symmetry, the calculations were carried out with three different relaxation schemes: 1) the cell volume, cell shape, and ionic positions are simultaneously relaxed, 2) the cell volume and shape are simultaneously relaxed, and 3) only the cell volume is relaxed. The relaxed structure with the lowest energy that preserved the bcc symmetry was used. There are two ways to verify whether the SQS is still bcc or not after the relaxations. The first is to merge different elements into one element, and then, use codes available to check the symmetry or space group (such as VASP [62] and phonopy [75]). The second is to visualize the structure directly using a visualization software and compare the symmetry to the unrelaxed bcc structure. For the present work, the relaxed structures were plotted with a visualization software and compared to the unrelaxed structure. After the relaxation, at least five different volumes were generated and the ions were allowed to relax. This yields the different volumes needed for the EOS fitting described above, which allows a better prediction of the different properties as a function of composition.

2.1.5 First-principles calculation error/difference

The error/difference between the previous results (experimental or calculation) and present results was calculated using:

$$\sqrt{\frac{\sum[(A_{calc} - A_{ref})]^2}{\kappa}} = Difference/Error \quad (2.24)$$

where A_{calc} is from the present calculation and A_{ref} is from the previous experiment or calculation, and κ is the total number of data points.

2.2 CALPHAD method

The CALPHAD method evaluates parameters to represent the Gibbs energy of individual phases as a function of temperature, pressure and composition. Thermochemical and phase boundary data obtained from experiments and first-principles calculations were used in the PARROT module of Thermo-Calc to evaluate the thermodynamic interaction parameters [76]. The Gibbs free energy is described by enthalpy H , temperature T and entropy S as follows:

$$G = H - TS \quad (2.25)$$

The Gibbs energy is then parameterized and expressed by:

$$G - H^{SER} = a + bT + cT\ln T + dT^2 + \sum_2^n e_n T^n \quad (2.26)$$

where H^{SER} refers to the elemental enthalpy in the SER state and a, b, c, d, e are coefficients. Other thermodynamic properties such as enthalpy, entropy and heat capacity can be derived from this equation. The parameterized equations for the pure elements have been determined and widely adopted from the SGTE to ensure global compatibility between different databases [32].

2.2.1 Solution phases

The databases were built upon the pure elements and then the effects of the binary and ternary interactions are modeled. Normally, the effects of alloying are modeled as solution phases or stoichiometric phases. The solution phases with one sublattice are described by:

$$G_m^\phi = \sum x_A^0 G_A^\phi + RT \sum x_A \ln x_A + ^{XS} G_m^\phi \quad (2.27)$$

where x_A is the mole fraction of element A and ${}^0 G_A^\phi$ is the molar Gibbs energy of pure element A in the specific phase (ϕ) being modeled and this is summed for all elements in the alloy system of interest. The second term describes the ideal interaction between elements and is again summed for every element in the alloy system of interest. The last term represents the excess mixing energy,

representing the non-ideal interactions between different species A and B . The non-ideal interactions are modeled between every set of binary and ternary elements in the system of interest. The excess mixing energy can be expressed by the Redlich-Kister polynomial as [77]:

$${}^{XS}G_m^\phi = \sum x_A x_B \sum_{k=0}^k L_{A,B}^\phi (x_A - x_B)^k \quad (2.28)$$

where $L_{A,B}^\phi$ represents the interaction parameter for elements A and B in phase ϕ described by:

$$L_{A,B}^\phi = {}^k a + {}^k b T \quad (2.29)$$

where ${}^k a$ and ${}^k b$ are evaluated model parameters. Eq. 2.28 can be extended to multi-component systems as:

$$\begin{aligned} {}^{XS}G_m^\phi = & \sum x_A x_B \sum_{k=0}^k L_{A,B}^\phi (x_A - x_B)^k + \sum x_A x_B x_C \\ & \left[{}^0 L_{A,B,C}^\phi (x_A + \delta_{A,B,C}) + {}^1 L_{A,B,C}^\phi (x_B + \delta_{A,B,C}) + {}^2 L_{A,B,C}^\phi (x_C + \delta_{A,B,C}) \right] \end{aligned} \quad (2.30)$$

where the ternary interaction parameters $L_{A,B,C}^\phi$ are described the same as the binary interaction parameters in Eq. 2.29 and $\delta_{A,B,C}$ is defined as $\delta_{A,B,C} = (1 - x_A - x_B - x_C)/3$.

Many alloys go through a disorder to order transition within a phase which requires modeling both the ordered and disordered part. For example, at low temperatures in many of the Ti-containing binary alloys, the randomly substituted bcc phase goes through a second order transition to become the ordered bcc#2 phase (CsCl-type). In the present work, no modeling is done for the ordered bcc#2 phase. However, previous modeling of the bcc#2 phase is incorporated in to the database. The modeling of ordered phases was discussed extensively by Ansara [16].

2.2.2 Stoichiometric compounds

The Gibbs energy of stoichiometric compounds was modeled in per mole unit formula. For the stoichiometric compound, $A_p B_q$, the Gibbs energy is expressed

by [78]:

$${}^0G_m^{A_pB_q} = a + bT + p * {}^0G_A^{SER} + q * {}^0G_B^{SER} \quad (2.31)$$

where a and b are the evaluated parameters, ${}^0G_A^{SER}$ is the Gibbs energy of pure element A in the SER phase, ${}^0G_B^{SER}$ is the Gibbs energy of pure element B in the SER phase, p is the number of atoms per unit formula of element A , and q is the number of atoms per unit formula of element B .

2.2.3 Elastic Properties

To obtain the elastic properties as a function of composition, the CALPHAD modeling approach was adopted and the Redlich-Kister polynomial was used to describe the elastic stiffness coefficients by [77, 79–81]:

$$E(x) = \sum x_A E_A^\phi + \sum x_A x_B L_{A,B}^\phi + \sum x_A x_B x_C L_{A,B,C}^\phi \quad (2.32)$$

where similar to Eq. 2.28 and 2.30 the x_A , x_B , and x_C refer to the mole fraction of element A , B , and C respectively, E_A is the elastic property of element A , $L_{A,B}^\phi$ and $L_{A,B,C}^\phi$ are the binary and ternary interaction parameters, respectively. The binary and ternary interaction parameters were described in terms of Eq. 2.29 but with solely an a coefficient. For the binary modeling, the addition of one or two interaction parameters were studied to ensure the best fit. For the ternary systems, only one interaction parameter is needed [79, 80, 82]. The fittings of the binary and ternary interaction parameters were completed using the Mathematica code in appendix C. The binary interaction parameters were fitted using the difference between the linear combination of pure elements and the first-principles results for each Ti-X ($X = \text{Mo, Nb, Sn, Ta, Zr}$) composition. The ternary interaction parameters were fitted using the difference between the interpolation of the pure elements and binary interaction parameters and the first-principles based on DFT results. The present work evaluated interaction parameters for the elastic stiffness coefficients and incorporated them into a database. Pycalphad [42] was then used to calculate the moduli values as a function of composition based on the Voigt-Reuss-Hill approach.

2.3 Experimental

2.3.1 Ti-Nb sample preparation

To study the effect of the metastable phase formation on Ti-alloys, two sets of Ti-Nb alloy samples were prepared. Each set contained one sample with 0.10, 0.12, 0.18, and 0.20 mole fractions of Nb and 0.90, 0.88, 0.82, 0.80 mole fractions of Ti, respectively. The samples were made using pieces of Ti (99.8 % Ti Alfa Aesar, Chicago, IL, USA, for set one, and 99.8 % Sigma Aldrich, St. Louis, MO, USA) and Nb (99.8 % Alfa Aesar, Chicago, IL, USA, for set one and set two). Two different titanium pieces were used because the Alfa Aesar titanium pieces were out of stock but they both had the same purity and thus should not lead to any issues with the data analysis. The alloyed samples were arc melted (MAM1, Edmund Buhler GmbH, Germany) under argon atmosphere. The alloys were machined into a cylindrical shape (0.7 inches in diameter and 0.7 inches in thickness). The samples were then heat treated using a Lindberg 59544 tube furnace. The tube was made of Al_2O_3 and was under vacuum. The samples were annealed at 1273 K for 24 hours. The samples from set 1 were quenched in water to form the α'' phase. The samples in set 2 were slow cooled to form the ω phase.

2.3.2 Neutron Scattering

2.3.2.1 ARCS

The inelastic neutron scattering measurements were carried out using the Wide Angular-Range Chopper Spectrometer (ARCS) at the Spallation Neutron Source (SNS) at Oak Ridge National Laboratory. ARCS is a time-of-flight spectrometer meaning that the incident neutron beam energy is fixed and the ARCS detectors measure the neutrons final position and the time elapse. From this information, the data output on ARCS is momentum and energy. The measurements were taken with the samples loaded in a customized vanadium sample holder. The holder was mounted into the furnace and kept under vacuum throughout all measurements. Two incident neutron energies, $E_i = 25\text{meV}$ and $E_i = 50\text{meV}$, were used at each temperature (300, 500, 700, 900, 1110 K). Vanadium was chosen for the sample holders because vanadium has a very low coherent scattering for neutrons. The

empty vanadium sample holder was measured at the same conditions at each temperature. The measurements of the scattering from the empty sample holder and a linear background from the ARCS instrument were subtracted from the data of the sample.

2.3.2.2 Data Analysis

From the corrected momentum and energy plots of the samples, the diffraction patterns and phonon density of states were obtained.

Diffraction is an elastic scattering process. The intensities of neutrons, with no change in energy, at each momentum are calculated and modeled as a Gaussian function [83,84]. In the present work, each alloy sample contained some combination of the bcc, hcp, α'' and ω phases. In order to obtain the phase fractions, diffraction patterns, from the literature, of Ti and Nb in each of the individual phases were combined and fit to the diffraction pattern of the alloy in question. In order to do the fitting, the distance between scattering planes was taken into account for each phase. By fitting the literature diffraction patterns to the diffraction pattern of the alloys being studied the phase fractions were obtained.

From the energy vs momentum plots the phonon density of states (DOS) was obtained using an iterative method to remove the elastic and multi-phonon contributions to the phonon DOS and thus plot just the single-phonon DOS [85,86]. First, a trial phonon DOS from the momenta vs energy plots was used to calculate the time dependent self-correlation function ($G(t)$) and the mean square atomic displacement $\langle u^2 \rangle$. The trial single-phonon DOS ($S'(\varrho)$) was obtained by modifying the measured signal ($S(\varrho)$) by suppressing the elastic peak and constraining $S(\varrho)$ such that $dS(\varrho)/d\varrho=0$ when $\varrho \rightarrow 0$ according to the hydrodynamic limit. ϱ is normally expressed in the literature as ω , however, due to the extensive discussion of the ω phase in this work the phonon frequency is expressed as ϱ to avoid confusion. Using the trial phonon DOS, $G(t)$ was expressed by [87,88]:

$$G(t) = \int_{-\infty}^{\infty} d\varrho \frac{Z(\varrho)}{\varrho} n(\varrho) e^{-i\varrho t} \quad (2.33)$$

where $Z(\varrho)$ is the phonon density of states as a function of phonon frequency ϱ and $n(\varrho)$ is the thermal occupancy factor. From $G(t)$ the dynamic structure factor from the incoherent scattering was calculated by [87,88]:

$$\bar{S}_{total}^{inc}(\varrho) = \sum_{\theta} \frac{1}{2\pi\hbar} e^{-Q^2(\theta,\varrho)\langle u^2 \rangle} \int_{-\infty}^{\infty} dt e^{-i\varrho t} e^{\hbar^2 Q^2(\theta,\varrho)G(t)/2M} \left[e^{\frac{-t^2}{2} \left(\frac{\Delta E(\varrho)}{2\hbar} \right)^2} \right] \quad (2.34)$$

where $e^{-Q^2(\theta,\varrho)\langle u^2 \rangle}$ is the Debye-Waller factor described with the mean square atomic displacement $\langle u^2 \rangle$ [86]. The anisotropy in the Debye-Waller factor was neglected because the resulting errors were negligible [87]. M is the mass of a neutron, \hbar is Planck's constant and the bracketed area is the Gaussian instrument energy resolution. Q is defined by [87, 88]:

$$Q(\theta, \varrho) = \sqrt{\frac{2M}{\hbar^2} \left(2E - \hbar\varrho - 2E\sqrt{1 - \frac{\hbar\varrho}{E}} \cos(2\theta) \right)} \quad (2.35)$$

From $G(t)$, the incoherent single-phonon \bar{S}_1^{inc} and elastic scattering \bar{S}_0^{inc} were determined. \bar{S}_0^{inc} and \bar{S}_1^{inc} are the zeroth and first order terms in the Taylor expansion of the \bar{S}_{total}^{inc} when $G(t) = 0$ and the multi-phonon incoherent scattering (S_m^{inc}) contribution can be calculated by [87, 88]:

$$\bar{S}_m^{inc} = \bar{S}_{total}^{inc} - \bar{S}_0^{inc} - \bar{S}_1^{inc} \quad (2.36)$$

The calculated \bar{S}_m^{inc} is then a good approximation for the multiphonon coherent scattering contribution and the single-phonon DOS was calculated by:

$$Z(\varrho) = S_1(\varrho) * \frac{\varrho}{n(\varrho)} \quad (2.37)$$

The procedure was repeated three times to converge the phonon DOS based on previous recommendations that showed three iterations were enough to converge within statistical errors [87, 88].

Chapter 3 | Ti-Mo-Nb-Sn-Ta-Zr Thermodynamic Database

3.1 Introduction

The design of Ti-alloys for biomedical applications necessitates a completed thermodynamic database that will facilitate the prediction of phase compositions and fractions as a function of composition and temperature. However, there is no completed thermodynamic database for the Ti-Mo-Nb-Sn-Ta-Zr system and thus the present work aims at building a complete database with special focus on the Ti-rich alloys and bcc phase models. With this in mind the pure elements have been extensively studied and are widely adopted from the SGTE database [32]. The modeling of the binary systems has been widely documented with the exception of the Sn-Ta and Mo-Sn systems, while the ternary systems have been studied experimentally but not been modeled. The Mo-Sn and Sn-Ta subsystems have high melting temperatures and little to no experimental data. In these cases, first-principles calculations based on DFT can be used to aid in modeling and supplement the lack of experimental data. The complete modeling of the Sn-Ta system is discussed in Chapter 4.

While the alloys in this Ti system have been studied experimentally, yielding phase equilibrium data, only limited calorimetry data is available. With the present work focused on bcc Ti-rich alloys, first-principles calculations based on DFT of the enthalpy of formation of the bcc phase were calculated. The thermodynamic descriptions were built or evaluated using the available experimental phase boundary

data and present calculated thermochemical data. In the present chapter, the thermodynamic descriptions of the Ti-Mo-Nb-Sn-Ta-Zr system are described.

3.2 Computational details

First-principles results based on Density Functional Theory (DFT) are used to predict the enthalpy of formation of specific phases. In the present work, the enthalpy of formation of the bcc phase was calculated for the Ti-X and Ti-X-Y ($X \neq Y = Mo, Nb, Sn, Ta, Zr$) systems using the calculated energy of the pure elements in their SER states. For each binary system, 3 special quasirandom structures at different compositions, $Ti_{0.25}X_{0.75}$, $Ti_{0.50}X_{0.50}$, $Ti_{0.75}X_{0.25}$, were calculated ($X = Mo, Nb, Sn, Ta, Zr$). The SQS were each 16-atom supercells that were previously generated and relaxed according to the methodology in chapter 2 [73]. For each binary system other dilute compositions were calculated, i.e. Ti-Mo 4 dilute structures ($Mo_{0.98}Ti_{0.02}$ 54-atoms, $Mo_{0.94}Ti_{0.06}$ 16-atoms, $Ti_{0.88}Mo_{0.12}$ 8-atoms, $Ti_{0.94}Mo_{0.06}$ 16-atoms), Ti-Nb 4 dilute structures ($Nb_{0.98}Ti_{0.02}$ 54-atoms, $Nb_{0.94}Ti_{0.06}$ 16-atoms, $Ti_{0.88}Nb_{0.12}$ 8-atoms, $Ti_{0.98}Nb_{0.02}$ 54-atoms), Ti-Sn 1 dilute structure ($Ti_{0.94}Sn_{0.06}$ 16-atoms), Ti-Ta 5 dilute structures ($Ta_{0.98}Ti_{0.02}$ 54-atoms, $Ta_{0.94}Ti_{0.06}$ 16-atoms, $Ti_{0.88}Ta_{0.12}$ 8-atoms, $Ti_{0.94}Ta_{0.06}$ 16-atoms, $Ti_{0.98}Ta_{0.02}$ 54-atoms), and Ti-Zr 2 dilute structures ($Zr_{0.94}Ti_{0.06}$ 16-atoms, $Ti_{0.98}Zr_{0.02}$ 54-atoms). A different number of dilute structures were done based on the complexity of some of the structures being unstable. For the Ti-X-Y ($X \neq Y = Mo, Nb, Sn, Ta, Zr$) ternary systems, three SQS calculations were completed at the compositions $Ti_{0.33}X_{0.33}Y_{0.33}$ (36-atom), $Ti_{0.50}X_{0.25}Y_{0.25}$ (32-atom), $Ti_{0.74}X_{0.13}Y_{0.13}$ (64-atom). In order to be able to effectively visualize the DFT-based first-principles results for the Ti-X-Y systems versus the modeling the plots went from a 50-50 binary mixture of the alloying elements to pure Ti. For this graph, DFT-based first-principles results for the binary SQS structure (X_8Y_8 16-atom) at the 50-50 mixture of alloying elements X and Y ($XY=Mo, Nb, Ta, Zr$) were completed. The binary and ternary SQS were previously generated and also relaxed according to the details outlined in chapter 2 [73, 74]. The DFT calculations are completed using VASP (Vienna ab-initio Simulation Package) [61]. The ion-electron interactions were described using the projector augmented wave (PAW) [62, 89] method. Based on the work of comparing X-C functionals (Figure 5.1), the exchange-correlation functional of the

generalized gradient approach depicted by Perdew, Burke, and Ernzerhof (PBE) was employed [58]. For consistency, a 310 eV energy cutoff was adopted for all calculations, which is roughly 1.3 times higher than the default values suggested by VASP for the elements Ti, Mo, Nb, Sn, Ta, and Zr. The energy convergence criterion of the electronic self-consistency was set as 10^{-6} eV/atom, and the Brillouin zone sampling was done with Blöchl corrections [89] using a gamma centered Monkhorst-Pack (MP) scheme [61,90]. The k-points grid for each calculation are listed in appendix C.

3.3 Sn binaries and ternaries

The thermodynamic description of the Mo-Sn system has never been modeled and there is little to no experimental data available. With this fact, first-principles calculations can be used to fill in the missing data points. However, this is not a hugely important sub-system and the modeling will be part of the future work. The Sn-Ta system is modeled in chapter 4. For the Sn-Zr system, the thermodynamic description was previously modeled. However, these models do not use compatible sublattice modeling with the current database. While the, Nb-Sn and Ti-Sn binary systems have been previously modeled, Sn will only be included in small percentages to the overall Ti-based alloy and until the rest of Sn binaries are modeled, Sn will not be included in the database.

3.4 Pure element calculation results

In order to build the Ti-Mo-Nb-Ta-Zr thermodynamic database, thermodynamic descriptions for the all the binary systems are evaluated first for accuracy and model compatibility (see Chapter 2) and incorporated into the database. For the ternary systems, only thermodynamic descriptions for the Ti-containing ternary systems are developed, including Ti-Mo-Nb, Ti-Mo-Ta, Ti-Mo-Zr, Ti-Nb-Ta, Ti-Nb-Zr, and Ti-Ta-Zr. The thermodynamic description of a non Ti-containing Mo-Nb-Ta ternary system [11] is incorporated in the present database.

Table 3.1 shows the energy E_0 , bulk modulus B , and the lattice parameters of the pure elements obtained from Eq. 2.6 at 0 K. The values are compared with previous first-principles calculations at 0 K and experimentally obtained values

both from the literature. The comparison shows a good agreement. The variances between the present calculations and previous calculations can be attributed to the different input parameters such as a different exchange correlation functional (PBE vs PW91) and higher energy cutoff values. The differences between the present calculations (0 K) and experimental values (300 K) can be partially attributed to the temperature difference. Based on the small variances shown in Table 3.1, the present calculations are deemed accurate.

3.5 Enthalpy of formation of bcc phase from first-principles

The enthalpies of formation of the bcc phase ($\text{bcc-}H_{Form}$) for the binary and ternary systems are presented in Table 3.2 and Table 3.3, respectively. As discussed in the methodology chapter, the $\text{bcc-}H_{Form}$ is calculated by Eq. 2.7. Table 3.2 shows the first-principles results for binary $\text{bcc-}H_{Form}$: the Ti-Mo system goes from positive to negative to positive indicating the formation of a bcc miscibility gap, and the Ti-Nb, Ti-Ta, and Ti-Zr systems, are positive across the entire composition range. Table 3.3 shows the values of the ternary $\text{bcc-}H_{Form}$. The $\text{bcc-}H_{Form}$ values, for the Ti-Mo-Nb, Ti-Mo-Ta and Ti-Nb-Ta systems, go from positive at pure Ti to negative at $X_{0.50}Y_{0.50}$, while $\text{bcc-}H_{Form}$ remains positive for the Ti-Mo-Zr, Ti-Nb-Zr, and Ti-Ta-Zr systems. For each system that the $\text{bcc-}H_{Form}$ is calculated, the values are compared with the CALPHAD modeling predictions and in some cases, are compared with experimentally obtained results. For some of the systems, when comparing the first-principles results of the $\text{bcc-}H_{Form}$ and the CALPAHD modeling prediction of the $\text{bcc-}H_{Form}$, no large discrepancies are seen and thus no new modeling is completed. In other cases, comparing the first-principles results of the $\text{bcc-}H_{Form}$ and the CALPAHD modeling prediction of the $\text{bcc-}H_{Form}$ showed larger discrepancies and then the first-principles $\text{bcc-}H_{Form}$ values are used to introduce new bcc interaction parameters. Each binary and Ti-containing ternary system is discussed in detail in the sections below.

3.6 Thermodynamic modeling of the ten binary systems

3.6.1 Mo-Nb, Mo-Ta, Nb-Ta

Figure 3.1 shows the calculated phase diagrams for the Mo-Nb, Mo-Ta, and Nb-Ta systems from thermodynamic descriptions in the literature in comparison with experiments. The Mo-Nb, Mo-Ta and Nb-Ta descriptions are adopted from the modeling completed by Xiong et al. [11]. Xiong et al. [11] who modeled these three binary systems and the Mo-Nb-Ta ternary system. Binary interaction parameters were introduced for the liquid and bcc solution phases. The thermodynamic description, for the Mo-Nb system, was obtained using experimental data from differential thermal analysis that measured both the liquidus and solidus temperatures [11]. Xiong et al. [11] decided to only use the experiments (shown in Figure 3.1 as X and +) that estimated the pure elements melting temperatures reasonably well when evaluating the binary interaction parameters. Xiong et al. [11] discussed, that after evaluating the binary interaction parameters for the Mo-Nb system, the experiments, shown by \circ , \triangle , \square , agreed well with the predicted phase diagram. Even though, the remaining experimental data points (\diamond , $*$) were quite low as compared to the predicted phase diagram, they were also quite low compared to all the other experiments [11] and were considered inaccurate. Thus Xiong et al. [11] concluded that the thermodynamic description generated is adequate at predicting the experimental data.

The thermodynamic description, for the Mo-Ta system, was obtained using two sets of experimental data (\triangle , $*$, \diamond , \square) [11]. These particular experimental data points were chosen because they accurately measured the melting temperatures of Mo and Ta. The predicted phase diagram accurately reproduced the experimental data with the exception of the experimental data [11] denoted as " \circ ". This set of data was 343.15 K higher than all other experimental data. Xiong et. al. [11] thought the dataset was not reliable and was thus ignored.

For the Nb-Ta system, the thermodynamic description was completed using the experimental liquidus data [11] depicted in Figure 3.1 by \circ , \triangle , and \square , because it predicts the melting temperatures of Nb and Ta accurately. The experimentally measured solidus temperatures (*) were not used because the data for both Nb and

Ta showed discrepancy. The predicted phase diagram reproduces the experimental data well with the exception of the experimental work depicted by \diamond . This dataset was ignored because the values were 343.15 K higher than the other experimental values and thus it was determined by Xiong et al. [11] to be unreliable.

The present work agrees with the conclusion reached by Xiong et al. [11] that the phase diagrams reproduce the experimental data accurately. The sublattice models used by Xiong et al. [11] are compatible with our working database and the binary descriptions are incorporated without any changes. The interaction parameters for the binary systems incorporated into the database are listed in Table 3.4.

3.6.2 Mo-Zr, Nb-Zr and Ta-Zr

Figure 3.2 shows the predicted phase diagrams for the Mo-Zr, Nb-Zr, and Ta-Zr systems. For the Mo-Zr system, there are several existing thermodynamic descriptions and experimental results available. In the present work, the evaluation by Perez et al. [12] is chosen to be incorporated due to the fact that their model was also incorporated into the Ti-Mo-Zr ternary modeling found in the literature. The experimental data plotted in Figure 3.2 includes the single-phase regions, two-phase regions, phase boundaries, and peritectic and eutectoid reactions (\blacksquare , $*$, $+$, Y , \diamond , \blacklozenge , \square , \diamondsuit , \bullet , \circ , \triangle , \boxtimes). Each symbol represents a different set of data from different authors and Perez et al. [12] went into more details on the available experimental data and discussed what was included in their evaluation. They [12] introduced interaction parameters for the liquid, bcc, hcp, and Laves_C15 phases. The thermodynamic description generally reproduces all experimental data very satisfactorily.

The thermodynamic description, for the Nb-Zr system, was previously evaluated by Guillermet [13]. Figure 3.2 plots the predicted phase diagram with the experimental solidus data (\diamond , $*$) as well as the hcp solvus (Y , \circ) and bcc miscibility gap (\triangle , \square , $+$) data [13, 14, 21]. The description includes interaction parameters for the liquid, bcc, and hcp solution phases and reproduces the experimental data well.

For the Ta-Zr system, the thermodynamic description was also evaluated by Guillermet [15]. There are quite a lot of experimental datasets for this binary system, including phase boundary results from at least five different investigations

and thermodynamic results from three different studies [15]. Figure 3.2 plots the single-phase (\bullet , \blacksquare), two-phase (\circ , \square), and phase boundary (*, +) experimental data in comparison with the CALPHAD results. Interaction parameters were introduced for the bcc, hcp, and liquid phases. The predicted phase diagram reproduces the data fairly well.

The thermodynamic descriptions of the three binary systems Mo-Zr, Nb-Zr, and Ta-Zr are determined to be accurate and the sublattice modeling used is compatible with our working database. Thus, the thermodynamic descriptions are incorporated into the database. The interaction parameters for the binary systems incorporated into the database are listed in Table 3.4.

3.6.3 Ti-Mo

The thermodynamic description in the COST 507 database, modeled by Saunders, [16] is looked at for the Ti-Mo system. This model is chosen because it is the model incorporated into the Ti-Mo-Zr thermodynamic modeling [24]. Interaction parameters were evaluated for the liquid, fcc, hcp, bcc (ordered bcc#1 and disordered bcc#2), AlM_D019, AlM-D022, and the AlTi-L10 phases. Figure 3.3a compares the predicted phase diagram [16] with the available experimental phase boundary data [17]. The phase boundary data is reproduced very well. Figure 3.3b plots the predicted enthalpy of formation of the bcc phase (solid line) versus the results from the present DFT-based first-principles calculations (circles) and are compared to the enthalpies of formation of the bcc phase obtained experimentally (red squares) [18]. The experimental bcc- H_{Form} values and the prediction from the model are at 300 K while the first-principles results are at 0 K. The experimental values of bcc- H_{Form} compare well with the calculations but become more negative closer to the Mo-rich side which can be attributed to the temperature difference. The CALPHAD predicted enthalpy of formation of the bcc phase drastically deviates from the first-principles calculation results between 20 and 80 at.% Mo. This discrepancy is mostly due to the disagreement on the existence of a bcc miscibility gap. Previous experimental research, including the values plotted here, have shown an equilibrium bcc miscibility gap which would fit what is seen in the first-principles calculations [18, 91, 92]. While there is an interaction parameter for the bcc order and disorder, Saunders [16] did not model the bcc miscibility gap. While there

are previous thermodynamic descriptions that model the bcc miscibility gap, Kar et al. [24] showed that the experimental data from higher-component systems fits better with the description without the miscibility gap. Based on this and the fact that the sublattice modeling is compatible with the working database, the thermodynamic description by Saunders [16] is adopted without changes. The interaction parameters for the binary system incorporated into the database are listed in Table 3.4.

3.6.4 Ti-Nb

For the Ti-Nb system, its thermodynamic description is taken from Zhang et al. [19]. Originally the thermodynamic description by Kumar et al. [20, 21] was evaluated because it was used in the modeling of the Ti-Nb-Zr system. However, new experimental phase boundary data on the Nb rich side (Δ) showed the need to switch to the thermodynamic description of Zhang et al. [19] who introduced interaction parameters for the liquid, bcc, hcp and omega phases. Figure 3.4a plots the predicted phase diagram from Zhang et al. [19] against solidus data (\square), hcp and bcc solvus data (\circ) [20, 21] and the new Nb-rich bcc solvus data (\triangle) [19]. Figure 3.4b plots the predicted enthalpy of formation (solid line) versus the present first-principles calculations (circles) and are compared to the enthalpies of formation of the bcc phase obtained experimentally (red squares) [18]. The experimental bcc- H_{Form} values and the prediction from the model are at 300 K while the first-principles results are at 0 K. The experimental bcc- H_{Form} values compare well with the calculations and any variance can be mostly attributed to the temperature difference. There is an average variance of 0.17 kJ/mol-atom between the DFT results and CALPHAD predictions of the bcc- H_{Form} which is also attributed to the temperature difference. However, even with the variance, the CALPHAD prediction compares well with the DFT results and the phase diagram reproduces the experimental data very well. The sublattice models are compatible and the thermodynamic description from Zhang et al. [19] is incorporated into the present database with no alterations. The interaction parameters for the binary system incorporated into the database are listed in Table 3.4.

3.6.5 Ti-Ta

The thermodynamic description for the Ti-Ta system is taken from the COST 507 database [16]. The predicted phase diagram is plotted in Figure 3.5a and compared with the experimental liquidus and solidus data (\diamond and Y) as well as the bcc and hcp solvus data (\triangle , \square , and \circ). The evaluation includes interaction parameters for the fcc, hcp, liquid, ALM-D019, ALM-D022, AlTi-L10, and the bcc (ordered bcc#1, disordered bcc#2) phases [22]. The thermodynamic description reproduces the experimental data well. The enthalpy of formation of the bcc phase predicted by the CALPHAD modeling (solid line) is plotted with the first-principles results (circles) in Figure 3.5b. The CALPHAD prediction of the bcc- H_{Form} reproduces the results from first-principles reasonably well on the Ti-rich and Ta-rich sides. The first-principles results vary on an average by 0.17 kJ/mol-atom. However, the CALPHAD prediction is at 300 K and the first-principles are at 0 K which may be mostly responsible for the variance. Based on these discussions, the thermodynamic description is deemed reliable and since the sublattice modeling is compatible, the thermodynamic description is incorporated into the database without alteration. The interaction parameters for the binary system incorporated into the database are listed in Table 3.4.

3.6.6 Ti-Zr

The thermodynamic description of the Ti-Zr system evaluated by Kumar et al. [21] is used in the present work. The model by Kumar et al. [21] is chosen because it was used in the ternary modeling of the Ti-Mo-Zr and Ti-Nb-Zr systems. The evaluation introduces interaction parameters for the liquid, bcc, and hcp solution phases. Figure 3.6a compares the predicted phase diagram with phase boundary data for the bcc to hcp (\circ) phase transformation and solidus (\triangle). The thermodynamic description accurately reproduces the phase boundary data. When doing the evaluation, heat of transformation data was also used and was discussed by Kumar et al. [21]. Figure 3.6b plots the present DFT-based first-principles results (circles) against the CALPHAD prediction (solid line) for the bcc- H_{Form} . The first-principles results and CALPHAD modeling vary on average by 1.2 kJ/mol-atom. The variance is larger than the other binary alloys due to the instability of the bcc phase at both 0 K and 300 K for the Ti-Zr alloy but the calculations and CALPHAD prediction

follow the same trend. Based on the agreement with the experimental data and the compatible sublattice models, no alterations were made to the thermodynamic description which was incorporated into the database. The interaction parameters for the binary system incorporated into the database are listed in Table 3.4.

3.7 Thermodynamic modeling of six Ti-containing ternary systems

In this section, the enthalpy of formation of the bcc phase is plotted from a 50-50 mixture of the alloying elements $X_{0.5}Y_{0.5}$ to Ti. When doing the evaluations, the enthalpy of formation of the bcc phase was plotted for all compositions. The plot shown here is just the easiest way to show the comparison between the modeling prediction and the DFT-based first-principles results.

3.7.1 Ti-Mo-Nb

There has never been a thermodynamic description for the Ti-Mo-Nb system in literature. Two experimental investigations were performed on the Ti-Mo-Nb system at 873 K and 1373 K [25, 93]. While both investigations agree that the isothermal section at 1373 K is solely the bcc phase, the investigations differed on the phase boundary at 873 K. It is suspected that at such a low temperature the samples were hard to reach equilibrium, which may have led to the discrepancy. Based on this, the binary interpolation of the isothermal sections at 1373 K and 873 K are plotted. The predicted phase diagram at 1373 K agreed with the experimentally determined phase diagram to be solely the bcc phase. The phase diagram at 873 K is plotted in Figure 3.7a. The discrepancy, at 873 K, is the existence of the bcc miscibility gaps as well as what compositions the phase boundary lines lie at. The enthalpy of formation of the bcc phase is predicted using an interpolation of the binary interaction parameters (solid line) and plotted with the first-principles results, in Figure 3.7b, starting from a 50-50 mixture of the alloying elements ($Mo_{0.50}Nb_{0.50}$) to 100 at.% Ti. While the first-principles calculations are at 0 K and the binary interpolation is at 300 K, the DFT-based first-principles calculation results agree with the CALPHAD prediction. The prediction varies by less than 1.5 kJ/mol-atom for all the calculations except at $Mo_{0.50}Nb_{0.50}$ where the calculation

varies substantially from the prediction. In order to improve this, the Mo-Nb binary system would have to be adjusted. In the present work, no thermochemical data was used to ensure the accuracy of the non Ti-containing binary systems but the previous binary models were able to reproduce the phase boundary data as discussed above. Based on the discrepancy between the experimental data and the fact that the first-principles thermochemical results are reproduced well by the binary interpolation, no ternary interaction parameters are evaluated.

3.7.2 Ti-Mo-Ta

The thermodynamic description of the Ti-Mo-Ta system has not been previously modeled. The binary interpolation of the Ti-Mo-Ta system is plotted in Figure 3.8a at 873 K at which the Ti-Mo-Ta system has the bcc and hcp solution phases with the tie-triangle showing a three-phase region in the Ti-rich corner, but did not show a bcc miscibility gap or tie-triangle [23]. Figure 3.8b shows the present DFT-based first-principles results (circles) of the bcc- H_{Form} compared with the binary interpolation from the CALPHAD prediction (solid black line). The first-principles results line up fairly well with the CALPHAD prediction. However, due to the discrepancy of the experimental data, ternary interaction parameters are investigated for the hcp and bcc phases using the first-principles results and experimental phase boundary data. The evaluated interaction parameters are listed in Table 3.4. After assessing the ternary interaction parameters, the isothermal section at 873 K is again plotted and compared with experimental data in Figure 3.9a and zoomed in for Figure 3.9b. The enthalpy of formation of the newly assessed bcc phase is plotted as a red dashed line in Figure 3.8b. The assessment reproduces the first-principles results very well. With the introduction of the interaction parameters, the isothermal section agrees well with the experimental data [23]. The hcp phase boundary data from Nikitin [23] were plotted as \circ and two phase experimental data as \bullet . The two phase experimental data is reproduced by the present model. The hcp phase boundary data are not well reproduced. However, reliable solid phase boundary data are difficult to obtain at such a low temperature and if the evaluation is altered to fit the data; it then over fits and stabilizes non-equilibrium phases.

3.7.3 Ti-Mo-Zr

The thermodynamic description of the Ti-Mo-Zr system was previously modeled by Kar et al. [24]. The same binary phases used in the modeling by Kar et al. are included in the present database. The phases in this ternary system are liquid, bcc, hcp, and Laves_C15 (Mo_2Zr). After interpolating the ternary system from the binary models and comparing to two sets of available experimental data, Kar et al. [24] introduced interaction parameters for the Laves_C15 (Mo_2Zr) phase. After interpolating the ternary system from the binary models and comparing to two sets of available experimental data, Kar et al. [24] introduced interaction parameters for the Laves_C15 phase. As discussed by Kar et al. [24], there is phase boundary data at 1273 K, from two investigations [24]. The phase boundary datasets deviate on how far the two-phase region extends toward the Ti-rich corner and whether there is a bcc miscibility gap. Due to the discrepancy, Kar et al. [24] decided not to introduce any bcc, liquid, or hcp interaction parameters. The prediction of the phase diagram at 1273 K by Kar et al. [24] is plotted in 3.10a and compared with one set of phase boundary data [24]. The phase boundary data fits well on the Zr-Mo binary side but extends further in the Ti-rich corner. This is where the discrepancy lies, the other set of phase boundary data, not shown here, shows a shallower two-phase region than the current CALPHAD prediction. The predicted enthalpy of formation of the bcc phase is compared with the present first-principles results in Figure 3.10b. The first-principles results vary by 1.5 kJ/mol-atom from the CALPHAD prediction but the largest variance is seen at $\text{Mo}_{0.50}\text{Zr}_{0.50}$ which would only be improved by adjusting the binary Mo-Zr interaction parameters. Based on the available experimental data [24], the present first-principles calculations, and the conclusions from Kar et al. [24], the present study decides to include the ternary Laves_C15 interaction parameters without introducing the ternary interaction parameters for the liquid, bcc, and hcp phases. The ternary Laves_C15 (Mo_2Zr) interaction parameters are listed in Table 3.4.

3.7.4 Ti-Nb-Ta

A thermodynamic description of the Ti-Nb-Ta system had not previously been evaluated in the literature but different isothermal sections had been estimated by Na et al. [26] using phase boundary data obtained through x-ray diffraction. Na et

al. [26] looked at samples at 823 K and 673 K. The authors [26] pointed out that it is likely that the alloys at 673 K never reached equilibrium conditions. The experimental results [26] were plotted on the ternary isothermal sections predicted purely based on binary interpolation in Figure 3.11a and Figure 3.11b. The bcc phase boundary data do not match with the binary interpolation. Figure 3.12 plots the enthalpy of formation of the bcc phase predicted by the binary interpolation (solid line) and the first-principles results (circles). The first-principles results deviate significantly from the binary interpolation. Due to the variance, ternary interaction parameters for the bcc and hcp phases are investigated. The evaluation was done using the 823 K experimental data and the present first-principles calculations with 673 K data being neglected due to concerns of true equilibrium at such a low temperature. The evaluated ternary interaction parameters are listed in Table 3.4. After evaluation, the ternary isothermal sections are plotted with the phase boundary data in Figure 3.13a and Figure 3.13b. The isothermal sections at both 673 and 823 K reproduce the experimental data [26] well. The assessed prediction (red dashed line in Figure 3.12) of the enthalpy of formation of the bcc phase also matches better with the first-principles results.

3.7.5 Ti-Nb-Zr

The thermodynamic description, of the Ti-Nb-Zr system was previously evaluated by several studies [21, 27]. In the present work, the binary interpolation of the ternary isothermal section at multiple temperatures are compared with the experimental data [21, 27]. Figure 3.14a plots the isothermal section at 843 K in comparison with the two-phase equilibria data and the tie-triangle phase boundary data [27]. The binary interpolation reproduced the experimental results well. The enthalpy of formation of the bcc phase is plotted in Figure 3.14b. The CALPHAD prediction (solid line) of the bcc- H_{Form} varies on an average by 1.34 kJ/mol-atom from the first-principles results (circles). While there is some variance, it may be attributed to the temperature difference and overall the variance isn't large. Therefore, a decision was made to not introduce ternary interaction parameters, which is in agreement with past authors [21, 27].

3.7.6 Ti-Ta-Zr

For the Ti-Ta-Zr system, Lin et al. [28] calculated the isothermal sections using binary interpolations without introducing any interaction parameters. The isothermal sections at 1273 and 1773 K are plotted in Figure 3.15a and Figure 3.15b, respectively. Experimental phase boundary data along the bcc miscibility gap at 1273 K and single phase • and two phase region ● data using x-ray diffraction at 1773 K are plotted to compare with the binary interpolations [28, 29]. The phase boundary data is reproduced well. Figure 3.16 plots the binary interpolation prediction (solid line) of the bcc- H_{Form} compared to the present first-principles results (circles). On average the first-principles varies by 3.69 kJ/mol-atom attributed partially to the temperature difference. While the variance is larger for the enthalpy of formation, the experimental data points [28] are reproduced and thus no ternary interaction parameters are evaluated

It is worth mentioning that all the interaction parameters for the Ti-Mo-Nb-Ta-Zr system are listed in Table 3.4 and combined into a single thermodynamic database (TDB) file in appendix A.

3.8 Conclusion

The present study builds a compatible and complete thermodynamic database for the Ti-Mo-Nb-Ta-Zr system using descriptions of five pure elements (Ti, Mo, Nb, Ta, Zr), ten binary systems (Ti-Mo, Ti-Nb, Ti-Ta, Ti-Zr, Mo-Nb, Mo-Ta, Mo-Zr, Nb-Ta, Nb-Zr, Ta-Zr), and six Ti-containing ternary systems (Ti-Mo-Nb, Ti-Mo-Ta, Ti-Mo-Zr, Ti-Nb-Ta, Ti-Nb-Zr, Ti-Ta-Zr). Sn was excluded from the database due to the lack of modeling for the Sn binary systems. The Sn-Ta and Mo-Sn systems lacked a thermodynamic description and the thermodynamic modeling of the Sn-Zr system is incompatible with the current database. The present work began modeling the Sn binaries with the Sn-Ta system discussed chapter 4. Until the binaries are properly modeled, Sn was not included in the database which shouldn't affect the use of the database for biomedical applications since Sn will only be added to biomedical alloys in small percentages. The thermodynamic descriptions of the pure elements were adopted from the SGTE database [32]. All of the binary systems had previous thermodynamic descriptions available in literature.

Previous models for all binary systems were evaluated for accuracy and incorporated into the present database. The binary interpolations of the Ti-containing ternary systems were plotted and compared with the available experimental data as well as the enthalpy of formation of the bcc phase calculated from first-principles based on DFT. The Ti-Sn-X systems ($X = \text{Mo, Nb, Ta, Zr}$) will be modeled in the future work once the Sn binaries are modeled. The binary interpolations of both the Ti-Nb-Zr and Ti-Ta-Zr systems had previously been plotted but no interaction parameters had been introduced. The Ti-Mo-Zr system had previously been modeled and the present work agreed with the evaluation. The Ti-Mo-Nb, Ti-Mo-Ta and Ti-Nb-Ta systems had never previously been modeled. The present work evaluated interaction parameters for the Ti-Mo-Ta and Ti-Nb-Ta systems but didn't introduce any interaction parameters for the Ti-Mo-Nb system. The thermodynamic descriptions were all incorporated into a complete database that can reliably predicts the phase stability of the Ti-Mo-Nb-Ta-Zr systems.

Table 3.1: Equilibrium properties energy E_0 , bulk modulus B and the lattice parameters from the first-principles calculations for each pure elements in their SER state. The presently calculated results are also compared with available experimental data and previously calculated results.

Phase	E_0 (eV/atom)	$a(\text{\AA})$	$c(\text{\AA})$	B (GPa)	Reference
hcp-Ti	-7.80	2.92	4.6	113	This work
	-7.89	2.93	4.64	113	Calc 0 K [94, 95]
		2.96	4.7	110	Expt 300 K [96, 97]
bcc-Mo	-10.84	2.74	-	262	This work
	-10.86	2.74	-	262	Calc 0 K [95, 98]
		2.72	-	261	Expt 300 K [99, 100]
bcc-Nb	-10.22	2.86	-	171	This work
	-10.12	2.88	-	174	Calc 0 K [95, 101]
		2.86	-	172	Expt 300 K [102, 103]
bcc-Ta	-11.85	2.87	-	196	This work
	-11.85	2.87	-	194	Calc 0 K [95, 104]
		2.86	-	196	Expt 300 K [102, 105]
hcp-Zr	-8.51	3.04	4.98	94	This work
	-8.55	3.23	5.17	94	Calc 0 K [95, 106–108]
		3.23	5.15	97	Expt 300 K [109, 110]

Table 3.2: First-principles results at 0 K for the enthalpy of formation (H_{Form}) of the bcc phase for different mole fractions (x) of alloying element X in the Ti-X binary systems (X = Mo, Nb, Ta, Zr).

Alloy	Type of Calc	H_{Form} (kJ/mol-atom)
Ti	Elemental	7.29
Mo, Nb, Ta	Elemental	0.00
Zr	Elemental	8.19
Ti _{0.94} Mo _{0.06}	Dilute	3.08
Ti _{0.88} Mo _{0.12}	Dilute	2.82
Ti _{0.75} Mo _{0.25}	SQS	1.12
Ti _{0.50} Mo _{0.50}	SQS	-3.67
Ti _{0.25} Mo _{0.75}	SQS	-5.18
Ti _{0.06} Mo _{0.94}	Dilute	1.79
Ti _{0.02} Mo _{0.98}	Dilute	5.82
Ti _{0.98} Nb _{0.02}	Dilute	6.92
Ti _{0.88} Nb _{0.12}	Dilute	5.88
Ti _{0.75} Nb _{0.25}	SQS	7.57
Ti _{0.50} Nb _{0.50}	SQS	8.54
Ti _{0.25} Nb _{0.75}	SQS	1.15
Ti _{0.06} Nb _{0.94}	Dilute	0.59
Ti _{0.02} Nb _{0.98}	Dilute	0.20
Ti _{0.98} Ta _{0.02}	Dilute	7.21
Ti _{0.94} Ta _{0.06}	Dilute	7.04
Ti _{0.88} Ta _{0.12}	Dilute	9.28
Ti _{0.75} Ta _{0.25}	SQS	4.89
Ti _{0.50} Ta _{0.50}	SQS	3.94
Ti _{0.25} Ta _{0.75}	SQS	3.10
Ti _{0.12} Ta _{0.88}	Dilute	0.94
Ti _{0.02} Ta _{0.98}	Dilute	0.28
Ti _{0.98} Zr _{0.02}	Dilute	5.49
Ti _{0.75} Zr _{0.25}	SQS	4.59
Ti _{0.50} Zr _{0.50}	SQS	1.94
Ti _{0.25} Zr _{0.75}	SQS	3.50
Ti _{0.06} Zr _{0.94}	Dilute	5.72

Table 3.3: First-principles results at 0 K for the enthalpy of formation (H_{Form}) of the bcc phase for different mole fractions (x) of Ti in the Ti-X-Y ternary systems (X \neq Y = Mo, Nb, Ta, Zr).

Alloy	Type of Calc	H_{Form} (kJ/mol-atom)
Mo _{0.50} Nb _{0.50}	SQS	-38.69
Ti _{0.33} Mo _{0.33} Nb _{0.33}	SQS	5.08
Ti _{0.50} Mo _{0.25} Nb _{0.25}	SQS	-2.10
Ti _{0.74} Mo _{0.13} Nb _{0.13}	SQS	2.18
Mo _{0.50} Ta _{0.50}	SQS	-15.64
Ti _{0.33} Mo _{0.33} Ta _{0.33}	SQS	-5.34
Ti _{0.50} Mo _{0.25} Ta _{0.25}	SQS	-1.82
Ti _{0.74} Mo _{0.13} Ta _{0.13}	SQS	2.77
Mo _{0.50} Zr _{0.50}	SQS	10.31
Ti _{0.33} Mo _{0.33} Zr _{0.33}	SQS	8.36
Ti _{0.50} Mo _{0.25} Zr _{0.25}	SQS	7.73
Ti _{0.74} Mo _{0.13} Zr _{0.13}	SQS	6.82
Nb _{0.50} Ta _{0.50}	SQS	-0.41
Ti _{0.33} Nb _{0.33} Ta _{0.33}	SQS	1.82
Ti _{0.50} Nb _{0.25} Ta _{0.25}	SQS	3.80
Ti _{0.74} Nb _{0.13} Ta _{0.13}	SQS	5.59
Nb _{0.50} Zr _{0.50}	SQS	6.21
Ti _{0.33} Nb _{0.33} Zr _{0.33}	SQS	9.82
Ti _{0.50} Nb _{0.25} Zr _{0.25}	SQS	10.06
Ti _{0.74} Nb _{0.13} Zr _{0.13}	SQS	8.75
Ta _{0.50} Zr _{0.50}	SQS	5.75
Ti _{0.33} Ta _{0.33} Zr _{0.33}	SQS	2.98
Ti _{0.50} Ta _{0.25} Zr _{0.25}	SQS	2.79
Ti _{0.74} Ta _{0.13} Zr _{0.13}	SQS	0.79

Table 3.4: Modelled binary and ternary thermodynamic parameters for the Ti-Mo-Nb-Ta-Zr system. The thermodynamic description of pure elements is not included. The pure element functions, such as GFCCTI, describe the Gibbs energy (G) of the phase (fcc) for the element (Ti) were adopted from the SGTE database [32] are listed in the Supplementary TDB (thermodynamic database) file (appendix A).

Phase	Reference	Interaction Parameter
Liquid	[16]	$0_{Ti,Mo}^L = -9000.0 + 2.00 * T$
	[19]	$0_{Ti,Nb}^L = 7406.1$
	[16]	$0_{Ti,Ta}^L = 1000.0$
	[16]	$0_{Ti,Ta}^L = -7000.0$
	[21]	$0_{Ti,Zr}^L = -967.7$
	[11]	$0_{Mo,Nb}^L = 15253.7$
	[11]	$1_{Mo,Nb}^L = 10594.2$
	[11]	$0_{Mo,Ta}^L = 13978.9$
	[12]	$0_{Mo,Zr}^L = -24055.1 + 8.146 * T$
	[12]	$1_{Mo,Zr}^L = -5132.17 + 4.804 * T$
	[13]	$0_{Nb,Zr}^L = 10311.0$
	[13]	$1_{Nb,Zr}^L = 6709.0$
	[15]	$0_{Ta,Zr}^L = 13832.1$
	[15]	$1_{Ta,Zr}^L = -7150$
	bcc	$0_{Ti,Mo}^L = 2000.0$
	[16]	$1_{Ti,Mo}^L = -2000.0$
	[19]	$0_{Ti,Nb}^L = 13045.3$
	[16]	$0_{Ti,Ta}^L = 12000.0$
	[16]	$1_{Ti,Ta}^L = -2500.0$
	[21]	$0_{Ti,Zr}^L = -4346.2 + 5.49 * T$
	[11]	$0_{Mo,Nb}^L = -68202.6 + 29.86 * T$
	[11]	$1_{Mo,Nb}^L = 8201.3$
	[11]	$0_{Mo,Ta}^L = -75129.2 + 30.00 * T$
	[11]	$1_{Mo,Ta}^L = 6039.2$
	[12]	$0_{Mo,Zr}^L = 17936.0 + 3.10 * T$
	[12]	$1_{Mo,Zr}^L = -991.0 + 4.30 * T$
	[11]	$0_{Nb,Ta}^L = 1298.0$
	[13]	$0_{Nb,Zr}^L = 15911.0 + 3.35 * T$

Table 3.4: Modelled binary and ternary thermodynamic parameters for the Ti-Mo-Nb-Ta-Zr system. The thermodynamic description of pure elements is not included. The pure element functions, such as GFCCTI, describe the Gibbs energy (G) of the phase (fcc) for the element (Ti) were adopted from the SGTE database [32] are listed in the Supplementary TDB (thermodynamic database) file (appendix A).

Phase	Reference	Interaction Parameter
	[13]	$1_{Nb,Zr}^L = 3919.0 - 1.09 * T$
	[15]	$0_{Ta,Zr}^L = 29499.6 + 2.67 * T$
	[15]	$1_{Ta,Zr}^L = -4396.2 + 4.43 * T$
	[15]	$2_{Ta,Zr}^L = -6353.3 + 4.91 * T$
	This work	$0_{Ti,Mo,Ta}^L = -154731.2$
	This work	$0_{Nb,Ta,Ti}^L = -136603.3$
	This work	$1_{Nb,Ta,Ti}^L = -136602.7$
hcp	[16]	$0_{Ti,Mo}^L = 22760.0 - 6.00 * T$
	[19]	$0_{Ti,Nb}^L = 11742.4$
	[16]	$0_{Ti,Ta}^L = 8500.0$
	[21]	$0_{Ti,Zr}^L = 5133.0$
	[12]	$0_{Mo,Zr}^L = 26753.8 + 4.56 * T$
	[13]	$0_{Nb,Zr}^L = 24411.0$
	[15]	$0_{Ta,Zr}^L = 30051.7$
fcc	[16]	$0_{Ti,Mo}^L = 16500.0$
	[16]	$0_{Ti,Ta}^L = 8500.0$
Al3M_D022	[16]	$0_{Ti:Ti}^L = 4 * GFCCTI$
	[16]	$0_{Mo:Mo}^L = 4 * GFCCMO$
	[16]	$0_{Ti:Mo}^L = GFCCMO + 3.0 * GFCCTI$
	[16]	$0_{Mo:Ti}^L = 3.0 * GFCCMO + GFCCTI$
	[16]	$0_{Ti:Ta}^L = GFCCTA + 3.0 * GFCCTI$
AlM_D019	[16]	$0_{Ti:Ti}^L = 4.0 + 4.0 * GHSERTI$
	[16]	$0_{Mo:Mo}^L = 4.0 * GHCPMO$
	[16]	$0_{Ta:Ta}^L = 4.0 * GHCPTA$
	[16]	$0_{Ti:Mo}^L = 17072.0 - 4.5 * T$
		$+GHCPMO + 3.0 * GHSERTI$
	[16]	$0_{Mo:Ti}^L = 17072.0 - 4.5 * T$
		$+3.0 * GHCPMO + GHSERTI$

Table 3.4: Modelled binary and ternary thermodynamic parameters for the Ti-Mo-Nb-Ta-Zr system. The thermodynamic description of pure elements is not included. The pure element functions, such as GFCCTI, describe the Gibbs energy (G) of the phase (fcc) for the element (Ti) were adopted from the SGTE database [32] are listed in the Supplementary TDB (thermodynamic database) file (appendix A).

Phase	Reference	Interaction Parameter
AlTi	[16]	$0_{Ti:Ta}^L = 6376.0 + GHCPCTA + 3.0 * GHSERTI$
	[16]	$0_{Ta:Ti}^L = 6376.0 + 3.0 * GHCPCTA + GHSERTI$
	[16]	$0_{Ti:Mo}^L = 51212.0 - 13.5 * T$
	[16]	$0_{Mo,Ti:Ti}^L = 51212.0 - 13.5 * T$
	[16]	$0_{Mo:Mo,Ti}^L = 5692.0 - 1.5 * T$
	[16]	$0_{Ti:Ti,Mo}^L = 5692.0 - 1.5 * T$
	[16]	$0_{Ta,Ti:Ta}^L = 19128.0$
	[16]	$0_{Ta,Ti:Ti}^L = 19128.0$
	[16]	$0_{Ta:Ta,Ti}^L = 2128.0$
	[16]	$0_{Ti:Ta,Ti}^L = 2128.0$
bcc#2	[16]	$0_{Ti:Ti}^L = 2.0 * GFCCTI$
disordered phase	[16]	$0_{Mo:Mo}^L = 2.0 * GFCCMO$
	[16]	$0_{Ta:Ta}^L = 2.0 * GFCCTA$
	[16]	$0_{Ti:Mo}^L = 8250.0 + GFCCMO + GFCCTI$
	[16]	$0_{Mo:Ti}^L = 8250.0 + GFCCMO + GFCCTI$
	[16]	$0_{Ti:Ta}^L = 4250.0 + GFCCTA + GFCCTI$
	[16]	$0_{Ta:Ti}^L = 4250.0 + GFCCTA + GFCCTI$
	[16]	$0_{Mo,Ti:Mo}^L = 8250.0$
	[16]	$0_{Mo,Ti:Ti}^L = 8250.0$
	[16]	$0_{Mo:Mo,Ti}^L = 8250.0$
	[16]	$0_{Ti:Mo,Ti}^L = 8250.0$
	[16]	$0_{Ta,Ti:Ta}^L = 4250.0$
	[16]	$0_{Ta,Ti:Ti}^L = 4250.0$
	[16]	$0_{Ta:Ta,Ti}^L = 4250.0$
	[16]	$0_{Ti:Ta,Ti}^L = 4250.0$
	[16]	$0_{Ti:Mo}^L = 10000.0$
	[16]	$0_{Mo:Ti}^L = 10000.0$
	[16]	$0_{Ti:Ta}^L = 5000.0$

Table 3.4: Modelled binary and ternary thermodynamic parameters for the Ti-Mo-Nb-Ta-Zr system. The thermodynamic description of pure elements is not included. The pure element functions, such as GFCCTI, describe the Gibbs energy (G) of the phase (fcc) for the element (Ti) were adopted from the SGTE database [32] are listed in the Supplementary TDB (thermodynamic database) file (appendix A).

Phase	Reference	Interaction Parameter
Laves_C15	[16]	$0_{Ta:Ti}^L = 5000.0$
	[24]	$0_{Ti:Ti}^L = 15000.0 + 3.0 * GHSERTI$
	[12]	$0_{Mo:Mo}^L = 15000.0 + 3.0 * GHSERMO$
	[12]	$0_{Zr:Zr}^L = 15000.0 + 3.0 * GHSERZR$
	[24]	$0_{Ti:Mo}^L = 15000.0 + GHSERMO$ + $2.0 * GHSERTI$
	[24]	$0_{Mo:Ti}^L = 15000.0$ + $2.0 * GHSERMO + GHSERTI$
	[24]	$0_{Ti:Zr}^L = 9000.0$ + $GHSERZR + 2.0 * GHSERTI$
	[24]	$0_{Zr:Ti}^L = 15000.0 + 2.0 * GHSERZR + GHSERTI$
	[12]	$0_{Mo:Zr}^L = -21734.8 + 0.14 * T$ + $GHSERZR + 2.0 * GHSERMO$
	[12]	$0_{Zr:Mo}^L = 21734.8 - 0.14 * T$ + $2.0 * GHSERZR + GHSERMO$
omega	[12]	$0_{Mo:Mo,Zr}^L = 60000.0$
	[12]	$0_{Zr:Mo,Zr}^L = 60000.0$
	[12]	$0_{Mo,Zr:Mo}^L = 100000.0$
	[12]	$0_{Mo,Zr:Zr}^L = 100000.0$
	[24]	$0_{Ti:Mo,Zr}^L = 60000.0$
	[24]	$0_{Mo,Zr:Ti}^L = 100000.0$
	[19]	$0_{Ti}^L = 1886.7 - 0.15 * T + GHSERTI$
	[19]	$0_{Nb}^L = 15000.0 + 2.4 * T + GHSERNB$
	[32]	$0_{Zr}^L = -8878.082 + 144.432234 * T$ - $26.8556 * T * LN(T) - .002799446 * T^2$ + $38376 * T^{-1}$ $298.15 < T < 2128$ - $29500.524 + 265.290858 * T$ $-42.144 * T * LN(T) + 7.17445E + 31 * T^{-9}$

Table 3.4: Modelled binary and ternary thermodynamic parameters for the Ti-Mo-Nb-Ta-Zr system. The thermodynamic description of pure elements is not included. The pure element functions, such as GFCCTI, describe the Gibbs energy (G) of the phase (fcc) for the element (Ti) were adopted from the SGTE database [32] are listed in the Supplementary TDB (thermodynamic database) file (appendix A).

Phase	Reference	Interaction Parameter
		$2128 < T < 6000$
	[19]	$0_{Ti,Nb}^L = -3775.9$

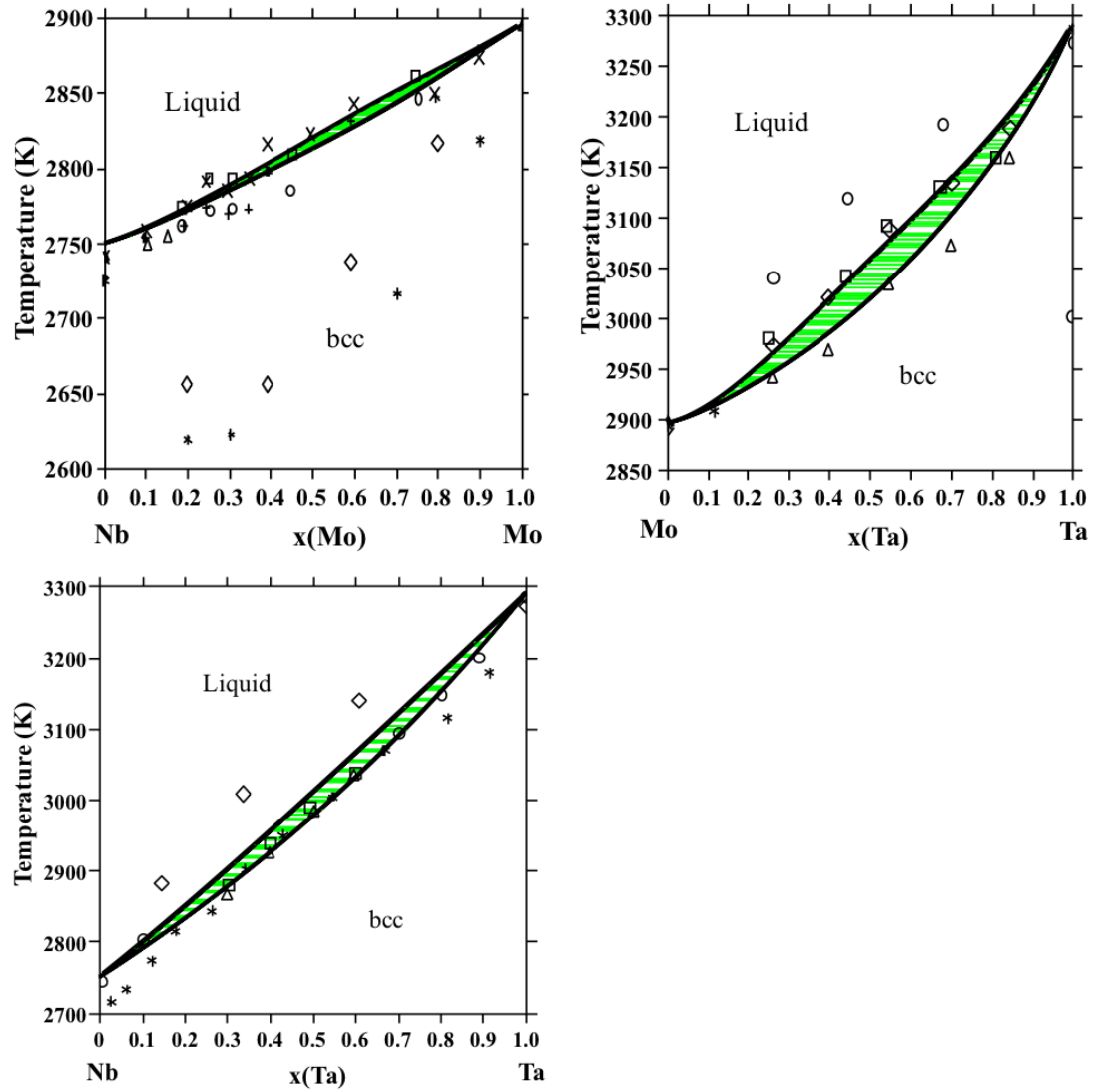


Figure 3.1: Previously modeled thermodynamic descriptions of the Mo-Nb (a) [11], Mo-Ta (b) [11] and Nb-Ta (c) [11] binary systems in comparison with available liquidus and solidus phase boundary experimental data to ensure accuracy (as detailed in [11]).

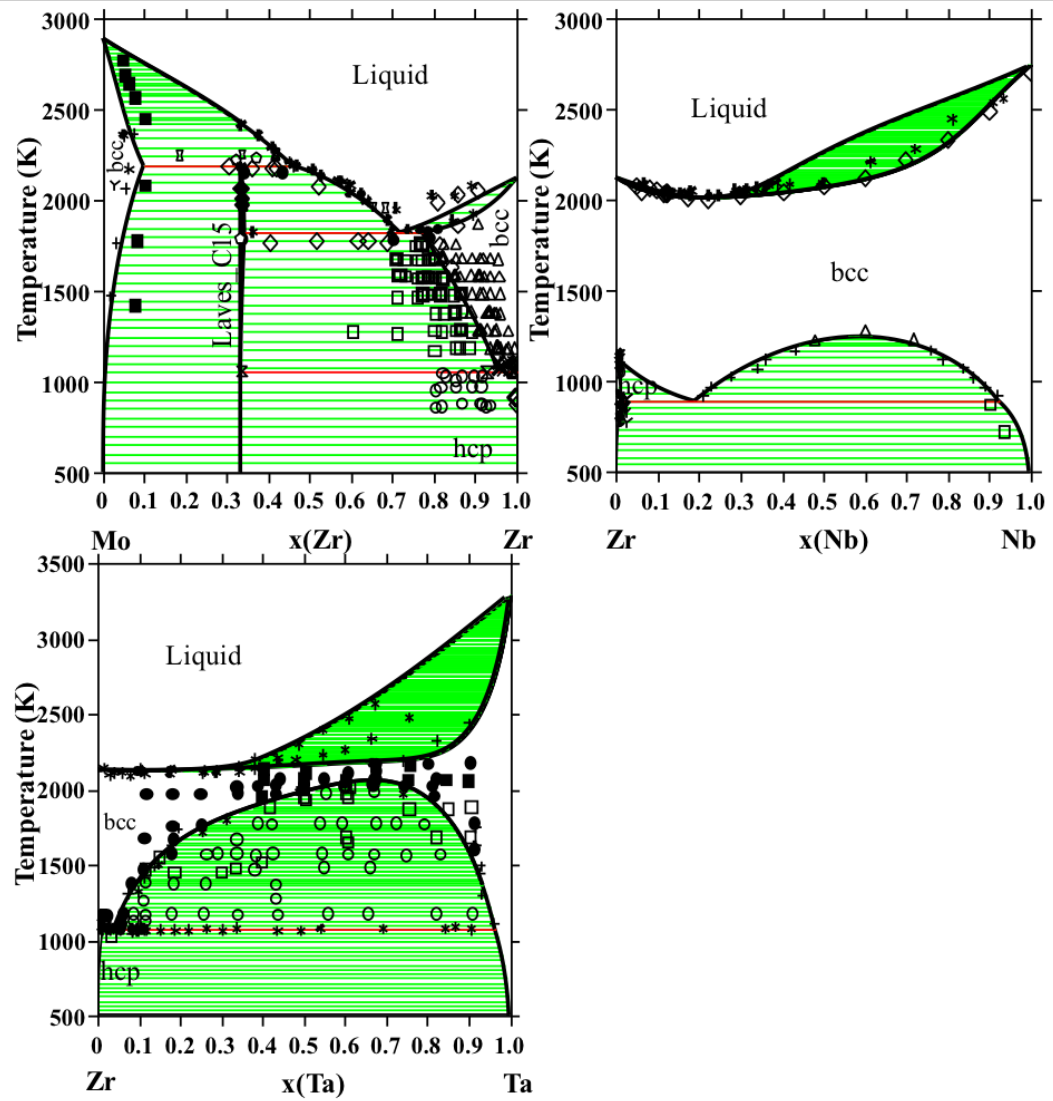


Figure 3.2: Previously modeled thermodynamic description of the Mo-Zr [12] system is plotted with phase boundary, reaction, single phase and two phase experimental data. The previously modeled Nb-Zr [13, 14] system is plotted with solidus, hcp solvus and bcc solvus experimental data. The previously modeled Ta-Zr [15] system is plotted with single-phase, two-phase, phase boundary and solidus experimental data (detailed in the mentioned references).

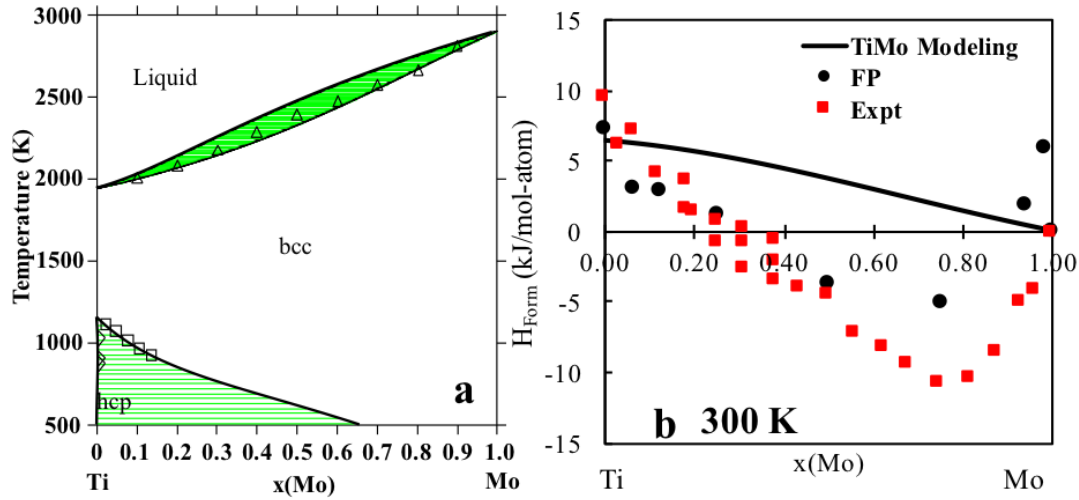


Figure 3.3: Previously modeled thermodynamic description of the Ti-Mo system versus available phase boundary and solidus experimental data to ensure accuracy [16, 17] (a), and enthalpy of formation of the bcc phase predicted by the previous thermodynamic modeling (solid line) at 300 K versus the present first-principles calculations (circles) at 0 K and compared with the enthalpy of formation of the bcc phase obtained from experiments (square) [18] (b).

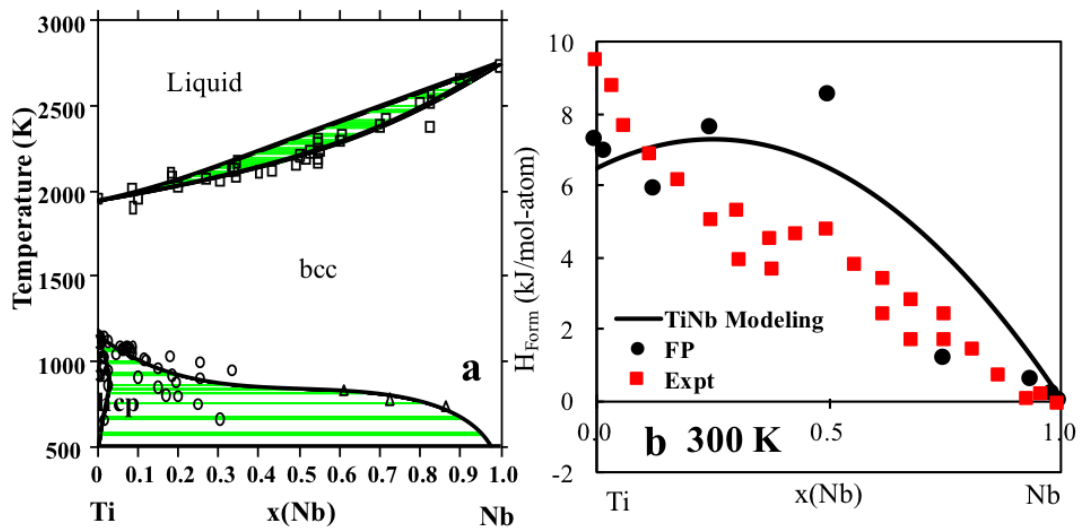


Figure 3.4: Previously modeled thermodynamic description of the Ti-Nb system versus available phase boundary and solidus experimental data to ensure accuracy [19–21][20,48] (a), and enthalpy of formation of the bcc phase predicted by the previous thermodynamic modeling (solid line) at 300 K versus the present first-principles calculations (circles) at 0 K compared with the enthalpy of formation of the bcc phase obtained from experiments (square) [18] (b).

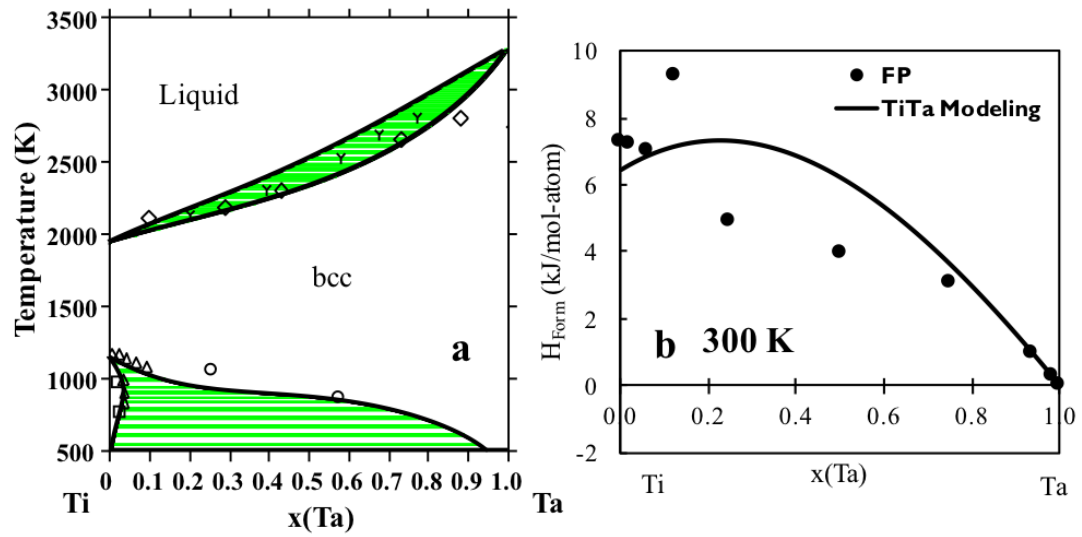


Figure 3.5: Previously modeled thermodynamic description of the Ti-Ta system versus available phase boundary and solidus experimental data to ensure accuracy [16, 22] (a), and enthalpy of formation of the bcc phase predicted by the previous thermodynamic modeling (solid line) at 300 K versus the present first-principles calculations (circles) at 0 K (b).

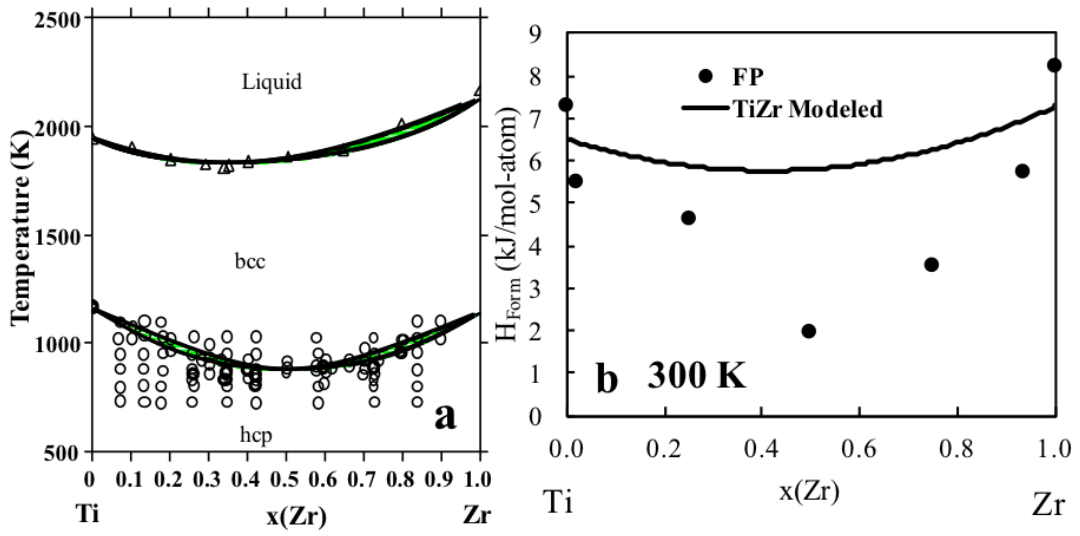


Figure 3.6: Previously modeled thermodynamic description of the Ti-Zr system versus available phase boundary and solidus experimental data to ensure accuracy [21] (a), and enthalpy of formation of the bcc phase predicted by the previous thermodynamic modeling (solid line) at 300 K versus the present first-principles calculations (circles) at 0 K (b).

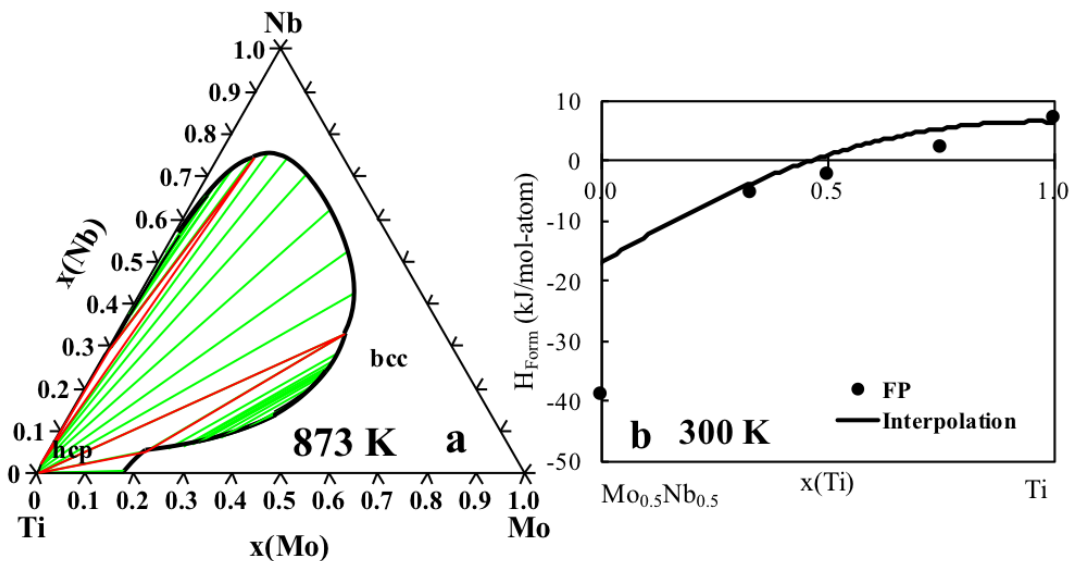


Figure 3.7: Binary interpolation of the isothermal section of the Ti-Mo-Nb system plotted at 873 K (a), and enthalpy of formation of the bcc phase predicted by the binary interpolation of the thermodynamic modeling (solid line) at 300 K versus the present first-principles calculations (circles) at 0 K (b).

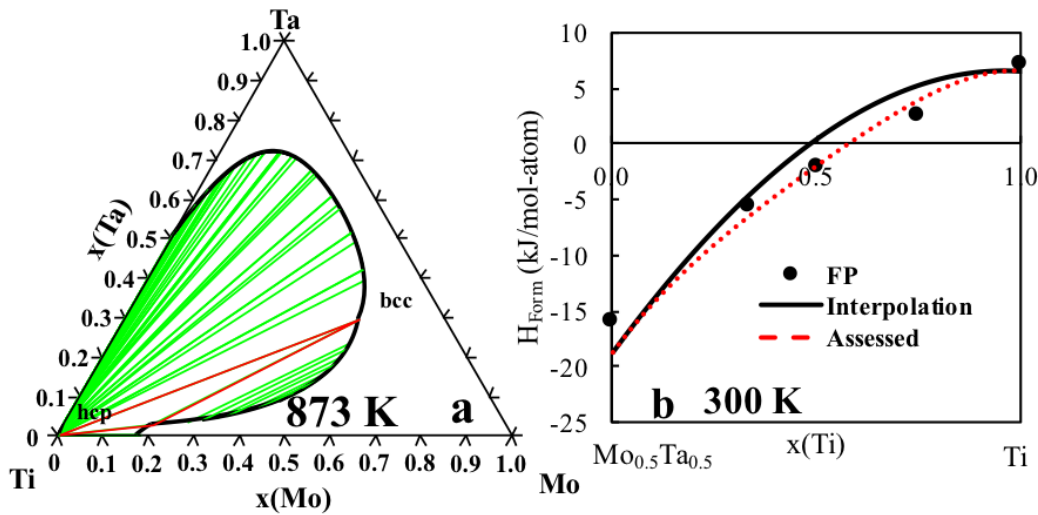


Figure 3.8: Binary interpolation of the isothermal section of the Ti-Mo-Ta system plotted at 873 K (a), and enthalpy of formation of the bcc phase predicted by the previous thermodynamic modeling (solid line) at 300 K and the ternary assessed thermodynamic modeling (red dotted line) versus the present first-principles calculations (circles) at 0 K (b).

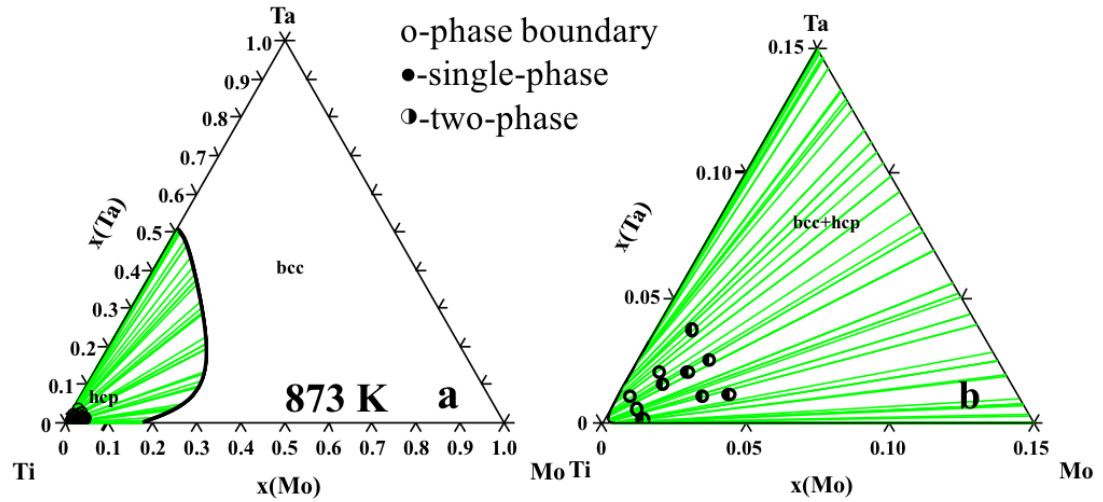


Figure 3.9: Ternary assessed isothermal section of the Ti-Mo-Ta system plotted at 873 K (a), and zoomed in ternary assessed isothermal section at 873 K (b) with the phase boundary and two-phase region experimental data [23] to ensure accuracy of the ternary assessment.

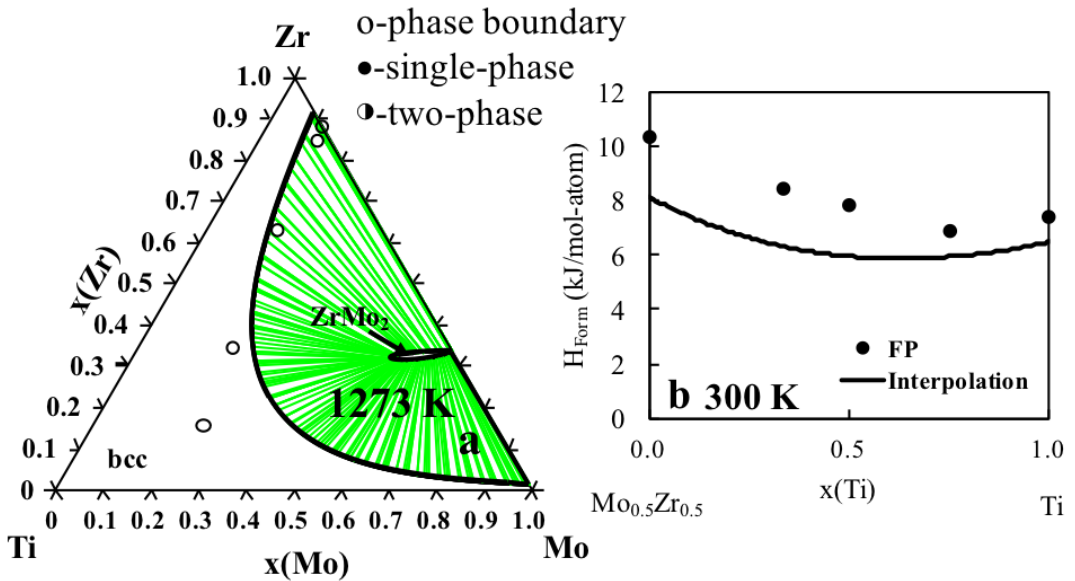


Figure 3.10: The assessed ternary isothermal section of the Ti-Mo-Zr system plotted at 1273 K compared with experimental phase boundary data [24,25] (a), and enthalpy of formation of the bcc phase predicted by the previous thermodynamic modeling (solid line) at 300 K versus the present first-principles calculations (circles) at 0 K (b).

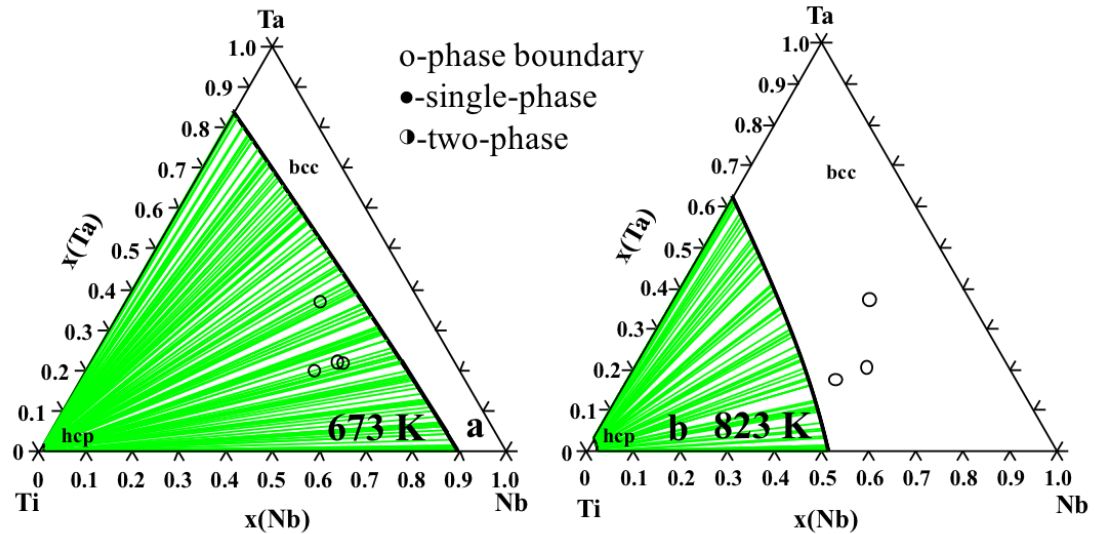


Figure 3.11: Binary interpolation of the isothermal section of the Ti-Nb-Ta system plotted at 673 K compared with experimental phase boundary data [26] (a), and binary interpolation of the isothermal section of the Ti-Nb-Ta system plotted at 823 K compared with experimental phase boundary data [26] (b).

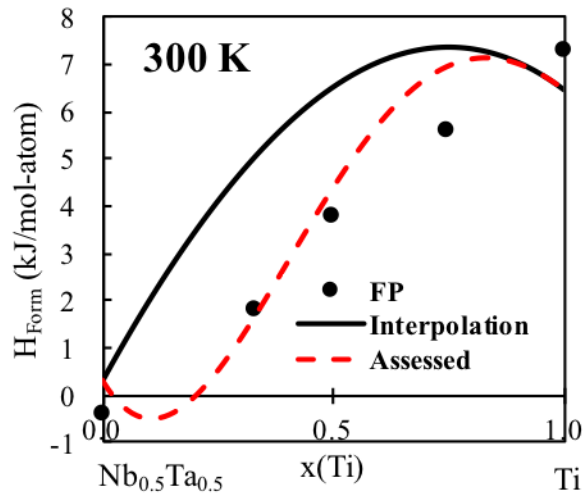


Figure 3.12: Enthalpy of formation of the bcc phase predicted by the previous thermodynamic modeling (solid line) at 300 K and the ternary assessed thermodynamic modeling (red dotted line) versus the present first-principles calculations (circles) at 0 K.

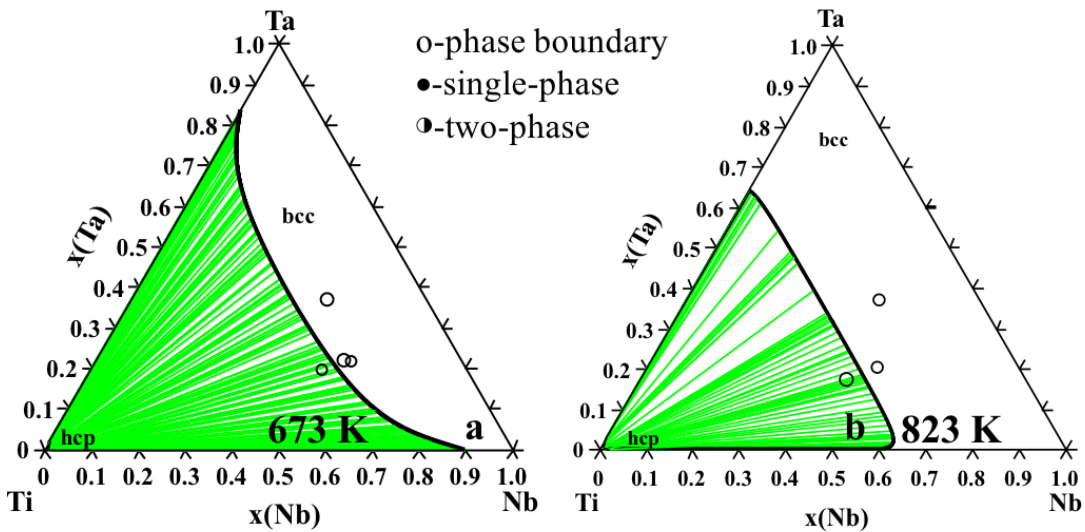


Figure 3.13: Ternary assessed isothermal section of the Ti-Nb-Ta system plotted at 673 K compared with experimental phase boundary data [26] to ensure accuracy of the ternary assessment (a), and ternary assessed isothermal section at 823 K compared with experimental phase boundary data [26] to ensure accuracy of the ternary assessment (b).

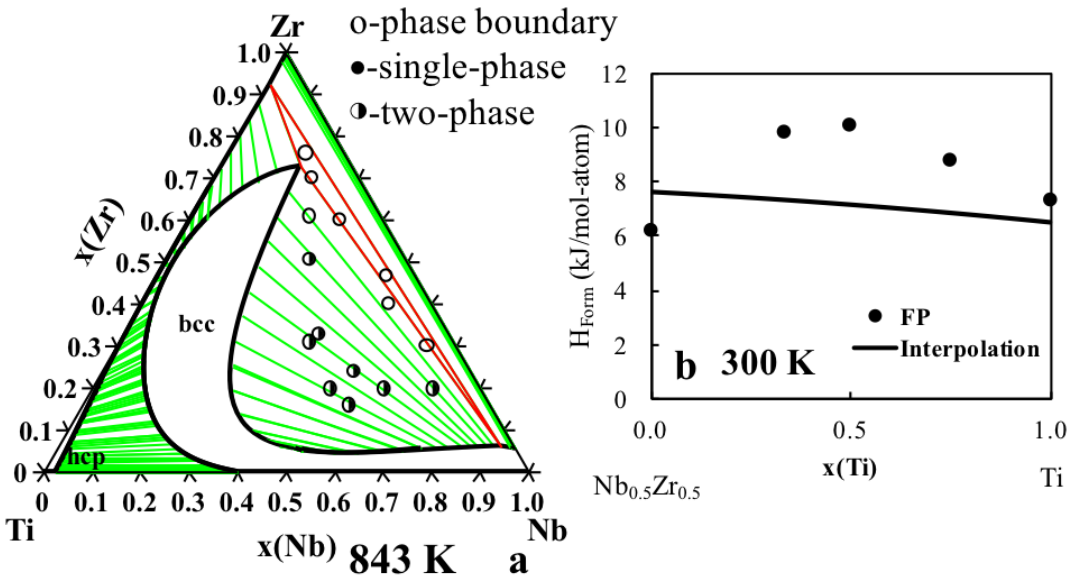


Figure 3.14: Binary interpolation of the isothermal section of the Ti-Nb-Zr system plotted at 843 K compared with experimental phase boundary and two-phase region data [27] (a), and enthalpy of formation of the bcc phase predicted by the previous thermodynamic modeling (solid line) at 300 K versus the present first-principles calculations (circles) at 0 K (b).

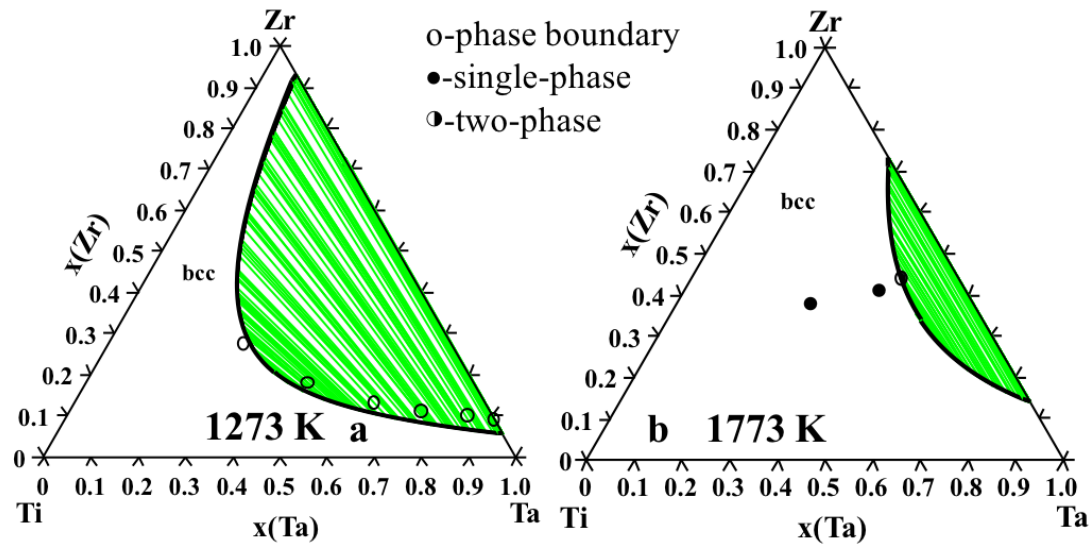


Figure 3.15: Binary interpolation of the isothermal section of the Ti-Ta-Zr system plotted at 1273 K compared with experimental phase boundary data [28, 29] (a), and binary interpolation of the isothermal section of the Ti-Ta-Zr system plotted at 1773 K compared with experimental single phase and two-phase region data [28, 29] (b).

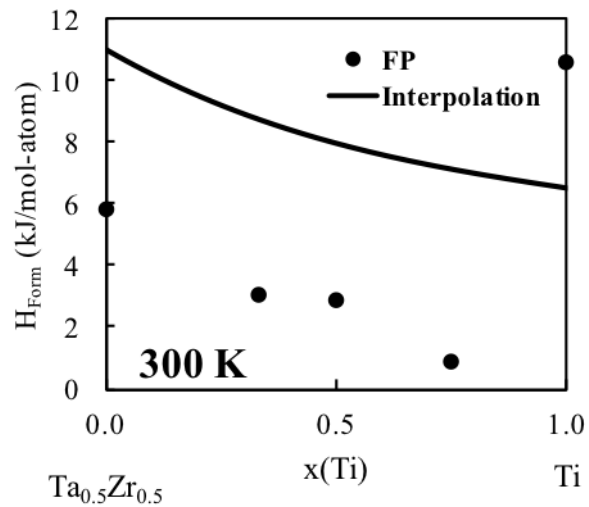


Figure 3.16: Enthalpy of formation of the bcc phase predicted by the previous thermodynamic modeling (solid line) at 300 K versus the present first-principles calculations (circles) at 0 K.

Chapter 4

Thermodynamic modeling of the Sn-Ta system

4.1 Introduction

Currently, the biomaterial implant research of Ti alloys is focused on biocompatible elements that stabilize the body centered cubic (bcc, β) phase of Ti and help to lower its elastic modulus. Tantalum (Ta) is a biocompatible element and is considered to be a strong β -stabilizers [51]. Recently, tin (Sn) has also been researched for use in Ti-alloys due to its low cost and in low concentrations does not affect the biocompatibility of Ti-alloys [40]. Kuroba et al. [111] studied various Ti-alloys such as Ti-29-Nb-13Ta-2Sn (weight percentage, and similarly hereinafter unless specified otherwise), Ti-29Nb-13Ta-4Mo, and Ti-29Nb-13Ta-6Sn for use as biocompatible implant materials. Kuroba and Hagiwara [112] also studied new Ti-Cu-Ni-Sn-Ta alloys for the artificial materials used in orthopedic surgeries. The Sn-Ta system is thus an important sub-system for this purpose [113]. A complete knowledge base of the thermodynamic description of Sn-Ta can be used to examine the effects of temperature and composition on phase stability for higher order systems and help to tailor experimental alloy selections to viable options. The CALPHAD technique, in combination with DFT-based first-principles calculations, has been proven to provide valuable data to model the thermodynamic properties of binary systems such as Sn-Ta that lack sufficient experimental data [79]. The Sn-Ta system has three solid solution phases (bcc, body centered tetragonal bct, and diamond) and two intermetallic compounds, i.e. Ta_3Sn with space group $Pm\bar{3}n$ and $TaSn_2$

$(Ta_{1.2}Sn_{1.8})$ with space group $Fddd$ [114].

In the present work, thermodynamic data was predicted using first-principles calculations for the two intermetallics and for the bcc, bct and diamond solution phases. The finite temperature properties of the phases were obtained using the Debye-Grüneisen model [60] and phonon calculations based on the supercell approach [63]. The DFT data was used to model the parameters of the Gibbs energy of each phase using the CALPHAD technique.

4.2 Literature Review

The Sn-Ta binary system was studied by Okamoto [114], Studnitzky and Schmid-Fetzer [115], and Basile [116]. Both of the intermetallic phases, Ta_3Sn and $TaSn_2$, were shown to have a very narrow homogeneity range. Basile [116] observed that $TaSn_2$ is located around $Ta_{1.2}Sn_{1.8}$ which was then designated as Ta_2Sn_3 by Okamoto [114]. It seems that $TaSn_2$ is a more compatible description of the stoichiometric compound based on the descriptions of similar systems (V-Sn, and Nb-Sn) [33, 117, 118], and thus will be used in the present work. Basile [116] determined $TaSn_2$ has a peritectic reaction at 868 K (595 °C) and used x-ray diffraction (XRD) to elucidate the lattice parameters of $TaSn_2$.

Studnitzky and Schmid-Fetzer [115] used powder samples to study the Ta_3Sn and $TaSn_2$ intermetallic phases and verified the results previously reported by Basile [116]. They cold pressed the pure element powders at 600 MPa and then heated the pellets at 1000 °C for up to 48 hours. The resulting pellet was then cold pressed at 600 MPa again. Under these conditions $TaSn_2$ was observed at 400 °C, but was not present as the temperature increased to 600 °C. In the work by Courtney et al. [119], Ta_3Sn was studied to see how the temperature affects the long-range ordering parameter. In Courtney et al.'s work [119], Ta_3Sn powder samples were sintered at 600, 700, 950, 1200, and 1450 °C for 2, 4, 7, and 16 days, respectively. Each sample was then studied using x-ray diffraction at room temperature to examine the phases present and the long-range ordering. They concluded that the transition temperature of superconductivity for Ta_3Sn varied by a maximum of 4 K based on heat treatment and sintering times due to long-range ordering that occurred. Courtney et al. [119] also measured the lattice parameter of each sample and reported the average value of this cubic phase being 5.285 Å.

4.3 Modeling and Calculations

In the present work, the Vienna Ab-initio Simulation Package (VASP) was used to perform the first-principles calculations [61]. The projector augmented-wave (PAW) [62, 89] method was used to describe the electron-ion interactions. Based on the work of comparing X-C functionals (Figure 5.1) the exchange-correlation functional of the generalized gradient approach depicted by Perdew, Burke, and Ernzerhof (PBE) was employed [58]. A sigma value of 0.2 eV and a plane wave energy cutoff of 1.3 times higher than the highest default cutoff was adopted. The Brillouin zone sampling was done with Blöchl corrections [89] using a gamma centered Monkhorst-Pack (MP) scheme [90]. The k-points grid for diamond-Sn, bcc-Ta, TaSn₂, and bcc-Sn were 4x4x4, 6x6x6, 10x10x5, and 6x6x6 respectively. The k-point grids for the bct-Sn, Ta₃Sn and bcc SQS calculations used an automated k-point mesh generator in VASP with the length of the subdivisions specified as 80. The energy convergence criterion of the electronic self-consistency was set as 10⁻⁴ eV/atom and 10⁻⁴ eV/Å was set as the stopping criteria for the ionic relaxation loop for all of the calculations.

To calculate the enthalpy of formation of the bcc phase across the entire composition range, the enthalpy of formation of Ta and Sn in the bcc phase were calculated with five different compositions of Sn_xTa_{1-x}, where x=0.0185 (SnTa₅₃, 54 atoms), 0.25, 0.5, 0.75, and 0.9815 (Sn₅₃Ta, 54 atoms). For x=0.0185 and 0.9815, calculations were performed on a diluted 54 atom cell where all atoms but one was Sn or Ta (SnTa₅₃ and Sn₅₃Ta). For x=0.25, 0.5, and 0.75, 16-atom special quasirandom structures (SQS) in the bcc phase developed by Jiang et al. [73] were used to mimic the behavior of random structures as discussed in chapter 2. The enthalpy of formation was plotted as a function of composition and then used for the modeling.

The Gibbs energy functions of the pure elements were adopted from the SGTE (SSUB) database [32]. In the present work, the bcc and liquid phases were modeled in conjunction with the two intermetallics Ta₃Sn and TaSn₂. Dilute first-principles calculations of Ta in Sn were done for the diamond and bct phases. However, there is little solubility of Ta in these phases and there is no description of pure Ta in these phases available in SGTE. So, no binary interaction parameters were introduced in the modeling similar to other Sn systems such as Nb-Sn and V-Sn [117, 118]. The

interaction parameters of the liquid and bcc solution phases were modeled using Eq. 2.27 and 2.28, while Ta_3Sn and $TaSn_2$ were modeled according to Eq. 2.31.

4.4 Results and discussion

4.4.1 First-principles

To evaluate the accuracy of the phonon calculations for the present system, both the dispersion curves and the phonon DOS are plotted for bcc-Ta, bct-Sn, $TaSn_2$, and Ta_3Sn in Figure 4.1, 4.2, 4.3, and 4.4, respectively. The bcc-Ta phonon dispersion curve in Figure 4.1 is compared with values obtained by Taioli et al. [30] using neutron scattering, showing good agreement. The longitudinal modes (LO) and the transverse modes (TO) measured by Raman spectroscopy [31] (open square) along with the previous theoretical predictions at the M point (filled square) for bct-Sn are compared with the calculated phonon dispersion curve in Figure 4.2. The substantial difference for the LO mode may be due to the temperature and pressure differences as pointed out by Olijnyk [31]. No imaginary phonon frequencies are obtained in the phonon DOS plots for bcc-Ta, bct-Sn, $TaSn_2$, Ta_3Sn , indicating that they are all mechanically and dynamically stable at 0 K.

The calculated lattice parameters at 0 K from the EOS fitting and with the Debye and phonon models at 298 K are compared to available experimental and previous DFT results in Table 4.1. The lattice parameters of Ta are compared with the experimental lattice parameters by Predmore and Arsenault [120] at room temperature and the previous 0 K DFT results by Shang et al. [121] who used the GGA-PW91 exchange correlation functional. The Sn lattice parameters are compared to experimental work by Allen et al. [122] at 298 K and calculations by Arróyave et al. [123]. The properties of the $TaSn_2$ and Ta_3Sn intermetallics are compared to experimental values by Calvert et al. [124] and Courtney et al. [119], respectively. The results show a less than 0.5% difference when compared with other DFT results at 0 K. There is a less than 2% difference between the DFT 0 K results and the experiments, which are listed in Table 4.1. The variance is due to the fact that the calculations are at 0 K and the experiments are at a higher temperature. When comparing the calculated lattice parameters at 298 K to the experiments, all of the predictions improve to show a less than 1% difference with

the exception of Sn, which shows a less than 2% difference.

Table 4.2 shows the equilibrium volume, V_0 , bulk modulus, B , and the derivative of bulk modulus B' obtained by the EOS E-V fitting of the first-principles data at 0 K. The Sn and Ta calculations are compared with previous first-principles calculations and available experiments. The volume shows a less than 0.5% difference between the previous DFT results and current DFT results for both Sn and Ta [120, 125]. The comparison of the DFT results at 0 K and the experimental results at 298 K for volume show a slightly higher variance of less than 5 % due to the difference in temperature [121, 125]. The B comparison of previous 0 K DFT results and the present 0 K DFT results show a less than 7 GPa difference and the DFT results at 0 K vary by less than 11 GPa from the experimental results at 298 K [120, 121, 125]. The difference between the current calculations and the previous values may be due to many reasons; e.g. the different choices in input parameters used by Peltzer et al. [125] and different exchange correlation functionals. Another reason is due to the temperature difference 0 K (calculations) versus 298 K (experiments). Figure 4.5 shows the enthalpy and entropy of Ta from the Debye and phonon approaches in comparison with the data from the SGTE pure element database [32]. Figure 4.6 shows the comparison of the enthalpy and entropy calculated for Sn from the phonon and Debye model to the SGTE pure element database [32]. Both show excellent agreement.

The elastic stiffness coefficients and polycrystalline elastic properties calculated by the Hill approach and the scaling factors for the Debye model are shown in Table 4.3. To ensure the accuracy of the scaling factor, the elastic stiffness coefficients and moduli are compared with previous first-principles results [95, 107, 108, 126, 127]. The previous calculation results and present calculation results only vary slightly for the TaSn_2 structure. The present work calculated the elastic stiffness coefficients for the Ta_3Sn structure at 2 different atom sizes and compared the results with previous calculations by the Materials Project [95, 107, 108, 126, 127]. The present elastic stiffness results are quite similar. There is a larger variance between the present results and the Materials Project results. This can be attributed to the different input parameters and exchange correlation functional used (PBE in the present work and GGA-PW91 in Materials Project). B calculated from the c_{ij} methodology (designated as B_{cij}) is compared with the B obtained from the EOS fitting (designated as B_{EOS}), showing a difference of less than 3%. Since the B_{EOS}

from the EOS fitting is already compared to experiments, the elastic calculations and the scaling factor for the Debye model are thus deemed accurate.

4.4.2 CALPHAD

The PARROT module in the Thermo-Calc software [76] is used to optimize the parameters of the Gibbs energy function of the TaSn_2 and Ta_3Sn intermetallics as well as the binary interaction parameters for the bcc and liquid phases. The Gibbs energy parameters of the intermetallics are first estimated from the thermodynamic properties obtained by the phonon supercell method because the phonon calculations are regarded as more accurate than the Debye model. While the decomposition temperature of the TaSn_2 intermetallic is known to be 868 K (595 °C) from experiments, the decomposition of the Ta_3Sn intermetallic has not been reported in the literature. It is noted that both the Nb-Sn and V-Sn systems, which are quite similar to the Ta-Sn system, have the X_3Sn phase forming through a peritectic reaction of $\text{bcc} + \text{Liquid} \rightarrow \text{X}_3\text{Sn}$ [33, 117, 118]. Based on the assumption from similar works that Ta_3Sn is also formed through a peritectic reaction, the Ta_3Sn parameters are adjusted and the parameters for the liquid phase are evaluated. The enthalpy and entropy obtained from the evaluated Gibbs parameters along with the results from the Debye model and the phonon quasiharmonic approach for TaSn_2 and Ta_3Sn are plotted in Figure 4.7 and Figure 4.8, respectively. As seen in both figures, the data from the phonon method correlates well with the current CALPHAD modeling. This is to be expected since this data was used to evaluate the parameters. It is noted in Figure 4.7, that the heat capacity and entropy of TaSn_2 from the current CALPHAD modeling is higher than those from the first-principles calculations. This is due to the fact that the enthalpy and entropy values from DFT were adjusted with the experimental data of the peritectic temperature.

The bct and diamond phases are treated as ideal due to the little solubility. As previously stated, the enthalpies of formation of the bcc phase for five different Sn-Ta compositions are calculated and plotted in Figure 4.9, showing asymmetrical behavior. There is a discrepancy between the first-principles value and the CALPHAD modeling for the lattice stability of bcc-Sn. The first-principles predicts a value of 15.48 kJ/mol-atom and the CALPHAD model gives 4.42 kJ/mol-atom. This difference is expected to be due to the instability of Sn in the bcc phase.

Wang et al. [128] concluded and discussed the same discrepancy when comparing first-principles DFT results to SGTE data for Os and Ru. Wang et al. [128] calculated the lattice stability of bcc and fcc (face centered cubic) structures for Os and Ru, both stable in the hexagonal close packed phase at standard temperature and pressure, and concluded a difference of approximately 40 and 60 kJ/mol for Ru and Os, respectively. Wang et al. [128] attributed this difference to the fact that when using first-principles calculations of unstable structures, frequencies of some of the phonon modes would become imaginary and thus the results would be less accurate. On the other hand, the CALPHAD technique can extrapolate lattice stabilities from binary solutions for which an alloying element has stabilized the otherwise unstable structure. These enthalpies of formation calculated from the SQS first-principles calculations are used to evaluate the bcc binary interaction parameters in the present CALPHAD modeling. The enthalpy of formation of the bcc phase is negative at the Ta rich side and becomes positive at the Sn rich side. This is common for X-Sn systems [117, 118], such as the Nb-Sn system [118] shown in Figure 4.9. It should be noted that Toffolon et al. [33, 118] used experimental data on the Sn-rich bcc phase to evaluate the Nb-Sn system's bcc interaction parameters. Due to the asymmetry of the enthalpy of formation for the bcc phase, a subregular 1L interaction parameters is introduced.

The interaction parameters obtained in the present work are listed in Table 4.4. Based on these model parameters, the phase diagram is calculated and shown in Figure 4.10. The melting temperature of Ta_3Sn is predicted to be 2884 K. Both the intermetallics decompose incongruently similar to those in the Nb-Sn and V-Sn systems. As seen in Table 4.4, both intermetallic phases have a negative enthalpy of formation and a negative entropy of formation. This goes along with previous predictions by Arroyave and Liu [129] where they showed that the enthalpy and entropy of formation have the same sign. The calculated enthalpy of mixing of the liquid phase is plotted in Figure 4.11. The interaction parameter for the liquid phase allows for an accurate representation of the phase stability in Figure 4.10 but may need to be slightly adjusted if experimental data would come available.

4.5 Conclusion

The present work incorporates the thermodynamic data from DFT-based first-principles calculations and the available experimental data in the literature to model the Gibbs energies for the bcc and liquid solution phases and the stoichiometric Ta_3Sn and TaSn_2 phases of the Sn-Ta system. First-principles calculations were used to predict the enthalpy of formation of the bcc phase for the evaluation of interaction parameters in the phase. The decomposition temperature of Ta_3Sn was predicted to be 2884 K. The completed thermodynamic description is compiled into a tdb file in appendix B.

Table 4.1: Lattice parameters from first-principles calculations compared with experimental values.

Phase	Space Group	a (Å)	b (Å)	c (Å)	Reference
bcc-Ta	$I\bar{m}\bar{3}m$	3.316			This work (0 K)
		3.328			This work phonon (298 K)
		3.330			This work Debye (298 K)
		3.30			Expt. [120]
		3.32			DFT (0 K) [121]
		5.939	3.214		This work (0 K)
bct-Sn	$I4_1/amd$	5.959	3.236		This work phonon (298 K)
		5.954	3.222		This work Debye (298 K)
		5.83	3.18		Expt. [122]
		5.93	3.23		DFT (0 K) [123]
		5.641	9.766	19.200	This work (0 K)
TaSn ₂	$Fddd$	5.652	9.786	19.238	This work phonon (298 K)
		5.652	9.785	19.238	This work Debye (298 K)
		5.63	9.80	19.18	Expt. [124]
		5.304			This work (0 K)
Ta ₃ Sn	$Pm\bar{3}n$	5.319			This work phonon (298 K)
		5.319			This work Debye (298 K)
		5.29			Expt. [119]

Table 4.2: Equilibrium volume V_0 , bulk modulus B , and the first derivative of bulk modulus with respect to pressure B' , from fitted equilibrium properties from the EOS at 0 K compared to experimental work and previous DFT studies.

Phase	V_0 ($\text{\AA}^3/\text{atom}$)	B (GPa)	B'	Reference
bcc-Ta	18.241	193.7	3.84	This work
	17.9685	200		Expt. [120]
	18.313	195.3	3.82	DFT [121]
bct-Sn	28.431	47.7	4.61	This work
	27.055	58.0		Expt. [125]
	28.396	54.0		DFT [125]
TaSn ₂	22.631	104.3	4.80	This work
Ta ₃ Sn	18.668	182.4	4.27	This work

Table 4.3: Elastic stiffness coefficients and elastic properties predicted using the Hill approach and the scaling factors used in the Debye model, calculated from the Poisson ratio, see Eq. 2.12. To ensure the accuracy of the calculated scaling factor, the bulk modulus (B_{cij}) calculated from the elastic coefficients was compared to the B_{EOS} calculated from the EOS fitting Eq. 2.6.

	TaSn ₂		Ta ₃ Sn		FP
	This Work	FP	This Work	This Work	
		8 atoms	32 atoms		
C ₁₁ (GPa)	166	161	297	310	226
C ₁₂ (GPa)	79	78	127	131	155
C ₁₃ (GPa)	62	57			
C ₂₂ (GPa)	189	182			
C ₂₃ (GPa)	68	68			
C ₃₃ (GPa)	187	183			
C ₄₄ (GPa)	37	35	65	68	22
C ₅₅ (GPa)	59	55			
C ₆₆ (GPa)	61	60			
E (GPa)	135		210	202	
G (GPa)	53	51	80	76	27
Poisson Ratio	0.288	0.29	0.32	0.32	0.43
Scaling factor	0.789		0.71	0.71	
B_{cij} (GPa)	107	107	184	190	179
B_{EOS} (GPa)	104		182		

References [95, 107, 108, 126, 127]

Table 4.4: Modeled parameters in SI units in the present work for the phases in the Sn-Ta binary system. These parameters were incorporated with the SGTE data for the pure elements [32].

Phase (model)	Modeled Parameters
bcc (Sn,Ta)	${}^0L_{Ta,Sn}^{bcc} = + 70451$ ${}^1L_{Ta,Sn}^{bcc} = + 112237$
Liquid (Sn,Ta)	${}^0L_{Ta,Sn}^{Liq} = -17118$
TaSn ₂	$G^{TaSn_2} = 2 * {}^0G_{Sn}^{bct} + {}^0G_{Ta}^{bcc} - 29678 - 4.202T$
Ta ₃ Sn	$G^{Ta_3Sn} = {}^0G_{Sn}^{bct} + 3 * {}^0G_{Ta}^{bcc} - 68844 - 6.000T$

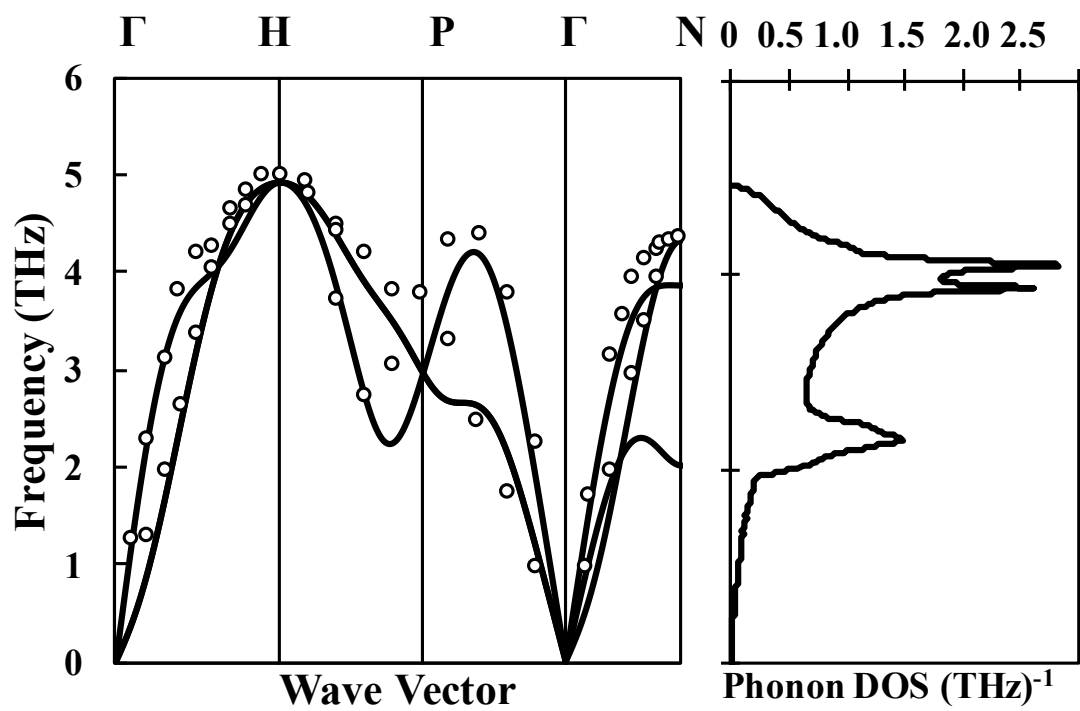


Figure 4.1: Calculated phonon dispersion curve of bcc-Ta, compared with neutron diffraction experiments (\circ) [30] along with the phonon DOS.

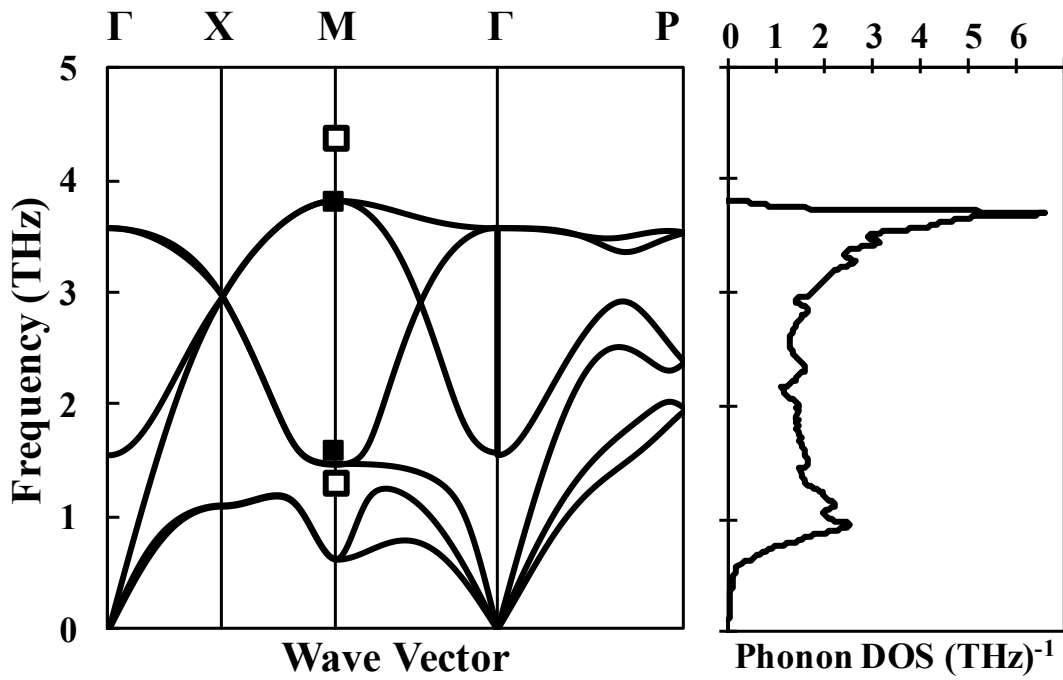


Figure 4.2: Calculated phonon dispersion curve of bct-Sn on the left and phonon DOS on the right. The open squares (\square) are the LO and TO modes from Raman [31] and the filled squares the theoretical prediction of the LO and TO modes at the M point [31].

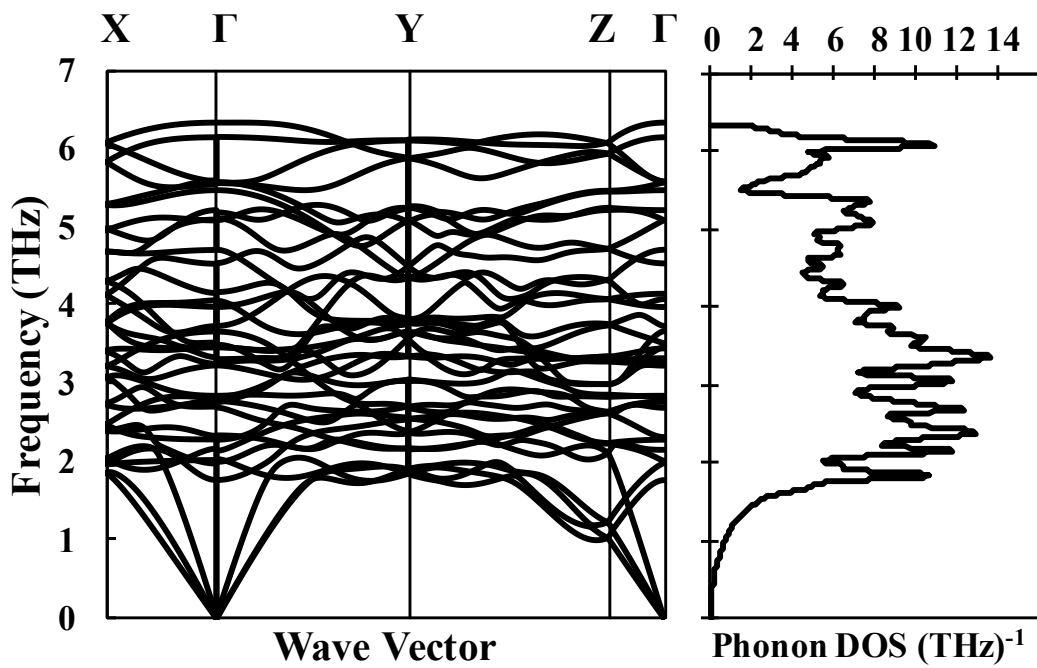


Figure 4.3: Calculated phonon dispersion curve for TaSn_2 at 0 K and the phonon DOS.

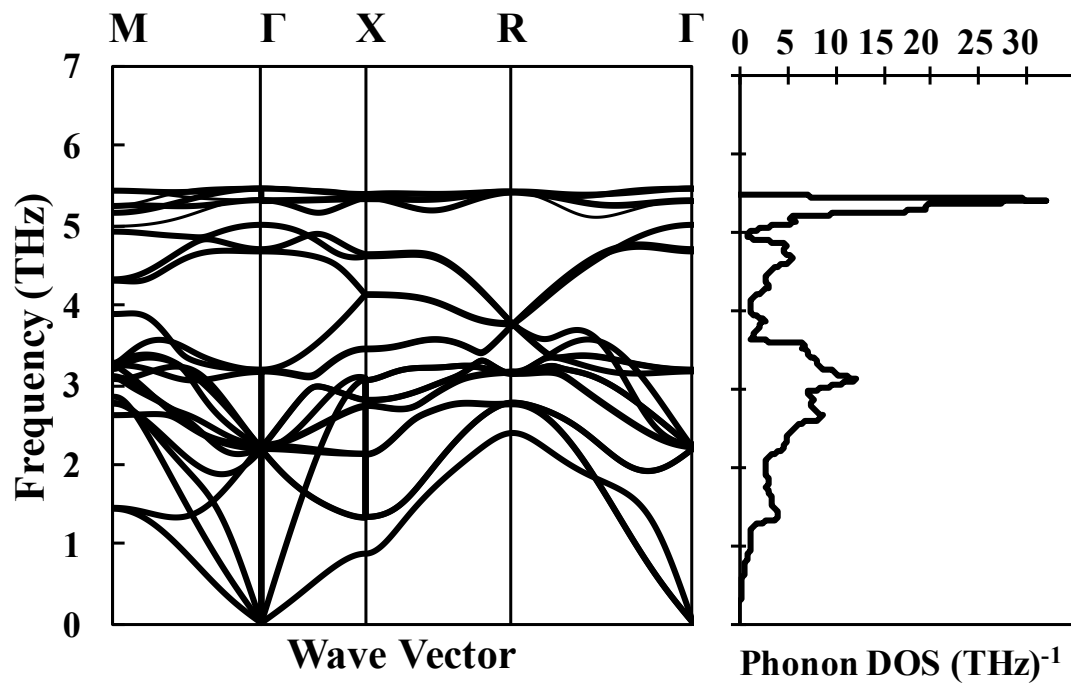


Figure 4.4: Calculated phonon dispersion curve of Ta_3Sn at 0 K on the left and the phonon DOS on the right.

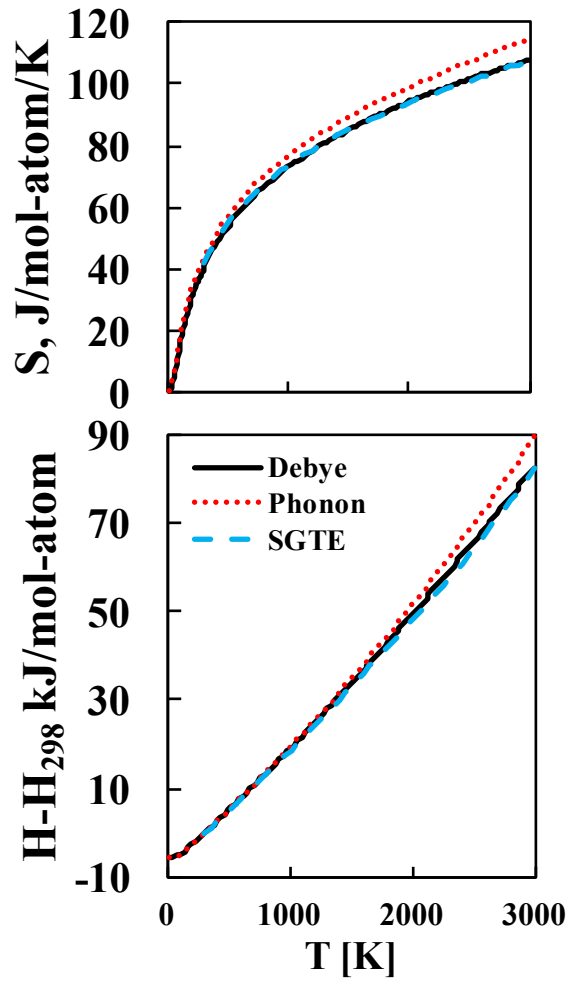


Figure 4.5: Comparison of the enthalpy and entropy of bcc-Ta from the Debye model (solid line) and the quasiharmonic phonon calculations (red dotted line) to the SGTE data (blue dashed line) [32].

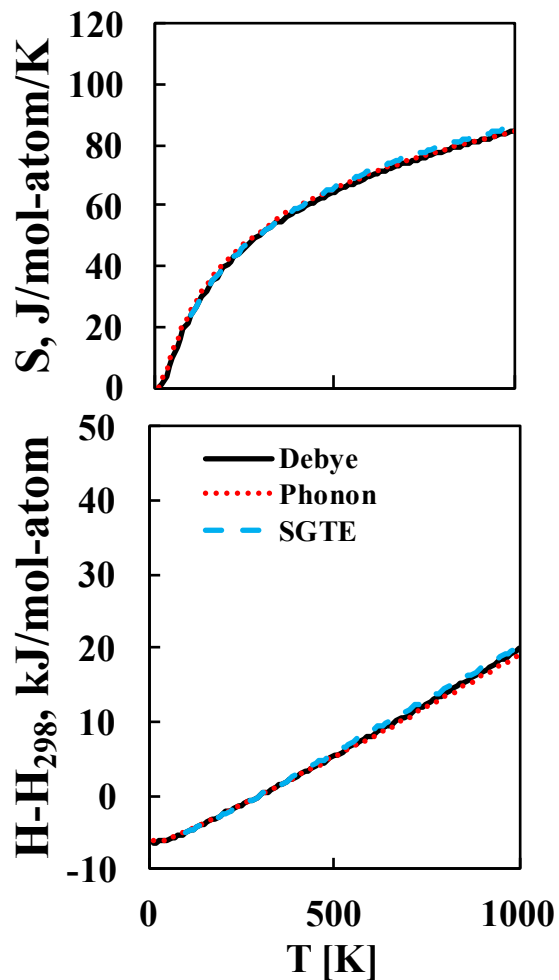


Figure 4.6: Comparison of the enthalpy and entropy of bct-Sn from the Debye model (solid line) and the quasiharmonic phonon calculations (red dotted line) to the SGTE data (blue dashed line) [32].

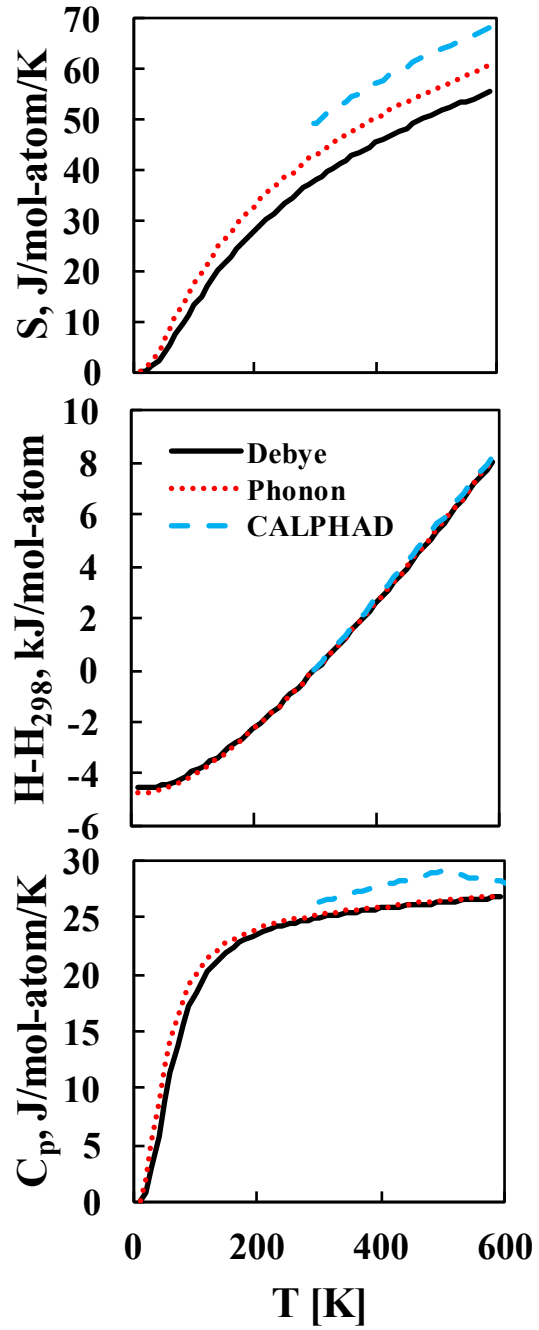


Figure 4.7: Heat capacity, enthalpy and entropy of TaSn_2 using the Debye model (solid line) and the quasiharmonic phonon calculation (red dotted line) from first-principles calculations, compared with those from the current CALPHAD modeling (blue dashed line).

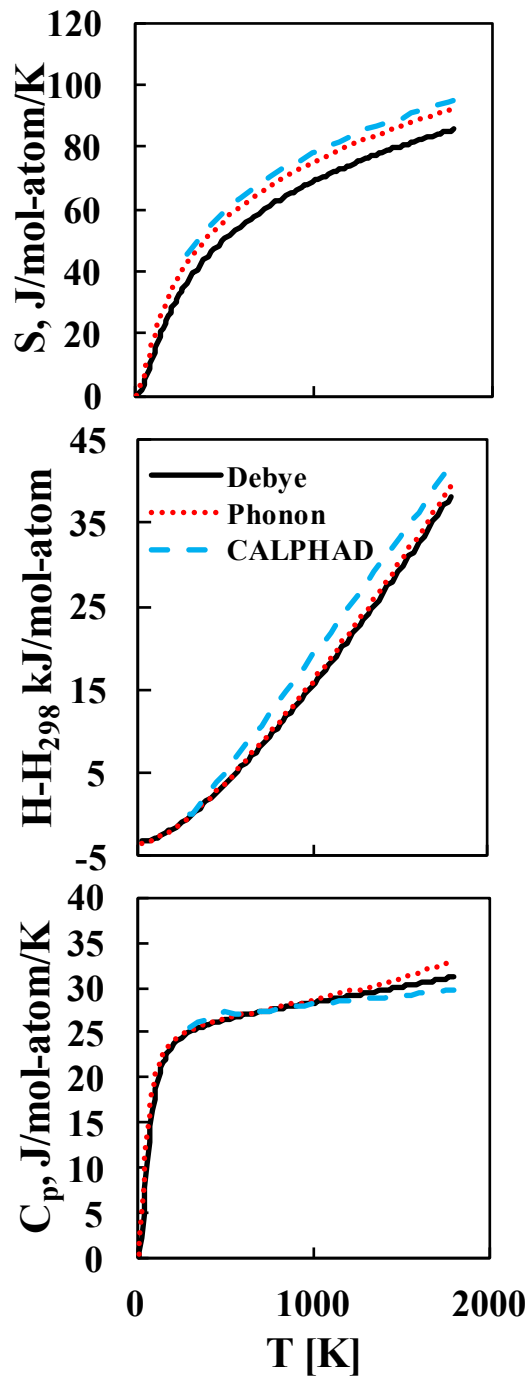


Figure 4.8: Heat capacity, enthalpy and entropy of Ta_3Sn using the Debye model (solid line) and the quasiharmonic phonon calculation (red dotted line) compared with those from the current CALPHAD modeling (blue dashed line).

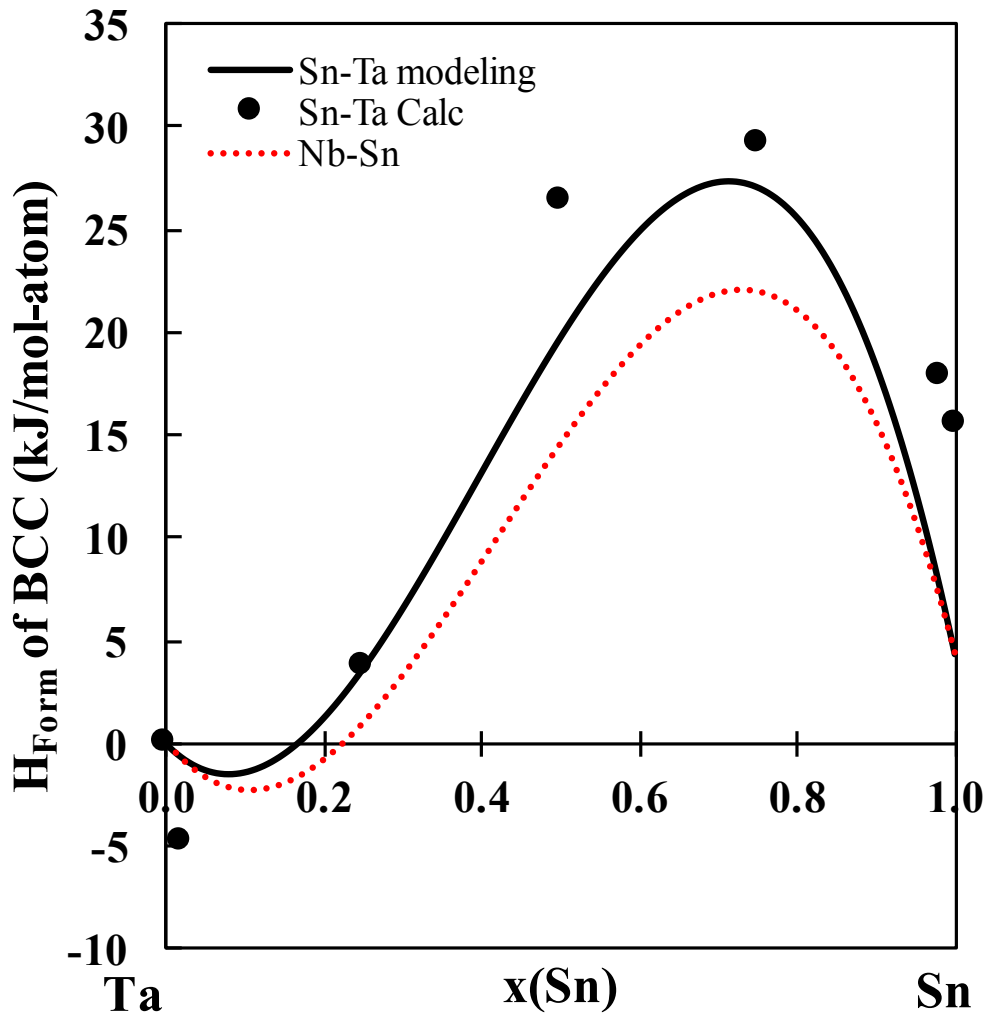


Figure 4.9: Enthalpy of formation of the bcc phase of the Sn-Ta system as a function of composition at 298 K and ambient pressure from the current CALPHAD modeling (solid line) and from the first-principles calculations at 0 K (dots), showing asymmetric behavior. This was compared with data of the Nb-Sn system from Toffolon et al. [33] (dashed red line) which was modeled using experimental data, showing similar asymmetric behavior.

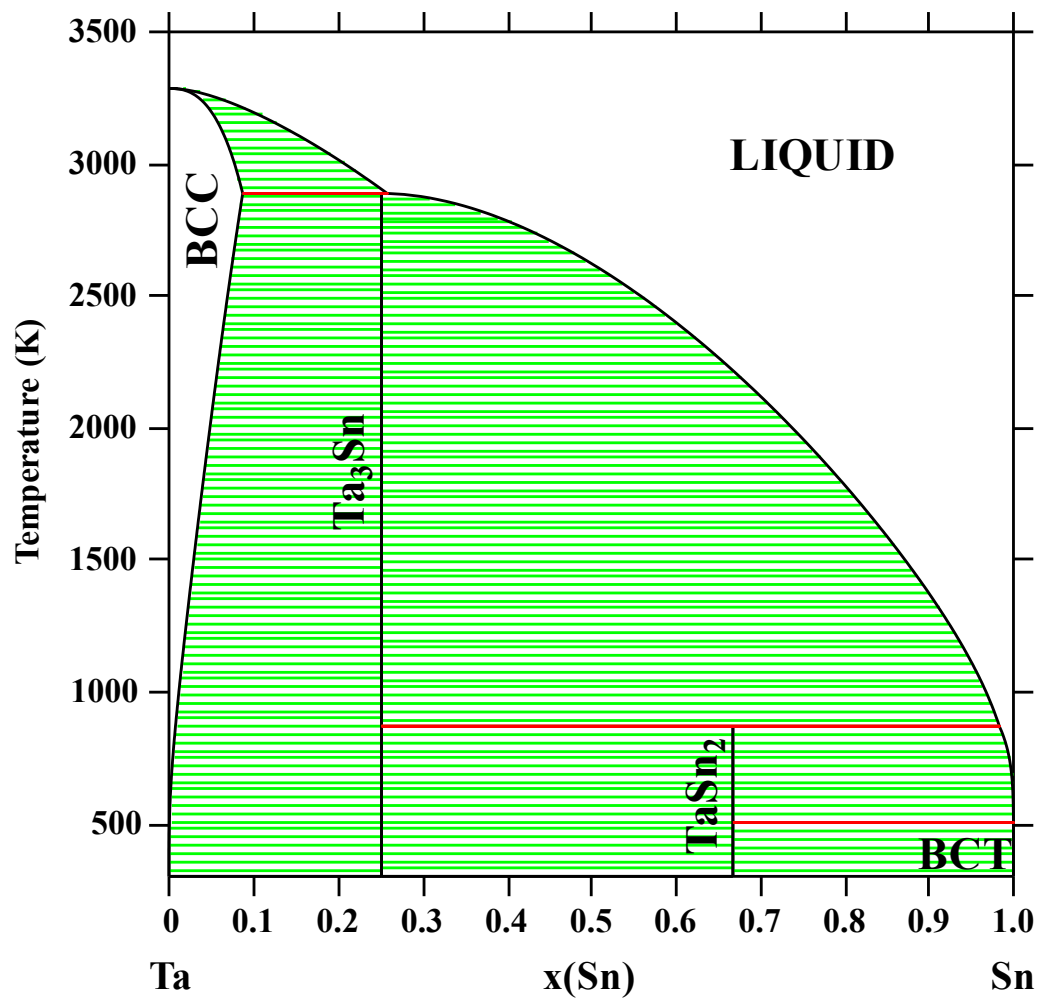


Figure 4.10: Calculated Sn-Ta phase diagram using the present thermodynamic description.

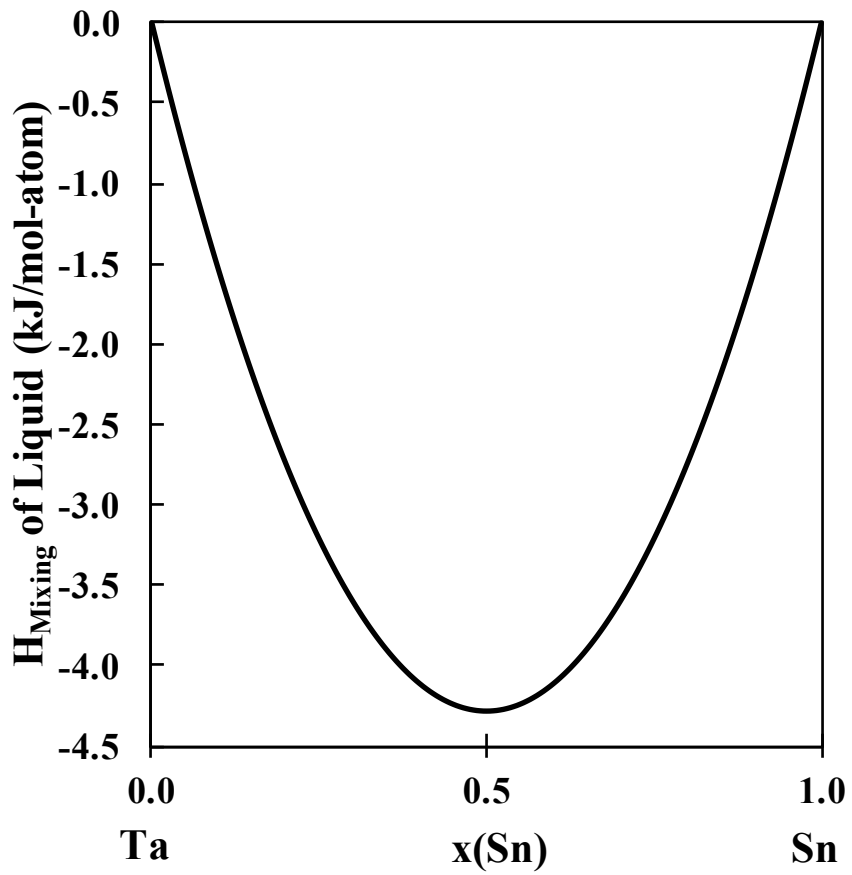


Figure 4.11: Enthalpy of mixing of the liquid phase as a function of composition at 298 K and ambient pressure in the Sn-Ta system.

Chapter 5 |

Effects of alloying elements on the elastic properties of bcc Ti- X alloys

5.1 Introduction

The present chapter is aimed at studying the effects of alloying elements on the mechanical properties of Ti-alloys as well as completing a database to calculate the elastic properties as a function of composition. This is accomplished by systematically studying the single crystal elastic stiffness coefficients (c_{ij} 's) and polycrystalline aggregate properties of bcc Ti-X (X = Mo, Nb, Ta, Sn, Zr) alloys. The elastic properties are calculated using first-principles calculations based on density functional theory (DFT). The composition dependence of the elastic properties of Ti-X alloys is explored through dilute solutions and special quasirandom structures (SQS) [73] for concentrated solutions using the methodologies outlined in chapter 2. The obtained elastic properties are then fit using the CALPHAD method and extrapolated to higher order Ti-alloys.

5.2 Modeling and Calculations

In the present work, the Vienna Ab-initio Simulation Package (VASP) [61] was employed to calculate the elastic properties of pure elements and Ti-containing binary systems in the bcc phase. The ion-electron interactions were described using

the projector augmented wave (PAW) [62, 89] method. As discussed previously, the use of two X-C functionals were compared in this chapter and based on the results the generalized gradient approximations depicted by Perdew, Burke, and Ernzerhof (PBE-GGA) was employed [58]. For consistency, a 310 eV energy cutoff was adopted for all calculations, which is roughly 1.3 times higher than the default value. The energy convergence criterion of the electronic self-consistency was set as 10^{-6} eV/atom, and the Γ -centered Monkhorst-Pack scheme was used for Brillouin zone sampling [61, 90]. The k-points grid used for each calculation are listed in appendix C.

For the Ti-X binary systems, calculations for both dilute and SQS solutions were carried out. Three SQS cells with mole fractions of alloying element X atoms at 0.25, 0.5, and 0.75 were employed. Dilute solutions were calculated for each Ti-X binary alloy using different supercell sizes, i.e., Ti-Mo 4 dilute structures ($\text{Mo}_{0.98}\text{Ti}_{0.02}$ 54-atoms, $\text{Mo}_{0.94}\text{Ti}_{0.06}$ 16-atoms, $\text{Ti}_{0.88}\text{Mo}_{0.12}$ 8-atoms, $\text{Ti}_{0.94}\text{Mo}_{0.06}$ 16-atoms), Ti-Nb 4 dilute structures ($\text{Nb}_{0.98}\text{Ti}_{0.02}$ 54-atoms, $\text{Nb}_{0.94}\text{Ti}_{0.06}$ 16-atoms, $\text{Ti}_{0.88}\text{Nb}_{0.12}$ 8-atoms, $\text{Ti}_{0.98}\text{Nb}_{0.02}$ 54-atoms), Ti-Sn 1 dilute structure ($\text{Ti}_{0.94}\text{Sn}_{0.06}$ 16-atoms), Ti-Ta 5 dilute structures ($\text{Ta}_{0.98}\text{Ti}_{0.02}$ 54-atoms, $\text{Ta}_{0.94}\text{Ti}_{0.06}$ 16-atoms, $\text{Ti}_{0.88}\text{Ta}_{0.12}$ 8-atoms, $\text{Ti}_{0.94}\text{Ta}_{0.06}$ 16-atoms, $\text{Ti}_{0.98}\text{Ta}_{0.02}$ 54-atoms), Ti-Zr 2 dilute structures ($\text{Zr}_{0.94}\text{Ti}_{0.06}$ 16-atoms, $\text{Ti}_{0.98}\text{Zr}_{0.02}$ 54-atoms). The interaction parameters for the elastic stiffness coefficients were then determined according to the methodology laid out in chapter 2.

The first-principles results were then used to model the elastic stiffness coefficients. The modeling was completed by calculating the difference between the first-principles calculations and a linear extrapolation between pure elements. The differences were then used to fit to the interaction parameters. Due to the limitations within the PARROT module, a Mathematica script was used to fit the interaction parameters. The Mathematica script is appended in appendix C. With the focus being Ti-rich alloys, the first-principles results with 70 at. % Ti or higher were weighted heavier (x6, according to the authors' practices) than the other points for the fittings. The best fit was found by comparing the fittings obtained with one interaction parameter or with two interaction parameters. The moduli values were then calculated from the elastic stiffness coefficients according to the methodology in chapter 2.

5.3 Results and discussion

5.3.1 Evaluation of calculation settings

The X-C functionals of PW91 and PBE were tested on the Ti-Ta binary system. The results are plotted in Figure 5.1, showing the \bar{C}_{44} values differing by 10 GPa or less and the \bar{C}_{11} and \bar{C}_{12} values by less than 5 GPa for high Ta contents and by 26 GPa and 13 GPa with 25 at. % Ta, respectively. Since overall the values vary by an error of less than 0.2 (calculated with Eq. 2.24), and the PBE functional was developed as an improvement of the PW91 functional for metals, the PBE functional is chosen for the present work.

Three magnitudes of strain are tested on the Ti-Mo binary system and plotted in Figure 5.2. The different strain magnitudes do not affect the results significantly. For example, the \bar{C}_{11} values calculated using ± 0.01 , ± 0.013 , and ± 0.007 strains at $\text{Mo}_{0.94}\text{Ti}_{0.06}$ are 451 GPa, 450 GPa, and 450 GPa, respectively, varying within 1 GPa (< 0.01). The variances in the \bar{C}_{12} and \bar{C}_{44} results are similar. Overall, the variances in the \bar{C}_{11} and \bar{C}_{12} are less than 0.02 (Eq. 2.24). The largest variance is in the $\text{Ti}_{0.50}\text{Mo}_{0.50}$ where the \bar{C}_{44} values are 42 GPa, 42 GPa, and 65 GPa calculated with ± 0.01 , ± 0.013 , and ± 0.007 strains, respectively. Overall, the strain magnitude does not affect the calculated results significantly, and thus the ± 0.01 strain magnitude is used for all the calculations.

5.3.2 Calculations of elastic coefficients in Ti-X binary systems

The elastic stiffness coefficients and bulk moduli (B) are calculated for the pure elements in the bcc structure and reported in Table 5.1. The results in the present work are all obtained at 0 K. The results for Mo, Nb and Ta, which are stable in the bcc structure at low temperatures, are compared with experimental data at temperatures shown in Table 5.1 [99, 102]. The error (Eq. 2.24) between the present results and previous results for Mo, Nb and Ta are 0.0261, 0.075, and 0.0425, respectively [68, 99, 102]. This discrepancy is due to the temperature difference between the experiments and calculations. The calculations are at 0 K while the experimental values were measured at higher temperatures.

Ti and Zr are stable in the hcp structure at low temperatures, and Sn is stable in the body centered tetragonal and diamond structures at low temperatures. Due

to the instability of Ti, Sn and Zr in the bcc structure at low temperatures, their elastic stiffness coefficients are compared to previous first-principles calculations at 0 K [121] that used the PW91 functional, and the errors/differences are 0.024, 0.528 and 0.051, respectively. The differences are related to the instability of the bcc structure, the different exchange correlation functionals and the different input parameters chosen. Due to the bcc instability, multiple relaxation schemes are compared in the present work to find the lowest energy structure retaining the bcc symmetry, making the results the most accurate representation of the bcc pure elements.

Figure 5.3 to Figure 5.5 compare the calculated elastic stiffness coefficients, \bar{C}_{11} , \bar{C}_{12} , \bar{C}_{44} (circles) with the currently modeled elastic stiffness coefficients (solid line) and linear combination from the pure elements for the Ti-Mo, Ti-Nb, Ti-Sn, Ti-Ta, and Ti-Zr systems. The model parameters are shown in Table 5.2. The results calculated for the Ti-Mo, Ti-Nb, and Ti-Ta systems are compared with previous calculated results from Ikehata et al. [2], and the differences are due to the different input parameters and structures used at each composition. Ikehata et al. [2] used the s orbital electrons as the valance electrons for Ti and used the B2 structure for their $Ti_{0.50}X_{0.50}$ compositions with Ti at the body centered site and X at the corner sites. For the $Ti_{0.25}X_{0.75}$ and $Ti_{0.75}X_{0.25}$ structures they used the DO_3 structure with space group $Fm\bar{3}m$, and not the bcc space group of $Im\bar{3}m$. The present work uses the p electrons as valance electrons for Ti based on updated recommendations by VASP and 16-atom SQS from Jiang et al. [73]. The SQS mimic the random substitution of elements with less error and represent the atomic structures of solution phases better than ordered structures. It can be seen that Mo, Nb, and Ta affect the elastic stiffness coefficients in a similar fashion. As shown in Figure 5.3a, 5.3b and 5.3d the \bar{C}_{11} increases in value from Ti to X (X = Mo, Nb, Ta). Figures 5.5a, 5.5b and 5.5d show that the \bar{C}_{44} values first decrease and then increase with the addition of the alloying element X (X = Mo, Nb and Ta). The \bar{C}_{12} values increase by the addition of Mo or Ta (Figure 5.4a and Figure 5.4d, respectively), and the \bar{C}_{12} values first decrease and then increase by the addition of Nb (Figure 5.4b). A similar trend is shown in the \bar{C}_{11} and \bar{C}_{12} data for the Ti-Sn system (Figure 5.3 and Figure 5.4c). The \bar{C}_{11} and \bar{C}_{12} values first increase and then decrease from pure Ti to pure Sn. As seen in Figure 5.5c, \bar{C}_{44} first increases in value, then decreases, and then increases again from pure Ti

to pure Sn. In the Ti-Zr system, the \bar{C}_{11} and \bar{C}_{44} values first increase and then decrease with increasing Zr concentration (Figure 5.3e and Figure 5.5e). For the Ti-Zr system, the \bar{C}_{12} values first decrease and then increase, as shown in Figure 5.4e. The first-principles calculations based on DFT results for the elastic stiffness coefficients are listed in Table 5.3.

Figure 5.6 summarizes the present Young's moduli results for each Ti-X binary system (circles). The E results for the pure elements and Ti-X binary systems are listed in Table 5.4. The lines are the estimated E using the Voigt-Reuss-Hill approach and predicted from the elastic stiffness coefficients that were modeled using Eq. 2.32. The elastic stiffness coefficients model parameters are shown in Table 5.2. The average from the Hill approach is plotted as a solid black line while those from the Voigt (high bound) and Reuss (low bound) approaches are plotted as dotted and dashed lines, respectively. For stable structures the Voigt and Reuss approaches do not vary drastically but when the structures are unstable the variance is larger with the average from the Hill approach being the value that the database will predict. The results for the Ti-Mo, Ti-Nb and Ti-Ta systems are compared to available experimental results [3–5, 7, 34–36] also shown in Figure 5.6 and listed in Table 5.4. Figure 5.6a compares the present E results for the Ti-Mo alloy system with experimental data from Zhang et al. [34], Collings et al. [35] and Sung et al. [36]. It can be seen that the E increases in value from pure Ti to pure Mo. The results from Sung et al. [36] differ by about 60 GPa from the present work. However, during the XRD and TEM investigations by Sung et al. [36], one of the metastable phases, α'' and ω , was observed in the samples in addition to the bcc phase. The formation of the α'' and ω phases causes variations in the elastic properties from those of the single bcc phase. Zhang et al. [34] and Collings et al. [35] did not observe the formation of either metastable phase. The Young's moduli determined by Zhang et al. [34] and Collings et al. [35] agree with the present Voigt-Reuss bounds and have an error of 0.39 (Eq. 2.24) from the Hill average Young's modulus.

The present E of the Ti-Nb system are compared with data from Ozaki et al. [7] and Collings et al. [35] in Figure 5.6b, showing an increase in E values with an increase in the Nb concentration. The analyses of the samples from the work by Ozaki et al. [7] and Collings et al. [35] depict that all alloys contained the single bcc phase. The E from the present first-principles calculations have an error of

0.09 (Eq. 2.24) compared to the E determined by Ozaki et al. [7] and Collings et al. [35].

Figure 5.6d shows the calculated E for the Ti-Ta system in comparison with the experimental values determined by Fedotov et al. [5] and Zhou et al. [3,4]. The E values, in the Ti-Ta system, increase from pure Ti to pure Ta, and the calculated Young's moduli have an error of 0.19 (Eq. 2.24) compared to the experimental Young's moduli [3–5].

The error between the experimentally determined Young's moduli and the calculated Young's moduli is expected due to the temperature difference (calculations at 0 K and experiments at 298 K). The experimentally determined Young's moduli agree well within the Voigt and Reuss bounds, and the present calculations provide good prediction of the elastic properties of the Ti-Mo, Ti-Nb and Ti-Ta alloys as a function of composition.

The calculated Young's moduli for the Ti-Sn (Figure 5.6c) and Ti-Zr (Figure 5.6e) systems cannot be compared to experimental data because the bcc phase is not stable in these systems at low temperatures. For the Ti-Sn alloy system the E values increase from 0 to 35 at. % Sn and then decrease from 35 to 100 at. % Sn. The E , of the Ti-Zr system, increases in value from 0 to 40 at. % Zr, and then decreases from 40 to 100 at. % Zr. Figure 5.7 plots the Young's modulus as a function of composition from pure Ti in the bcc structure to the alloying element ($X = Mo, Nb, Sn, Ta, Zr$) and compares the effects of each alloying element on the Young's modulus. This mapping can be used to find alloy compositions that have the target E values (10-40 GPa). From Figure 5.7 there are multiple different compositions that have the target E .

As discussed in chapter 2, the instability of the bcc phase can be determined by Born's criteria (Eq. 2.21-2.23). Figure 5.8 shows the $\bar{C}_{11} - \bar{C}_{12}$ values from first-principles calculations and the present modeling, indicating the stability and instability regions of the bcc phase in different Ti-alloys. When the $\bar{C}_{11} - \bar{C}_{12}$ is positive the bcc phase is mechanically stable and when the $\bar{C}_{11} - \bar{C}_{12}$ is negative the bcc phase is mechanically unstable. The bcc phase is mechanically unstable at Mo, Nb, Sn, Ta, and Zr concentrations of less than 5.5, 11.5, 51.5, 9.5 and 4.0 at. %, respectively. Alloying with only 4.0 at. % Zr stabilizes the bcc phase, which is the lowest alloying concentration of any of the alloying elements even though it is known as a weak β -stabilizer. 5.5, 9.5 and 11.5 at. % of Mo, Ta and Nb,

respectively, are needed to alloy with Ti in order to stabilize the bcc phase. Mo, Nb, and Ta are similar elements that are all stable in the bcc phase and known to be β -stabilizers. 51.5 at. % of Sn is needed to stabilize the bcc phase when alloyed with Ti. Sn is not stable in the bcc phase and is not a β -stabilizer. Based on the E mapping in Figure 5.7, the compositions that fall into the target E range for the biomedical application (10-40 GPa) are targeted. However, the bcc phase of the targeted alloy compositions needs to be stable, which is determined by Figure 5.8. Using these results, the composition range for each Ti-X alloy that has the target E and the bcc phase stable are listed in Table 5.5. The Ti-Mo, Ti-Nb, Ti-Ta and Ti-Zr alloys show small compositions ranges where both the criteria are met while Ti-Sn has no composition range that stabilizes the bcc phase and has the target E . From these results, there are compositions that can be targeted and alloying with more than one element will show other compositions that have the properties desired.

Figure 5.9 and Figure 5.10 show the bulk (B) and shear (G) moduli of the Ti-X (X = Mo, Nb, Sn, Ta, Zr) systems, with the present results (circles), the Hill average (solid black line), and Voigt (purple dashed line) and Reuss (yellow dashed line) bounds plotted. Similar trends in the B and G data are seen for the Ti-Mo, Ti-Nb and Ti-Ta systems. The B and G increase in value with increasing Mo, Nb and Ta concentration, as shown in Figure 5.9 and Figure 5.10, respectively. The B and G values increase and then decrease from pure Ti to pure Sn in the Ti-Sn system (Figure 9c and Figure 10c). In the Ti-Zr system, the B decreases in value from pure Ti to pure Zr (Figure 5.9e) and the G first increases in value and then decreases from pure Ti to pure Zr (Figure 5.10e). The predicted B and G values are listed in Table 5.4.

5.3.3 Extrapolation to ternary and higher ordered systems

The interaction parameters in Table 5.2 can be used to predict the elastic stiffness coefficients of higher order Ti-alloys by summing the interaction parameters of each binary alloy contained in the multi-component alloy from Eq. 2.32. The predicted elastic stiffness coefficients of the multi-component alloys can be used to calculate the Young's modulus as a function of composition. The accuracy of prediction of the elastic properties of higher order Ti alloys are evaluated by comparing the

predicted results with previous experimental results [37–40] as shown in Figure 5.11 and Table 5.6. The black diagonal line represents a perfect correlation between the predicted and experimental Young’s moduli. The grey region indicates the error (3 GPa) in the first-principles calculations, which is the average variance in \overline{C}_{11} , \overline{C}_{12} and \overline{C}_{44} from Eq. 2.18-2.20.

It can be seen that the difference between experimental Young’s moduli at the same composition from Niinomi et al. [40], Geetha et al. [38], Tane et al. [37] and Mohammad et al. [39] varies from 2 GPa to 46 GPa with different heat treatments and measuring techniques. The scattering in the Young’s moduli among experimental measurements is denoted by the vertical error bars in Figure 5.11. The horizontal error bars show the Young’s moduli ranges from the Reuss and Voigt bounds with the average from the Hill approach marked by the circle. The experimental Young’s moduli deviate from the present predictions by 0.69 to 14 GPa. This difference can be contributed to the temperature difference between the first-principles data and the experimental results and uncertainties in calculations and experiments. Considering the fact that the experimental results from the literature at the same composition vary drastically, the present first-principles calculations give a good representation of the elastic properties of higher order Ti-alloys. It is hypothesized that introducing the binary interaction parameters of non-Ti containing alloys in the system and the ternary interaction parameters can further improve the database predictions.

5.4 Conclusion

The elastic properties of five bcc Ti-X (X = Mo, Nb, Sn, Ta, Zr) systems, including the elastic stiffness coefficients, bulk modulus, shear modulus, and Young’s modulus, were systematically studied using first-principles calculations at different compositions. The CALPAHD methodology was used to evaluate interaction parameters for the Ti-X elastic stiffness coefficients as a function of composition and the polycrystalline aggregate properties were predicted using the Voigt-Reuss-Hill approach. The present calculations showed that 5.5, 11.5, 51.5, 9.5, and 4.0 at. % of Mo, Nb, Sn, Ta and Zr, respectively, are required to stabilize the bcc structure according to the Born criteria. The trends observed were summarized for each Ti-X (X= Mo, Nb, Sn, Ta, Zr) binary system. Alloying with Mo, Nb, and Ta resulted in

similar trends, which is probably because Mo, Nb, and Ta are strong bcc stabilizers and stable in the bcc structure at room temperature. The interaction parameters determined in the current work were used to predict the elastic properties of higher order alloys. The accuracy of the databases predictions of the Young's modulus was evaluated by comparing the calculated and experimental Young's moduli. Overall, the database predicted the E values on average within 7 GPa and provided good predictions of the elastic properties of Ti-alloys in the bcc phase as a function of composition.

Table 5.1: Calculated pure element elastic stiffness coefficients and the bulk modulus B (in GPa) by X-C functional of PBE are compared with the previous first-principles calculations (FP) by X-C functional PW91 and experiments (Expt). Sv, pv and d referring to the s, p, and d states being treated as valance, respectively.

Pure Elements		\bar{C}_{11}	\bar{C}_{11}	\bar{C}_{11}	B
Ti_sv	This work 0 K	93	115	41	108
	Calc 0 K [121]	96	116	40	107
Mo_pv	This work 0 K	475	164	108	268
	Expt 73 K [68]	473	156	111	
	Expt 300 K [99]	473	160	109	261
Nb_sv	This work 0 K	245	144	27	178
	Expt 4 K [68]	253	133	31	
	Expt 300 K [102]	247	135	29	172
Sn_d	This work 0 K	50	52	29	51
	Calc 0 K [121]	30	60	18	48
Ta_pv	This work 0 K	278	164	81	202
	Expt 0 K [68]	266	158	87	
	Expt 300 K [102]	267	161	83	196
Zr_sv	This work 0 K	86	91	32	89
	Calc 0 K [121]	82	94	30	90

Table 5.2: Evaluated interaction parameters L_0 and L_1 using the R-K polynomial Eq. 2.32 for the elastic stiffness coefficients for the Ti-X binary systems.

Alloy	Interaction Parameter	Ti-Mo	Ti-Nb	Ti-Sn	Ti-Ta	Ti-Zr
\bar{C}_{11}	L_0	-22.16	40.46	119.46	83.65	246.97
	L_1	0	0	0	-67.76	-135.95
\bar{C}_{12}	L_0	-36.40	-32.39	15.90	38.05	-110.53
	L_1	0	0	-146.80	0	78.00
\bar{C}_{44}	L_0	-142.9	-41.54	59.79	-51.96	70.06
	L_1	0	-41.95	-94.38	0	0

Table 5.3: First-principles calculations of the elastic stiffness coefficients \overline{C}_{11} , \overline{C}_{12} , and \overline{C}_{44} for different atomic percent compositions of the bcc Ti-X binary systems at 0 K.

Reference	Ti _{1-b} X _b	\overline{C}_{11}	\overline{C}_{12}	\overline{C}_{44}
This work	Ti	93	115	41
This work	Ti _{0.94} Mo _{0.06}	124	111	38
This work	Ti _{0.87} Mo _{0.13}	146	113	29
This work	Ti _{0.75} Mo _{0.25}	178 ±3	123 ±15	32 ±11
This work	Ti _{0.50} Mo _{0.50}	268 ±9	136 ±19	42 ±9
This work	Ti _{0.25} Mo _{0.75}	385 ±9	146 ±6	66 ±6
This work	Ti _{0.06} Mo _{0.94}	451	158	96
This work	Ti _{0.02} Mo _{0.98}	464	163	100
This work	Mo	475	164	108
This work	Ti _{0.98} Nb _{0.02}	93	115	35
This work	Ti _{0.87} Nb _{0.13}	116	116	37
This work	Ti _{0.75} Nb _{0.25}	140 ±11	116 ±13	34 ±10
This work	Ti _{0.50} Nb _{0.50}	181 ±9	121 ±2	31 ±10
This work	Ti _{0.25} Nb _{0.75}	208 ±3	130 ±4	15 ±10
This work	Ti _{0.06} Nb _{0.94}	242	134	18
This work	Ti _{0.02} Nb _{0.98}	242	134	18
This work	Nb	245	144	27
This work	Ti _{0.94} Sn _{0.06}	100	122	46
This work	Ti _{0.75} Sn _{0.25}	105 ±5	114 ±2	60 ±4
This work	Ti _{0.50} Sn _{0.50}	88 ±9	93 ±9	46 ±4
This work	Ti _{0.25} Sn _{0.75}	92 ±9	55 ±7	35 ±8
This work	Sn	50	52	29
This work	Ti _{0.98} Ta _{0.02}	100	115	39
This work	Ti _{0.94} Ta _{0.06}	116	113	30
This work	Ti _{0.87} Ta _{0.13}	120	121	39
This work	Ti _{0.75} Ta _{0.25}	167 ±1	140 ±3	45
This work	Ti _{0.50} Ta _{0.50}	208 ±1	159	51 ±3
This work	Ti _{0.25} Ta _{0.75}	239 ±7	143 ±5	62 ±3
This work	Ti _{0.06} Ta _{0.94}	257	158	72

Table 5.3: First-principles calculations of the elastic stiffness coefficients \overline{C}_{11} , \overline{C}_{12} , and \overline{C}_{44} for different atomic percent compositions of the bcc Ti-X binary systems at 0 K.

Reference	Ti _{1-b} X _b	\overline{C}_{11}	\overline{C}_{12}	\overline{C}_{44}
This work	Ti _{0.02} Ta _{0.98}	264	163	72
This work	Ta	278	164	81
This work	Ti _{0.98} Zr _{0.02}	112	106	43
This work	Ti _{0.75} Zr _{0.25}	148 ±14	82 ±7	54 ±7
This work	Ti _{0.50} Zr _{0.50}	152 ±17	76 ±12	48 ±12
This work	Ti _{0.25} Zr _{0.75}	126 ±12	82 ±3	45 ±3
This work	Ti _{0.06} Zr _{0.94}	89	90	34
This work	Zr	86	91	32

Table 5.4: First-principles calculations of the bulk modulus B , shear modulus G , and Young's modulus E in GPa for different atomic percent compositions of the bcc Ti-X binary systems at 0 K. As well as experimental data for the Young's modulus obtained at 300 K by the reference stated.

Reference	Ti _{1-b} X _b	B	G	E
This work	Ti	108	-12.91	-40.34
This work	Ti _{0.94} Mo _{0.06}	115	20	54
This work	Ti _{0.87} Mo _{0.13}	124	23	65
This work	Ti _{0.75} Mo _{0.25}	141 ±15	30 ±15	84 ±15
This work	Ti _{0.50} Mo _{0.50}	180 ±19	51 ±19	138 ±19
This work	Ti _{0.25} Mo _{0.75}	226 ±9	84 ±9	224 ±9
This work	Ti _{0.06} Mo _{0.94}	256	114	397
This work	Ti _{0.02} Mo _{0.98}	263	118	308
This work	Mo	268	125	325
Expt 300 K [34]	Ti _{0.92} Mo _{0.08}			83
Expt 300 K [34]	Ti _{0.88} Mo _{0.12}			90
Expt 300 K [35]	Ti _{0.92} Mo _{0.08}			84
Expt 300 K [35]	Ti _{0.89} Mo _{0.11}			89
Expt 300 K [35]	Ti _{0.82} Mo _{0.18}			101
This work	Ti _{0.98} Nb _{0.02}	108	-18	-56
This work	Ti _{0.87} Nb _{0.13}	116	11	31
This work	Ti _{0.75} Nb _{0.25}	124 ±13	22 ±13	63 ±13
This work	Ti _{0.50} Nb _{0.50}	141 ±9	31 ±10	86 ±10
This work	Ti _{0.25} Nb _{0.75}	156 ±4	22 ±10	64 ±10
This work	Ti _{0.06} Nb _{0.94}	170	28	81
This work	Ti _{0.02} Nb _{0.98}	170	28	81
This work	Nb	178	35	98
Expt 300 K [7]	Ti _{0.71} Nb _{0.29}			67
Expt 300 K [7]	Ti _{0.66} Nb _{0.34}			74
Expt 300 K [7]	Ti _{0.56} Nb _{0.44}			84
Expt 300 K [35]	Ti _{0.74} Nb _{0.26}			64
Expt 300 K [35]	Ti _{0.70} Nb _{0.30}			65
Expt 300 K [35]	Ti _{0.66} Nb _{0.34}			73
Expt 300 K [35]	Ti _{0.56} Nb _{0.44}			83

Table 5.4: First-principles calculations of the bulk modulus B , shear modulus G , and Young's modulus E in GPa for different atomic percent compositions of the bcc Ti-X binary systems at 0 K. As well as experimental data for the Young's modulus obtained at 300 K by the reference stated.

Reference	Ti _{1-b} X _b	B	G	E
This work	Ti _{0.94} Sn _{0.06}	115	-10	-30
This work	Ti _{0.75} Sn _{0.25}	111 ±5	11 ±5	31 ±5
This work	Ti _{0.50} Sn _{0.50}	91 ±9	10 ±9	29 ±9
This work	Ti _{0.25} Sn _{0.75}	67 ±9	27 ±9	72 ±9
This work	Sn	51	7	21
This work	Ti _{0.98} Ta _{0.02}	110	-3	-9
This work	Ti _{0.94} Ta _{0.06}	114	11	32
This work	Ti _{0.87} Ta _{0.13}	121	11	32
This work	Ti _{0.75} Ta _{0.25}	149 ±3	28 ±3	78 ±3
This work	Ti _{0.50} Ta _{0.50}	175 ±1	38 ±3	106 ±3
This work	Ti _{0.25} Ta _{0.75}	175 ±7	56 ±7	152 ±7
This work	Ti _{0.06} Ta _{0.94}	191	62	168
This work	Ti _{0.02} Ta _{0.98}	197	62	169
This work	Ta	202	70	189
Expt 300 K [5]	Ti _{0.62} Ta _{0.38}			62
Expt 300 K [5]	Ti _{0.58} Ta _{0.42}			79
Expt 300 K [5]	Ti _{0.52} Ta _{0.48}			95
Expt 300 K [3]	Ti _{0.62} Ta _{0.38}			67
Expt 300 K [3]	Ti _{0.49} Ta _{0.51}			105
This work	Ti _{0.98} Zr _{0.02}	108	17	48
This work	Ti _{0.75} Zr _{0.25}	104 ±14	44 ±14	116 ±14
This work	Ti _{0.50} Zr _{0.50}	101 ±17	44 ±17	115 ±17
This work	Ti _{0.25} Zr _{0.75}	97 ±12	34 ±12	91 ±12
This work	Ti _{0.06} Zr _{0.94}	90	9	27
This work	Zr	89	6	16

Table 5.5: Compositions of the binary alloys that fall in the target E range compared to the bcc phase stability can predict the alloy compositions where the E is close to bone and the bcc phase is stable and those compositions can be targeted.

Alloy	at Target E	bcc stabilized	Target Compositions
Ti-Mo	Pure Ti to 0.10 mol Mo	> 0.055 mol Mo	0.055 to 0.10 mol Mo
Ti-Nb	Pure Ti to 0.20 mol Nb	> 0.115 mol Nb	0.115 to 0.20 mol Nb
Ti-Sn	Pure Ti to 0.40 mol Sn	> 0.515 mol Sn	N/A
Ti-Ta	Pure Ti to 0.15 mol Ta	> 0.095 mol Ta	0.095 to 0.15 mol Ta
Ti-Zr	Pure Ti to 0.05 mol Zr	> 0.040 mol Zr	0.040 to 0.05 mol Zr

Table 5.6: Predicted Young's moduli (in GPa) of higher order alloys in the bcc phase compared to experimental values found with both the weight percent and atomic percent listed.

Alloy Name (wt. %)	at. %	Calc E	Expt E
Ti-35Nb-7Zr-5Ta [38]	Ti-24Nb-5Zr-2Ta	81	80
Ti-29Nb-13Ta-4.6Zr [38]	Ti-20Nb-5Ta-3Zr	76	75
Ti-29Nb-13Ta-6Sn [38]	Ti-21Nb-5Ta-3Sn	68	74
Ti-29Nb-13Ta-4.6Sn [38]	Ti-20Nb-5Ta-3Sn	67	66
Ti-29Nb-13Ta-4.5Zr [38]	Ti-20Nb-5Ta-3Zr	76	65
Ti-29Nb-13Ta-4.6Zr [37]	Ti-21Nb-5Ta-3Zr	76	64
Ti-30Nb-10Ta-5Zr [37]	Ti-23Nb-4Ta-3Zr	77	64
Ti-35Nb-10Ta-5Zr [37]	Ti-25Nb-4Ta-4Zr	80	65
Ti-24Nb-4Zr-7.9Sn [39]	Ti-15Nb-3Zr-4Sn	65	54
Ti-35Nb-2Ta-3Zr [39]	Ti-23Nb-1Ta-2Zr	69	61
Ti-29Nb-11Ta-5Zr [39]	Ti-20Nb-6Ta-2Zr	74	60
Ti-10Zr-5Ta-5Nb [39]	Ti-6Zr-1Ta-3Nb	64	52
Ti-29Nb-13Ta-2Sn [39]	Ti-20Nb-5Ta-1Sn	66	62

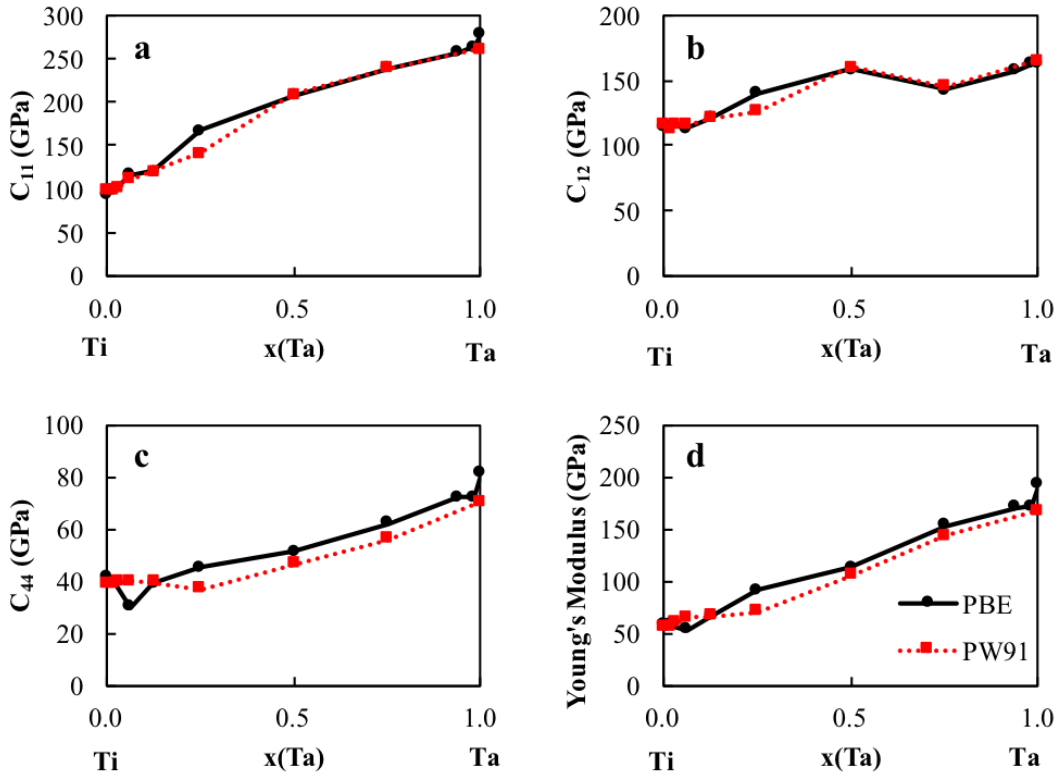


Figure 5.1: Elastic stiffness coefficients of the bcc Ti-Ta binary system calculated with the PW91 and PBE exchange correction functions, respectively.

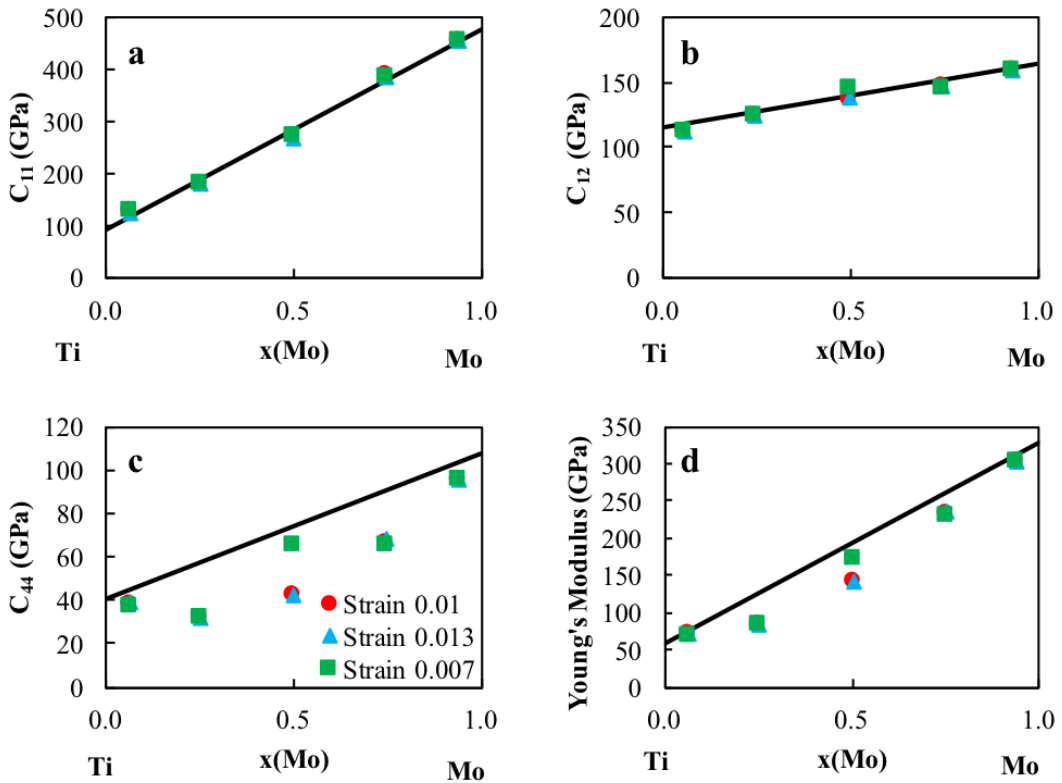


Figure 5.2: Elastic stiffness coefficients for the bcc Ti-Mo binary system calculated with strains, ± 0.01 , ± 0.013 and ± 0.07 , respectively, showing comparable results.

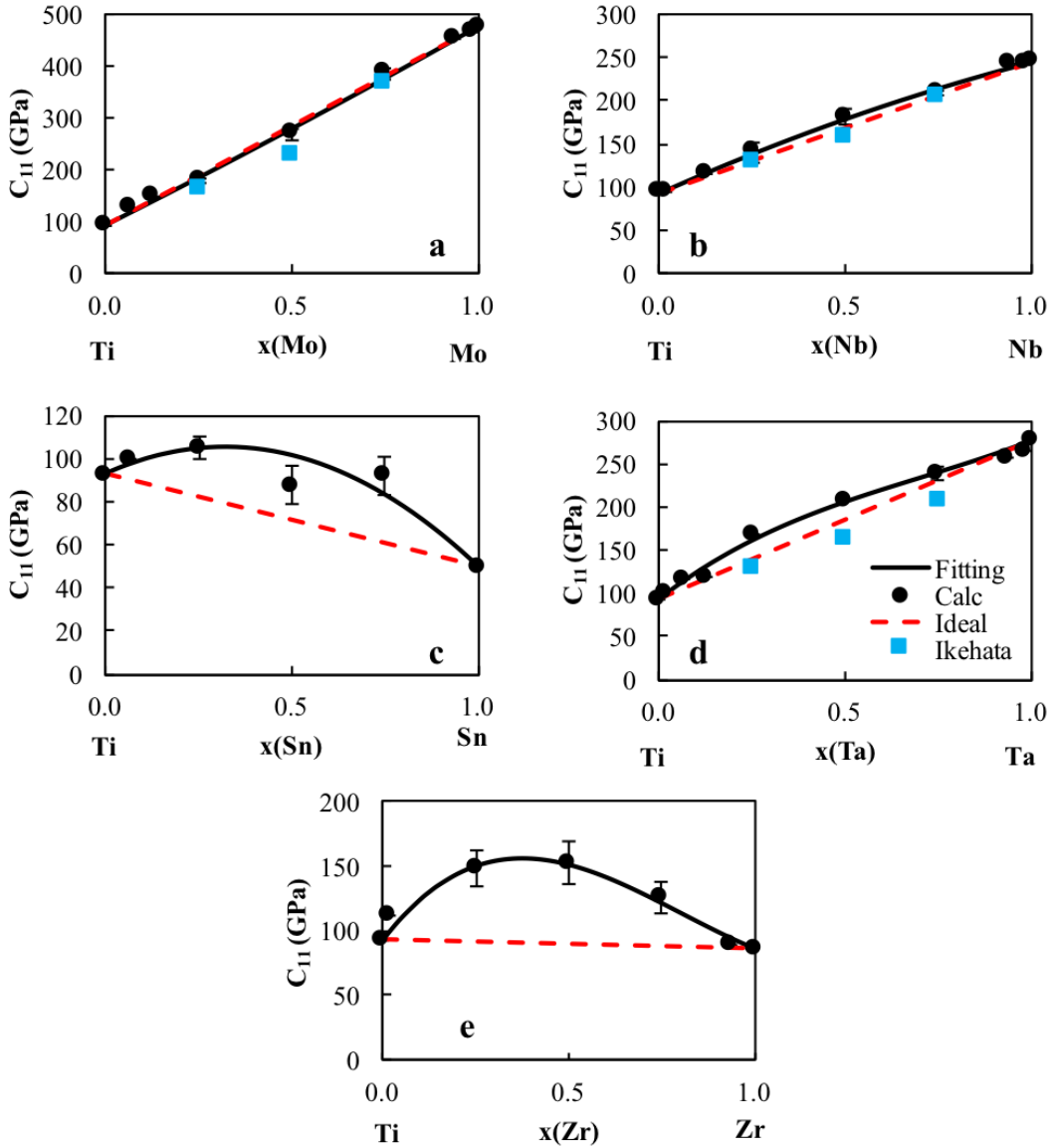


Figure 5.3: Calculated \bar{C}_{11} values (circles) plotted with their errors as well as the linear combination of the pure element (red dashed line) and the present modeling (black dashed line) for five Ti-X binary systems ($X = \text{Mo}, \text{Nb}, \text{Ta}, \text{Sn}, \text{Zr}$). Ti-Mo, Ti-Nb, and Ti-Ta alloys are compared with previous calculations from Ikehata et al. [2].

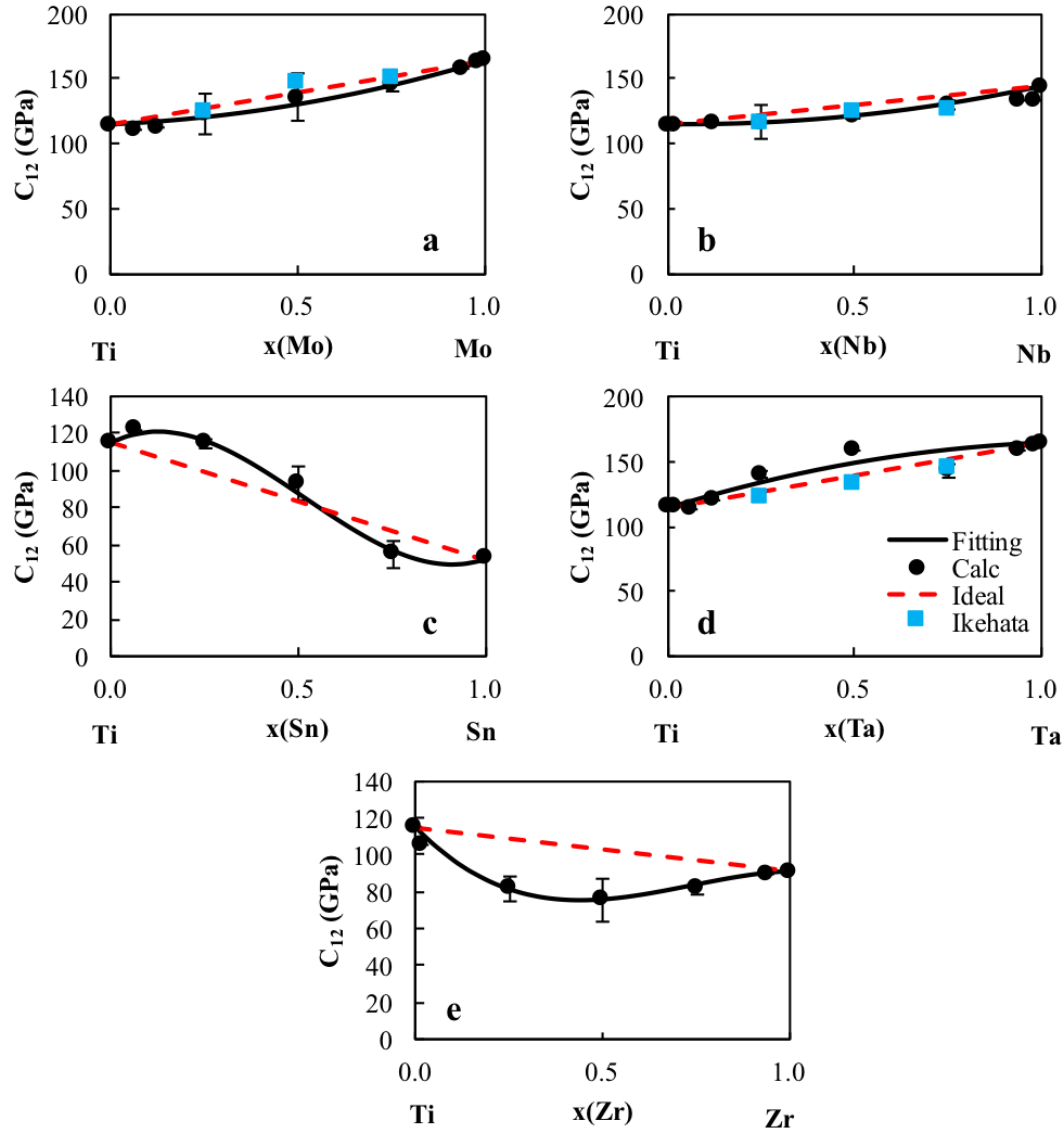


Figure 5.4: Calculated \bar{C}_{12} values (circles) plotted with their errors as well as the linear combination of the pure element (red dashed line) and the present modeling (black dashed line) for five Ti-X binary systems ($X = \text{Mo}, \text{Nb}, \text{Ta}, \text{Sn}, \text{Zr}$). Ti-Mo, Ti-Nb, and Ti-Ta alloys are compared with previous calculations from Ikehata et al. [2].

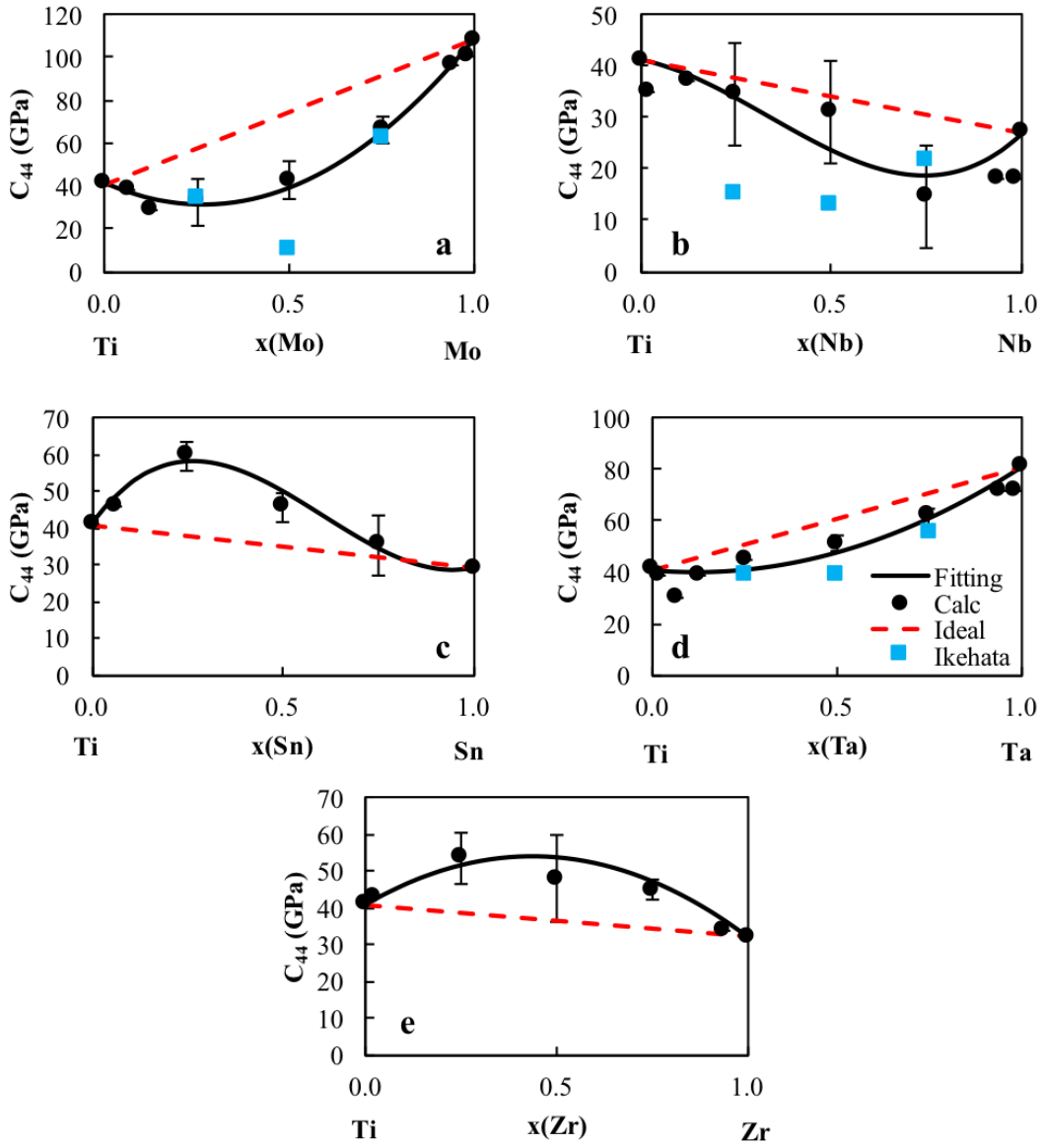


Figure 5.5: Calculated \bar{C}_{44} values (circles) plotted with their errors as well as the linear combination of the pure element (red dashed line) and the present modeling (black dashed line) for five Ti-X binary systems ($X = \text{Mo}, \text{Nb}, \text{Ta}, \text{Sn}, \text{Zr}$). Ti-Mo, Ti-Nb, and Ti-Ta alloys are compared with previous calculations from Ikehata et al. [2].

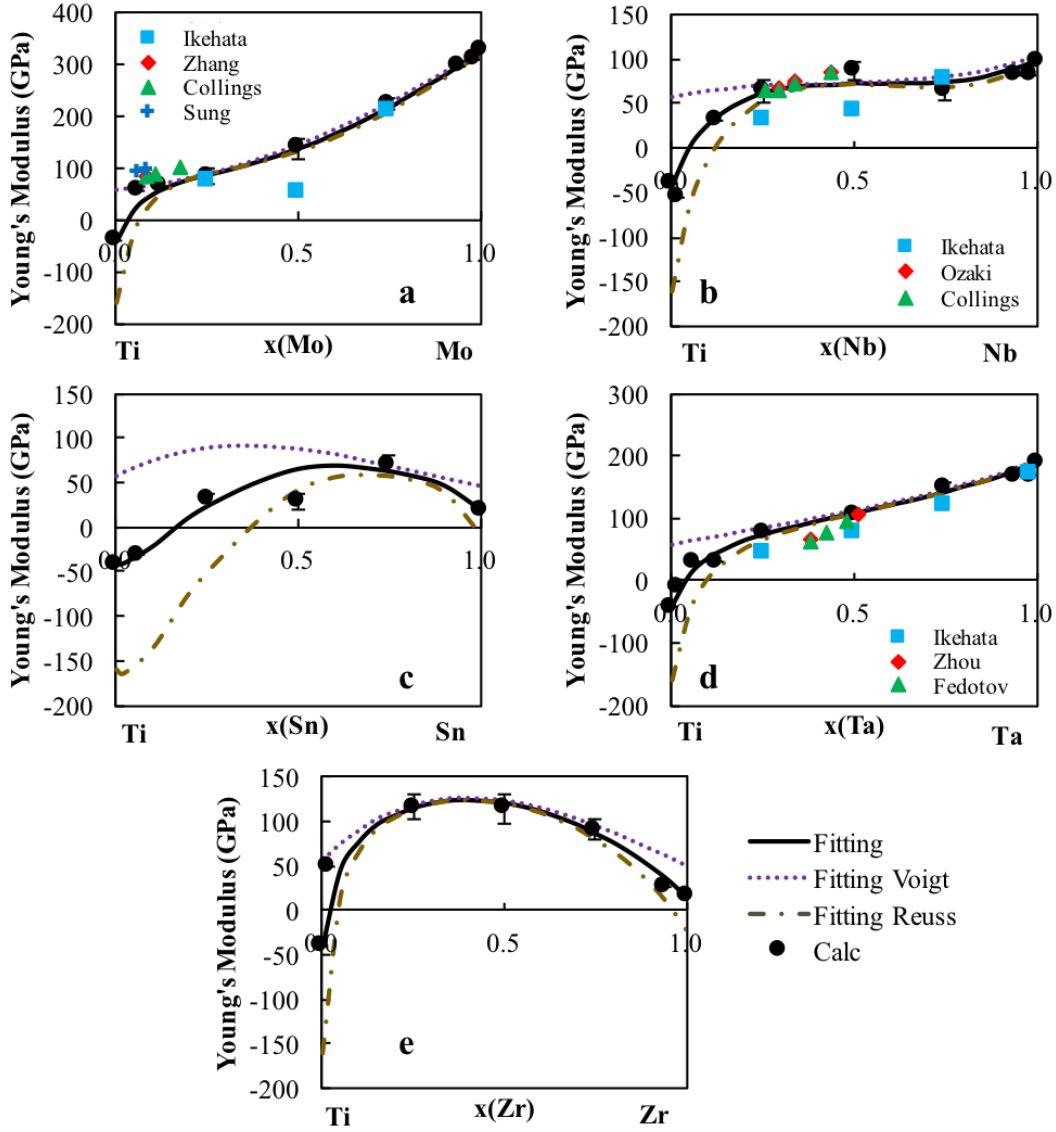


Figure 5.6: Young's modulus E of the Ti-X binary systems. The present calculations are plotted as the filled circles with the error bars. The dotted purple line is the Voigt upper Young's modulus bound, the gold dot dashed line is the lower Reuss Young's modulus bound and the black line is the Hill Young's modulus average. The experimental values [1–5, 7, 8, 34–36] are also included for comparison.

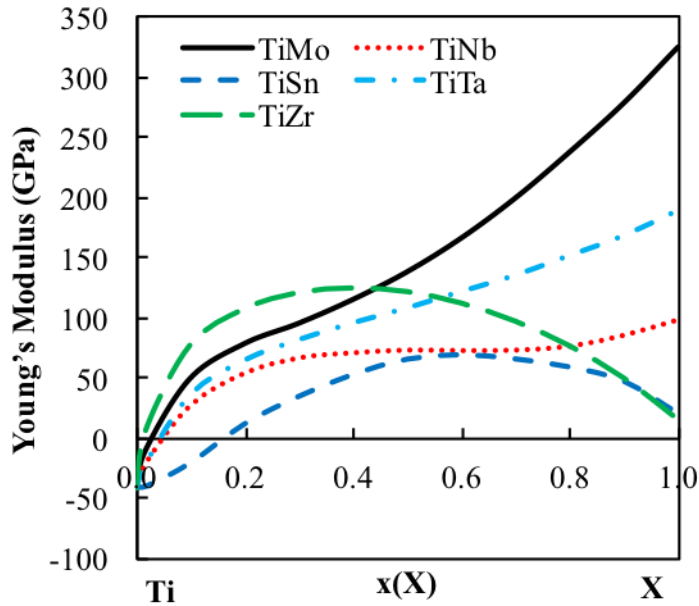


Figure 5.7: Young's moduli mapped as a function of composition from bcc Ti to bcc X ($X = \text{Mo, Nb, Sn, Ta, Zr}$).

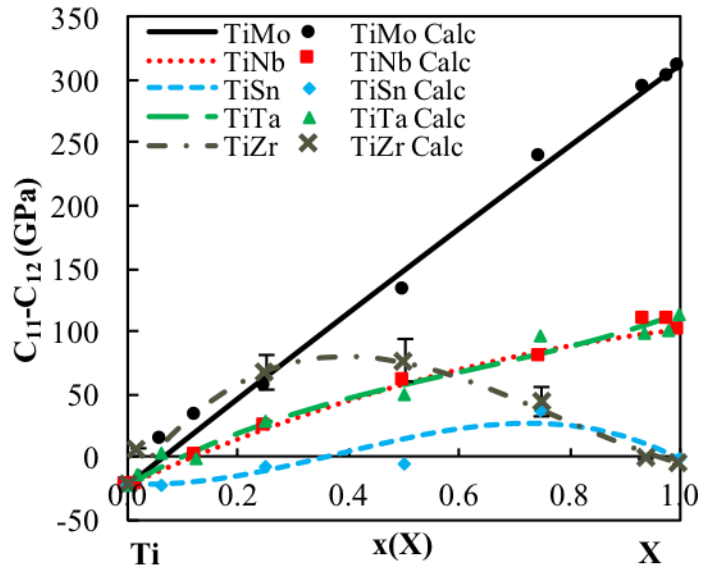


Figure 5.8: Calculated \bar{C}_{11} - \bar{C}_{12} values (circles) plotted with the present modeling (solid lines) for five Ti-X binary systems ($X = \text{Mo, Nb, Ta, Sn, Zr}$). The \bar{C}_{11} - \bar{C}_{12} shows the stability of the bcc phase. When the \bar{C}_{11} - \bar{C}_{12} value is negative the bcc phase is not stable in the corresponding composition ranges.

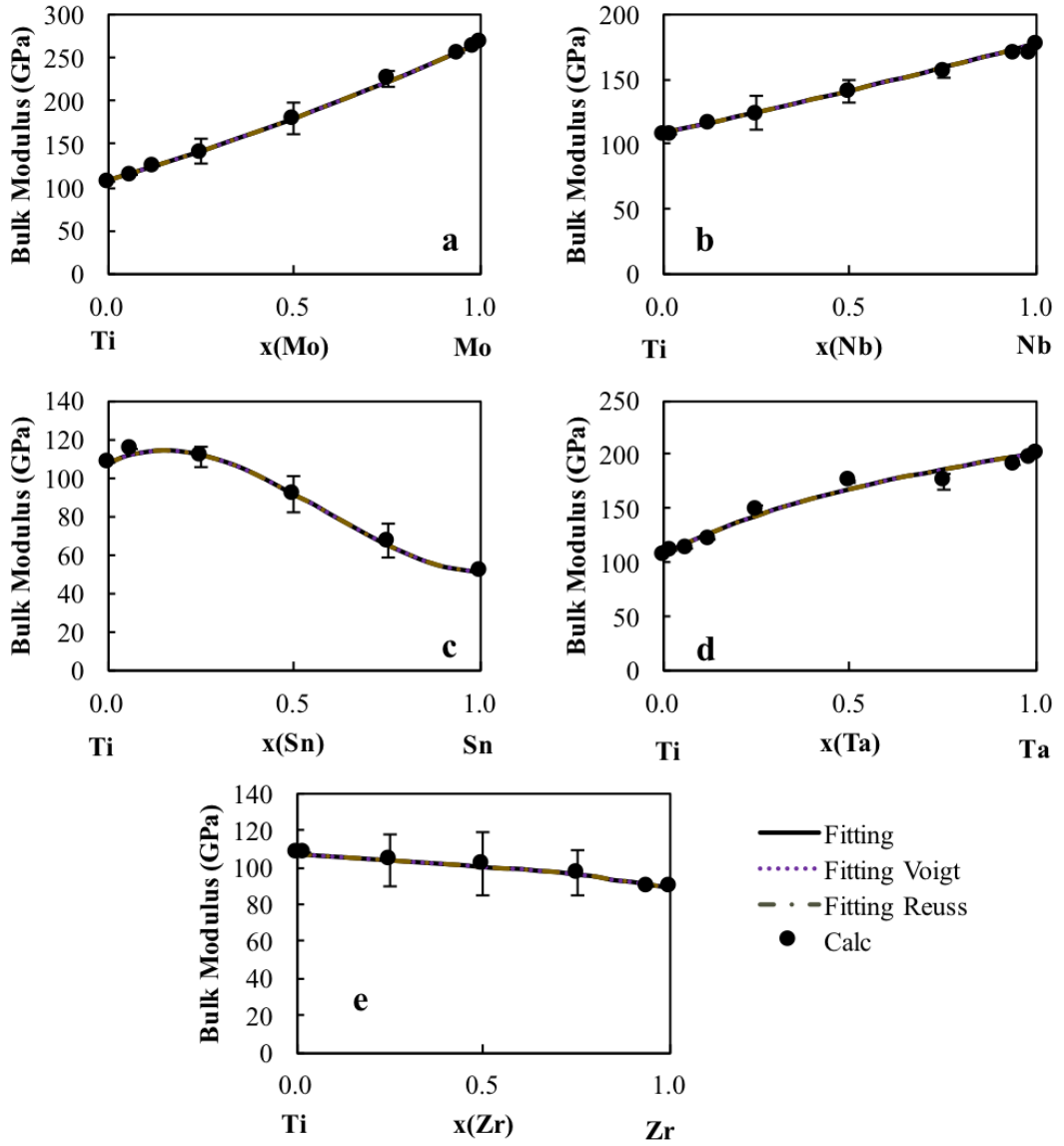


Figure 5.9: Bulk moduli B of the $Ti-X$ binary systems. The present calculations are plotted as the filled circles with the error bars. The dotted purple line is the Voigt upper bulk modulus bound, the gold dot dashed line is the lower Reuss bulk modulus bound and the black line is the bulk modulus from the Hill approach.

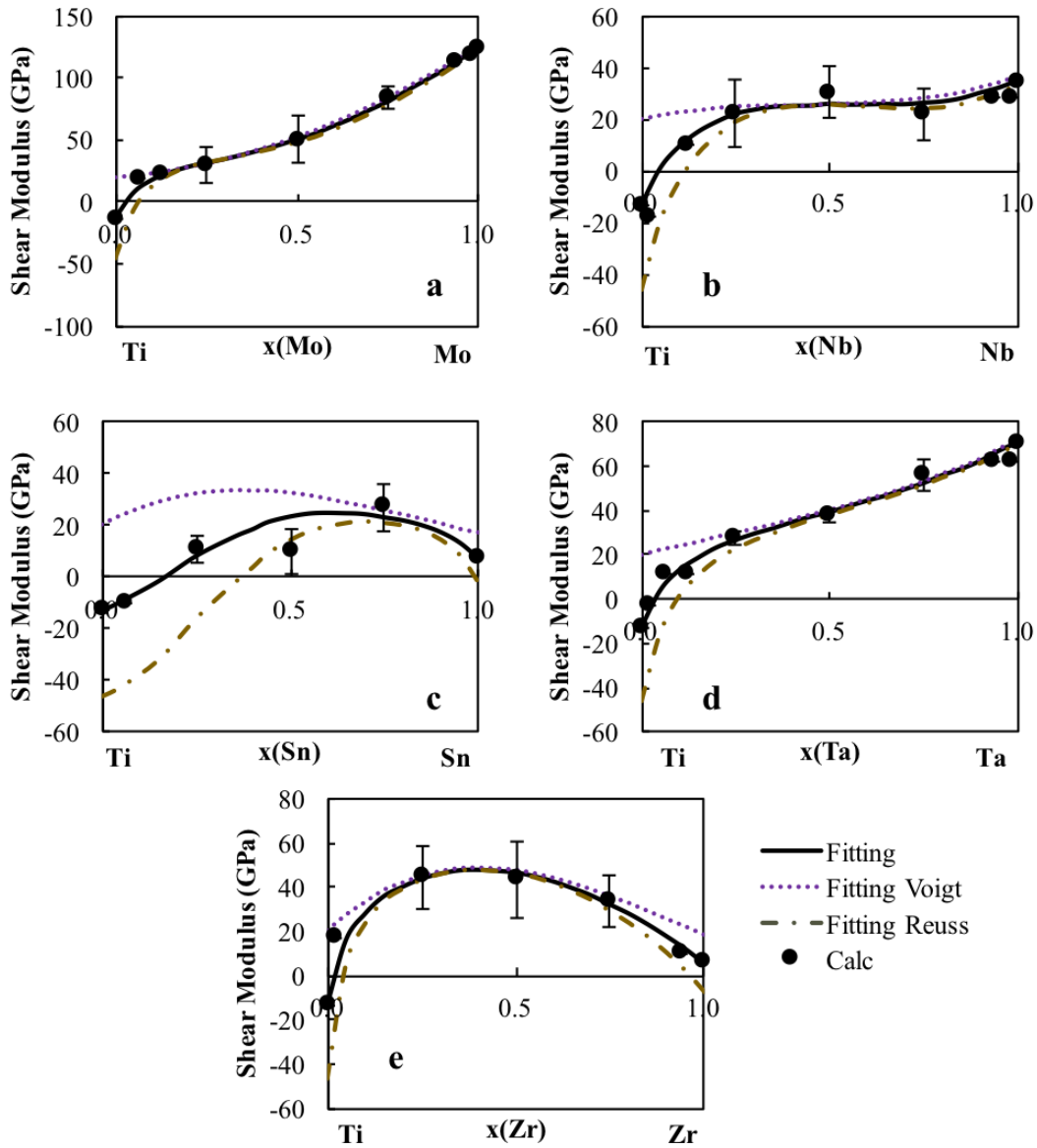


Figure 5.10: Shear moduli G of the Ti-X binary systems. The present calculations are plotted as the filled circles with the error bars. The dotted purple line is the Voigt upper shear modulus bound, the gold dot dashed line is the lower Reuss shear modulus bound and the black line is the shear modulus from the Hill approach.

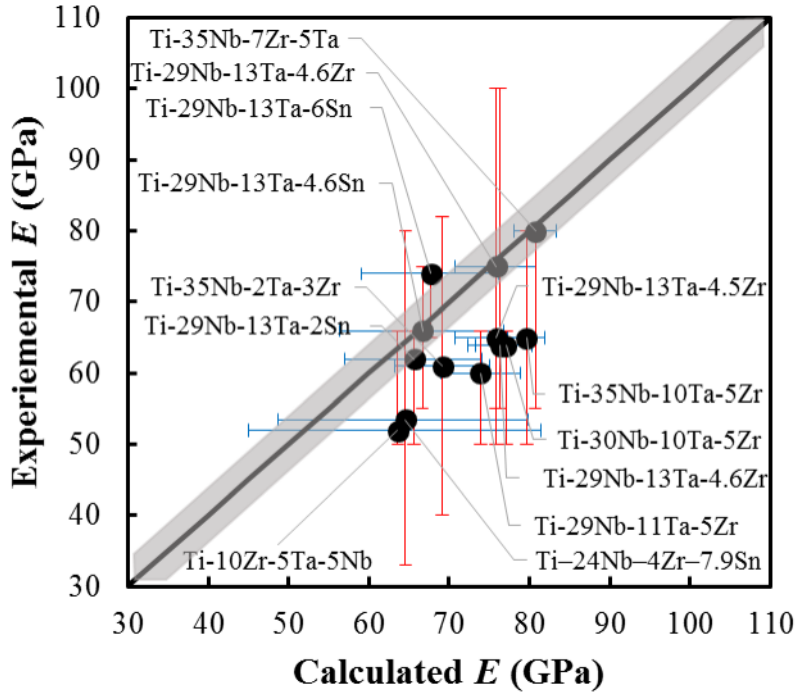


Figure 5.11: Young's moduli values of multicomponent bcc Ti alloys measured experimentally plotted against the predicted Young's moduli from the pure elements and binary interaction parameters with the black diagonal line showing the exact correlation between the experimental and calculated values. Error in the experiments and the bounds from Reuss and Voigt approximations are plotted as the vertical and horizontal error bars, respectively. The variance in the first-principles calculations from Eq.2.18-Eq.2.20 was averaged and plotted as the grey region. More information on the alloys is in Table 5.6 [37–39]

Chapter 6 |

Effects of alloying elements on the elastic properties of bcc ternary and higher ordered Ti-alloys

6.1 Introduction

In order to develop a better understanding about the alloying effect on the elastic properties of Ti alloys, the present work is developing an elastic database for the Ti-Mo-Nb-Sn-Ta-Zr system. With the focus being on bcc Ti-alloys, the effects of alloying elements on the pure elements and Ti-X binary alloys in the bcc phase were calculated in chapter 5. After extrapolating to higher order systems, it was hypothesized that studying the effects of alloying on the elastic properties of ternary alloys would improve the database. The present work calculates the elastic properties of the Ti-X-Y ($X \neq Y = \text{Mo, Nb, Ta, Sn, and Zr}$) ternary alloys in the bcc phase. The single crystal elastic stiffness coefficients (c_{ij} 's) and polycrystalline aggregate properties are predicted across the composition range using first-principles based on Density Functional Theory (DFT) at 0 K outlined in the methodology chapter. Based on the DFT results, the CALPHAD approach outlined in the methodology is used to evaluate ternary interaction parameters. The interaction parameters are then incorporated into the database and the database accuracy is again tested similarly to the testing in chapter 5. The completed database is used to map the elastic modulus as a function of composition.

6.2 Modeling and Calculations

To study the elastic properties of the ternary bcc Ti alloys in the Ti-Mo-Nb-Sn-Ta-Zr system, DFT-based first-principles calculations were employed using VASP (Vienna Ab-initio Simulation Package) [61, 62]. Four kinds of calculations were performed for each ternary alloy Ti-X-Y, with the varying compositions of $X_{0.50}Y_{0.50}$ (16-atom supercell), $Ti_{0.33}X_{0.33}Y_{0.33}$ (36 atoms), $Ti_{0.50}X_{0.25}Y_{0.25}$ (32 atoms), $Ti_{0.74}X_{0.13}Y_{0.13}$ (64 atoms). The relaxation and use of SQS are discussed extensively in chapter 2. The SQS used in this chapter were generated by Jiang et al. [73, 74]. The projector augmented wave (PAW) method was used to describe the ion-electron interactions. Based on our previous work done in chapter 5 (Figure 5.1), the X-C functional of the generalized gradient approximation depicted by Perdew, Burke, and Ernzerhof (PBE-GGA) [58] was employed. An energy cutoff roughly 1.3 times higher than the default values among all elements (i.e., 310 eV) was used for all calculations. The Brillouin zone sampling was done using the Γ -centered Monkhorst-Pack scheme [90]. The k-point grids used for the ternary SQS were 4x4x4 and the k-point grids used for the binary $X_{0.50}Y_{0.50}$ SQS structures were an automated k-point mesh generator in VASP with the length of the subdivision specified at 80. The elastic calculations were completed using a strain magnitude of ± 0.01 based on the study done in chapter 5 and the results seen in Figure 5.2.

The first-principles results were then used to model the ternary interaction parameters of the elastic stiffness coefficients. The modeling was completed by plotting the binary interpolation from the working database build in chapter 5. The plotting was done at all compositions but shown here are plots started at a 50-50 mixture ($X_{0.50}Y_{0.50}$) of the alloying elements ($X \neq Y = Mo, Nb, Sn, Ta, and Zr$) and plotted to pure Ti to be able to more easily show the DFT-based first-principles versus the modeling. The elastic stiffness coefficients of the pure elements and the binary interaction parameters from Table 5.2 were used to plot the binary interpolation. The differences between the ternary first-principles calculations and the binary interpolation were then used to obtain a single fitting parameter using the Mathematica code in appendix C. With the focus being Ti-rich alloys and wanting to follow the same modeling technique used on the binary alloys (chapter 5), the first-principles results with 70 at.% Ti or higher were weighted heavier (x6, according to the authors' practices) than the other points for the fittings. The best

fit was found and the ternary interaction parameters were incorporated into the database. The database was then used to predict the moduli values of the ternary and higher order alloys.

6.3 Results and discussion

6.3.1 Elastic calculation results

The elastic stiffness coefficients \bar{C}_{11} , \bar{C}_{12} , and \bar{C}_{44} are plotted in Figure 6.1 to Figure 6.6 for the Ti-X-Y alloys ($X \neq Y = Mo, Nb, Sn, Ta, Zr$). The elastic stiffness constants were plotted as a function of compositions. However, in this work the plots start from a 50-50 mixture of the alloying elements $X_{0.50}Y_{0.50}$ to Ti because it is easiest to visualize the results. The calculations are plotted as circles, the red dashed line shows the data interpolated from just the binary interaction parameters. The difference between the calculations and binary interpolation was used to evaluate the ternary interaction parameters. The properties are then plotted using both the ternary and binary interaction parameters as a solid black line. The calculated elastic stiffness coefficients are listed in Table 6.1 together with experimental values [38–41] for comparison.

The composition dependences of elastic efficiencies from $X_{0.50}Y_{0.50}$ to Ti are observed as follows

1. \bar{C}_{11}

- (a) decreases (see Figure 6.1 and Figure 6.2), except the Ti-Sn-Zr and Ti-Ta-Zr systems;
- (b) \bar{C}_{11} in the Ti-Sn-Zr system (Figure 6.2d), first increase from $Sn_{0.50}Zr_{0.50}$ to 60 at. % Ti and then decrease from 60 to 100 at. % Ti;
- (c) \bar{C}_{11} in the Ti-Ta-Zr system (Figure 6.2e), first increase from $Ta_{0.50}Zr_{0.50}$ to 35 at. % Ti and then decrease from 35 to 100 at. % Ti

2. \bar{C}_{12}

- (a) decreases in the Ti-Mo-Nb, Ti-Mo-Ta and Ti-Nb-Ta systems (Figure 6.3 and Figure 6.4);

- (b) \overline{C}_{12} first decrease from $X_{0.50}Y_{0.50}$ to 15 at. % Ti then increase from 15 to 85 at. % Ti and then decrease from 85 to 100 at. % Ti in the Ti-Mo-Sn and Ti-Nb-Sn systems;
- (c) \overline{C}_{12} decrease from $X_{0.50}Y_{0.50}$ to 60 at. % Ti and then an increase from 60 to 100 at. % Ti in the Ti-Mo-Zr and Ti-Nb-Zr systems;
- (d) \overline{C}_{12} increase from $X_{0.50}Y_{0.50}$ to 70 at. % Ti and then decrease from 70 to 100 at. % Ti in the Ti-Sn-Ta system;
- (e) \overline{C}_{12} increase from 0 to 100 at. % Ti in the Ti-Sn-Zr system;
- (f) \overline{C}_{12} first decrease from 0 to 70 at. % Ti and then increase from 70 to 100 at. % Ti in the Ti-Ta-Zr system.

3. \overline{C}_{44}

- (a) decreases in the Ti-Mo-Sn and Ti-Ta-Zr systems (Figure 6.5 and Figure 6.6);
- (b) \overline{C}_{44} first decrease from 0 to 80 at. % Ti and then increase from 80 to 100 at. % Ti in the Ti-Mo-Zr and Ti-Mo-Ta systems;
- (c) \overline{C}_{44} first decrease from 0 to 65 at. % Ti and then increase from 65 to 100 at. % Ti in the Ti-Mo-Nb and Ti-Nb-Ta systems;
- (d) \overline{C}_{44} first increase from 0 to 80 at. % Ti and then decrease from 80 to 100 at. % Ti in the Ti-Nb-Sn and Ti-Nb-Zr systems;
- (e) \overline{C}_{44} values decrease from 0 until 20 at. % Ti, then increase from 20 to 50 at. % Ti and then decrease from 50 to 100 at. % Ti in the Ti-Sn-Ta system;
- (f) \overline{C}_{44} first increase from 0 to 60 at. % Ti and then decrease from 60 to 100 at. % Ti in the Ti-Sn-Zr system.

Two things to notice in the figures is that the ternary interaction parameters do not seem to improve the predicted properties much from the predictions with just the binary interaction parameters and there is discrepancy at between the first-principles calculations based DFT results and the modeling at the 50-50 mixture of the alloying elements $X_{0.50}Y_{0.50}$. While it does not seem that the introduction of the ternary interaction parameters improves the predicted property values, the

effect is seen more drastically with the moduli values. The discrepancy between the calculated results and modeled results at the 50-50 mixture of the alloying elements $X_{0.50}Y_{0.50}$ can be explained by the lack of non-Ti containing binary interaction parameters. The introduction of non-Ti containing binary interaction would improve this. However, the current application is focused on Ti-rich alloys and thus the non-Ti containing binary systems were not studied in the present work. The trends in the ternary elastic stiffness coefficients can be summarized and explained by the elastic stiffness coefficients of pure elements and Ti-X ($X = Mo, Nb, Sn, Ta, Zr$). The c_{11} and c_{12} of Mo, Nb and Ta are higher than Ti, while Sn and Zr are lower. The c_{44} for Mo and Ta are higher than Ti, while Nb, Sn, and Zr are lower. This is because Mo, Nb and Ta are stable in the bcc structure at low temperatures while Ti, Sn and Zr are not. The similarities of Mo, Nb and Ta are again noticed in the Ti-X data trends. The \bar{C}_{11} , \bar{C}_{12} , and \bar{C}_{44} all follow the same trends in the Ti-Mo, Ti-Nb, and Ti-Ta systems with the \bar{C}_{11} and \bar{C}_{12} increasing in value from 100 to 0 at. % Ti, and the \bar{C}_{44} decreasing and then increasing from 100 to 0 at. % Ti. Based on this information, it is no surprise that the Ti-Mo-Nb, Ti-Mo-Ta and Ti-Nb-Ta systems have the same trends in their c_{ij} values. When the binary Ti-Mo, Ti-Nb, and Ti-Ta systems are alloyed with Sn, they show similar trends for the most, not all, of the c_{ij} . The same is true for the Ti-Mo, Ti-Nb, and Ti-Ta systems alloyed with Zr.

Based on the discussion in the methodology, Born's criteria is used to look at the mechanical stability of the bcc phase. When $\bar{C}_{11}-\bar{C}_{12}$ becomes negative then the bcc phase loses mechanical stability and is plotted in Figure 6.7. Based on the present results, the bcc phase loses mechanical stability in the Ti-Mo-Nb, Ti-Mo-Ta, Ti-Mo-Zr, Ti-Nb-Zr, Ti-Sn-Zr, and Ti-Ta-Zr systems when the Ti concentration is more than 90 at. %, with the values being 91, 92, 95, 93, 91, and 94 at. % Ti, respectively. In the Ti-Mo-Sn, Ti-Nb-Sn, Ti-Nb-Ta and Ti-Sn-Ta systems the Ti concentrations are 87, 77, 89, and 80 at %, respectively. As discussed above, Mo, Nb and Ta are strong β -stabilizers, and thus the bcc phase in the Ti-Mo-Nb, Ti-Mo-Ta, and Ti-Nb-Ta systems are stabilized more accordingly. Zr is a weak β -stabilizer. However, when alloyed with other elements Zr acts a strong β -stabilizer as observed in the Ti-Mo-Zr, Ti-Nb-Zr, Ti-Ta-Zr systems in which the bcc phase is stable at high Ti concentrations (95, 93, and 94 at. %, respectively). Zr is even able to stabilize the Ti-Sn-Zr system at a high Ti concentration of 91 at. % Ti though Sn

is not stable in the bcc phase, thus not a β -stabilizer. So, when alloyed with Sn, a higher concentration of Mo, Nb, Ta and Zr is needed to stabilize the bcc phase.

Figure 6.8 and Figure 6.9 plot the Young's moduli (E) (circles) for each Ti-X-Y ternary system ($X \neq Y = \text{Mo, Nb, Sn, Ta, Zr}$) starting from a 50-50 mixture of the two alloying elements ($X_{0.50}Y_{0.50}$) to Ti. The red dashed line is the average from the Hill approach interpolated from the binary interaction parameters shown in Table 5.2. The average from the Hill approach (black solid line), Voigt (purple dotted line), Reuss (gold dotted-dashed line) bounds are plotted using the binary and ternary interaction parameters. The Voigt and Reuss bounds vary more drastically when the bcc structure is unstable as opposed to when the bcc structure is stable. The values from the Hill approach using the binary and ternary interaction parameters is what the database predicts because it has been shown to be a more accurate representation of the Young's modulus than the Voigt or Reuss approximations [70,117]. Whenever possible experimentally determined Young's moduli [38–41] (data listed in Table 6.2) are plotted for comparison. The discrepancy between the previous experimental results (E_{expt}) and the present first-principles results (E_{DFT}) are calculated by Eq. 2.24.

The E_{DFT} , for the Ti-Mo-Nb (Figure 6.8a) system decreases in value from 0 to 100 at. % Ti with the experimental data compiled by Niinomi et al. [40] superimposed. The E_{expt} were obtained for this alloy, using a nanoindenter after solution treatment and are higher than the calculated Hill average values (a discrepancy of 0.65 using Eq. 2.24) and more closely match the Voigt bound (difference of 46 GPa). Niinomi [40] pointed out that Young's moduli obtained from the microhardness testing are higher than the polycrystalline Young's moduli value, thus our calculation results should be close to the polycrystalline E values.

In the Ti-Mo-Sn (Figure 6.8b) no E_{expt} results were found. The calculated Voigt-Reuss bounds and the Hill average E_{DFT} and the E predicted by the modeling (E_{model}) values decrease from 0 to 100 at. % Ti and are quite similar until around 65 at. % Ti.

The E_{DFT} results for the Ti-Mo-Ta alloy system (Figure 6.9c) are compared with experimental data by Niinomi et al. [40] and Mohammed et al. [39]. The E_{expt} values reported by Niinomi et al. [40] were obtained using an ultrasonic measurement after the samples were solution treated. Niinomi et al. [40] pointed out that E_{expt} values by the ultrasonic method are normally between the tensile

testing or microhardness testing. Niinomi et al. [40] also showed that when multiple authors test the same composition using the ultrasonic technique their answers vary less drastically than using tensile or microhardness methods. The E_{expt} fit well with the present Voigt bound (difference of 9 GPa) and had an error of 0.46 (Eq. 2.24) from the Hill average (difference of 33 GPa). The E_{model} and E_{DFT} values decrease from 0 to 100 at. % Ti.

The E_{DFT} of the Ti-Mo-Zr system (Figure 6.8d) is compared with experimental values reported by Mohammed et al. [39]. The review paper by Mohammed et al. [39] did not discuss the methodology used to determine the E_{expt} . The E_{expt} [39] and the E_{model} (Hill average) vary by less than 6 GPa and the E_{model} and E_{DFT} values decrease from 0 to 100 at. % Ti.

E_{expt} from Niinomi et al. [40], Mohammed et al. [39], and Nozoe et al. [41] are compared with the present E_{DFT} for the Ti-Nb-Sn system (Figure 6.8e). The E_{expt} results reported by Niinomi et al. [40] were obtained through tensile testing of samples that were solution treated and cold rolled. Mohammed et al. [39] and Nozoe et al. [41] did not discuss the methodology used to obtain the E_{expt} results. The E_{expt} reported by Niinomi et al. [40] and Mohammed et al. [39] differ from the Hill average by 9 and 15 GPa, respectively (an error of 0.28 using Eq. 2.24). The E_{expt} results from Nozoe et al. [41] differ by 10, 32 and 78 GPa from the Voigt, Hill and Reuss results, respectively, and have an error of 0.56 (Eq. 2.24). However, Nozoe et al. reported that the samples formed the metastable ω phase. Nozoe et al. [41] also discussed how the aging of the Ti-Nb-Sn samples greatly affected the E_{expt} . The E_{model} and E_{DFT} values, for the Ti-Nb-Sn system, increase from 0 to 35 at. % Ti and then decrease from 35 to 100 at. % Ti. So overall the calculations satisfactorily predicted the Young's moduli of the Ti-Mo-Nb, Ti-Mo-Sn, Ti-Mo-Ta, Ti-Mo-Zr and Ti-Nb-Sn systems.

For the Ti-Nb-Ta system, the E_{DFT} , are compared with E_{expt} values reported by Mohammed et al. [39] (Figure 6.9a). The Voigt and Reuss bounds are very close to the Hill average. The E_{expt} results differ by 8, 15, and 21 GPa from the Reuss, Hill and Voigt modeling (0.28 discrepancy Eq. 2.24). The E_{DFT} and E_{model} decrease in value from 0 to 100 at. % Ti in the Ti-Nb-Ta ternary system.

The E_{DFT} results for the Ti-Nb-Zr (Figure 6.9b) system are compared with E_{expt} results from Geetha et al. [38], Mohammed et al. [39], and Niinomi et al. [40]. The E_{expt} results reported by Niinomi et al. [40] are for the Ti-13Nb-13Zr and

Ti-27Nb-8Zr alloys. The results for the Ti-13Nb-13Zr were obtained using both the ultrasonic and 3-point bending tests and varied by 50 GPa, while the Ti-27Nb-8Zr results were obtained using tensile testing and varied by 50 GPa. The E_{expt} results varied from the present Voigt, Hill and Reuss results by an average of 9, 2, and 14 GPa, respectively and has an error of 0.08 (Eq. 2.24) from the Hill average. The E_{DFT} and E_{model} values first increase from 0 to 70 at. % Ti and then decrease from 70 to 100 at. % Ti.

The Ti-Sn-Ta, Ti-Sn-Zr and Ti-Ta-Zr systems did not have experimental data to be compared with and our results are shown in Figure 6.9c, Figure 6.9d, and Figure 6.9e, respectively. For the Ti-Sn-Ta system, the E values decrease from 0 to 100 at. % Ti. The E values, for the Ti-Sn-Zr system, first increase from 0 to 60 at. % Ti and then decrease from 60 to 100 at. % Ti. The E values for the Ti-Ta-Zr system first decrease from 0 to 15 at. % Ti, where the values begin to increase from 15 to 30 at. % Ti and then decrease from 30 to 100 at. % Ti.

The first-principles calculations were completed at 0 K and the CALPHAD modeling used the DFT data to fit parameters while the experiments are obtained using polycrystalline samples at 300 K. Considering this fact and that the experimental measured E values vary at the same composition, the experimental values fit well within the bounds set by Reuss and Voigt, and the average model by the Hill approach reproduces the E_{expt} data for the Ti-X-Y ternary alloys.

Using the complete database with interaction parameters listed in Table 5.2 and 6.3, the moduli values can be calculated and mapped. Figure 6.10 and Figure 6.11 depict E contours in the Ti-X-Y ternaries using the global minimization tool in pycalphad [42]. The ternary maps all have regions in the Ti rich corner that are light blue, i.e. low Young's moduli. With this fact plus the six Ti-X-Y ternaries with the stable bcc phase above 90 at. % Ti, the database points to multiple composition ranges that would yield possible implant materials with comparable elastic properties of the bone. Both the G and E are negative when they are close to Ti. This is due to the instability of the bcc phase close to Ti. As shown by Born's criteria, when $\bar{C}_{11}-\bar{C}_{12}$ is negative the bcc phase loses mechanical stability. Based on calculating G and E using the Voigt-Reuss-Hill approach when $\bar{C}_{11}-\bar{C}_{12}$ becomes negative, it can cause G and E to be negative. Therefore, bcc Ti alloys close to its stability limit can be candidates for low E values close to that of bones.

The modeled B and G calculated by the Hill average are plotted in Figures

6.12-6.15 for each Ti-X-Y ($X \neq Y = \text{Mo, Nb, Sn, Ta, Zr}$) system as a function of composition. The first-principles calculations of the B are 108, 268, 178, 51, 202, and 89 for Ti, Mo, Nb, Sn, Ta, and Zr, respectively. In the Ti-Mo-Nb, Ti-Mo-Ta, Ti-Mo-Zr, Ti-Nb-Ta, Ti-Nb-Zr, and Ti-Ta-Zr system, B increases from the Ti rich corner to the alloying elements. In the Ti-Mo-Sn, Ti-Nb-Sn, Ti-Sn-Ta and Ti-Sn-Zr systems, B increases from the Ti and alloying element sides to the Sn rich corner. The first-principles calculations of the G are -13, 125, 35, 7, 70 and 6 for Ti, Mo, Nb, Sn, Ta and Zr, respectively. The mapping of G in Figure 6.14 and Figure 6.15 show similar mapping in the Ti-Mo-Nb, Ti-Mo-Sn, Ti-Mo-Ta, Ti-Nb-Ta and Ti-Ta-Sn systems. The G values increase from Ti to the Mo or Ta corners. The Ti-Mo-Zr, Ti-Nb-Sn, Ti-Nb-Zr, Ti-Sn-Zr and Ti-Ta-Zr systems are similarly mapped with larger regions in the middle of the isothermal section that retain the same G value. The mapping can be used to target the alloy compositions with certain properties for different applications.

6.3.2 Extrapolation to higher ordered systems

The elastic coefficient database thus developed contains all binary and ternary interaction parameters and can be used to predict Young's moduli in multicomponent Ti alloys. To validate such predictions, the Young's moduli of alloys with available experimental data in the literature [37–39] are calculated and compared in Table 6.4 and Figure 6.16. The same comparison was made in chapter 5 with only binary interaction parameters. The black diagonal line would be a perfect correlation between the predictions and experiments. As discussed previously, the average \bar{C}_{11} , \bar{C}_{12} , and \bar{C}_{44} were calculated and the results varied on average by 3 GPa. The 3 GPa is plotted as the grey region in Figure 6.16. As discussed previously, the error bars plotted for the experimental data represent the variance among the values at the same composition from Niinomi et al. [40], Geetha et al. [38], Tane et al. [37], and Mohammed et al. [39]. The horizontal error bars denote the Voigt and Reuss bounds.

With only the binary interaction parameters, the predictions and experimental results varied between 0.69 and 14 GPa and on average by 7 GPa. The calculated Young's moduli at 0 K are usually larger than the experimental values usually obtained at 300 K. As expected, introducing ternary interaction parameters improves

the agreement with predictions about 0.39 to 13 GPa from the experimental values and an average variance of 5 GPa.

6.4 Conclusion

The elastic stiffness coefficients, bulk modulus, shear modulus, and Young's modulus of the bcc Ti ternary alloys containing Mo, Nb, Sn, Ta and Zr were predicted from first-principles calculations based on density functional theory. The CALPHAD method was used to evaluate ternary interaction parameters with the binary interaction parameters and pure elements calculated in chapter 5. The elastic stiffness coefficients in the Ti-X-Y (X Y = Mo, Nb, Ta) have the same trends because Mo, Nb, and Ta are similar elements, being strong β -stabilizers and stable in the bcc structure at low temperatures. By the same token, the Ti-X-Sn (X = Mo, Nb, Ta) alloys showed similar trends for most of elastic stiffness coefficients, so do the Ti-X-Zr (X = Mo, Nb, Ta) alloys. The present modeling predicted that the bcc Ti-alloys are stable with the Ti mole percent lower than 95 in Ti-Mo-Zr, 94 in Ti-Ta-Zr, 93 in Ti-Nb-Zr, 92 in Ti-Mo-Ta, 91 in Ti-Mo-Nb, 91 in Ti-Sn-Zr, 89 in Ti-Nb-Ta, 87 in Ti-Mo-Sn, 80 in Ti-Sn-Ta, and 77 in Ti-Nb-Sn, respectively. Zr is a weak β -stabilizer alone but become a strong β -stabilizer when alloyed with other elements such as in the Ti-Mo-Zr, Ti-Nb-Zr, Ti-Sn-Zr, Ti-Ta-Zr systems, even though Sn is not stable in the bcc structure and not a β -stabilizer.

The pure element elastic results along with the binary and ternary interaction parameters were combined into a database file in appendix D. Overall, the introduction of the ternary interaction parameters improved the database's ability to predict the E of higher order alloys by a small amount. The complete database satisfactorily predicts the elastic properties of higher order Ti-alloys. The database was used to map possible alloy compositions to find potential materials with a Young's modulus in the target range for biomedical load-bearing implants using the pycalphd code in appendix E. The database will help guide future research to develop low-modulus biocompatible Ti alloys.

Table 6.1: First-principles calculations of the elastic stiffness coefficients for different atomic percent compositions of the bcc Ti-X-Y ternary systems at 0 K.

Reference	$Ti_{1-bc}X_bY_c$	\overline{C}_{11}	\overline{C}_{11}	\overline{C}_{11}
This work	Ti	93	115	41
This work	$Ti_{0.74}Mo_{0.13}Nb_{0.13}$	155	121 ± 4	34 ± 4
This work	$Ti_{0.50}Mo_{0.25}Nb_{0.25}$	222 ± 3	129 ± 3	33 ± 3
This work	$Ti_{0.33}Mo_{0.33}Nb_{0.33}$	269 ± 5	134 ± 3	42 ± 4
This work	$Mo_{0.50}Nb_{0.50}$	414 ± 6	165 ± 3	68
This work	$Ti_{0.74}Mo_{0.13}Sn_{0.13}$	137 ± 15	121 ± 2	56 ± 13
This work	$Ti_{0.50}Mo_{0.25}Sn_{0.250}$	160 ± 3	130 ± 8	71 ± 2
This work	$Ti_{0.33}Mo_{0.33}Sn_{0.33}$	167 ± 8	133 ± 6	75 ± 2
This work	$Mo_{0.50}Sn_{0.50}$	192 ± 28	130 ± 36	40 ± 31
This work	$Ti_{0.74}Mo_{0.13}Ta_{0.13}$	153 ± 1	125 ± 4	38 ± 3
This work	$Ti_{0.50}Mo_{0.25}Ta_{0.25}$	222 ± 2	136 ± 1	45 ± 3
This work	$Ti_{0.33}Mo_{0.33}Ta_{0.33}$	263 ± 4	145 ± 6	49 ± 4
This work	$Mo_{0.50}Ta_{0.50}$	370 ± 13	163 ± 4	63 ± 4
This work	$Ti_{0.74}Mo_{0.13}Zr_{0.13}$	125 ± 1	109 ± 8	35 ± 1
This work	$Ti_{0.50}Mo_{0.25}Zr_{0.25}$	160 ± 1	116 ± 5	34 ± 2
This work	$Ti_{0.33}Mo_{0.33}Zr_{0.33}$	182 ± 1	116 ± 2	31 ± 8
This work	$Mo_{0.50}Zr_{0.50}$	231 ± 7	118 ± 5	33 ± 8
This work	$Ti_{0.74}Nb_{0.13}Sn_{0.13}$	115 ± 4	118 ± 3	55
This work	$Ti_{0.50}Nb_{0.25}Sn_{0.25}$	131 ± 9	121 ± 6	64 ± 3
This work	$Ti_{0.33}Nb_{0.33}Sn_{0.33}$	134 ± 2	122 ± 3	67 ± 6
This work	$Nb_{0.50}Sn_{0.50}$	132 ± 4	118 ± 8	56 ± 4
This work	$Ti_{0.74}Nb_{0.13}Ta_{0.13}$	130 ± 3	124 ± 4	37 ± 3
This work	$Ti_{0.50}Nb_{0.25}Ta_{0.25}$	182 ± 1	129 ± 4	43 ± 6
This work	$Ti_{0.33}Nb_{0.33}Ta_{0.33}$	208	135 ± 1	44 ± 1
This work	$Nb_{0.50}Ta_{0.50}$	260 ± 2	148 ± 3	47 ± 3
This work	$Ti_{0.74}Nb_{0.13}Zr_{0.13}$	101 ± 2	113 ± 4	32 ± 3
This work	$Ti_{0.50}Nb_{0.25}Zr_{0.25}$	122 ± 1	113 ± 3	28 ± 3
This work	$Ti_{0.33}Nb_{0.33}Zr_{0.33}$	143 ± 2	107 ± 5	28 ± 3
This work	$Nb_{0.50}Zr_{0.50}$	154 ± 5	110 ± 3	15 ± 2
This work	$Ti_{0.74}Sn_{0.13}Ta_{0.13}$	115 ± 6	121 ± 4	60 ± 2

Table 6.1: First-principles calculations of the elastic stiffness coefficients for different atomic percent compositions of the bcc Ti-X-Y ternary systems at 0 K.

Reference	$Ti_{1-bc}X_bY_c$	\overline{C}_{11}	\overline{C}_{11}	\overline{C}_{11}
This work	$Ti_{0.50}Sn_{0.25}Ta_{0.25}$	138 ± 13	125 ± 4	75 ± 4
This work	$Ti_{0.33}Sn_{0.33}Ta_{0.33}$	138 ± 6	131 ± 8	78 ± 1
This work	$Sn_{0.50}Ta_{0.50}$	133 ± 8	130 ± 4	60 ± 4
This work	$Ti_{0.74}Sn_{0.13}Zr_{0.13}$	97 ± 5	111 ± 4	55 ± 2
This work	$Ti_{0.50}Sn_{0.25}Zr_{0.25}$	99 ± 12	103 ± 4	59 ± 7
This work	$Ti_{0.33}Sn_{0.33}Zr_{0.33}$	96 ± 7	98 ± 3	55 ± 3
This work	$Sn_{0.50}Zr_{0.50}$	85 ± 7	87 ± 9	42 ± 3
This work	$Ti_{0.74}Ta_{0.13}Zr_{0.13}$	136 ± 36	103 ± 21	44 ± 5
This work	$Ti_{0.50}Ta_{0.25}Zr_{0.25}$	130 ± 3	117 ± 4	42 ± 7
This work	$Ti_{0.33}Ta_{0.33}Zr_{0.33}$	148 ± 1	115 ± 2	44 ± 2
This work	$Ta_{0.50}Zr_{0.50}$	157 ± 2	123 ± 3	35 ± 3

Table 6.2: First-principles calculations of the bulk modulus B , shear modulus G , and Young's modulus E in GPa for different atomic percent compositions of the bcc Ti-X-Y ternary systems at 0 K as well as experimental data obtained for the Young's modulus at 300 K by the references stated.

Reference	$Ti_{1-bc}X_bY_c$	B	G	E
This work	Ti	108	-12.91	-40.34
This work	$Ti_{0.74}Mo_{0.13}Nb_{0.13}$	132 ± 4	26 ± 4	73 ± 4
This work	$Ti_{0.50}Mo_{0.25}Nb_{0.25}$	160 ± 3	38 ± 3	105 ± 3
This work	$Ti_{0.33}Mo_{0.33}Nb_{0.33}$	179 ± 5	51 ± 5	139 ± 5
This work	$Mo_{0.50}Nb_{0.50}$	248 ± 6	87 ± 6	233 ± 6
Expt 300 K [40]	$Ti_{0.92}Mo_{0.06}Nb_{0.02}$			110
This work	$Ti_{0.74}Mo_{0.13}Sn_{0.13}$	126 ± 15	27 ± 15	75 ± 15
This work	$Ti_{0.50}Mo_{0.25}Sn_{0.25}$	140 ± 8	39 ± 8	106 ± 8
This work	$Ti_{0.33}Mo_{0.33}Sn_{0.33}$	144 ± 8	42 ± 8	114 ± 8
This work	$Mo_{0.50}Sn_{0.50}$	151 ± 36	36 ± 36	100 ± 36
This work	$Ti_{0.74}Mo_{0.13}Ta_{0.13}$	134 ± 4	25 ± 4	72 ± 4
This work	$Ti_{0.50}Mo_{0.25}Ta_{0.25}$	165 ± 2	44 ± 3	122 ± 3
This work	$Ti_{0.33}Mo_{0.33}Ta_{0.33}$	184 ± 6	53 ± 6	$145 \pm$
This work	$Mo_{0.50}Ta_{0.50}$	232 ± 13	77 ± 13	208 ± 13
Expt 300 K [39]	$Ti_{0.92}Mo_{0.07}Ta_{0.01}$			74
Expt 300 K [40]	$Ti_{0.92}Mo_{0.07}Ta_{0.01}$			74
This work	$Ti_{0.74}Mo_{0.13}Zr_{0.13}$	114 ± 8	20 ± 8	55 ± 8
This work	$Ti_{0.50}Mo_{0.25}Zr_{0.25}$	131 ± 5	29 ± 5	80 ± 5
This work	$Ti_{0.33}Mo_{0.33}Zr_{0.33}$	138 ± 2	32 ± 8	89 ± 8
This work	$Mo_{0.50}Zr_{0.50}$	156 ± 7	41 ± 8	113 ± 8
Expt 300 K [39]	$Ti_{0.91}Mo_{0.07}Zr_{0.03}$			64
This work	$Ti_{0.74}Nb_{0.13}Sn_{0.13}$	117 ± 4	14 ± 4	41 ± 4
This work	$Ti_{0.50}Nb_{0.25}Sn_{0.25}$	124 ± 9	26 ± 9	72 ± 9
This work	$Ti_{0.33}Nb_{0.33}Sn_{0.33}$	126 ± 6	28 ± 6	78 ± 6
This work	$Nb_{0.50}Sn_{0.50}$	123 ± 8	26 ± 8	72 ± 8
Expt 300 K [39]	$Ti_{0.76}Nb_{0.22}Sn_{0.02}$			44
Expt 300 K [40]	$Ti_{0.76}Nb_{0.22}Sn_{0.02}$			50
Expt 300 K [41]	$Ti_{0.88}Nb_{0.09}Sn_{0.03}$			58
This work	$Ti_{0.74}Nb_{0.13}Ta_{0.13}$	126 ± 4	15 ± 4	43 ± 4

Table 6.2: First-principles calculations of the bulk modulus B , shear modulus G , and Young's modulus E in GPa for different atomic percent compositions of the bcc Ti-X-Y ternary systems at 0 K as well as experimental data obtained for the Young's modulus at 300 K by the references stated.

Reference	$Ti_{1-bc}X_bY_c$	B	G	E
This work	$Ti_{0.50}Nb_{0.25}Ta_{0.25}$	147 ± 6	35 ± 6	98 ± 6
This work	$Ti_{0.33}Nb_{0.33}Ta_{0.33}$	159 ± 1	41 ± 1	113 ± 1
This work	$Nb_{0.50}Ta_{0.50}$	185 ± 3	50 ± 3	140 ± 3
Expt 300 K [39]	$Ti_{0.72}Nb_{0.10}Ta_{0.19}$			55
This work	$Ti_{0.74}Nb_{0.13}Zr_{0.13}$	109 ± 4	-2 ± 4	-6 ± 4
This work	$Ti_{0.50}Nb_{0.25}Zr_{0.25}$	116 ± 3	14 ± 3	40 ± 3
This work	$Ti_{0.33}Nb_{0.33}Zr_{0.33}$	119 ± 5	23 ± 5	66 ± 5
This work	$Nb_{0.50}Zr_{0.50}$	125 ± 5	17 ± 5	50 ± 5
Expt 300 K [39]	$Ti_{0.85}Nb_{0.08}Zr_{0.08}$			77
Expt 300 K [39]	$Ti_{0.86}Nb_{0.11}Zr_{0.03}$			50
Expt 300 K [40]	$Ti_{0.78}Nb_{0.17}Zr_{0.05}$			78
Expt 300 K [38]	$Ti_{0.85}Nb_{0.08}Zr_{0.08}$			81
This work	$Ti_{0.74}Sn_{0.13}Ta_{0.13}$	119 ± 6	13 ± 6	39 ± 6
This work	$Ti_{0.50}Sn_{0.25}Ta_{0.25}$	129 ± 13	31 ± 13	86 ± 13
This work	$Ti_{0.33}Sn_{0.33}Ta_{0.33}$	133 ± 8	28 ± 8	79 ± 8
This work	$Sn_{0.50}Ta_{0.50}$	131 ± 8	20 ± 8	57 ± 8
This work	$Ti_{0.74}Sn_{0.13}Zr_{0.13}$	106 ± 5	4 ± 5	13 ± 5
This work	$Ti_{0.50}Sn_{0.25}Zr_{0.25}$	102 ± 12	15 ± 12	42 ± 12
This work	$Ti_{0.33}Sn_{0.33}Zr_{0.33}$	97 ± 7	15 ± 7	43 ± 7
This work	$Sn_{0.50}Zr_{0.50}$	86 ± 9	11 ± 9	32 ± 9
This work	$Ti_{0.74}Ta_{0.13}Zr_{0.13}$	114 ± 21	30 ± 21	82 ± 21
This work	$Ti_{0.50}Ta_{0.25}Zr_{0.25}$	121 ± 4	20 ± 7	58 ± 7
This work	$Ti_{0.33}Ta_{0.33}Zr_{0.33}$	126 ± 2	30 ± 2	83 ± 2
This work	$Ta_{0.50}Zr_{0.50}$	134 ± 3	26 ± 3	74 ± 3

Table 6.3: Evaluated interactions parameters (L_2 , Eq. 2.24) for the elastic stiffness coefficients of the Ti-containing ternary alloys.

Alloy	Interaction Parameter	\bar{C}_{11}	\bar{C}_{12}	\bar{C}_{44}
Ti-Mo-Nb	L_2	-29.97	13.97	9.72
Ti-Mo-Sn	L_2	-83.85	31.80	74.73
Ti-Mo-Ta	L_2	-106.53	-12.35	5.27
Ti-Mo-Zr	L_2	-245.27	50.43	-44.96
Ti-Nb-Sn	L_2	-41.52	25.52	67.85
Ti-Nb-Ta	L_2	-93.77	-15.80	4.25
Ti-Nb-Zr	L_2	-220.35	72.10	-55.29
Ti-Sn-Ta	L_2	-95.39	-10.94	67.85
Ti-Sn-Zr	L_2	-155.34	68.86	3.85
Ti-Ta-Zr	L_2	-149.67	-8.91	-23.70

Table 6.4: Predicted Young's moduli (E) (in GPa) of higher order alloys using the binary and ternary interaction parameters in the bcc phase compared to the predicted Young's moduli (E_{BIN}) using just the binary interaction parameters and the experimental values found with both the weight percent and atomic percent listed.

Alloy Name (%wt)	at %	Calc E_{BIN}	Calc E	Expt E
Ti-35Nb-7Zr-5Ta [38]	Ti-24Nb-5Zr-2Ta	81	78	80
Ti-29Nb-13Ta-4.6Zr [38]	Ti-20Nb-5Ta-3Zr	76	73	75
Ti-29Nb-13Ta-6Sn [38]	Ti-21Nb-5Ta-3Sn	68	68	74
Ti-29Nb-13Ta-4.6Sn [38]	Ti-20Nb-5Ta-3Sn	67	66	66
Ti-29Nb-13Ta-4.5Zr [38]	Ti-20Nb-5Ta-3Zr	76	73	65
Ti-29Nb-13Ta-4.6Zr [37]	Ti-21Nb-5Ta-3Zr	76	75	64
Ti-30Nb-10Ta-5Zr [37]	Ti-23Nb-4Ta-3Zr	77	74	64
Ti-35Nb-10Ta-5Zr [37]	Ti-25Nb-4Ta-4Zr	80	78	65
Ti-24Nb-4Zr-7.9Sn [39]	Ti-15Nb-3Zr-4Sn	65	62	54
Ti-35Nb-2Ta-3Zr [39]	Ti-23Nb-1Ta-2Zr	69	68	61
Ti-29Nb-11Ta-5Zr [39]	Ti-20Nb-6Ta-2Zr	74	72	60
Ti-10Zr-5Ta-5Nb [39]	Ti-6Zr-1Ta-3Nb	64	62	52
Ti-29Nb-13Ta-2Sn [39]	Ti-20Nb-5Ta-1Sn	66	65	62

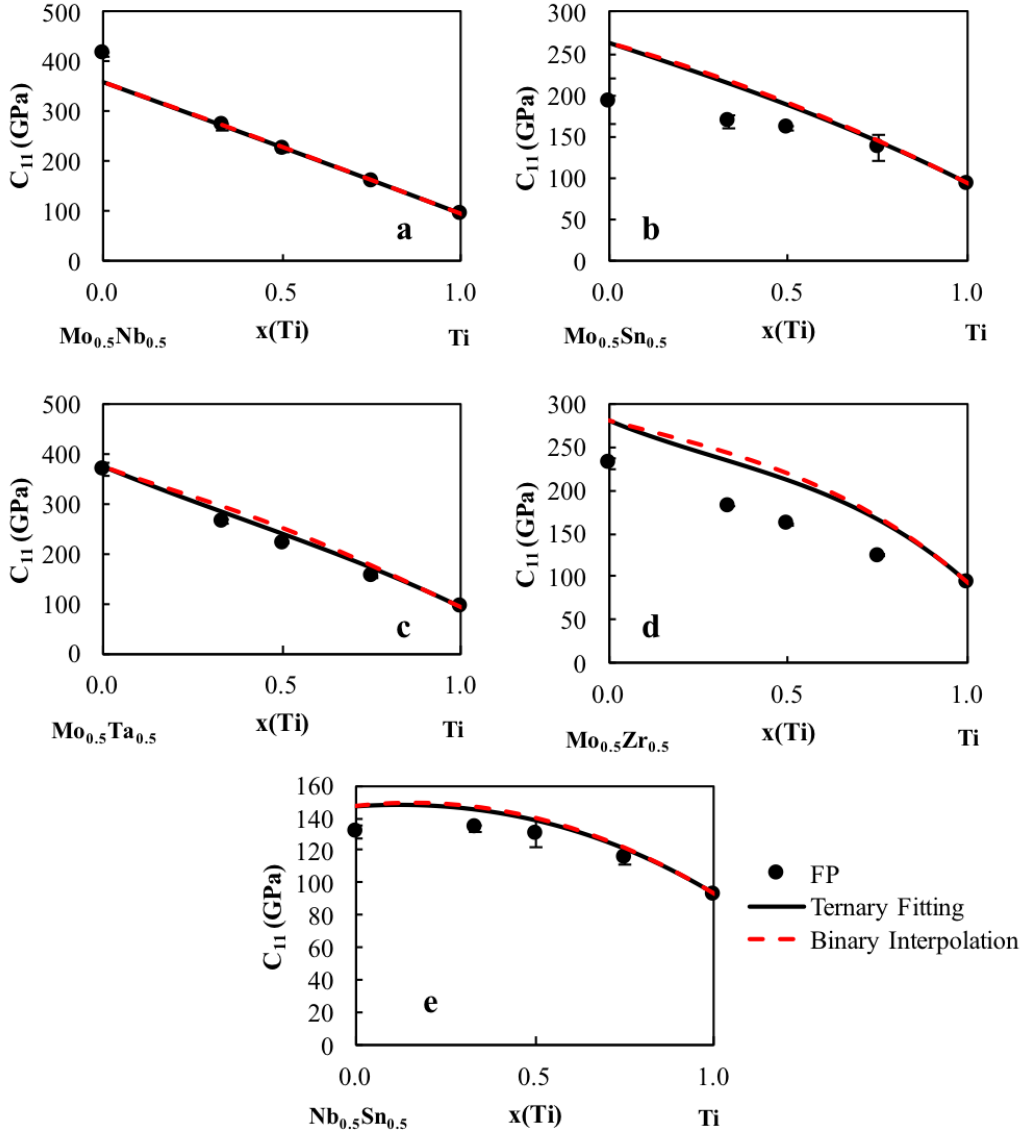


Figure 6.1: \overline{C}_{11} values (circles) from the current first-principles calculations plotted with their errors as well as the current modeling with (black solid line) and without ternary interaction parameters (red dashed line) for five of the Ti-X-Y binary systems from a 50-50 mixture of the alloying elements $X_{0.5}Y_{0.5}$ to Ti ($X \neq Y = \text{Mo, Nb, Ta, Sn, Zr}$).

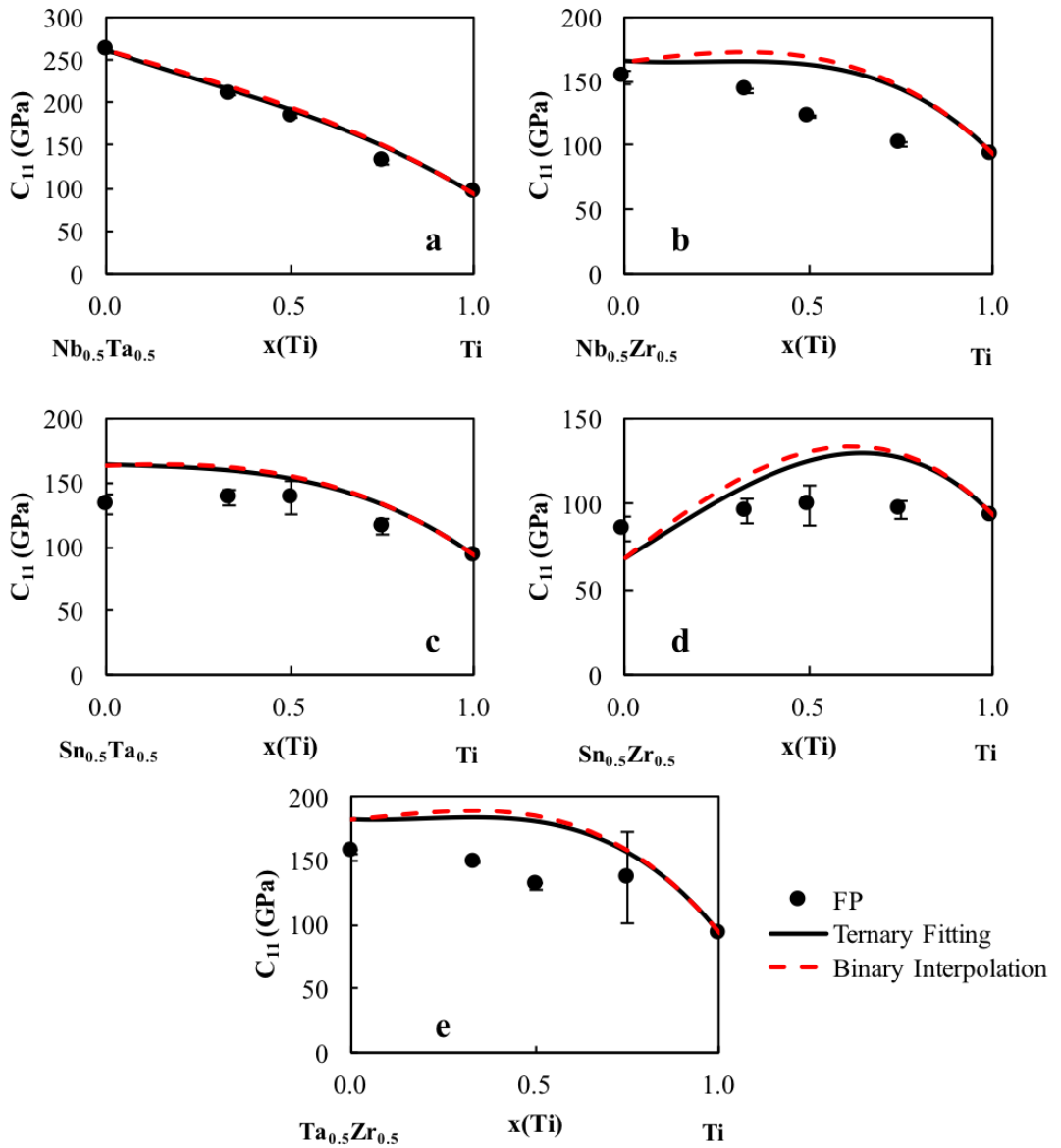


Figure 6.2: \overline{C}_{11} values (circles) from the current first-principles calculations plotted with their errors as well as the current modeling with (black solid line) and without ternary interaction parameters (red dashed line) for five of the Ti-X-Y binary systems from a 50-50 mixture of the alloying elements X_{0.5}Y_{0.5} to Ti (X ≠ Y = Mo, Nb, Ta, Sn, Zr).

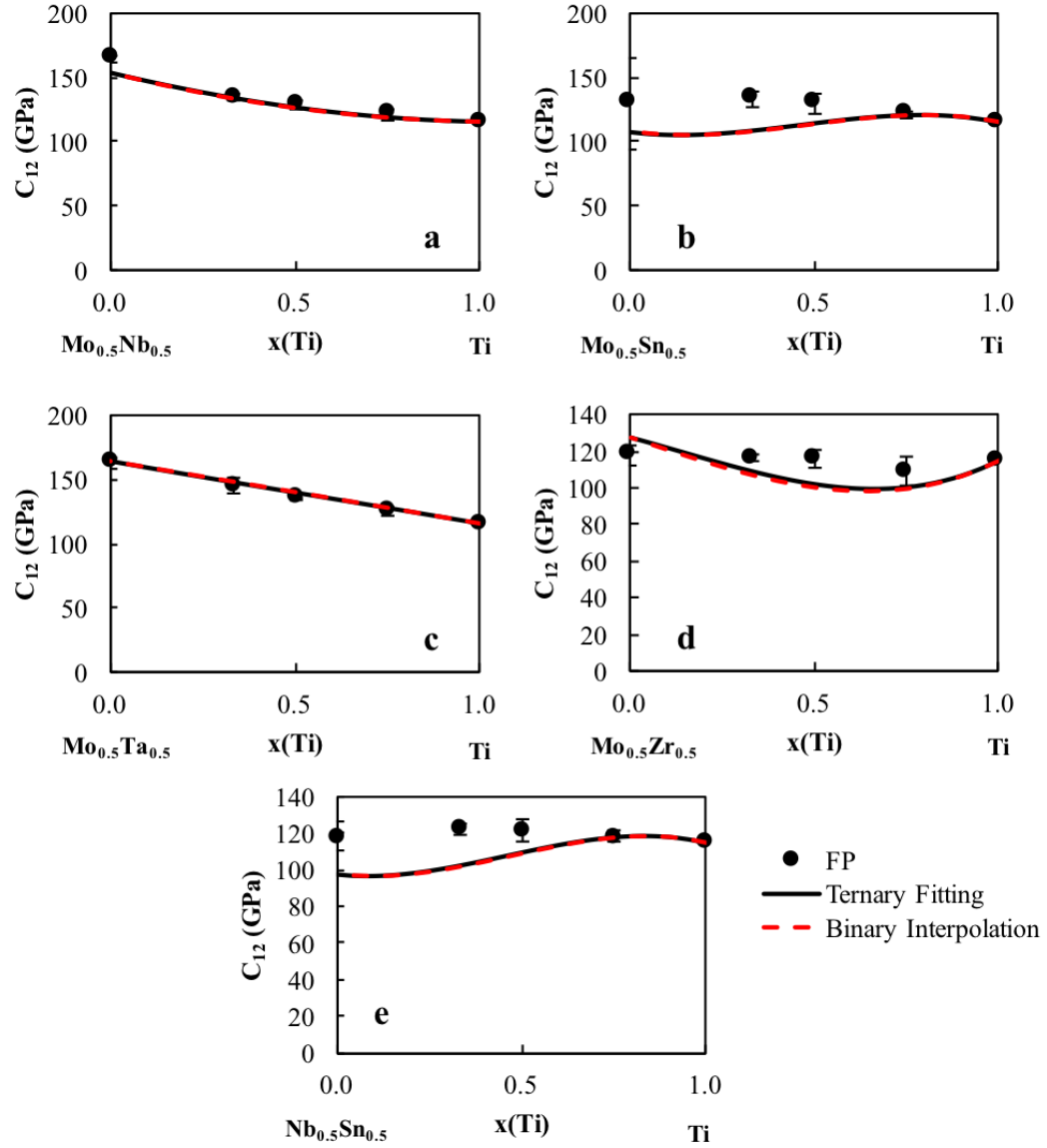


Figure 6.3: \overline{C}_{12} values (circles) from the current first-principles calculations plotted with their errors as well as the current modeling with (black solid line) and without ternary interaction parameters (red dashed line) for five of the $\text{Ti}-\text{X}-\text{Y}$ binary systems from a 50-50 mixture of the alloying elements $\text{X}_{0.5}\text{Y}_{0.5}$ to Ti ($\text{X} \neq \text{Y} = \text{Mo}, \text{Nb}, \text{Ta}, \text{Sn}, \text{Zr}$).

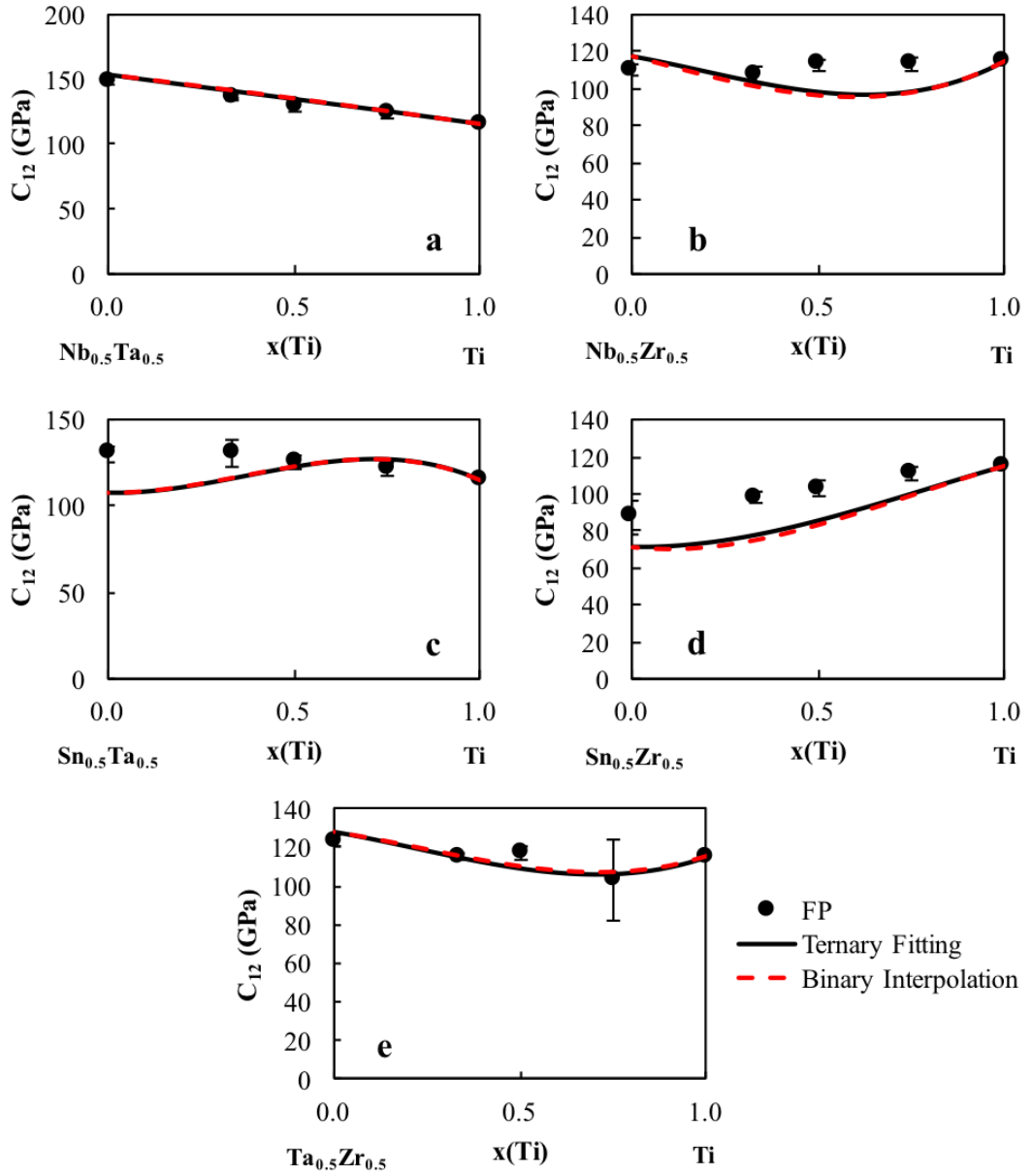


Figure 6.4: \overline{C}_{12} values (circles) from the current first-principles calculations plotted with their errors as well as the current modeling with (black solid line) and without ternary interaction parameters (red dashed line) for five of the Ti-X-Y binary systems from a 50-50 mixture of the alloying elements $X_{0.5}Y_{0.5}$ to Ti ($X \neq Y = \text{Mo, Nb, Ta, Sn, Zr}$).

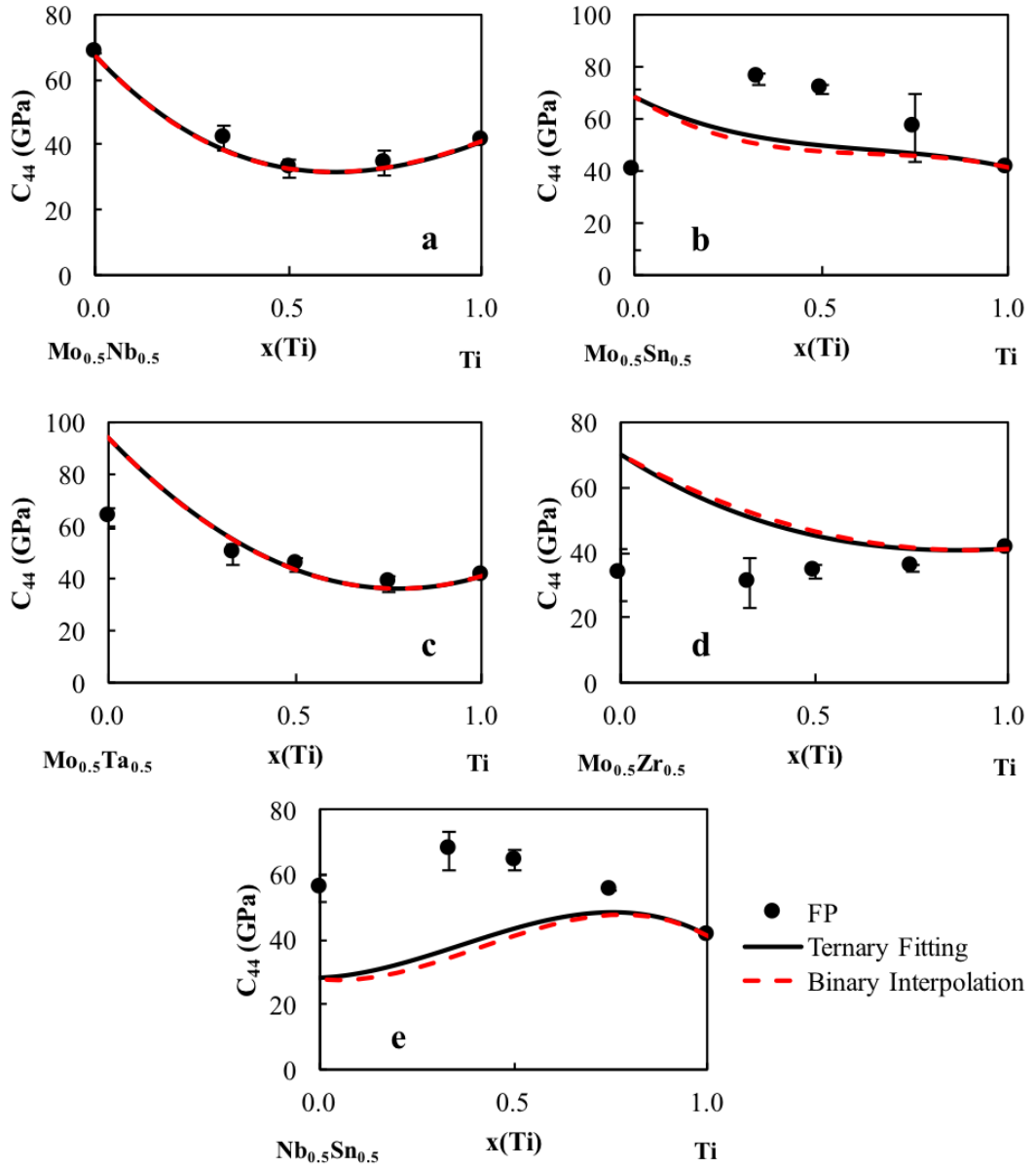


Figure 6.5: \overline{C}_{44} values (circles) from the current first-principles calculations plotted with their errors as well as the current modeling with (black solid line) and without ternary interaction parameters (red dashed line) for five of the Ti-X-Y binary systems from a 50-50 mixture of the alloying elements $X_{0.5}Y_{0.5}$ to Ti ($X \neq Y = \text{Mo, Nb, Ta, Sn, Zr}$).

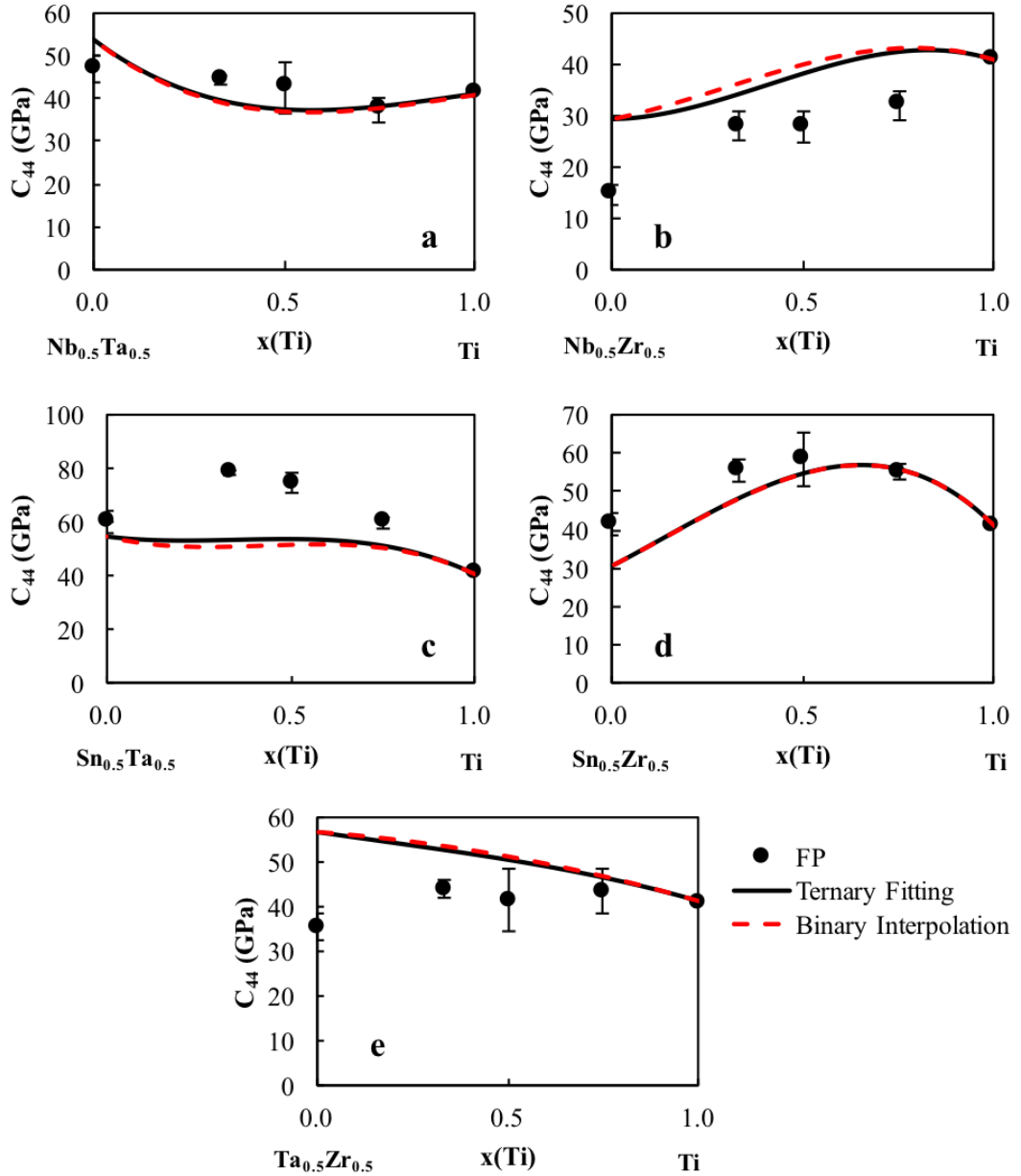


Figure 6.6: \bar{C}_{44} values (circles) from the current first-principles calculations plotted with their errors as well as the current modeling with (black solid line) and without ternary interaction parameters (red dashed line) for five of the Ti-X-Y binary systems from a 50-50 mixture of the alloying elements $X_{0.5}Y_{0.5}$ to Ti ($X \neq Y = \text{Mo, Nb, Ta, Sn, Zr}$).

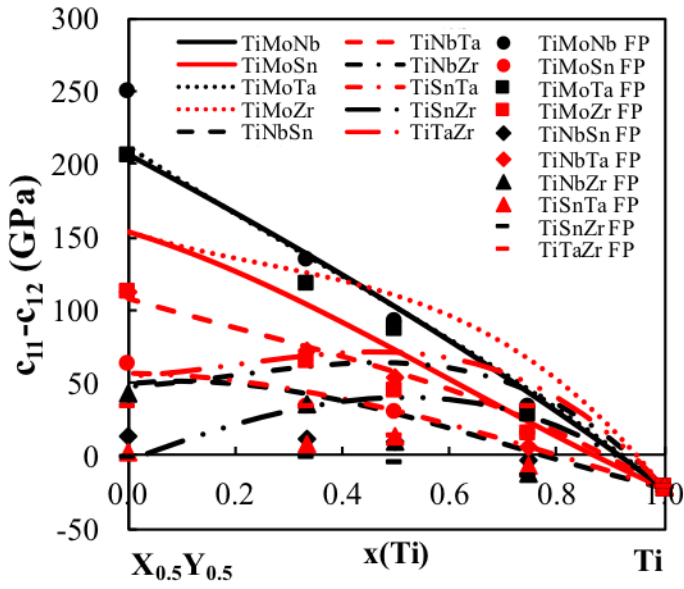


Figure 6.7: $\overline{C}_{11}-\overline{C}_{12}$ values (symbols) from the current first-principles calculations plotted with the current modeling (lines) plotted from a 50-50 mixture of the alloying elements X and Y to Ti ($X \neq Y = \text{Mo, Nb, Ta, Sn, Zr}$). The $\overline{C}_{11}-\overline{C}_{12}$ shows the stability of the bcc phase, when the value is negative the bcc phase is not stable in the corresponding composition ranges.

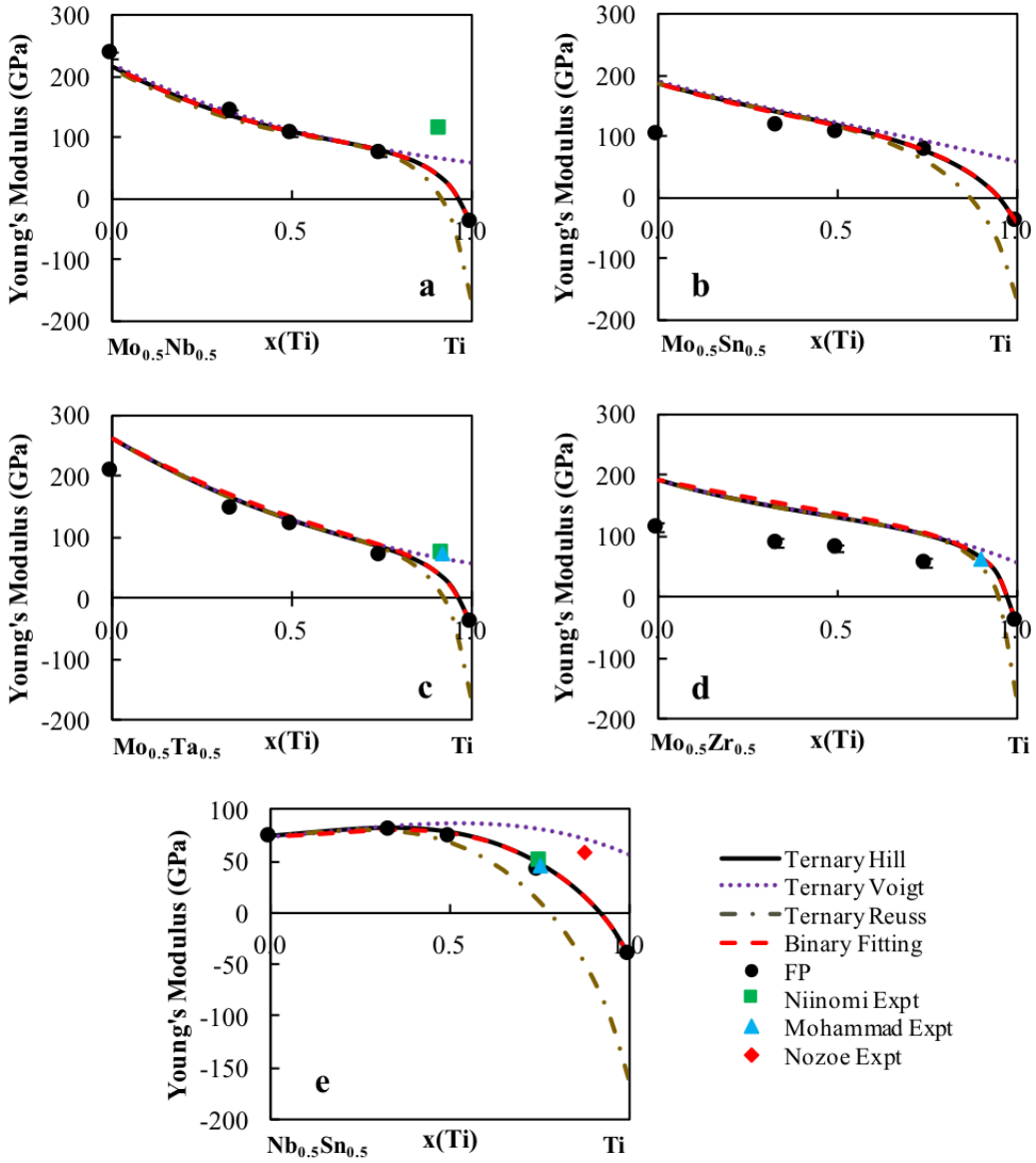


Figure 6.8: Young's modulus of five Ti-X-Y ternary systems plotted from a 50-50 mixture of the alloying elements to Ti in the bcc phase. The present calculations are plotted as filled circles with the error bars. The red dotted line is without the ternary interaction parameters. The dotted purple line is the Voigt upper Young's modulus bound, the gold dot dashed line is the lower Reuss Young's modulus bound and the black line is the Hill Young's modulus average. Experimental values are included for comparison [38–41].

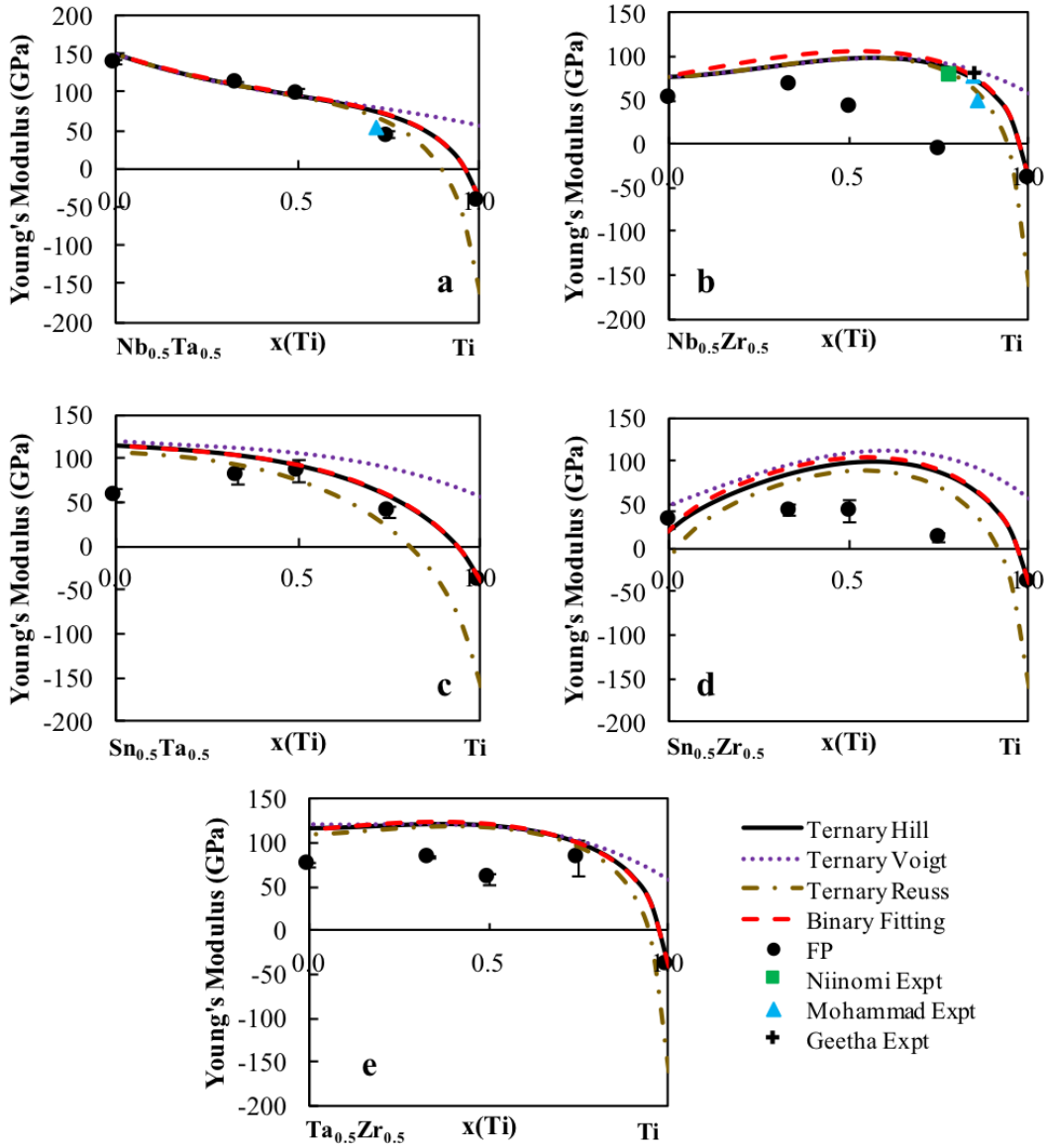


Figure 6.9: Young's modulus of five Ti-X-Y ternary systems plotted from a 50-50 mixture of the alloying elements to Ti in the bcc phase. The present calculations are plotted as filled circles with the error bars. The red dotted line is without the ternary interaction parameters. The dotted purple line is the Voigt upper Young's modulus bound, the gold dot dashed line is the lower Reuss Young's modulus bound and the black line is the Hill Young's modulus average. Experimental values are included for comparison [38–41].

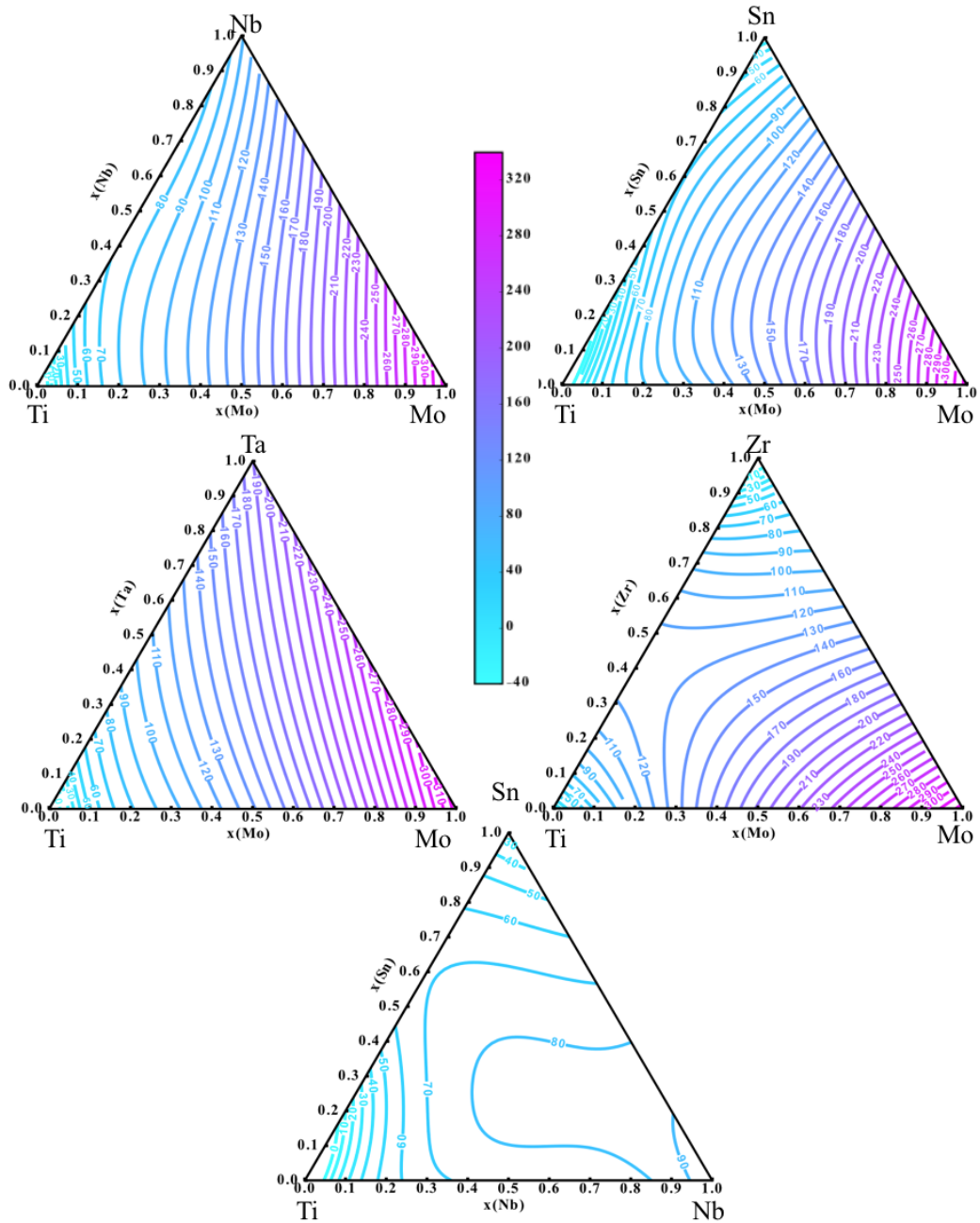


Figure 6.10: Young's modulus in GPa mapped as a function of composition for the Ti-Mo-Nb, Ti-Mo-Sn, Ti-Mo-Ta, Ti-Mo-Zr and Ti-Nb-Sn alloy systems using pycalphad [42].

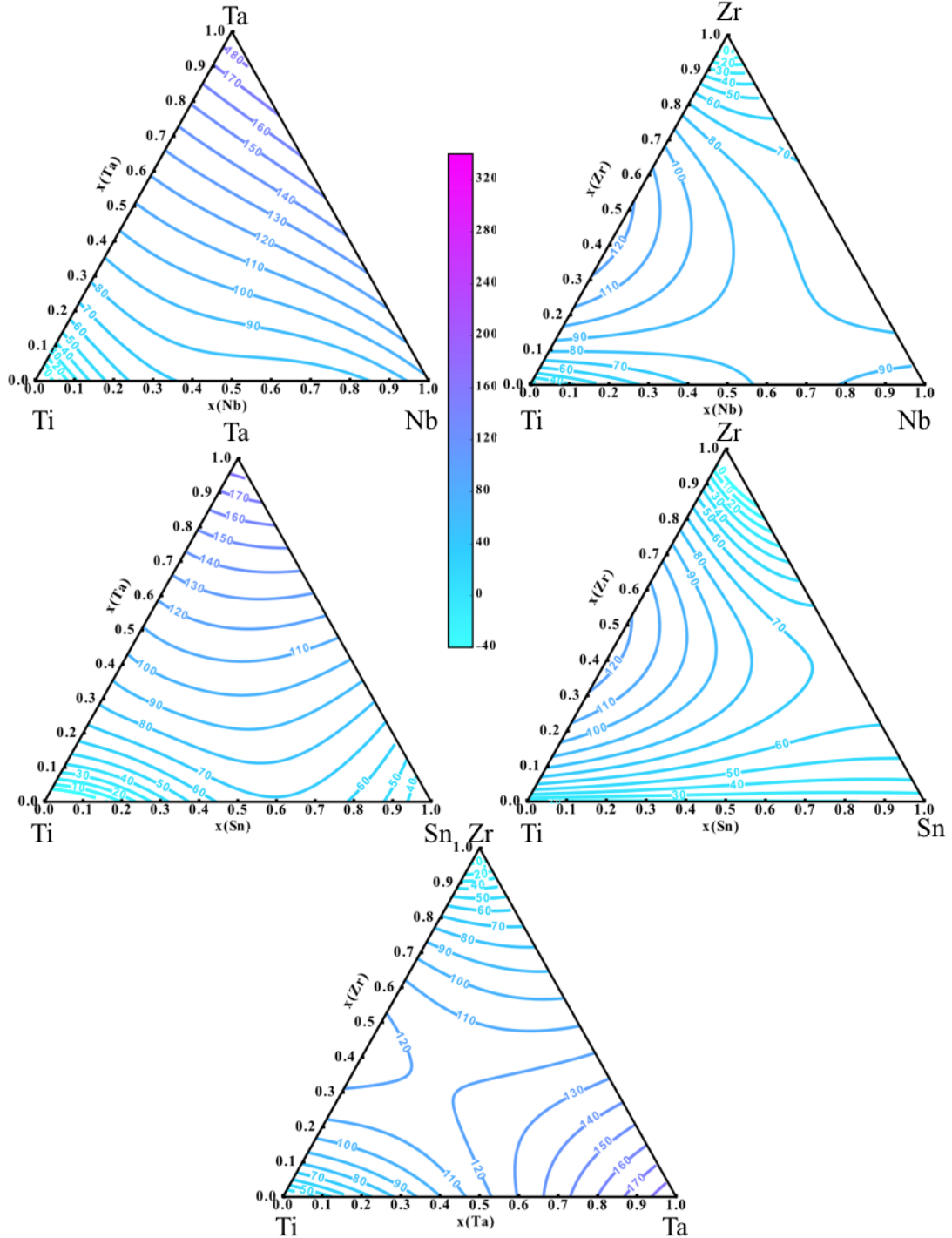


Figure 6.11: Young's modulus in GPa mapped as a function of composition for the Ti-Mo-Nb, Ti-Mo-Sn, Ti-Mo-Ta, Ti-Mo-Zr and Ti-Nb-Sn alloy systems using pycalphad [42].

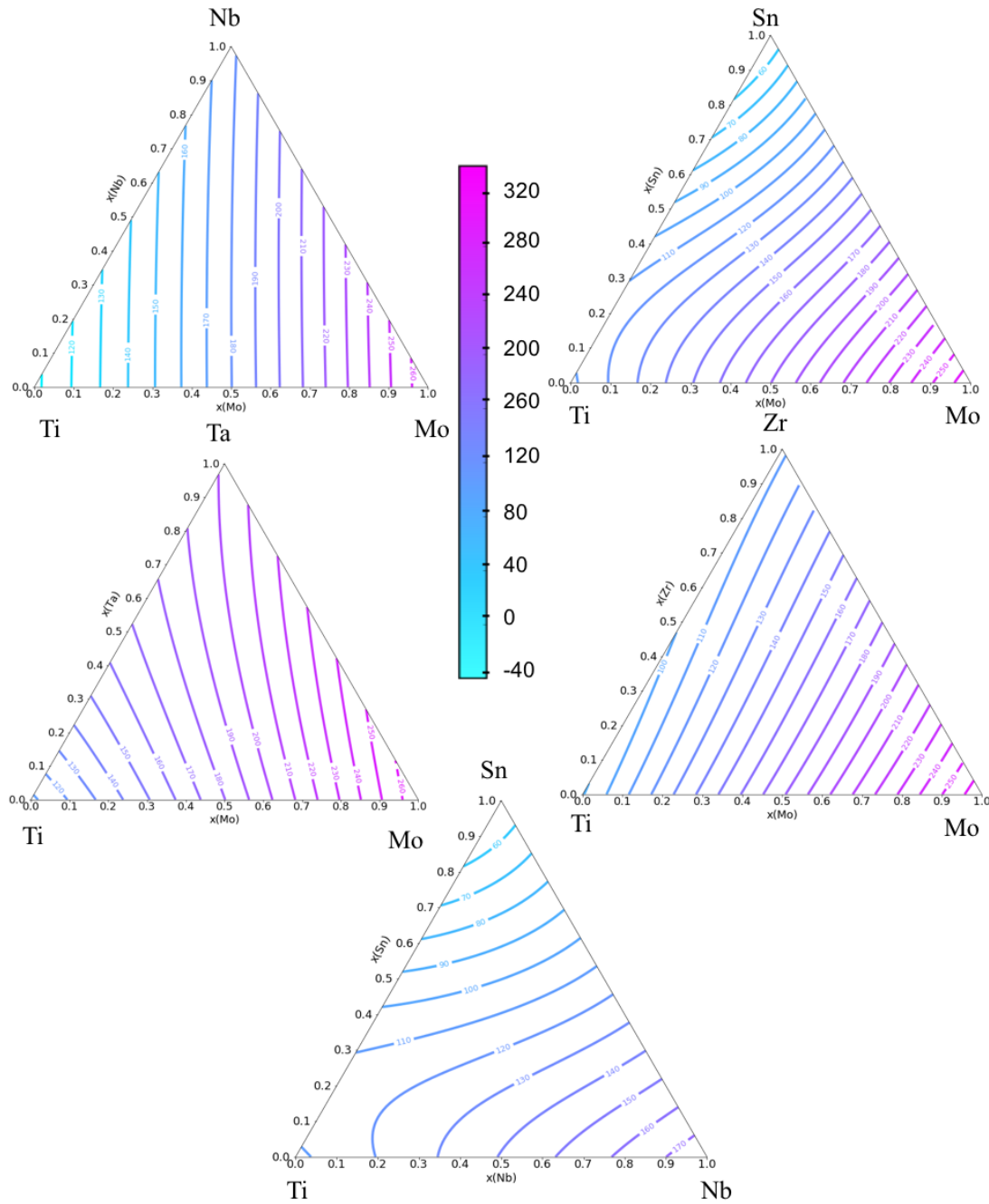


Figure 6.12: Bulk modulus in GPa mapped as a function of composition for the Ti-Mo-Nb, Ti-Mo-Sn, Ti-Mo-Ta, Ti-Mo-Zr and Ti-Nb-Sn alloy systems using pycalphad [42].

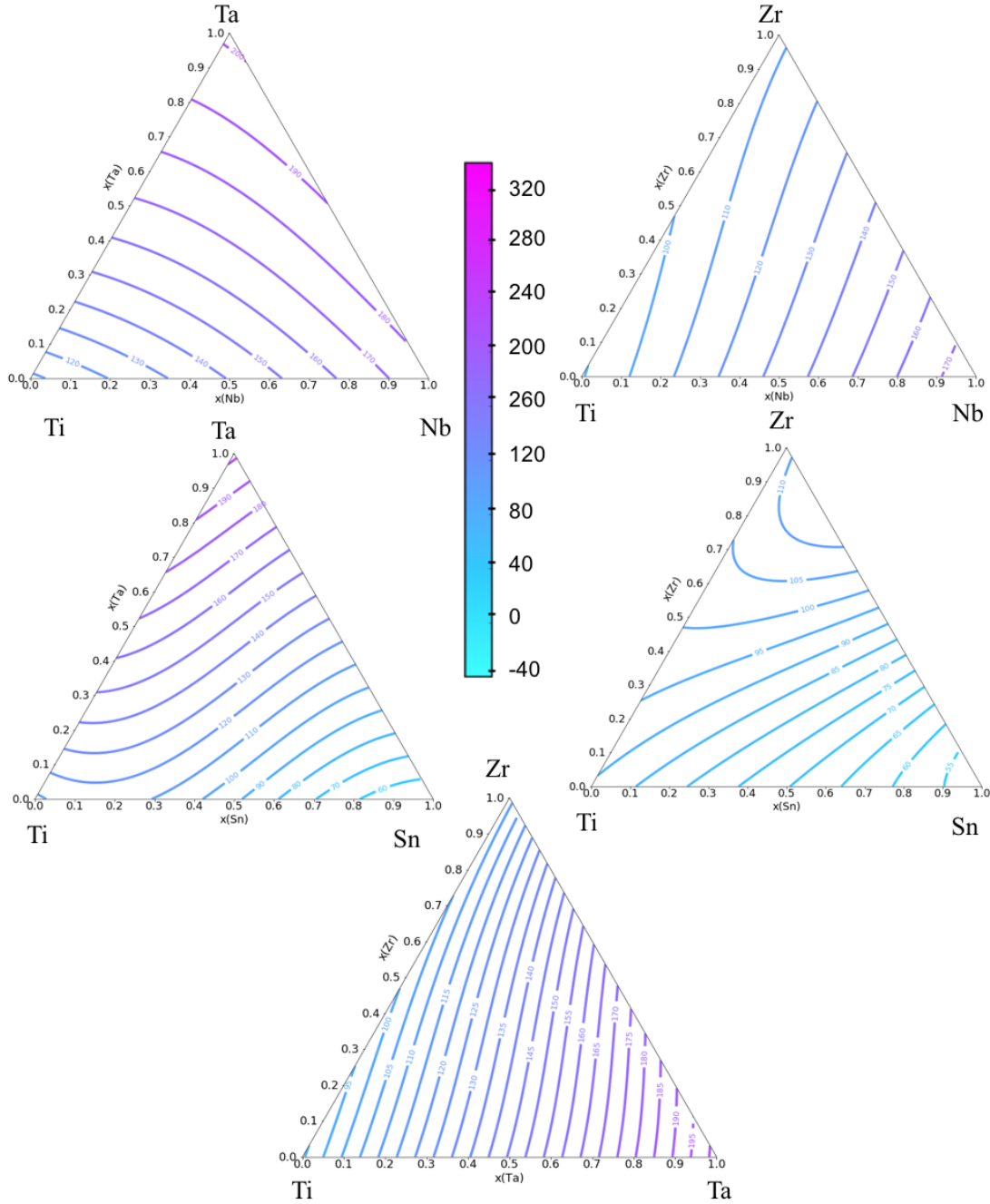


Figure 6.13: Bulk modulus in GPa mapped as a function of composition for the Ti-Nb-Ta, Ti-Nb-Zr, Ti-Sn-Ta, Ti-Sn-Zr and Ti-Ta-Zr alloy systems using pycalphad [42].

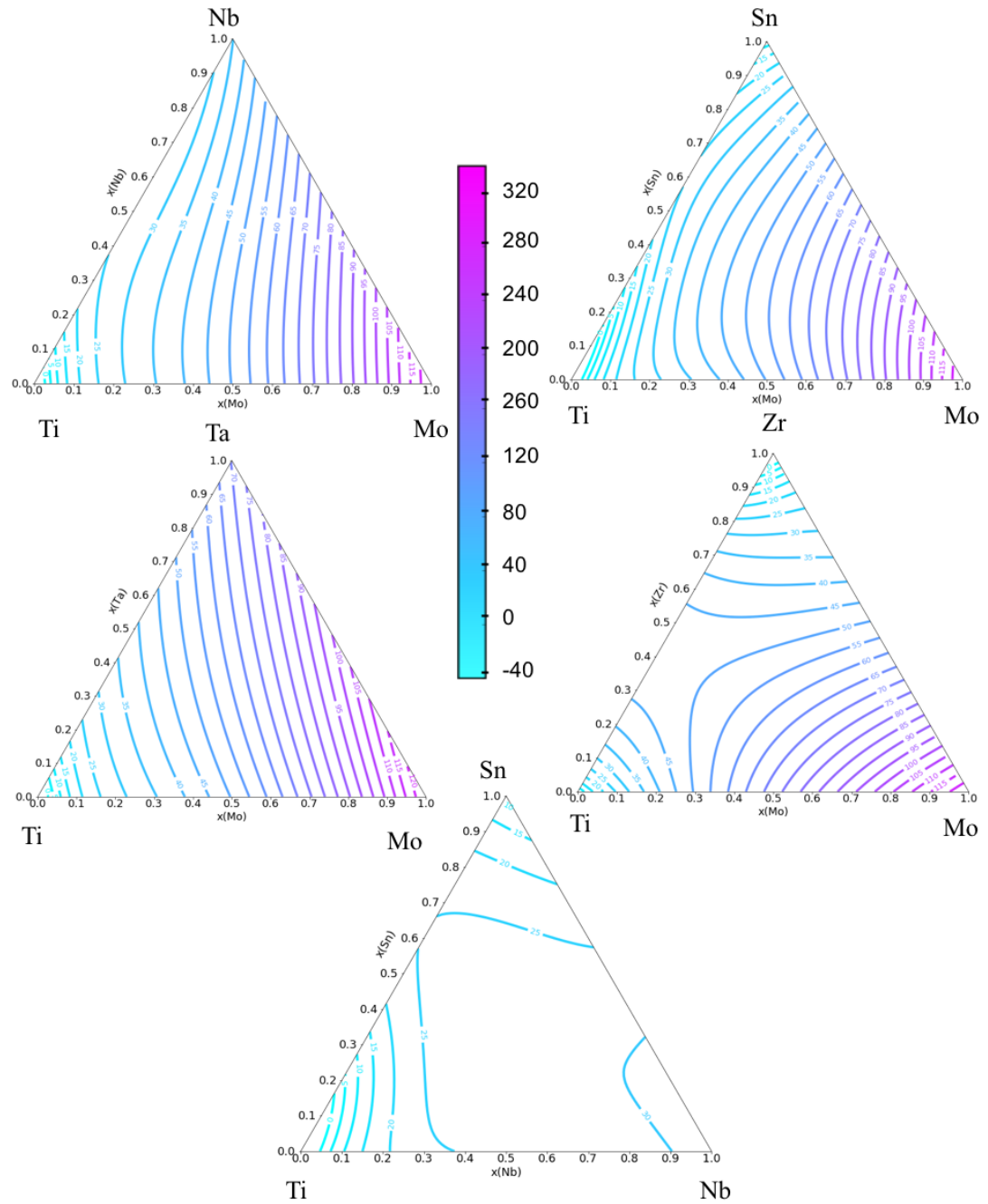


Figure 6.14: Shear modulus in GPa mapped as a function of composition for the Ti-Mo-Nb, Ti-Mo-Sn, Ti-Mo-Ta, Ti-Mo-Zr and Ti-Nb-Sn alloy systems using pycalphad [42].

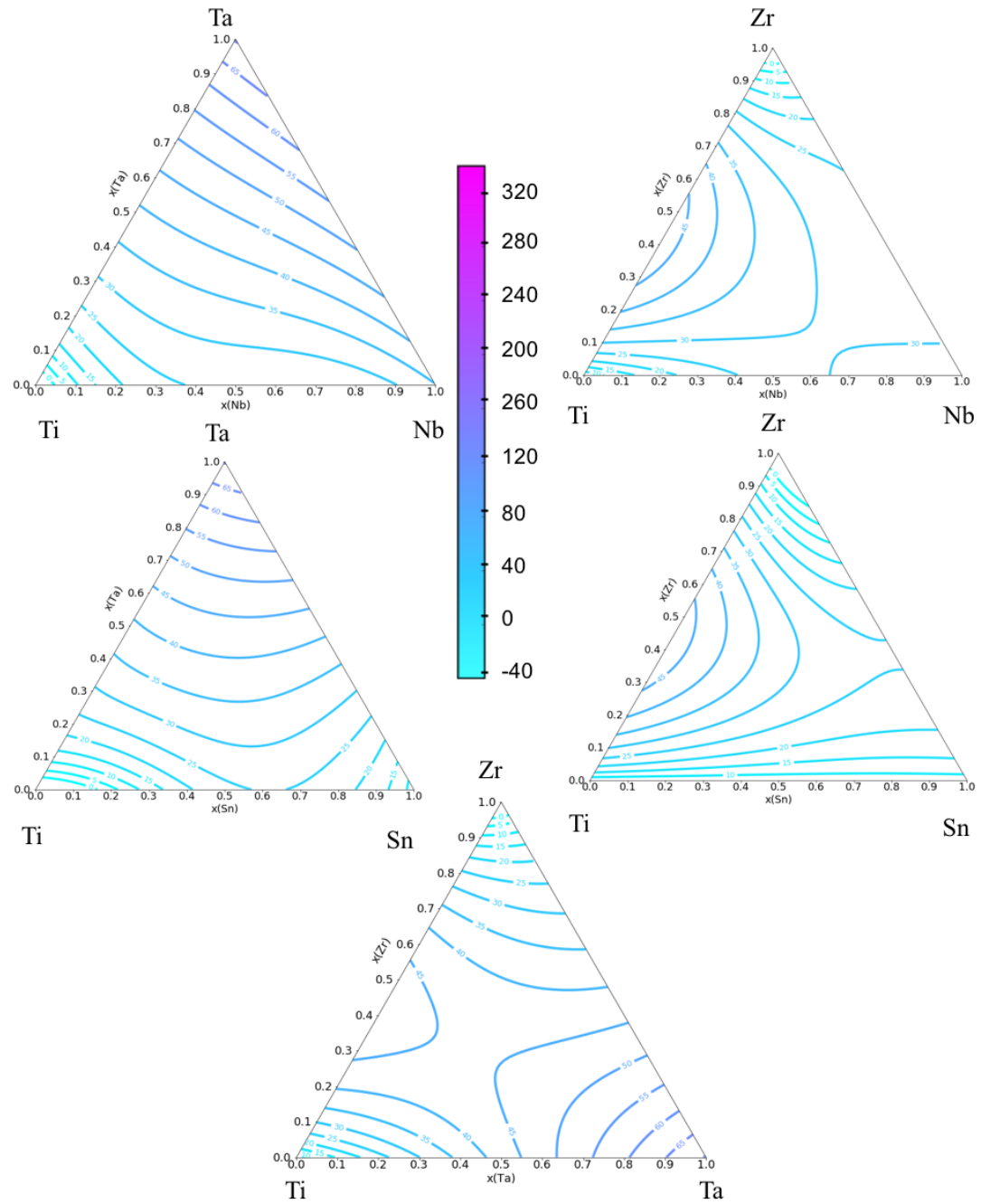


Figure 6.15: Shear modulus in GPa mapped as a function of composition for the Ti-Nb-Ta, Ti-Nb-Zr, Ti-Sn-Ta, Ti-Sn-Zr and Ti-Ta-Zr alloy systems using pycalphad [42].

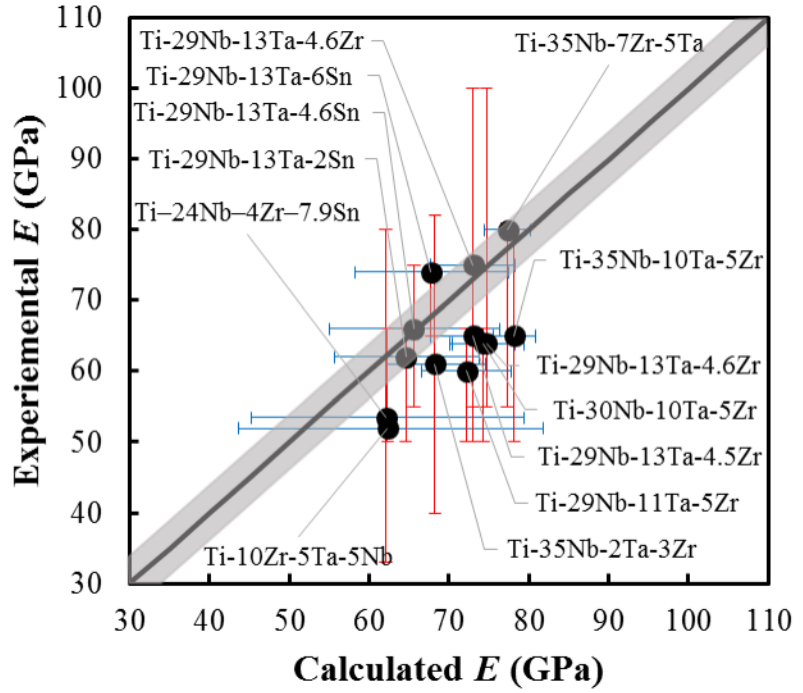


Figure 6.16: E of multicomponent bcc Ti alloys predicted from the database compared with measured experimental results. Vertical error bars plotted are from the variation in experimental data for given multi-component alloys, and horizontal error bars Voigt-Reuss bounds from the DFT-based first-principles. The grey region refers to the error introduced from the elastic stiffness coefficients in the first-principles calculations. More information on the alloys is Table 6.4 [37–39].

Chapter 7 |

Metastable phase study in the Ti-Ta and Ti-Nb systems

7.1 Introduction

The present chapter is aimed at studying the metastable phases ω and α'' in Ti-alloys. The first part of this work looked at the elastic properties of the metastable phases. As shown in Figures 1.1 and 1.2, the formation of the α'' and ω phases affects the elastic properties of Ti-Ta and Ti-Nb alloys. For Ti-Nb, the equilibrium calculation using the current database shows that the alloys will form either the single hcp or bcc phases or a two-phase mixture of bcc and hcp and does not have any modeling completed for the α'' phase. The second part of this work looks at improving the thermodynamic properties to predict the probability and formation of these phases. Understanding the effect of the metastable phases on the elastic properties and being able to predict at what compositions they form, will help with alloy design and increase the likelihood of finding a suitable alloy for load-bearing implants. The elastic properties of the four phases are calculated systematically and interaction parameters are introduced using the CALPHAD method, similar as described in chapter 5, to be able to predict the elastic properties as a function of composition. The stability of the bcc, hcp, ω , and α'' phases at 0 K is calculated and discussed for the Ti-Ta and Ti-Nb alloys using multiple structures across the entire composition range. The modeling of these four phases was then studied and in order to validate the modeling, elastic properties and transformation predicted, inelastic neutron scattering experiments were completed on 4 different Ti-Nb compositions.

The data from the experiments is used to determine the fraction of phases and phonon density of phases. The results from the neutron scattering were compared with the theoretical results.

7.2 Modeling and Calculations

In the present work, VASP [61] was employed to calculate the ground state energy and elastic properties of the pure elements and Ti-Nb and Ti-Ta systems in the bcc, hcp, ω , and α'' phases. The ion-electron interactions were described using the projector augmented wave (PAW) [62, 89] method and based on the previous work of comparing X-C functionals (Figure 5.1) the exchange-correlation functional of the generalized gradient approximation depicted by Perdew, Burke, and Ernzerhof (PBE-GGA) was employed [58]. The energy convergence criterion of the electronic self-consistency was set as 10^{-6} eV/atom. Independent structures based on the ATAT code [130] were generated for the four phases, bcc (330), hcp (21), α'' (33) and ω (73), across the entire composition range. The Brillouin zone sampling was done using the Γ -centered Monkhorst-Pack scheme [90]. The k-points grid for the hcp, ω and α'' phases were 10x10x13, 13x13x7, and 12x11x10, respectively. The k-point grids for the bcc calculations used the automated k-point mesh generator in VASP with the length of the subdivisions specified as 50. The elastic properties were then calculated using a ± 0.01 magnitude of strain.

The elastic stiffness coefficients were modeled using the results from the DFT-based first-principles calculations. The modeling was completed by the methodology outlined in chapter 2. The difference between the first-principles calculations and the linear combination from the pure elements was calculated and the fittings were completed using the code in appendix C. The best fit was found by comparing one interaction parameter or two interaction parameters. The moduli values were then calculated using pycalphad and the code in appendix D and E [42].

7.3 Results and discussion

7.3.1 Elastic properties

For the Ti-Nb system, the elastic stiffness coefficients of the bcc, hcp, α'' , and ω phases are calculated. The calculations and interaction parameters of the bcc phase are discussed in chapter 5. Figure 7.1 and 7.2 plot the elastic stiffness coefficients, c_{11} , c_{12} , c_{13} , c_{22} , c_{23} , c_{33} , c_{44} , c_{55} , and c_{66} , for the α'' phase. The plots show the first-principles results (circles), the linear combination from the pure elements (dashed red line) and the modeling prediction (solid line) using the interaction parameters in Table 7.1. Figure 7.1 shows a negative deviation from Vegard's law for the c_{11} , c_{22} and c_{33} elastic stiffness coefficients [131]. The c_{12} values show a positive deviation from Vegard's law while the c_{13} values show a positive deviation until approximately 50 at. % Nb when the values show a negative deviation from Vegard's law. Figure 7.2 shows that the c_{33} and c_{66} values have a negative deviation from Vegard's law. The c_{55} values show a negative deviation from Vegard's law until around 30 at. % Nb when the values begin to positively deviate. The c_{44} values show no deviation from Vegard's law [131].

Figure 7.3 plots the elastic stiffness coefficients, c_{11} , c_{12} , c_{13} , c_{33} , and c_{44} , for the ω phase. The plots show the first-principles results (circles), the linear combination from the pure elements (dashed red line) and the fitting (solid line) using the interaction parameters in Table 7.1. The c_{11} and c_{12} values show a negative deviation from Vegard's law while the c_{13} values show a positive deviation [131]. The c_{33} and c_{44} values show a negative deviation to start and then a positive deviation from Vegard's law.

Figure 7.4 plots the elastic stiffness coefficients, c_{11} , c_{12} , c_{13} , c_{33} , and c_{44} , for the hcp phase. The plots show the first-principles results (circles), the linear combination from the pure elements (dashed red line) and the fitting (solid line) using the interaction parameters in Table 7.1. The c_{11} values show a slight positive deviation and then a large negative deviation from Vegard's law while the c_{12} and c_{13} values show a negative deviation and then positive deviation from Vegard's law [131]. The c_{33} and c_{44} values show a negative deviation from Vegard's law.

The calculated elastic stiffness coefficients and E values are listed in Table 7.2. The Young's moduli values are calculated as a function of composition and are

plotted in Figure 7.5. The dotted lines are the modeling predictions calculated from the interaction parameters in Table 7.1. The calculations show that the Young's moduli for the hcp phase decrease (in value) from pure Ti (124 GPa) to pure Nb (-158 GPa). The Young's moduli, for the ω phase, follows a somewhat similar trend as the hcp phase. The E values, for the ω phase, decrease from pure Ti (152 GPa) to -163 GPa at 60 at. % Nb and then increase to 162 GPa at pure Nb. The E values for the bcc phase increase from -40 GPa at pure Ti to 98 GPa at pure Nb. The E values for the α'' phase decrease from 133 GPa at pure Ti to 82 GPa at 30 at. % Nb, then increase to 123 GPa at 80 at. % Nb and then decrease to 90 GPa at pure Nb. The E values for the hcp, ω , and bcc phases all become negative at certain compositions. Based on Born's criteria, a negative Young's modulus can indicate that the phase is not stable at that composition. From Figure 7.5 it can be seen that the E values of the α'' phase are higher than the E values of the hcp or bcc phases. This explains why the experimental Young's moduli increase in value with the formation of α , as seen in Figure 1.2.

Different authors experimentally determined the E of various Ti-Nb alloys at different compositions, as seen in Figure 1.2, [6, 8, 8, 9]. Ozaki et al. [7] showed that at certain compositions quenched Ti-Nb samples formed bcc and α'' while the slow cooled samples formed bcc and ω . For the quenched samples, there is more data available in the literature [6, 8, 8, 9], and therefore the present work averaged the E values obtained by different researchers for the same compositions. A full review of the experimental results is listed in appendix F and the averaged experimental values are listed in Table 7.3. From these experiments, some of the phase fractions were determined [8] and those phase fractions are listed in Table 7.3. For the compositions where the phase fractions were not determined, an extrapolation using the known phase fractions was used to estimate the unknown phase fractions. Those estimated phase fractions are differentiated from the experimentally determined phase fractions by labeling them with a *. Then, the rule of mixtures was used as a beginning estimate of the Young's moduli values based on these phase fractions and the interaction parameters in Table 7.1. The rule of mixtures is expressed by:

$$E_c = x_{p1}E_{p1} + x_{p2}E_{p2} \quad (7.1)$$

where x_{p1} and x_{p2} are the fractions of phase 1 and phase 2 and E_{p1} and E_{p2} are the E in phase 1 and phase 2, respectively. Based on the observations in the

literature [6,8,8,9], from pure Ti to 10 at. % Nb the samples are 100 % hcp and the predicted E vary, on average, from the experimental E by 3 GPa (Table 7.3). From 10 at. % Nb to 30 at. % Nb, the phase diagram predicts the hcp phase and bcc phase form. If the phase fractions of the hcp and bcc phase are taken from the phase diagram the values are off by 22 GPa from the experimentally determined values. However, this is the region that, experimentally, it was determined that the hcp phase is repressed and the α'' and bcc phase form. Using the phase fractions and rule of mixtures, for the bcc and α'' phases, the predicted E vary, on average, from the experimental E by 0.52 GPa, shown in Table 7.3. Above 33 at. % Nb the samples consist of the single bcc phase. The predicted E vary, on average, by 7 GPa from the experimental E (Table 7.3). Overall, the variances are small when compared to the variances in the experiments. As seen in appendix F, the experimental E values of pure Ti in the hcp phase vary by 24 GPa. The variance between the predicted E and experimental E can be partially attributed to the fact that the predicted E are at 0 K and the experimental E are measured at 300 K. It is evident that the database can be used, with the rule of mixtures, to accurately predict the elastic properties of Ti-Nb alloys if the phase fraction of the metastable phases can be predicted.

7.3.2 First-principles calculations at 0 K

With the elastic properties database accurate, the attention turned to improving the modeling predictions of the four phases. The formation energy of the phases at 0 K is calculated as a function of composition for the Ti-Nb and Ti-Ta systems. Figure 7.6 and 7.7 show the formation energy of the bcc, hcp, ω , and α'' phases from 100 at. % Ti to 100 at. % Nb or Ta at 0 K. The formation energies are calculated according to Eq. 2.7 using the ground state energies of the pure elements in the SER state as reference. More calculations in the bcc phase are being completed for the Ti-Nb system. The figures show that the formation energy of the hcp phase starts at 0 at pure Ti and then increases to 28 kJ/mol-atom at pure Nb or 27 kJ/mol-atom at pure Ta. The bcc phase starts with a higher formation energy at pure Ti (10 kJ/mol-atom) and then decreases to 0 kJ/mol-atom at pure Nb or Ta. The hcp phase has a lower formation energy to 30 at. % Nb or Ta when the bcc phase has a lower formation energy. The specific ω and α'' structures have similar

formation energies to the hcp and bcc phase from Ti to around 80 at. % Nb or Ta. This points to the need to study the finite temperature properties of the phases.

7.3.3 Neutron scattering results

In order to study the phase fractions, elastic properties and transformations occurring, four Ti-Nb alloys were measured using the ARCS neutron scattering instrument at the Spallation Neutron Source, Oak Ridge National Laboratory. As discussed in the methodology, two sets of samples were made. Each set contains a Ti-Nb alloy at the following compositions: 10, 12, 18, 20 at. % Nb. The two sets of samples were annealed at 1273 K for 24 hours. One set of samples was quenched in cold water to form the bcc and α'' phases while the second set of samples was slow cooled to form the bcc and ω phases. The neutron scattering was planned to be studied at 300, 500, 900 and 1110 K. These temperatures were chosen based on the work done by Kim et al. [132], which experimentally determined the martensitic transformation temperature for Ti-Nb alloys between 20 and 30 at. % Nb, plotted on the phase diagram shown in Figure 7.8. The temperature chosen will allow all the samples to pass through the martensitic temperature at each composition. The temperature dependence of the phonon DOS will provide information about the type of transformation taking place and the diffraction patterns will help to look at how the phase fractions change as a function of temperature. However, due to instrumental issues only the data at 300 K will be discussed here.

7.3.3.1 Phonon density of states at 300 K

In Figure 7.9, 7.10, 7.11, 7.12 the phonon density of states (DOS) at 300 K is plotted for each sample. The samples at the same compositions are plotted on the same figure for comparison. The phonon DOS of the slow cooled samples are plotted as dashed lines and the phonon DOS of the quenched samples are plotted as solid lines. It can be seen that the quenched samples show different phonon DOS compared with the slow cooled samples, which means that the samples have different phases. In some cases, the differences are not as large as expected. This is being investigated and could point to the quench not cooling the samples fast enough and the α'' phase not fully forming. In order to investigate the difference of the phonon DOS further the entropy of each sample is calculated from the phonon

DOS ($Z(\varrho)$):

$$S_{vib} = 3k_B \int_0^{E_{max}} [(n+1) \ln(n+1) - n \ln(n)] Z(\varrho) dZ \quad (7.2)$$

where n is the Bose-Einstein occupation factor [133]. The entropy difference between the alloys at the same compositions is plotted in 7.13. The figure shows that the entropy difference is less than 0.02 kB/atom between the two 10 at. % Nb samples. The entropy difference then increases to less than 0.03 between the two 12 at. % Nb samples and less than 0.06 between the two 18 at. % Nb samples. Finally, the entropy difference between the two 20 at. % Nb samples reaches a peak close to 0.1 kB/atom. This would result in a 30 kB/atom free energy difference between the samples. Further investigations on these samples are necessary to understand and explain this observation.

7.3.3.2 Diffraction patterns at 300 K

The diffraction patterns for each alloy are plotted in Figure 7.14, 7.15, 7.16, and 7.17. The slow cooled samples are plotted as solid lines and the quenched samples are plotted as dashed lines. The diffraction patterns plot the intensity vs. momenta (Q). The plots are compared with diffraction patterns of Ti and Nb in the four phases from the literature to determine an approximation of the phase fractions, which are listed in Table 7.4. It can be seen that the fractions of the bcc phase of the quenched samples are 0.12, 0.20, 0.57 and 0.70 for the samples containing 10, 12, 18 and 20 at. % Nb, respectively. The slow cooled samples showed a fraction of the bcc phase of 0.2, 0.3, 0.6, and 0.7 for the samples containing 10, 12, 18, and 20 at. % Nb, respectively. The phase fractions of the quenched samples with 10 and 20 at. % Nb compare well with the fractions determined by Friak et al. [8], as shown in Table 7.3.

The modeling of the ω phase has been started by Zhang et al. [19] but the α'' phase has not been modeled. The modeling of the ω phase is shown in Figure 7.18. When the hcp phase is suspended the ω phase is present. However, when comparing the phase fractions from the experiments to the modeling of the ω phase, there are some discrepancies as shown in Table 7.5 and thus the modeling needs to be further improved. The partition function approach, methodology in appendix F, is also being studied to be able to predict the probability that the phases form

and to more accurately predict the finite temperature properties of the bcc phase which is theorized to be a combination of multiple states.

7.4 Conclusion

The present study systematically calculated the elastic stiffness coefficients and Young's moduli of the Ti-Nb system in the bcc, hcp, ω , and α'' phases. The general CALPHAD modeling approach was used to fit binary interaction parameters. The E values were similar for the hcp and ω phases, which is reasonable since they both have hexagonal symmetry. The α'' phase has E values that were higher than the other three phases which explains why the E increases when the α'' phase forms. Experiments showed that up to 10 at. % Nb the samples formed solely the hcp phase and the database predicted the E values by an average variance of 3 GPa from the averaged E . The samples from 10 at. % Nb to 30 at. % Nb formed the bcc and α'' or ω phases. If the samples were slow cooled they form the bcc and ω phases. If the samples were quenched they form the bcc and α'' phases. Using experimentally determined phase fractions and the rule of mixtures, the database accurately predicted the E values by an average variance of 0.52 GPa when compared with the averaged E values. At Nb concentrations greater than 30 at. % Nb samples form solely the bcc phase and the database predicted the E values by an average variance of 7 GPa from the averaged E values.

The phonon DOS of the slow cooled samples and the quenched samples were plotted together for the same compositions and showed differences that were expected for the samples having different phases. This difference was also seen when looking at the entropy difference between the two samples. The entropy difference between the quenched and slow cooled samples increased from 10 at. % Nb to 20 at. % Nb. This increase in entropy difference must be investigated further in order to understand this observation. Using the diffraction patterns, the phase fractions in each sample were approximated.

The future work will include determining the elastic properties of the four Ti-Nb alloy samples made and compare the results to the elastic database. The temperature dependence of the phonon DOS will be completed to understand the effects on the bcc phase close to the transformation. The results from the DFT-based first-principles calculations will be used to accurately model the four

phases. The partition function approach will be used to more accurately model the finite temperature properties of the bcc phase and to predict the probability of the metastable phase formation.

Table 7.1: Evaluated interaction parameters L_0 and L_1 , using Eq. 2.32, for the elastic stiffness coefficients of the hcp, α'' and ω phases in the Ti-Nb systems.

Alloy	Interaction Parameter	α''	hcp	ω
c_{11}	L_0	-102.443	-298.443	-142.979
	L_1	606.748	-588.702	159.767
c_{12}	L_0	97.3105	-45.4449	-888.25
	L_1	-186.214	224.369	-1074.08
c_{13}	L_0	-11.5368	143.819	349.337
	L_1	-307.745	250.29	275.297
c_{22}	L_0	-100.063	N/A	N/A
	L_1	355.649	N/A	N/A
c_{23}	L_0	-75.1048	N/A	N/A
	L_1	283.22	N/A	N/A
c_{33}	L_0	-468.983	-143.313	-100.909
	L_1	-114.152	-77.5489	733.448
c_{44}	L_0	14.125	-43.0296	263.258
	L_1	-	-91.4667	475.336
c_{55}	L_0	204.71	N/A	N/A
	L_1	479.179	N/A	N/A
c_{66}	L_0	-59.1357	N/A	N/A
	L_1	139.625	N/A	N/A

Table 7.2: Results of the first-principles calculations of the elastic stiffness coefficients in GPa for different atomic percent compositions in the α'' , bcc, hcp, and ω phases in the Ti-Nb system at 0 K.

$Ti_{1-b}Nb_b$	c_{11}	c_{12}	c_{13}	c_{22}	c_{23}	c_{33}	c_{44}	c_{55}	c_{66}
α''									
Ti	198	69	84	197	84	189	40	40	63
$Ti_{0.97}Nb_{0.03}$	106	112	123	152	45	138	25	17	38
$Ti_{0.87}Nb_{0.13}$	171	88	105	171	67	170	47	13	43
$Ti_{0.06}Nb_{0.94}$	307	94	119	248	143	214	31	-24	13
$Ti_{0.03}Nb_{0.97}$	307	88	115	232	124	284	59	-58	8
$Ti_{0.02}Nb_{0.98}$	293	88	115	232	124	284	59	-58	8
Nb	306	88	125	240	135	284	47	-69	9
bcc									
Ti	93	115	-	-	-	-	41	-	-
$Ti_{0.98}Nb_{0.02}$	93	115	-	-	-	-	35	-	-
$Ti_{0.87}Nb_{0.13}$	116	116	-	-	-	-	37	-	-
$Ti_{0.75}Nb_{0.25}$	140	116	-	-	-	-	34	-	-
$Ti_{0.50}Nb_{0.50}$	181	121	-	-	-	-	31	-	-
$Ti_{0.25}Nb_{0.75}$	208	130	-	-	-	-	15	-	-
$Ti_{0.06}Nb_{0.94}$	242	134	-	-	-	-	18	-	-
$Ti_{0.02}Nb_{0.98}$	242	134	-	-	-	-	18	-	-
Nb	245	144	-	-	-	-	27	-	-
hcp									
Ti	175	88	80	-	-	190	41	-	-
$Ti_{0.98}Nb_{0.02}$	79	-44	-38	-	-	73	45	-	-
$Ti_{0.75}Nb_{0.25}$	156	113	104	-	-	200	13	-	-
$Ti_{0.50}Nb_{0.50}$	124	151	135	-	-	185	-19	-	-
$Ti_{0.25}Nb_{0.75}$	76	213	156	-	-	173	-61	-	-
$Ti_{0.06}Nb_{0.94}$	15	289	177	-	-	163	-104	-	-
$Ti_{0.02}Nb_{0.98}$	34	280	185	-	-	145	-106	-	-
Nb	24	18	11	-	-	25	-6	-	-
ω									
Ti	194	87	61	-	-	246	54	-	-

Table 7.2: Results of the first-principles calculations of the elastic stiffness coefficients in GPa for different atomic percent compositions in the α'' , bcc, hcp, and ω phases in the Ti-Nb system at 0 K.

Ti _{1-b} Nb _b	c ₁₁	c ₁₂	c ₁₃	c ₂₂	c ₂₃	c ₃₃	c ₄₄	c ₅₅	c ₆₆
Ti _{0.98} Nb _{0.02}	187	87	63	-	-	250	50	-	-
Ti _{0.87} Nb _{0.13}	171	89	83	-	-	165	30	-	-
Ti _{0.06} Nb _{0.94}	240	90	142	-	-	234	-22	-	-
Ti _{0.02} Nb _{0.98}	242	88	120	-	-	270	-5	-	-
Nb	243	181	110	-	-	212	-55	-	-

Table 7.3: Phase fractions and experimentally determined E (averaged from the data in appendix F [6, 8, 8, 9]) compared with the predicted E using the rule of mixtures and interaction parameters in Table 7.1 for the Ti-Nb system. The * denotes the estimated phase fractions as opposed to the experimentally determined phase fractions with no *.

x(Nb)	Phase Fraction	Expt E	Calc E
0.00	all hcp	118.31	123.8
0.01	all hcp	112.52	115.9
0.02	all hcp	108.33	108.8
0.05	all hcp	79.47	88.2
0.08	all hcp	66.41	69.9
0.09	all hcp	68.73	64.3
0.10	0.06 BCC/0.94 α''	84.64	95.89
0.11	0.15 BCC/0.85 α''^*	78.72	88.19
0.18	0.45 BCC/0.55 α''^*	93.02	70.08
0.19	0.49 BCC/0.51 α''^*	64.26	68.65
0.20	0.60 BCC/0.40 α''	77.62	65.74
0.22	0.63 BCC/0.37 α''^*	70.90	67.44
0.23	0.67 BCC/0.33 α''^*	75.85	67.00
0.24	0.71 BCC/0.29 α''^*	61.11	66.63
0.25	0.81 BCC/0.19 α''	72.52	66.10
0.26	0.80 BCC/0.20 α''^*	66.61	66.23
0.27	0.84 BCC/0.16 α''^*	54.61	66.98
0.29	0.91 BCC/0.09 α''^*	62.13	66.16
0.30	0.90 BCC/0.10 α''	68.11	68.21
0.34	all bcc	77.47	66.69
0.36	all bcc	73.78	69.00
0.39	all bcc	76.62	69.81
0.43	all bcc	84.05	69.77

Table 7.4: Phase fractions determined from the diffraction patterns for the Ti-Nb alloys.

Alloy	x(Nb)	Phase Fraction		
		bcc	ω	α''
Quenched	0.10	0.12	-	0.88
	0.12	0.20	-	0.80
	0.18	0.57	-	0.43
	0.20	0.70	-	0.30
Slow Cooled	0.10	0.20	0.80	-
	0.12	0.30	0.70	-
	0.18	0.60	0.40	-
	0.20	0.70	0.30	-

Table 7.5: Phase fractions determined from the diffraction patterns and the current phase diagram modeling for the bcc and ω phase in the Ti-Nb system.

x(Nb)	Phase Fraction			
	Experimental		Modeling	
	bcc	ω	bcc	ω
0.10	0.20	0.80	0.10	0.90
0.12	0.30	0.70	0.12	0.88
0.18	0.60	0.40	0.18	0.82
0.20	0.70	0.30	0.20	0.80

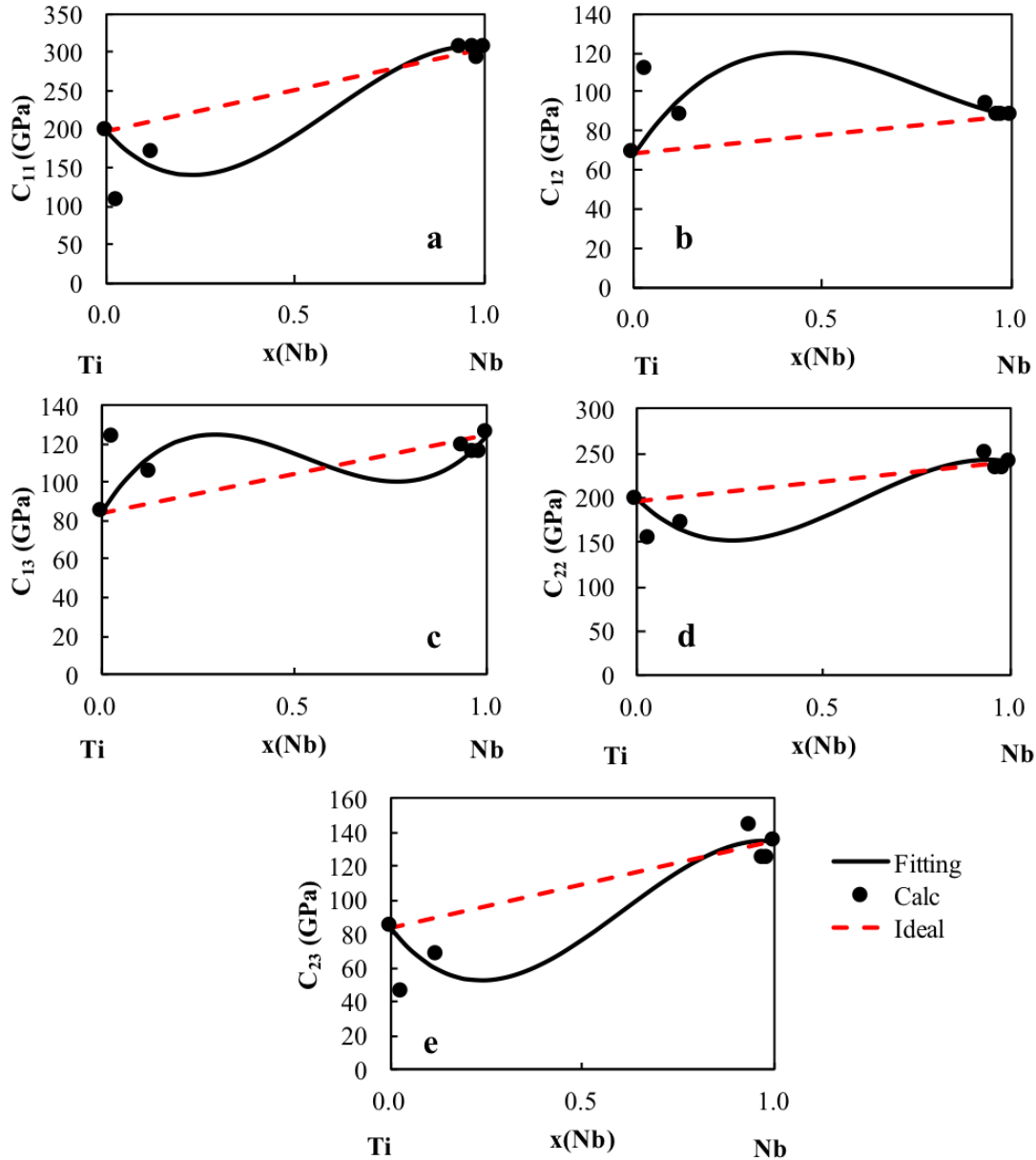


Figure 7.1: Calculated c_{11} , c_{12} , c_{13} , c_{22} , and c_{23} values (circles) plotted with the linear combination of the pure elements (red dashed line) and the present modeling (black solid line) for five of the elastic stiffness coefficients of Ti-Nb in the α'' phase.

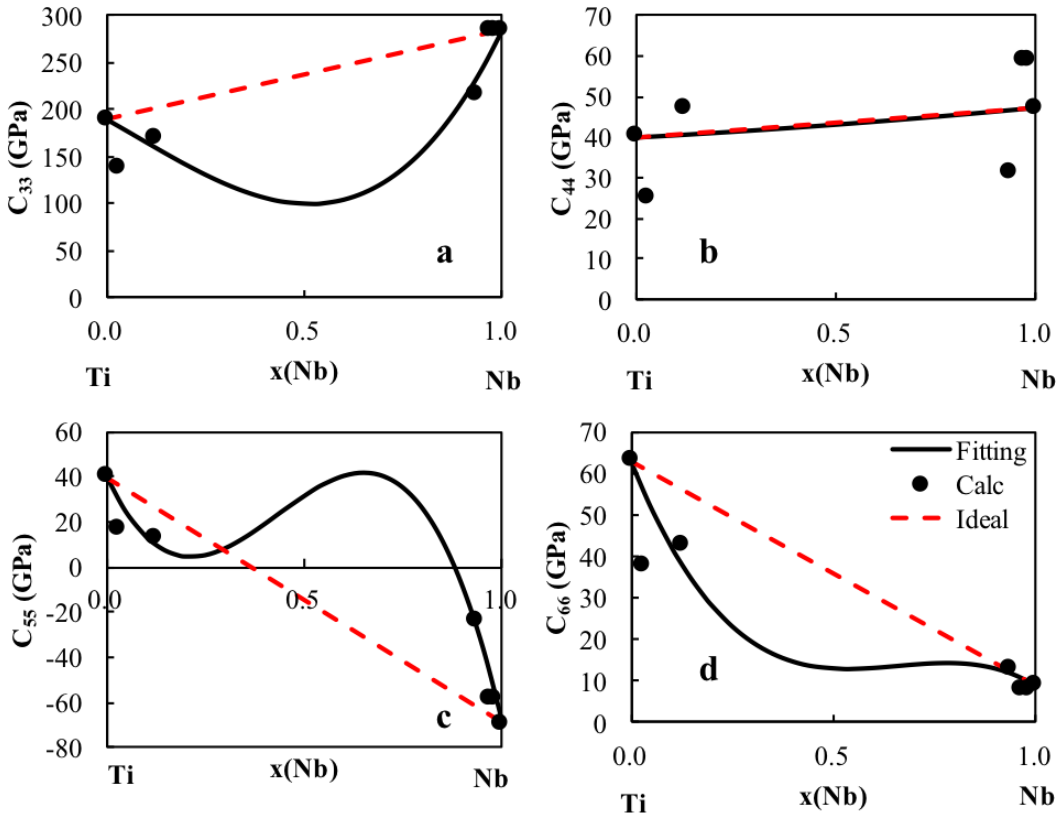


Figure 7.2: Calculated c_{33} , c_{44} , c_{55} , and c_{66} values (circles) plotted with the linear combination of the pure elements (red dashed line) and the present modeling (black solid line) for four of the elastic stiffness coefficients of Ti-Nb in the α'' phase.

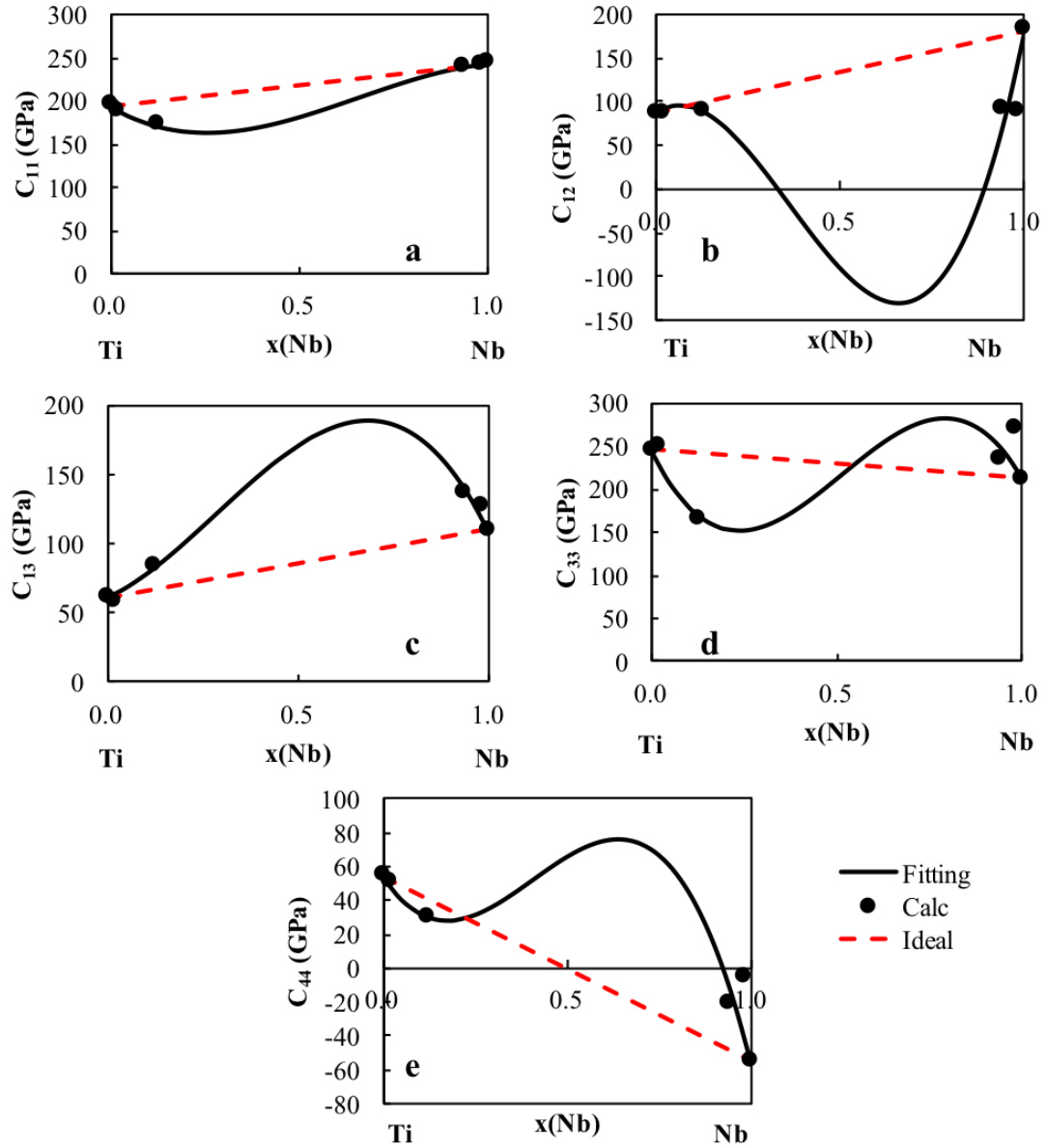


Figure 7.3: Calculated c_{11} , c_{12} , c_{13} , c_{33} , and c_{44} values (circles) plotted with the linear combination of the pure elements (red dashed line) and the present modeling (black solid line) for the elastic stiffness coefficients of Ti-Nb in the ω phase.

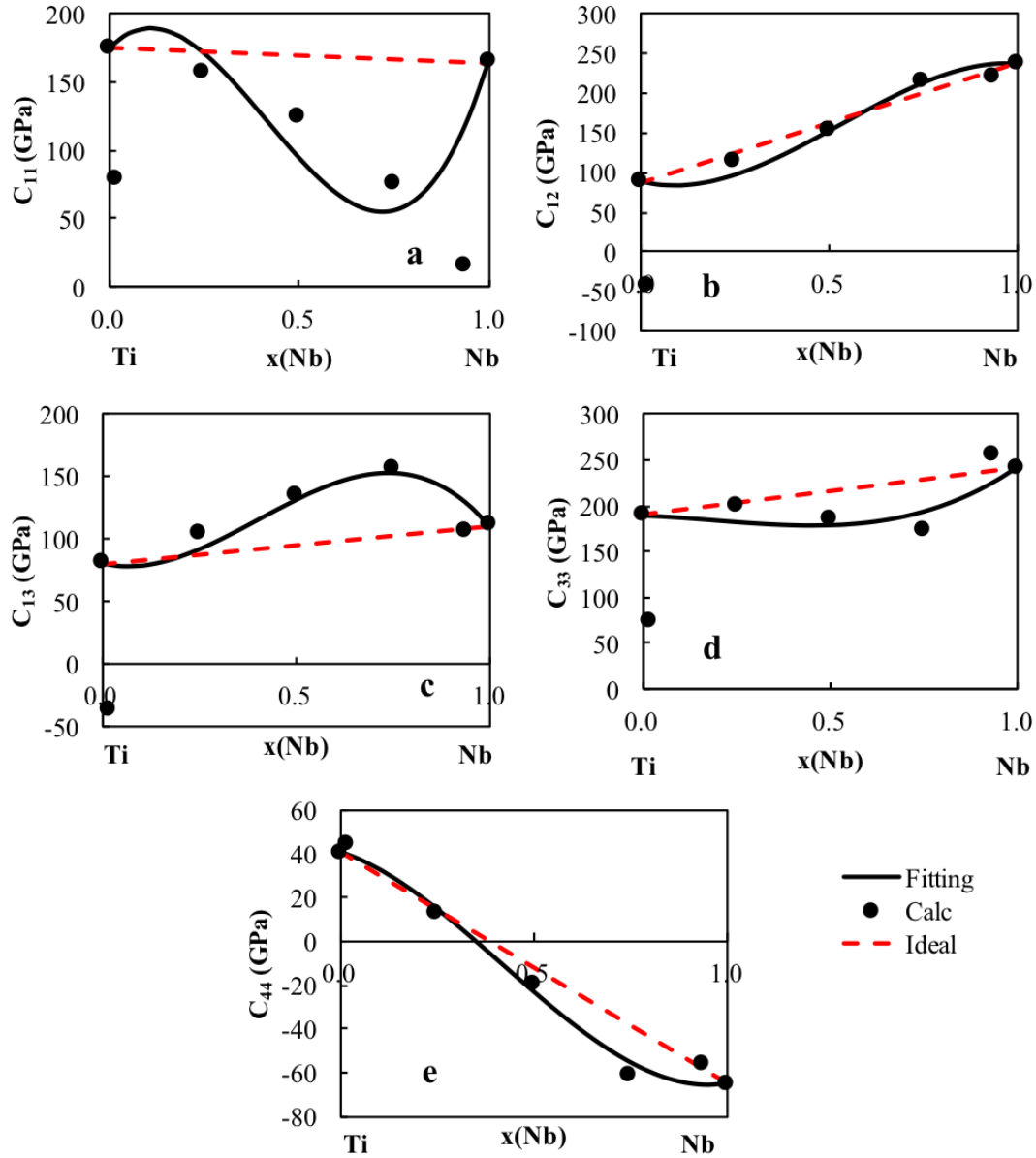


Figure 7.4: Calculated c_{11} , c_{12} , c_{13} , c_{33} , and c_{44} values (circles) plotted with the linear combination of the pure elements (red dashed line) and the present modeling (black solid line) for the elastic stiffness coefficients of Ti-Nb in the hcp phase.

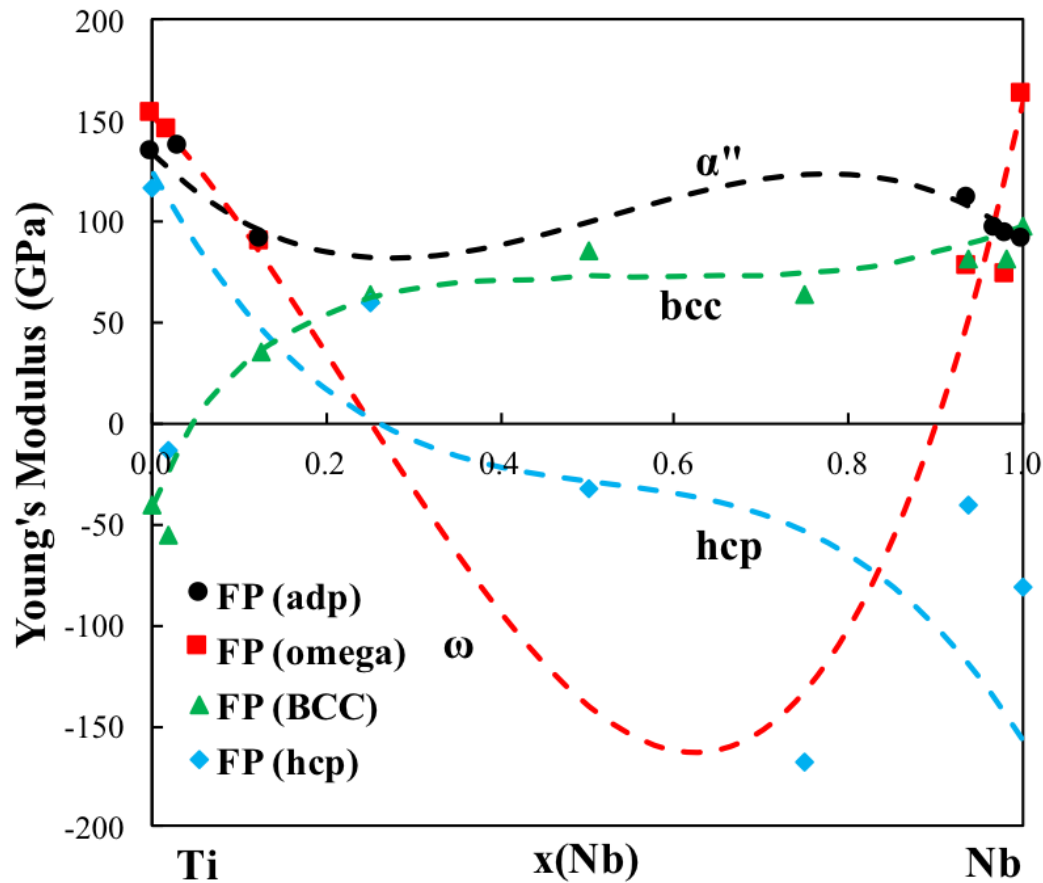


Figure 7.5: Elastic properties of the bcc, hcp, ω , α'' phases in the Ti-Nb system calculated from first-principles based on DFT are plotted as symbols. The CALPHAD fittings are plotted as the dashed lines. The figure is plotted from pure Ti to pure Nb.

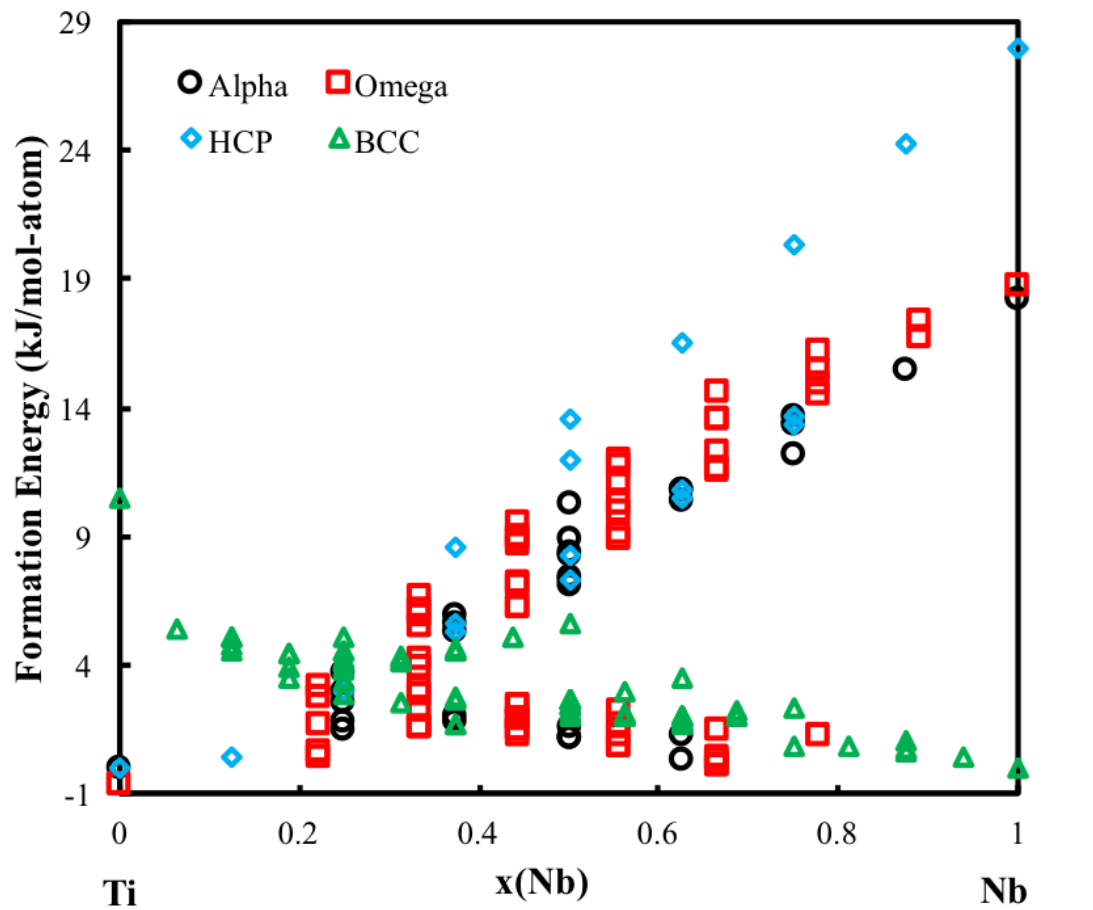


Figure 7.6: Formation energies of the bcc, hcp, ω , α'' phases in the Ti-Nb system are plotted from pure Ti to pure Nb.

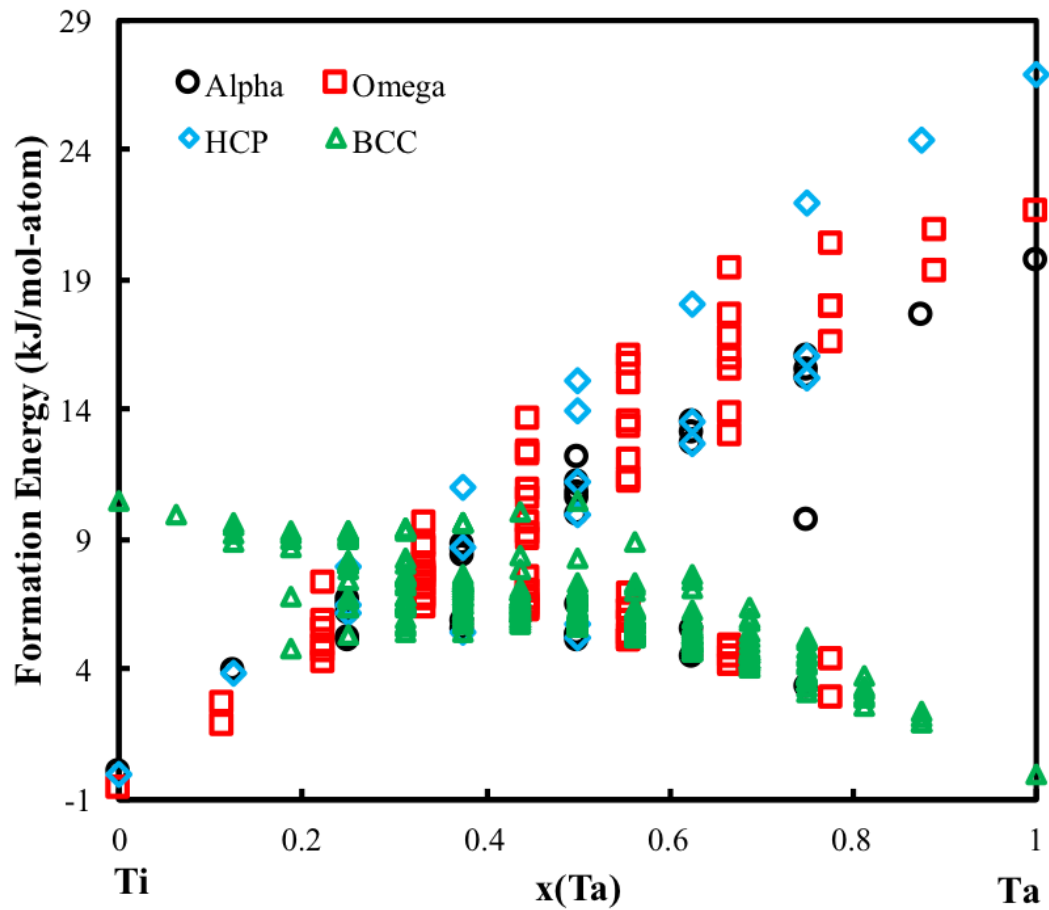


Figure 7.7: Formation energies of the bcc, hcp, ω , α'' phases in the Ti-Ta system are plotted from pure Ti to pure Ta.

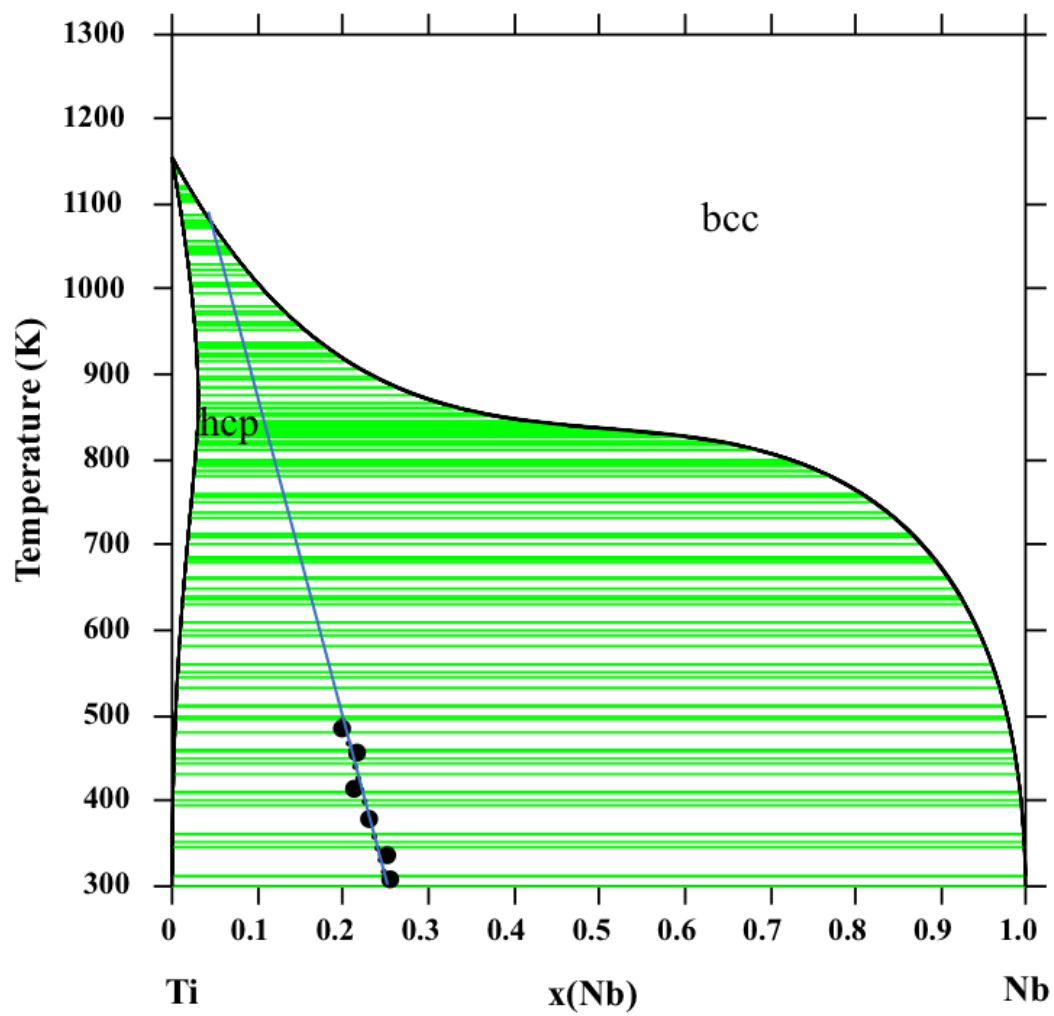


Figure 7.8: Martensitic transformation temperature is plotted versus the Ti-Nb composition.

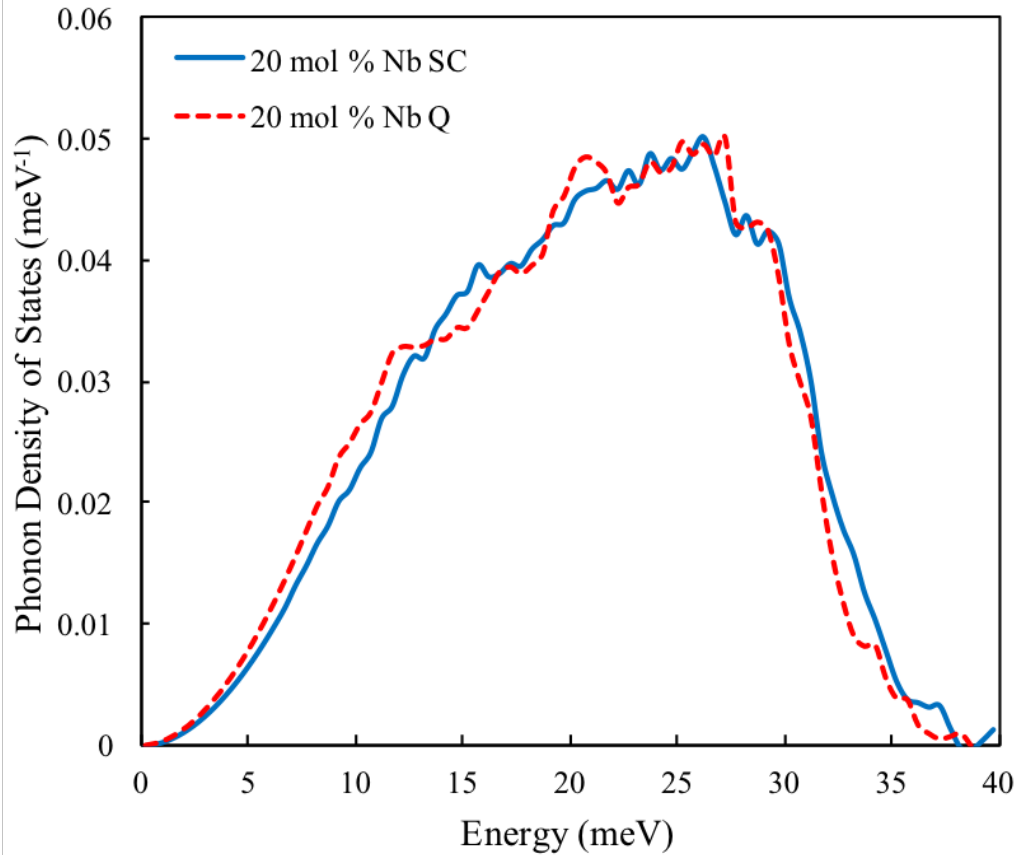


Figure 7.9: Phonon density of states for the Ti-Nb alloy at 20 at. % Nb. The dashed line represents the slow cooled sample while the solid line represents the quenched sample.

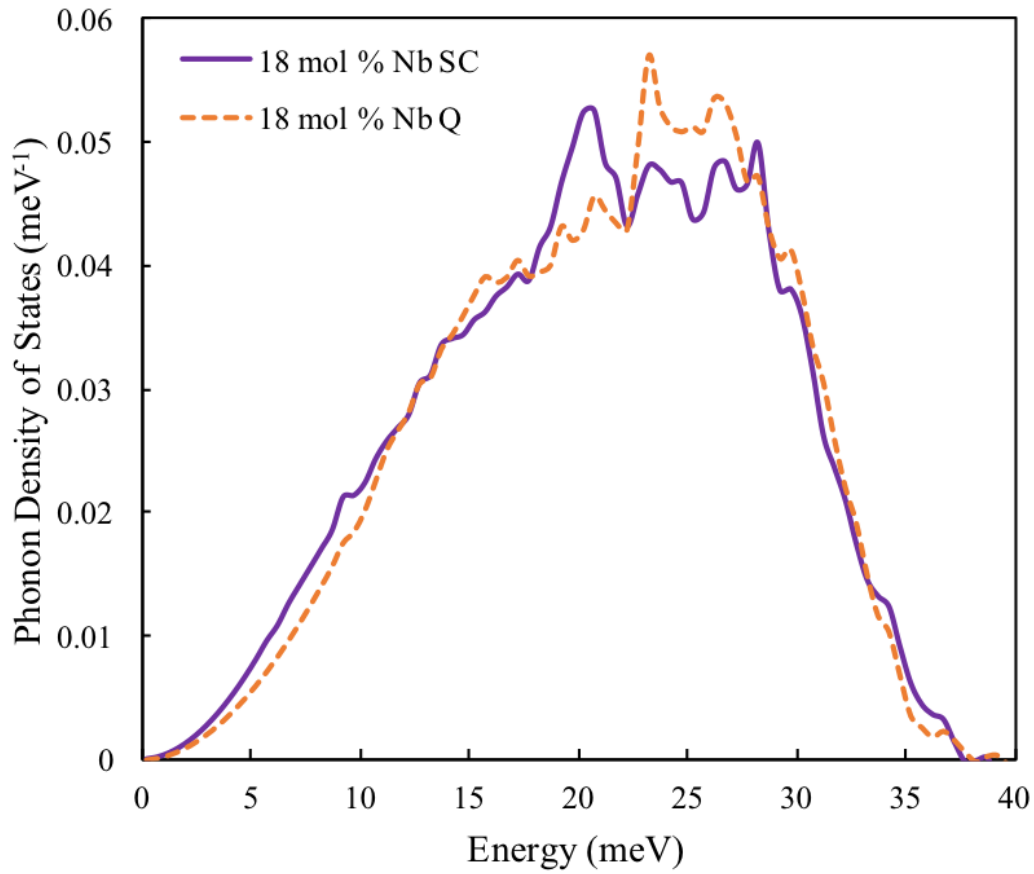


Figure 7.10: Phonon density of states for the Ti-Nb alloy at 18 at. % Nb. The dashed line represents the slow cooled sample while the solid line represents the quenched sample.

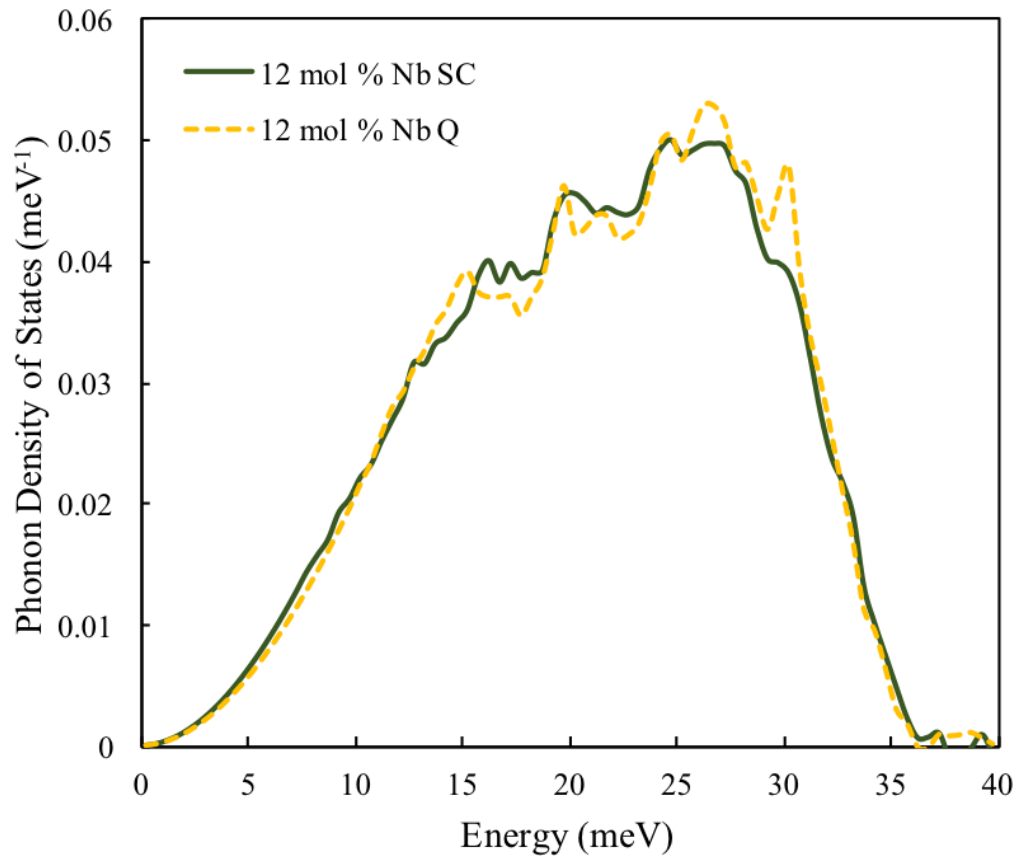


Figure 7.11: Phonon density of states for the Ti-Nb alloy at 12 at. % Nb. The dashed line represents the slow cooled sample while the solid line represents the quenched sample.

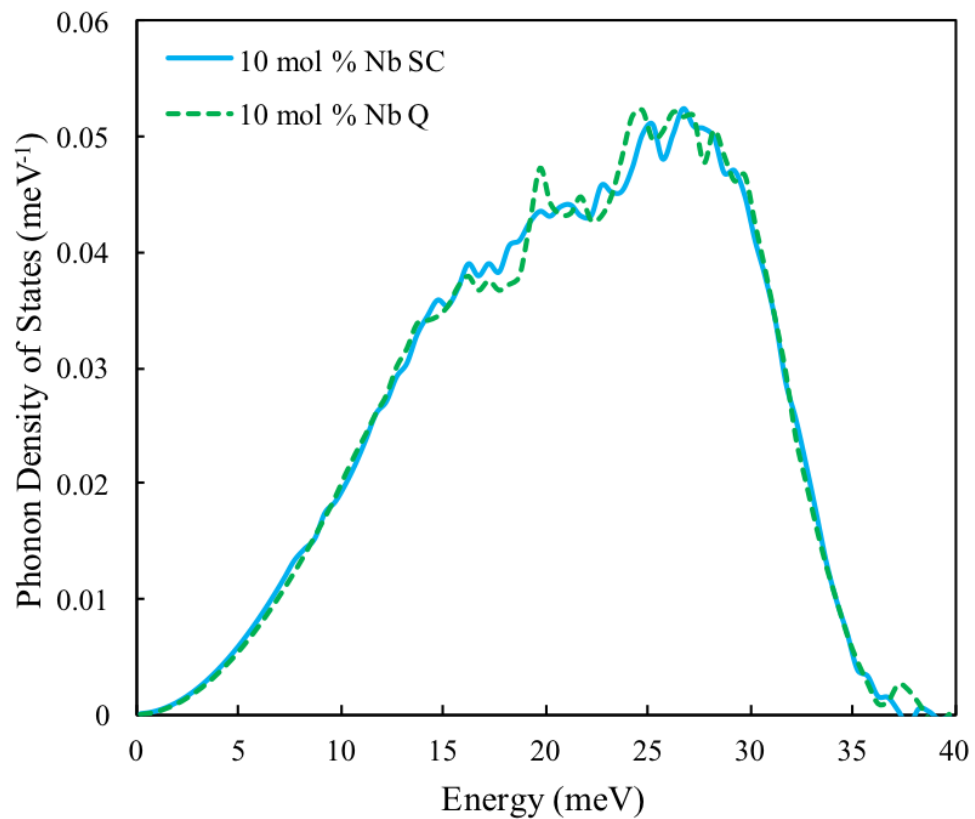


Figure 7.12: Phonon density of states for the Ti-Nb alloy at 10 at. % Nb. The dashed line represents the slow cooled sample while the solid line represents the quenched sample.

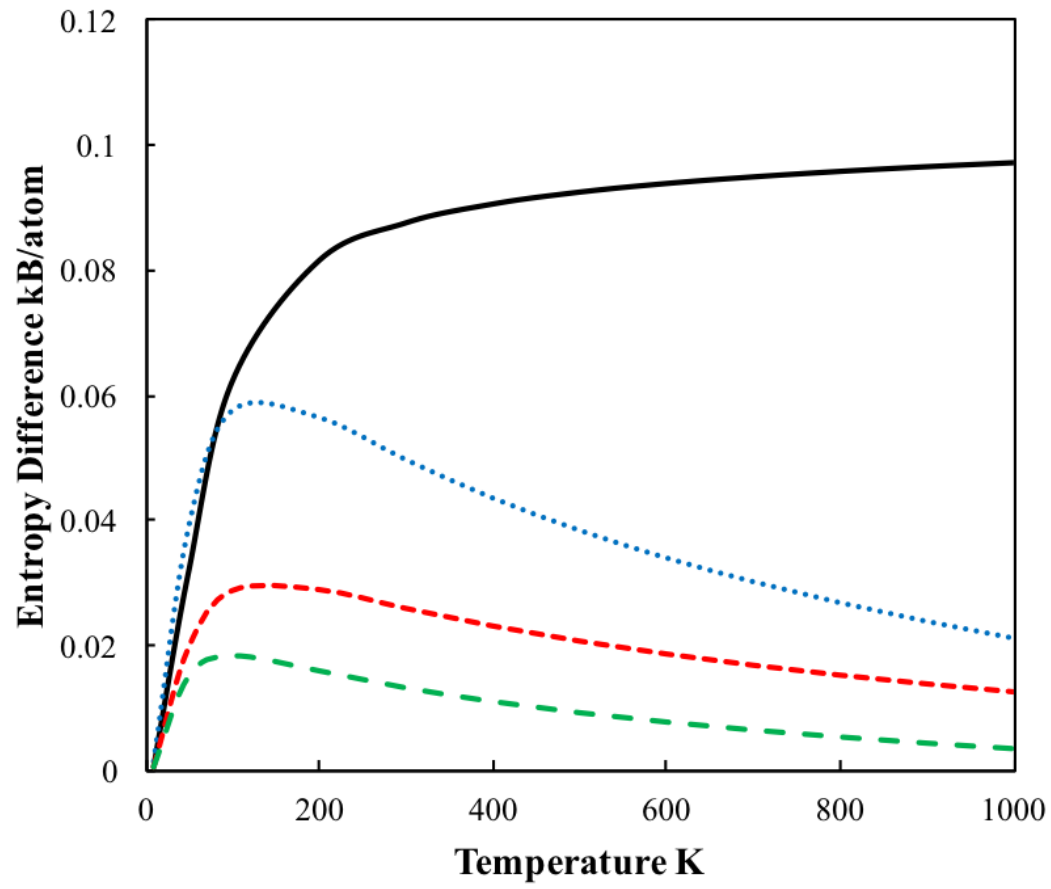


Figure 7.13: Entropy difference between the Ti-Nb alloys with the same alloy composition as a function of temperature.

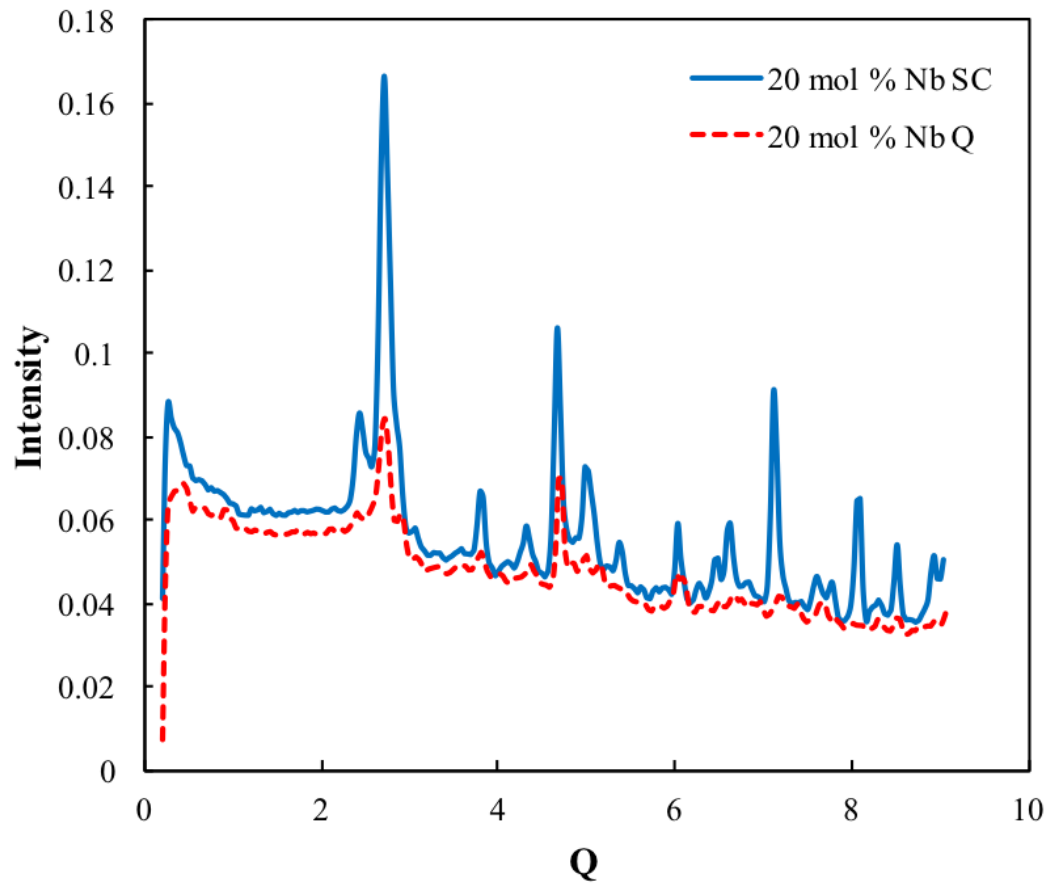


Figure 7.14: Diffraction pattern of the Ti-Nb alloy at 20 at. % Nb. The dashed line represents the slow cooled sample while the solid line represents the quenched sample.

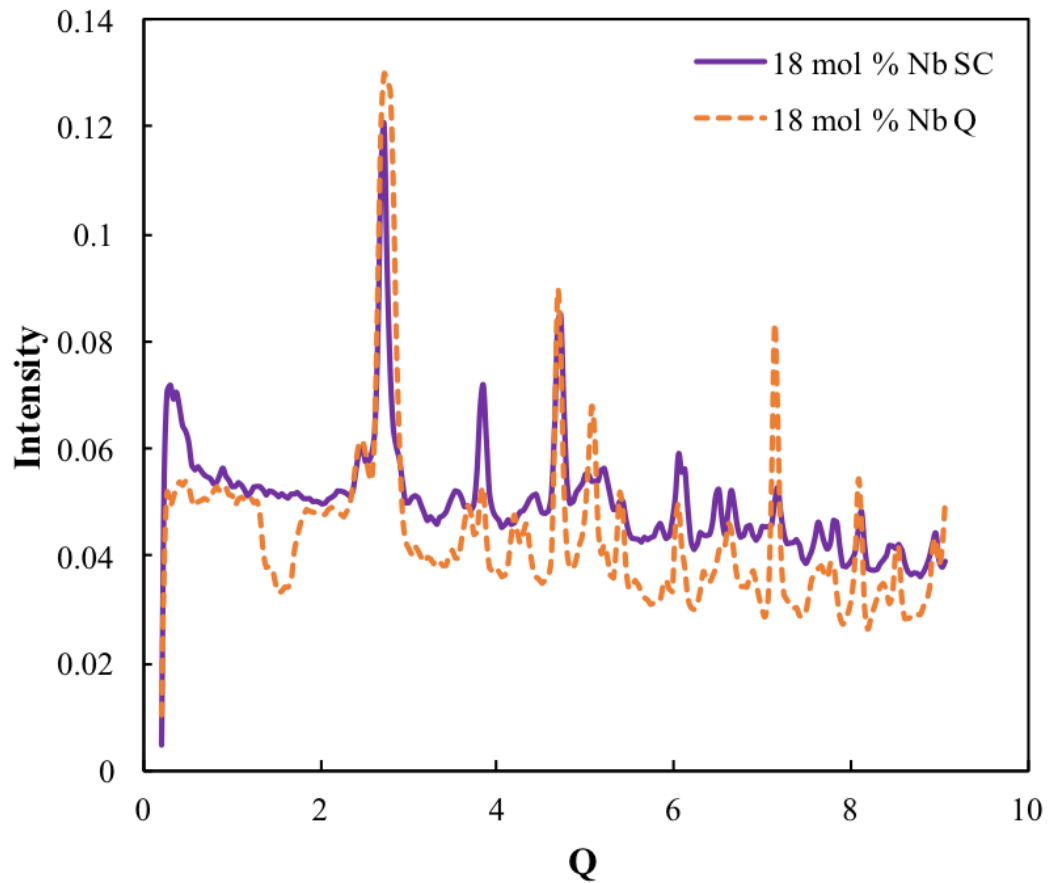


Figure 7.15: Diffraction pattern of the Ti-Nb alloy at 18 at. % Nb. The dashed line represents the slow cooled sample while the solid line represents the quenched sample.

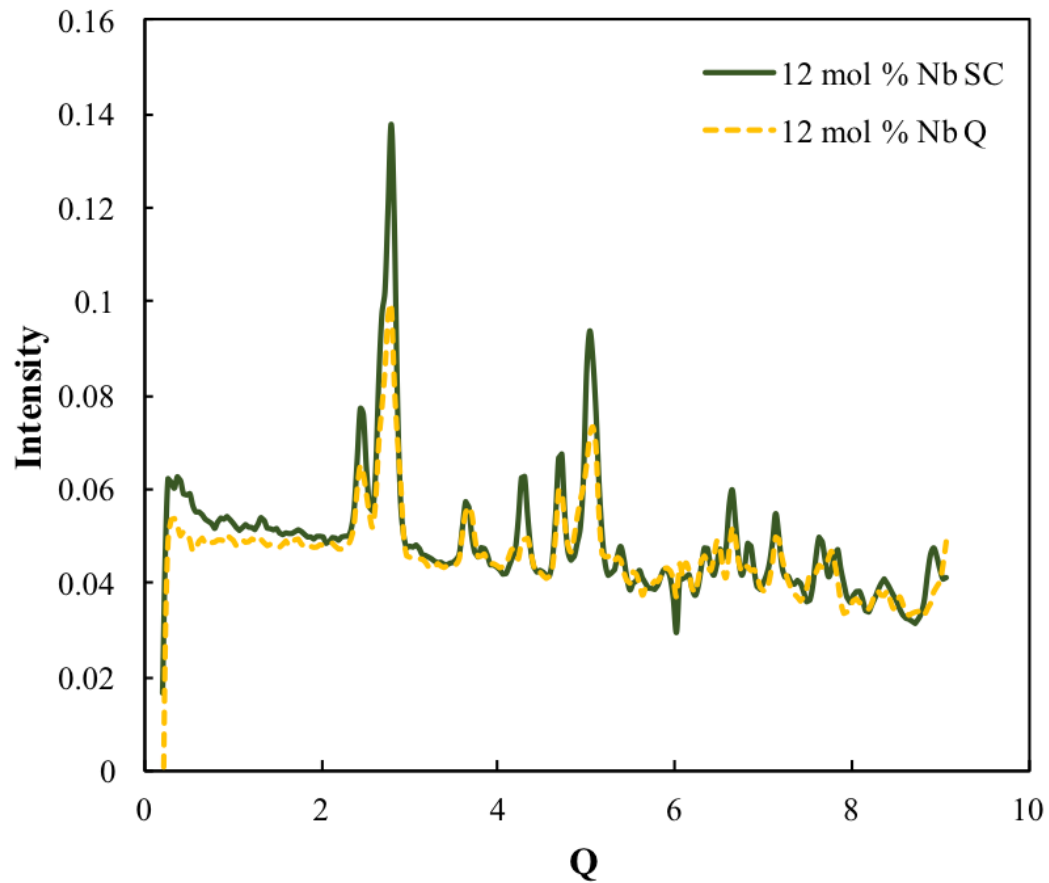


Figure 7.16: Diffraction pattern of the Ti-Nb alloy at 12 at. % Nb. The dashed line represents the slow cooled sample while the solid line represents the quenched sample.

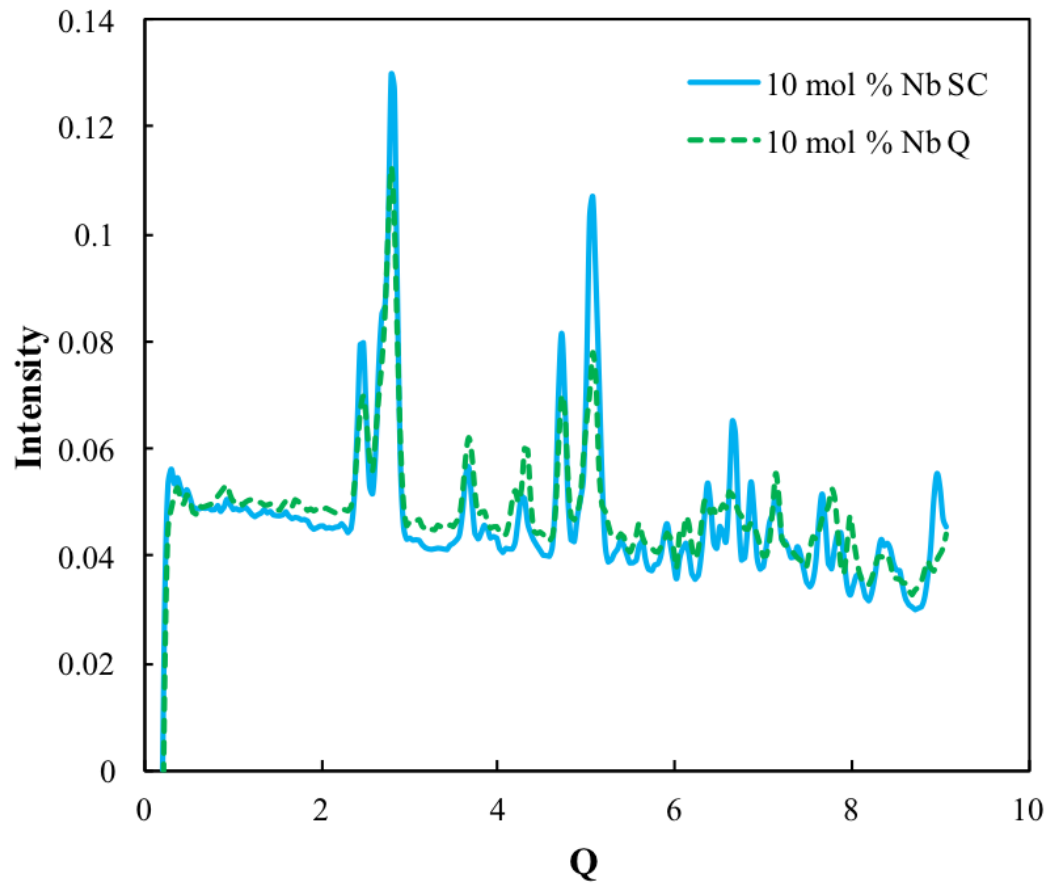


Figure 7.17: Diffraction pattern of the Ti-Nb alloy at 10 at. % Nb. The dashed line represents the slow cooled sample while the solid line represents the quenched sample.

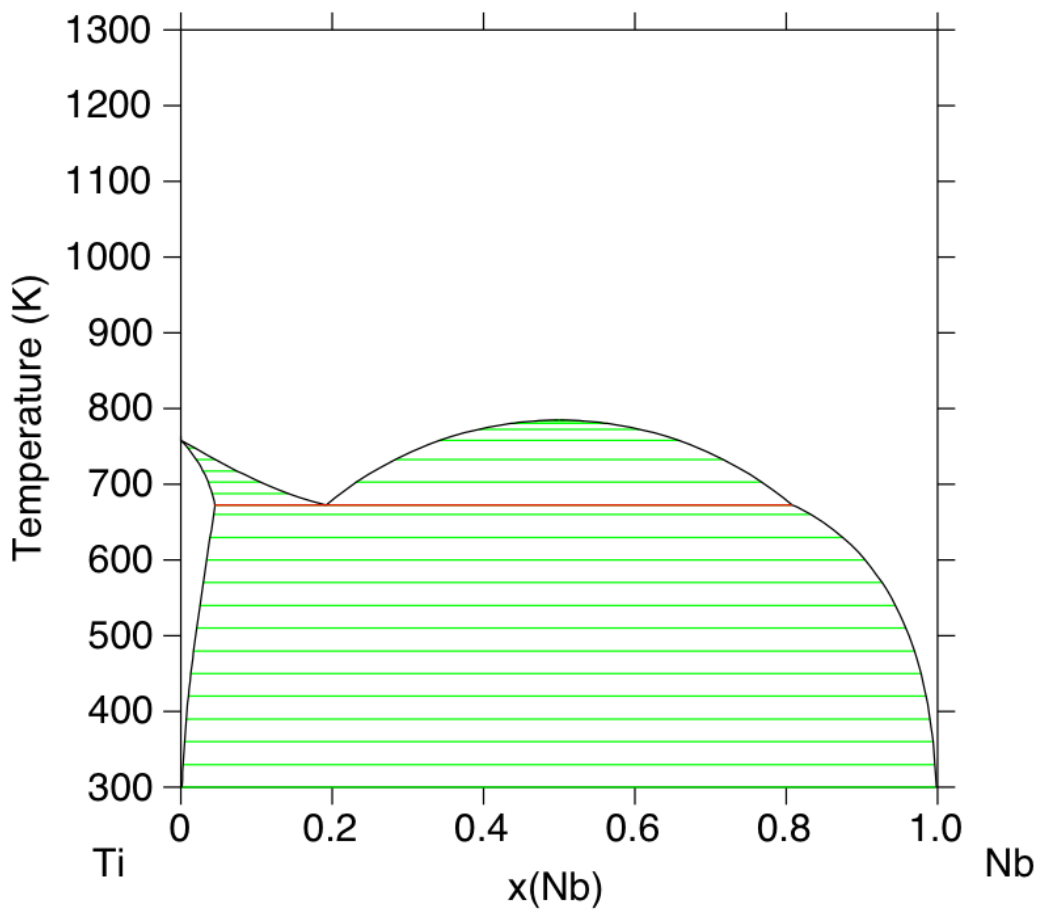


Figure 7.18: Ti-Nb phase diagram with the hcp suspended, shows the formation of the ω and bcc phase as well as the phase fractions.

Chapter 8 |

Conclusions and Future Work

8.1 Conclusions

In this dissertation, the effect of alloying elements on Ti-based alloys was systematically studied. The work began by using first-principles based DFT calculations and the CALPHAD method to study the effect that the alloying elements Mo, Nb, Sn, Ta and Zr have on the equilibrium phase stability, thermodynamics, and elastic properties. The work uses the equation of states fitting of the energy vs. volume curves to get the ground state equilibrium properties. The single crystal elastic stiffness coefficients were calculated using a stress-strain methodology. The Debye-Grüneisen model and phonon quasiharmonic approach were used to study the effect of temperature on the phase stability. The effect that the ω and α'' phases have on the elastic and thermodynamic properties were studied using DFT-based first-principles calculations, CALPHAD modeling and inelastic neutron scattering experiments. The compilation of the work develops a knowledge base for Ti-based alloys and will help to guide the future design of biocompatible implants. The main conclusions from this work are included below:

1. A compatible thermodynamic database for the Ti-Mo-Nb-Ta-Zr system was built using descriptions of the five pure elements (Ti, Mo, Nb, Ta, Zr), ten binary systems (Ti-Mo, Ti-Nb, Ti-Ta, Ti-Zr, Mo-Nb, Mo-Ta, Mo-Zr, Nb-Ta, Nb-Zr, Ta-Zr), and six Ti-containing ternary systems (Ti-Mo-Nb, Ti-Mo-Ta, Ti-Mo-Zr, Ti-Nb-Ta, Ti-Nb-Zr, Ti-Ta-Zr). Sn was excluded from the database due to the lack of modeling for the Sn binary systems. The Sn-Ta and Mo-Sn system lacked a thermodynamic description and the thermodynamic

modeling of the Sn-Zr system is incompatible with the current database. The present work began modeling the Sn binaries with the Sn-Ta system discussed in chapter 4. Until the binaries are properly modeled Sn was not included in the database which shouldn't affect the use of the database for biomedical applications since Sn will only be added to biomedical alloys in small percentages. The thermodynamic descriptions of the pure elements were adopted from the SGTE database [32]. All of the binary systems had previous thermodynamic descriptions available and the compatible descriptions were evaluated for accuracy and incorporated into the database. The binary interpolations of the Ti-containing ternary systems were plotted and compared with the available experimental data as well as the enthalpy of formation of the bcc phase calculated from first-principles based on DFT. The Ti-Sn-X systems ($X = Mo, Nb, Ta, Zr$) will be modeled in the future work once the Sn binaries are modeled. The binary interpolations of the Ti-Nb-Zr and Ti-Ta-Zr systems had previously been plotted but no interaction parameters had been introduced. The present evaluation agreed with the previous evaluations and no ternary interaction parameters were introduced. The Ti-Mo-Zr system had previously been modeled and the present work agreed with the evaluation. The Ti-Mo-Nb, Ti-Mo-Ta and Ti-Nb-Ta systems had never previously been modeled. The present work evaluated interaction parameters for the Ti-Mo-Ta and Ti-Nb-Ta systems but didn't introduce any ternary interaction parameters for the Ti-Mo-Nb system. The thermodynamic descriptions were all incorporated into a complete database that accurately predicts the phase stability of the Ti-Mo-Nb-Ta-Zr systems. The completed database is in appendix A.

2. Sn-Ta modeling was completed using data from DFT-based first-principles calculations and the available experimental data in the literature to model the Gibbs energies for the bcc and liquid solution phases and the stoichiometric Ta_3Sn and $TaSn_2$ phases of the Sn-Ta system. First-principles calculations were used to predict the enthalpy of formation of the bcc phase for the evaluation of interaction parameters in the phase. The decomposition temperature of Ta_3Sn was predicted to be 2884 K. The completed thermodynamic description was compiled into a tdb file in appendix B.

3. The effects of five alloying elements on the elastic properties of bcc Ti-X (X = Mo, Nb, Sn, Ta, Zr) alloys, including the elastic stiffness coefficients, bulk modulus, shear modulus, and Young's modulus, were systematically studied using DFT-based first-principles calculations. The CALPHAD methodology was used to evaluate interaction parameters to predict the elastic properties as a function of composition. The calculations showed that 4.0, 5.5, 9.5, 11.5 and 51.5 at. % of Zr, Mo, Ta, Nb and Sn, respectively, were required to stabilize the bcc phase according to the Born criteria. While the Mo, Nb and Ta elements are considered strong β -stabilizers and Zr is considered a weak β -stabilizer, this work shows that Zr stabilizes the bcc phase at the lowest concentration. The trends observed were summarized for each Ti-X (X= Mo, Nb, Sn, Ta, Zr) binary system. Alloying with Mo, Nb, and Ta results in similar trends, which is probably because Mo, Nb, and Ta are similar elements that strong bcc stabilizers and stable in the bcc structure at room temperature. The interaction parameters determined in the current work were used to predict the elastic properties of higher order alloys. The accuracy of the database predictions of the Young's modulus was evaluated by comparing the calculated and experimental Young's moduli. Overall, the database provides good predictions of the elastic properties of Ti-alloys in the bcc phase as a function of composition.
4. The elastic properties of the bcc Ti-X-Y ternary alloys ($X \neq Y = Mo, Nb, Sn, Ta, Zr$), including the elastic stiffness coefficients, bulk modulus, shear modulus, and Young's modulus were systematically studied using first-principles based on DFT calculations. The general CALPHAD modeling approach was used to fit ternary interaction parameters. From the elastic stiffness coefficients data, the Ti-X-Y ($X \neq Y = Mo, Nb, Ta$) show the same trends in the data. This is to be expected because Mo, Nb, and Ta are similar elements that are strong β -stabilizers and stable in the bcc phase at low temperatures. It was also seen that the Ti-X-Sn ($X = Mo, Nb, Ta$) alloys showed similar trends in the data for most of the elastic stiffness coefficients, so do the Ti-X-Zr ($X = Mo, Nb, Ta$) alloys. The present calculations showed that the bcc Ti-alloy was mechanically stabilized at compositions less than 95, 94, 93, 92, 91, 91, 89, 87, 80, and 77 at % Ti for the Ti-Mo-Zr, Ti-Ta-Zr, Ti-Nb-Zr, Ti-Mo-Ta, Ti-Mo-Nb, Ti-Sn-Zr, Ti-Nb-Ta, Ti-Mo-Sn, Ti-Sn-Ta

and Ti-Nb-Sn alloys, respectively. As discussed above, Mo, Nb and Ta are strong β -stabilizers and thus the Ti-Mo-Nb, Ti-Mo-Ta, and Ti-Nb-Ta systems stabilize the bcc phase similarly. Also, discussed previously, Zr is known as a weak β -stabilizer alone but when alloyed with other elements it acts a strong β -stabilizer. However, Zr was able to stabilize the bcc phase in the Ti-X alloys at a lower concentration than any other element. This is observed with the Ti-Mo-Zr, Ti-Nb-Zr, Ti-Ta-Zr systems all stabilizing the bcc phase at the highest Ti concentrations (95, 93, and 94 at.% respectively). Zr was even able to stabilize the Ti-Sn-Zr system at a high Ti concentration of 91 at.% Ti, even with Sn not being a β -stabilizer or stable in the bcc phase. The ternary interaction parameters were combined with the previously determined pure elements and binary interaction parameters into a complete database in appendix D. The introduction of the ternary interaction parameters improved the database's ability to predict the E of higher order alloys by a small amount and the database satisfactorily predicts the elastic properties of higher order Ti-alloys. The complete database was then used to map some of the possible alloy compositions to find potential materials with a Young's modulus in the target range for biomedical load-bearing implants.

5. The elastic stiffness coefficients and Young's moduli of the Ti-Nb system in the bcc, hcp, ω and α'' phases were systematically calculated. The general CALPHAD modeling approach was used to fit binary interaction parameters. The E values were similar for the hcp and ω phases, which is reasonable since they both have hexagonal symmetry. The α'' phase has E values that were higher than the other three phases which explains why the E increases when the α'' phase forms. Experiments showed that up to 10 at. % Nb the samples formed solely the hcp phase and the database predicted the E values by an average variance of 3 GPa from the experimental E . The samples from 10 at. % Nb to 30 at. % Nb formed the bcc and α'' or ω phases. If the samples were slow cooled they form the bcc and ω phases. If the samples were quenched they form the bcc and α'' phases. Using experimentally determined phase fractions and the rule of mixtures, the database accurately predicted the E values by an average variance of 0.52 GPa when compared with the experimental E values. At Nb concentrations greater than 30 at. % Nb samples form solely the bcc phase and the database predicted the E values by

an average variance of 7 GPa from the experimental E values. The phonon DOS of the slow cooled samples and the phonon DOS of the quenched samples were plotted together for the same compositions and showed differences that were expected for the samples having different phases. This difference was also seen when looking at the entropy difference between the two samples. The entropy difference between the quenched and slow cooled samples increased from 10 at. % Nb to 20 at. % Nb. This increase in entropy difference must be investigated further in order to understand this observation. Using the diffraction patterns, the phase fractions in each sample were approximated.

8.2 Future Work

The following are presented as future work to be able to improve this thesis work:

1. Elastic properties of the Ti-Nb samples will be determined and compared with the database predictions.
2. Temperature dependence of the phonon DOS to gain insight into the type of transformation occurring when α'' and ω form.
3. Results from the DFT-based first-principles calculations will be used to model the α'' and ω phases.
4. Partition function approach will be used to improve the Helmholtz predication of Ti in the bcc phase and the predicting the probability of the metastable phases forming will be investigated
5. Focusing on the modeling of the Sn binary and Ti-Sn-X ($X = \text{Mo, Nb, Ta, Zr}$) systems and incorporating them into this database would further improve the knowledge base of Ti-alloys that this thesis presents. As discussed, Sn is being added due to its low cost and the fact that at low concentrations it does not affect the alloys biocompatibility. But even at low compositions having a better understanding of how Sn effects the phase stability would be helpful.
6. As discussed, introducing interaction parameters to describe the elastic properties for the non Ti-containing binary and ternary systems and the hcp

phase would improve the databases accuracy and extend its uses to other applications

Appendix A | Ti-Mo-Nb-Ta-Zr Database

```
$*****  
$ The definition of the pure elements, vacancy and species  
$-----  
TEMPERATURE_LIMIT 0 6000.00 !  
ELEMENT /- ELECTRON_GAS 0.0000E+00 0.0000E+00 0.0000E+00!  
ELEMENT MO BCC_A2 95.94 4589.0 28.56 !  
ELEMENT NB BCC_A2 92.9064 5220.0 36.27 !  
ELEMENT TA BCC_A2 180.9479 5681.872 41.4718 !  
ELEMENT TI HCP_A3 4.7880E+01 4.8100E+03 3.0648E+01!  
ELEMENT ZR HCP_A3 9.1224E+01 5.5663E+03 3.9181E+01!  
ELEMENT VA VACUUM 0.0 0.0 0.0 !
```

```
$*****
```

```
$ The Gibbs energies of the elements  
$ in the stable and metastable forms from SGTE  
$-----  
$-----
```

```
* TI *
```

```
$-----  
$-----
```

```
FUNCTION GBCCTI
```

```
2.98150E+02 -1272.064+134.71418*T-25.5768*T*LN(T)
```

$-6.63845 \times 10^{-4} T^2 - 2.78803 \times 10^{-7} T^3 + 7208 T^*(-1); 1.15500 \times 10^3 Y$
 $+6667.385 + 105.366379 T - 22.3771 T \ln(T) + .00121707 T^2 - 8.4534 \times 10^{-7} T^3$
 $-2002750 T^*(-1); 1.94100 \times 10^3 Y$
 $+26483.26 - 182.426471 T + 19.0900905 T \ln(T) - .02200832 T^2$
 $+1.228863 \times 10^{-6} T^3 + 1400501 T^*(-1); 4.00000 \times 10^3 N$ REF:20 !

FUNCTION GHSERTI

$2.98150 \times 10^2 - 8059.921 + 133.615208 T - 23.9933 T \ln(T)$
 $-.004777975 T^2 + 1.06716 \times 10^{-7} T^3 + 72636 T^*(-1); 9.00000 \times 10^2 Y$
 $-7811.815 + 132.988068 T - 23.9887 T \ln(T) - .0042033 T^2 - 9.0876 \times 10^{-8} T^3$
 $+42680 T^*(-1); 1.15500 \times 10^3 Y$
 $+908.837 + 66.976538 T - 14.9466 T \ln(T) - .0081465 T^2 + 2.02715 \times 10^{-7} T^3$
 $-1477660 T^*(-1); 1.94100 \times 10^3 Y$
 $-124526.786 + 638.806871 T - 87.2182461 T \ln(T) + .008204849 T^2$
 $-3.04747 \times 10^{-7} T^3 + 36699805 T^*(-1); 4.00000 \times 10^3 N$ REF:20 !

FUNCTION GFCCTI

$2.98150 \times 10^2 + 6000.1 T + GHSERTI; 6.00000 \times 10^3 N$ REF:20 !

FUNCTION GLIQTI

$2.98150 \times 10^2 + 12194.415 - 6.980938 T + GHSERTI; 1.30000 \times 10^3 Y$
 $+368610.36 - 2620.99904 T + 357.005867 T \ln(T) - .155262855 T^2$
 $+1.2254402 \times 10^{-5} T^3 - 65556856 T^*(-1) + GHSERTI; 1.94100 \times 10^3 Y$
 $+104639.72 - 340.070171 T + 40.9282461 T \ln(T) - .008204849 T^2$
 $+3.04747 \times 10^{-7} T^3 - 36699805 T^*(-1) + GHSERTI; 6.00000 \times 10^3 N$ REF:20 !

\$

\$

* MO *

\$

\$

FUNCTION GHSERMO

$298.15 - 7746.302 + 131.9197 T - 23.56414 T \ln(T)$
 $-.003443396 T^2 + 5.662834 \times 10^{-7} T^3 + 65812.39 T^*(-1)$
 $-1.309265 \times 10^{-10} T^4; 2896.00 Y$
 $-30556.41 + 283.559746 T - 42.63829 T \ln(T)$
 $-4.849315 \times 10^{-9} T^*(-9); 4000.00 N$ REF:20 !

FUNCTION GLIQMO
298.15 41831.347-14.694912*T+4.24519E-22*T**7
+GHSERMO; 2896.00 Y
34095.373-11.890046*T+4.849315E33*T**(-9)+GHSERMO;
4000.00 N REF:20 !

FUNCTION GFCCMO
298.15 15200+0.63*T+GHSERMO; 4000.00 N REF:20 !

FUNCTION GHCPMO
298.15 11550+GHSERMO; 4000.00 N REF:20 !

\$_____

\$_____

* NB *

\$_____

\$_____

FUNCTION GHSERNB
2.98140E+02 -8519.353+142.045475*T
-26.4711*T*LN(T)+2.03475E-04*T**2-3.5012E-07*T**3
+93399*T**(-1); 2.75000E+03 Y
-37669.3+271.720843*T-41.77*T*LN(T)+1.528238E+32*T**(-9);
6.00000E+03 N REF:20 !

FUNCTION GHEXTNB
2.98150E+02 -8519.35+142.048*T
-26.4711*T*LN(T)+2.03475E-04*T**2-3.50119E-07*T**3
+93398.8*T**(-1); 6.00000E+03 N REF:23 !

FUNCTION GLIQNB
298.15 29781.555-10.816417*T
-3.06098E-23*T**7+GHSERNB; 2750.00 Y
+30169.901-10.964695*T-1.52824E32*T**(-9)+GHSERNB;
6000.00 N REF:20 !

FUNCTION GFCCNB
298.15 +13500+1.7*T+GHSERNB; 6000.00 N REF:20 !

FUNCTION GHCPNB
298.15 +10000+2.4*T+GHSERNB; 6000.00 N REF:20 !

\$

\$

* TA *

\$

\$

FUNCTION GHSERTA

2.98150E+02 -7285.889+119.139858*T
-23.7592624*T*LN(T)-.002623033*T**2+1.70109E-07*T**3
-3293*T**(-1); 1.30000E+03 Y
-22389.955+243.88676*T-41.137088*T*LN(T)+.006167572*T**2
-6.55136E-07*T**3+2429586*T**(-1); 2.50000E+03 Y
+229382.886-722.59722*T+78.5244752*T*LN(T)-.017983376*T**2
+1.95033E-07*T**3-93813648*T**(-1); 3.25800E+03 Y
-963392.734+2773.7774*T-337.227976*T*LN(T)+.039791303*T**2
-9.74251E-07*T**3+5.09949511E+08*T**(-1); 6.00000E+03 N REF:20 !

FUNCTION GFCCTA

2.98150E+02 +16000+1.7*T+GHSERTA; 6.00000E+03 N REF:20 !

FUNCTION GHCPTA

2.98150E+02 +12000+2.4*T+GHSERTA; 6.00000E+03 N REF:20 !

FUNCTION GLIQTA

2.98150E+02 +29160.975-7.578729*T+GHSERTA; 1.00000E+03 Y
+51170.228-181.121652*T+23.7872147*T*LN(T)-.009707033*T**2
+4.4449E-07*T**3-3520045*T**(-1)+GHSERTA; 1.30000E+03 Y
+66274.294-305.868555*T+41.1650403*T*LN(T)-.018497638*T**2
+1.269735E-06*T**3-5952924*T**(-1)+GHSERTA; 2.50000E+03 Y
-185498.547+660.615425*T-78.4965229*T*LN(T)+.00565331*T**2
+4.19566E-07*T**3+90290310*T**(-1)+GHSERTA; 3.29000E+03 Y
+1036069.47-2727.38037*T+320.319132*T*LN(T)-.043117795*T**2
+1.055148E-06*T**3-5.54714342E+08*T**(-1)+GHSERTA;
6.00000E+03 N REF:20 !

FUNCTION TATIB2

2.98150E+02 2500; 6.00000E+03 N REF:25 !

\$

\$
* ZR *
\$
\$
FUNCTION GLIQZR
2.98140E+02 +18147.69-9.080812*T
+1.6275E-22*T**7+GHSERZR; 2.12800E+03 Y
+17804.661-8.911574*T+1.342895E+31*T**(-9)+GHSERZR;
6.00000E+03 N REF:20 !
FUNCTION GBCCZR
2.98140E+02 -525.539+124.9457*T
-25.607406*T*LN(T)-3.40084E-04*T**2-9.729E-09*T**3
+25233*T**(-1)-7.6143E-11*T**4; 2.12800E+03 Y
-30705.955+264.284163*T-42.144*T*LN(T)+1.276058E+32*T**(-9);
6.00000E+03 N REF:20 !
FUNCTION GHSERZR
1.30000E+02 -7827.595+125.64905*T
-24.1618*T*LN(T)-.00437791*T**2+34971*T**(-1); 2.12800E+03 Y
-26085.921+262.724183*T-42.144*T*LN(T)-1.342895E+31*T**(-9);
6.00000E+03 N REF:20 !
\$
FUNCTION UN_ASS 298.15 0; 300 N !
\$

TYPE_DEFINITION % SEQ * !
TYPE_DEFINITION G SEQ * !
DEFINE_SYSTEM_DEFAULT SPECIE 5 !
DEFAULT_COMMAND DEF_SYS_ELEMENT VA !
\$

\$

PHASE LIQUID % 1 1.0 !

CONSTITUENT LIQUID :MO,TA,NB,TI,ZR: !

PARAMETER G(LIQUID, TI;0)
298.15 GLIQTI; 6000.00 N REF:20 !
PARAMETER G(LIQUID, MO;0)
298.15 GLIQMO; 6000.00 N REF:20 !
PARAMETER G(LIQUID, NB;0)
298.15 GLIQNB; 6000.00 N REF:20
PARAMETER G(LIQUID, TA;0)
298.15 GLIQT; 6000.00 N REF:20 !
PARAMETER G(LIQUID, ZR;0)
298.15 +GLIQZR; 6000.00 N REF:20 !
PARAMETER G(LIQUID, MO, TI;0)
298.15 -9000.0+2*T; 6000.00 N REF:25 !
PARAMETER G(LIQUID, NB, TI;0)
298.15 +7406.1; 6000.00 N REF:23 !
PARAMETER G(LIQUID, TA, TI;0)
298.15 +1000; 6000.00 N REF:25 !
PARAMETER G(LIQUID, TA, TI;1)
298.15 -7000; 6000.00 N REF:25 !
PARAMETER G(LIQUID, TI, ZR;0)
298.15 -967.66; 6000.00 N REF:22 !
PARAMETER G(LIQUID, MO, NB;0)
298.15 15253.7; 6000.00 N REF:21 !
PARAMETER G(LIQUID, MO, NB;1)
298.15 10594.2; 6000.00 N REF:21 !
PARAMETER G(LIQUID, MO, TA;0)
298.15 13978.9; 6000.00 N REF:21 !
PARAMETER G(LIQUID, MO, TA;1)
298.15 577.5; 6000.00 N REF:21 !
PARAMETER G(LIQUID, MO, ZR;0)
298.15 -24055.120+8.146158*T; 6000.00 N REF:26 !
PARAMETER G(LIQUID, MO, ZR;1)

298.15 -5132.1665+4.8041224*T; 6000.00 N REF:26 !

PARAMETER G(LIQUID,NB,TA;0)

298.15 0; 6000.00 N REF:21 !

PARAMETER G(LIQUID,NB,ZR;0)

298.15 10311; 6000.00 N REF:28 !

PARAMETER G(LIQUID,NB,ZR;1)

298.15 6709; 6000.00 N REF:28 !

PARAMETER G(LIQUID,TA,ZR;0)

298.15 13832.1; 6000.00 N REF:27 !

PARAMETER G(LIQUID,TA,ZR;1)

298.15 -7150; 6000.00 N REF:27 !

\$

PHASE BCC_A2 % 2 1 3 !

CONSTITUENT BCC_A2 :MO,TA,NB,TI,ZR:VA: !

PARAMETER G(BCC_A2,TI:VA;0)

298.15 +GBCCTI; 6000.0 N REF:20 !

PARAMETER G(BCC_A2,MO:VA;0)

298.15 +GHSERMO; 6000.00 N REF:20 !

PARAMETER G(BCC_A2,NB:VA;0)

298.15 +GHSERNB; 6000.00 N REF:20 !

PARAMETER G(BCC_A2,TA:VA;0)

298.15 +GHSERTA; 6000.00 N REF:20 !

PARAMETER G(BCC_A2,ZR:VA;0)

298.15 +GBCCZR; 6000.00 N REF:20 !

PARAMETER G(BCC_A2,MO,TI:VA;0)

298.15 2000.0; 6000.00 N REF:25 !

PARAMETER G(BCC_A2,MO,TI:VA;1)

298.15 -2000.0; 6000.00 N REF:25 !

PARAMETER G(BCC_A2,NB,TI:VA;0)

298.15 +13045.3; 6000.00 N REF:23 !

PARAMETER G(BCC_A2,TA,TI:VA;0)

298.15 12000; 6000.00 N REF:25 !

PARAMETER G(BCC_A2,TA,TI:VA;1)
298.15 -2500; 6000.00 N REF:25 !

PARAMETER G(BCC_A2,TI,ZR:VA;0)
298.15 -4346.16+5.48903*T; 6000.00 N REF:22 !

PARAMETER G(BCC_A2,MO,NB:VA;0)
298.15 -68202.6+29.85596*T; 6000.00 N REF:21 !

PARAMETER G(BCC_A2,MO,NB:VA;1)
298.15 8201.3; 6000.00 N REF:21 !

PARAMETER G(BCC_A2,MO,TA:VA;0)
298.15 -75129.2+30*T; 6000.00 N REF:21 !

PARAMETER G(BCC_A2,MO,TA:VA;1)
298.15 6039.24; 6000.00 N REF:21 !

PARAMETER G(BCC_A2,MO,ZR:VA;0)
298.15 +17935.985+3.102*T; 6000.00 N REF:26 !

PARAMETER G(BCC_A2,MO,ZR:VA;1)
298.15 -990.9911+4.299*T; 6000.00 N REF:26 !

PARAMETER G(BCC_A2,NB,TA:VA;0)
298.15 1298.02870; 6000.00 N REF:21 !

PARAMETER G(BCC_A2,NB,ZR:VA;0)
298.15 +15911+3.35*T; 6000.00 N REF:28 !

PARAMETER G(BCC_A2,NB,ZR:VA;1)
298.15 +3919-1.091*T; 6000.00 N REF:28 !

PARAMETER G(BCC_A2,ZR,TA:VA;0)
298.15 29499.6+2.6723*T; 6000.00 N REF:27 !

PARAMETER G(BCC_A2,ZR,TA:VA;1)
298.15 -4396.2+4.4302*T; 6000.00 N REF:27 !

PARAMETER G(BCC_A2,ZR,TA:VA;2)
298.15 -6353.3+4.9066*T; 6000.00 N REF:27 !

PARAMETER G(BCC_A2,MO,TA,TI:VA;0) 298.15 0; 6000.00 N !

PARAMETER G(BCC_A2,MO,TA,TI:VA;1) 298.15 0; 6000.00 N !

PARAMETER G(BCC_A2,MO,TA,TI:VA;2)
298.15 -1.5473118E+05; 6000.00 N !

PARAMETER G(BCC_A2,NB,TA,TI:VA;0)

2.98150E+02 -1.3660332E+05; 6.00000E+03 N !
PARAMETER G(BCC_A2,NB,TA,TI:VA;1)
2.98150E+02 -1.3660269E+05; 6.00000E+03 N !
PARAMETER G(BCC_A2,NB,TA,TI:VA;2)
2.98150E+02 0; 6.00000E+03 N !
\$
PHASE HCP_A3 % 2 1 .5 !
CONSTITUENT HCP_A3 :NB,TI%,ZR,TA,MO : VA% : !

PARAMETER G(HCP_A3,TA:VA;0)
298.15 +GHSERTI; 4000.00 N REF:20 !
PARAMETER G(HCP_A3,MO:VA;0)
298.15 +GHCPMO; 5000.00 N REF:20 !
PARAMETER G(HCP_A3,NB:VA;0)
298.15 +GHCPNB; 6000.00 N REF:20 !
PARAMETER G(HCP_A3,TA:VA;0)
298.15 +GHCPTA; 6000.00 N REF:20 !
PARAMETER G(HCP_A3,ZR:VA;0)
298.15 +GHSERZR; 6000.00 N REF:20 !
PARAMETER G(HCP_A3,MO,TA:VA;0)
298.15 22760-6*T; 6000.00 N REF:25 !
PARAMETER G(HCP_A3,NB,TA:VA;0)
298.15 +11742.4; 6000.00 N REF:23 !
PARAMETER G(HCP_A3,TA,TA:VA;0)
298.15 8500; 6000.00 N REF:25 !
PARAMETER G(HCP_A3,TA,ZR:VA;0)
298.15 +5133.02; 6000.00 N REF:22 !
PARAMETER G(HCP_A3,MO,ZR:VA;0)
298.15 +26753.79+4.556*T; 6000.00 N REF:26 !
PARAMETER G(HCP_A3,NB,ZR:VA;0)
298.15 24411; 6000.00 N REF:28 !
PARAMETER G(HCP_A3,ZR,TA:VA;0)
298.15 +30051.7; 6000.00 N REF:27 !

\$
TYPE_DEFINITION * GES A_P_D FCC_A1 MAGNETIC -3.0 2.80000E-01 !
PHASE FCC_A1 %* 2 1 1 !
CONSTITUENT FCC_A1 :MO,TA,ZR,NB : VA% : !

PARAMETER G(FCC_A1,TA:VA;0)
298.15 +GFCCTI; 4000.00 N REF:20 !
PARAMETER G(FCC_A1,MO:VA;0)
298.15 +GFCCMO; 5000.00 N REF:20 !
PARAMETER G(FCC_A1,NB:VA;0)
298.15 +GFCCNB; 6000.00 N REF:20 !
PARAMETER G(FCC_A1,TA:VA;0)
298.15 +GFCCTA; 6000.00 N REF:20 !
PARAMETER G(FCC_A1,MO,TA:VA;0)
298.15 16500.0; 6000.00 N REF:25 !
PARAMETER G(FCC_A1,TA,TI:VA;0)
298.15 8500; 6000.00 N REF:25 !

\$
PHASE AL3M_D022 % 2 3 1 !
CONSTITUENT AL3M_D022 :TI,MO : TA,TI,MO : !

PARAMETER G(AL3M_D022,TA:TI;0)
298.15 +4*GFCCTI; 6000.00 N REF:25 !
PARAMETER G(AL3M_D022,MO:MO;0)
298.15 +4*GFCCMO; 6000.00 N REF:25 !
PARAMETER G(AL3M_D022,TI:MO;0)
298.15 GFCCMO+3.0*GFCCTI; 6000.00 N REF:25 !
PARAMETER G(AL3M_D022,MO:TI;0)
298.15 3*GFCCMO+GFCCTI; 6000.00 N REF:25 !
PARAMETER G(AL3M_D022,TA:TA;0)
298.15 +3*GFCCTI+GFCCTA; 6000.00 N REF:25 !

TYPE_DEFINITION & GES A_P_D ALM_D019 MAGNETIC -3.0 2.80000E-01 !

PHASE ALM_D019 %& 2 3 1 !

CONSTITUENT ALM_D019 :MO,TA,TI% : MO,TA,TI : !

PARAMETER G(ALM_D019, TI:TI;0)
298.15 +4.0+4.0*GHSERTI; 6000.00 N REF:25 !
PARAMETER G(ALM_D019, TA:MO;0) 298.15 0; 6000 N!
PARAMETER G(ALM_D019, MO:TA;0) 298.15 0; 6000 N!
PARAMETER G(ALM_D019, MO:MO;0)
298.15 +4.0*GHCPMO; 6000.00 N REF:25 !
PARAMETER G(ALM_D019, TA:TA;0)
298.15 +4.0*GHCPTA; 6000.00 N REF:25 !
PARAMETER G(ALM_D019, TI:MO;0)
298.15 +17072.0-4.5*T+GHCPMO+3.0*GHSERTI; 6000.00 N REF:25 !
PARAMETER G(ALM_D019, MO:TI;0)
298.15 +17072.0-4.5*T+3.0*GHCPMO+GHSERTI; 6000.00 N REF:25 !
PARAMETER G(ALM_D019, TI:TA;0)
298.15 +6376+3.0*GHSERTI+GHCPTA; 6000.00 N REF:25 !
PARAMETER G(ALM_D019, TA:TI;0)
298.15 +6376+3.0*GHCPTA+GHSERTI; 6000.00 N REF:25 !
PARAMETER G(ALM_D019, MO, TI:MO;0)
298.15 +51212-13.5*T; 6000.00 N REF:25 !
PARAMETER G(ALM_D019, MO, TI:TI;0)
298.15 +51212-13.5*T; 6000.00 N REF:25 !
PARAMETER G(ALM_D019, MO:MO, TI;0)
298.15 +5692-1.5*T; 6000.00 N REF:25 !
PARAMETER G(ALM_D019, TI:MO, TI;0)
298.15 +5692-1.5*T; 6000.00 N REF:25 !
PARAMETER G(ALM_D019, TA, TI:TA;0)
298.15 +19128; 6000.00 N REF:25 !
PARAMETER G(ALM_D019, TA, TI:TI;0)
298.15 +19128; 6000.00 N REF:25 !
PARAMETER G(ALM_D019, TA:TA, TI;0)
298.15 2128; 6000.00 N REF:25 !

```
PARAMETER G(ALM_D019, TI:TA, TI;0)
298.15 +2128; 6000.00 N REF:25 !
$-----
TYPE_DEFINITION ' GES A_P_D ALTI MAGNETIC -1.0 4.00000E-01 !
PHASE ALTI %' 2 1 1 !
CONSTITUENT ALTI :MO,TA,TI : MO,TA,TI% : !
```

```
PARAMETER G(ALTI, TI:TI;0)
298.15 +2*GFCCTI; 6000.00 N REF:25 !
PARAMETER G(ALTI, MO:MO;0)
298.15 +2*GFCCMO; 6000.00 N REF:25 !
PARAMETER G(ALTI, TA:TA;0)
298.15 +2*GFCCTA; 6000.00 N REF:25 !
PARAMETER G(ALTI, TI:MO;0)
298.15 8250+GFCCMO+GFCCTI; 6000.00 N REF:25 !
PARAMETER G(ALTI, MO:TI;0)
298.15 8250+GFCCMO+GFCCTI; 6000.00 N REF:25 !
PARAMETER G(ALTI, TI:TA;0)
298.15 +4250+GFCCTI+GFCCTA; 6000.00 N REF:25 !
PARAMETER G(ALTI, TA:TI;0)
298.15 +4250+GFCCTA+GFCCTI; 6000.00 N REF:25 !
PARAMETER G(ALTI, MO, TI:MO;0)
298.15 8250; 6000.00 N REF:25 !
PARAMETER G(ALTI, MO, TI:TI;0)
298.15 8250; 6000.00 N REF:25 !
PARAMETER G(ALTI, MO:MO, TI;0)
298.15 8250; 6000.00 N REF:25 !
PARAMETER G(ALTI, TI:MO, TI;0)
298.15 8250; 6000.00 N REF:25 !
PARAMETER G(ALTI, TA, TI:TA;0)
298.15 4250; 6000.00 N REF:25 !
PARAMETER G(ALTI, TA, TI:TI;0)
298.15 4250; 6000.00 N REF:25 !
```

PARAMETER G(ALTI,TA:TA,TI;0)
298.15 4250; 6000.00 N REF:25 !
PARAMETER G(ALTI,TI:TA,TI;0)
298.15 4250; 6000.00 N REF:25 !
\$_____

TYPE_DEFINITION) GES AMEND_PHASE_DESCRIPTION
BCC_B2 DIS_PART BCC_A2,,,!
PHASE BCC_B2 %) 3 .5 .5 3 !
CONSTITUENT BCC_B2 :MO,NB,TA,TI,ZR : MO,NB,TA,TI%,ZR : VA : !

PARAMETER G(BCC_B2,MO:MO:VA;0) 298.15 0; 6000 N REF:25!
PARAMETER G(BCC_B2,TA:TA:VA;0) 298.15 0; 6000 N REF:25 !
PARAMETER G(BCC_B2,TI:TI:VA;0) 298.15 0; 6000 N REF:25 !
PARAMETER G(BCC_B2,TI:MO:VA;0)
298.15 10000.0; 6000.00 N REF:25 !
PARAMETER G(BCC_B2,MO:TI:VA;0)
298.15 10000.0; 6000.00 N REF:25 !
PARAMETER G(BCC_B2,TI:TA:VA;0)
298.15 +5000.0; 6000.00 N REF:25 !
PARAMETER G(BCC_B2,TA:TI:VA;0)
298.15 +5000.0; 6000.00 N REF:25 !
\$_____

PHASE BCT_A5 % 1 1.0 !
CONSTITUENT BCT_A5 :TI : !

PARAMETER G(BCT_A5,TI;0)
298.15 +4602.2+GHserti; 3000.00 N REF:20 !
\$_____

PHASE CBCC_A12 % 2 1 1 !
CONSTITUENT CBCC_A12 :TI : VA : !

PARAMETER G(CBCC_A12,TI:VA;0)
298.15 +4602.2+GHserti; 6000.00 N REF:20 !

\$

PHASE CUB_A13 % 2 1 1 !
CONSTITUENT CUB_A13 :TI : VA : !

PARAMETER G(CUB_A13, TI:VA;0)
298.15 +7531.2+GHserti; 6000.00 N REF:20 !

\$

PHASE DIAMOND_A4 % 1 1.0 !
CONSTITUENT DIAMOND_A4 :TI : !

PARAMETER G(DIAMOND_A4, TI;0)
298.15 +25000+GHserti; 6000.00 N REF:20 !

\$

PHASE LAVES_C14 % 2 2 1 !
CONSTITUENT LAVES_C14 :TI : TI% : !

PARAMETER G(LAVES_C14, TI:TI;0)
298.15 +15000+3*GHserti; 6000.00 N REF:20 !

\$

PHASE LAVES_C15 % 2 2 1 !
CONSTITUENT LAVES_C15 :TI,MO,ZR : TI,MO,ZR : !

PARAMETER G(LAVES_C15, TI:TI;0)

298.15 +15000+3*GHserti; 6.00000E+03 N REF:24!

PARAMETER G(LAVES_C15, MO:MO;0)

298.15 +3*GHSERMO+15000; 6000 N REF:26 !

PARAMETER G(LAVES_C15, ZR:ZR;0)

298.15 +3*GHSERZR+15000; 6000 N REF:26 !

PARAMETER G(LAVES_C15, TI:MO;0)

298.15 +GHSERMO+2*GHserti+15000; 6000 N REF:24 !

PARAMETER G(LAVES_C15, MO:TI;0)

298.15 +2*GHSERMO+GHserti+15000; 6000 N REF:24 !

PARAMETER G(LAVES_C15, TI:ZR;0)

298.15 +2*GHSERTI+GHSERZR+9000; 6000 N REF:24 !
PARAMETER G(LAVES_C15,ZR:TI;0)
298.15 +GHSERTI+2*GHSERZR+15000; 6000 N REF:24 !
PARAMETER G(LAVES_C15,MO:ZR;0)
298.15 +2*GHSERMO+GHSERZR-21734.78+0.1441789*T; 6000 N REF:26 !
PARAMETER G(LAVES_C15,ZR:MO;0)
298.15 +GHSERMO+2*GHSERZR+21734.78-0.1441789*T; 6000 N REF:26 !
PARAMETER G(LAVES_C15,MO:MO,ZR;0) 298.15 +60000; 6000 N REF:26 !
PARAMETER G(LAVES_C15,ZR:MO,ZR;0) 298.15 +60000; 6000 N REF:26 !
PARAMETER G(LAVES_C15,MO,ZR:MO;0) 298.15 +100000; 6000 N REF:26 !
PARAMETER G(LAVES_C15,MO,ZR:ZR;0) 298.15 +100000; 6000 N REF:26 !
PARAMETER G(LAVES_C15,TI:MO,ZR;0) 298.15 +60000; 6000 N REF:27 !
PARAMETER G(LAVES_C15,MO,ZR:TI;0) 298.15 +100000; 6000 N REF:27 !
\$

PHASE OMEGA % 2 1 .5 !
CONSTITUENT OMEGA :NB,TI% : VA% : !

PARAMETER G(OMEGA,ZR;0)
298.15 -8878.082+144.432234*T
-26.8556*T*LN(T)-.002799446*T**2+38376*T**(-1); 2128 Y
-29500.524+265.290858*T-42.144*T*LN(T)
+7.17445E+31*T**(-9); 6000 N REF:20 !
PARAMETER G(OMEGA,TI:VA;0)
298.15 1886.7-0.15161*T+GHSERTI; 4.00000E+03 N REF:23 !
PARAMETER G(OMEGA,NB:VA;0)
2.98150E+02 15000+2.4*T++GHSERNB; 6.00000E+03 N REF:23 !
PARAMETER G(OMEGA,NB,TI:VA;0)
298.15 -3775.9; 6000.00 N REF:23 !
\$

PHASE SI3TI5 % 3 2 3 3 !
CONSTITUENT SI3TI5 :TI : TI : TI : !

PARAMETER G(SI3TI5,TI:TI:TI;0)

298.15 +40000+20*T+8*GHSERTI; 6000.00 N REF:20 !

\$-----

PHASE SNTI3 % 2 1 3 !

CONSTITUENT SNTI3 :TI : TI% : !

PARAMETER G(SNTI3,TI:TI;0)

298.15 +4*GHSERTI+4; 6000.00 N REF:20 !

\$-----

PHASE ORTHORHOMBIC_A20 % 1 1.0 !

CONSTITUENT ORTHORHOMBIC_A20 :ZR : !

PARAMETER G(ORTHORHOMBIC_A20,ZR;0)

298.15 +4474.461+124.9457*T

-25.607406*T*LN(T)-3.40084E-04*T**2-9.729E-09*T**3

+25233*T**(-1)-7.6143E-11*T**4; 2128 Y

-25705.955+264.284163*T-42.144*T*LN(T)

+1.276058E+32*T**(-9); 6000 N REF:20 !

\$-----

PHASE TETRAGONAL_U % 1 1.0 !

CONSTITUENT TETRAGONAL_U :ZR : !

PARAMETER G(TETRAGONAL_U,ZR;0)

298.15 +4474.461+124.9457*T

-25.607406*T*LN(T)-3.40084E-04*T**2-9.729E-09*T**3

+25233*T**(-1)-7.6143E-11*T**4; 2128 Y

-25705.955+264.284163*T-42.144*T*LN(T)

+1.276058E+32*T**(-9); 6000 N REF:20 !

\$-----

DATABASE_INFO 'FOR THE TI_MO_NB_TA_ZR SYSTEM' !

LIST_OF_REFERENCES

NUMBER SOURCE

20 'A.T. Dinsdale, SGTE Data for Pure Elements, CALPHAD.

-
- 15 (1991) 317-425.'
- 21 'W. Xiong, Y. Du, Y. Liu, B.Y. Huang, H.H. Xu, H.L. Chen, et al., Thermodynamic assessment of the Mo-Nb-Ta system, Calphad-Computer Coupling Phase Diagrams Thermochem. 28 (2004) 133-140.'
- 22 'K.C.H. Kumar, P. Wollants, L. Delaey, Thermodynamic assessment of the Ti-Zr system and calculation of the Nb-Ti-Zr phase-diagram, J. Alloys Compd. 206 (1994) 121-127.'
- 23 'Y.L. Zhang, H.S. Liu, Z.P. Jin, Thermodynamic assessment of the Nb-Ti system, Calphad-Computer Coupling Phase Diagrams Thermochem. 25 (2001) 305-317.'
- 24 'S. Kar, D.M. Lipkin, A CALPHAD-based phase equilibrium model of Mo-Ti-Zr-C, in: TMS 2008 Annu. Meet. Suppl. Proceedings, Vol 2 Mater. Charact. Comput. Model., Minerals, Metals & Materials Soc, Warrendale, 2008: pp. 237-243.'
- 25 'I. Ansara, A.T. Dinsdale, M.H. Rand, COST 507: thermochemical database for light metal alloys, European Communities, Brussels and Luxembourg, 1998.'
- 26 'R.J. Perez, B. Sundman, Thermodynamic assessment of the Mo-Zr binary phase diagram, Calphad-Computer Coupling Phase Diagrams Thermochem. 27 (2003) 253-262.'
- 27 'A.F. Guillermet, Phase-diagram and thermochemical properties of the Zr-Ta system - an assessment based on Gibbs energy modeling, J. Alloys Compd. 226 (1995) 174-184.'
- 28 'A.F. Guillermet, Thermodynamic analysis of the stable phases in the Zr-Nb system and calculation of the phase-diagram, Zeitschrift Fur Met. 82 (1991) 478-487.'
- !
-

Appendix B |

Sn-Ta Database

```
$*****  
$ The definition of the pure elements, vacancy and species  
$-----  
ELEMENT /- ELECTRON_GAS 0.0000E+00 0.0000E+00 0.0000E+00!  
ELEMENT VA VACUUM 0.0000E+00 0.0000E+00 0.0000E+00!  
ELEMENT SN BCT_A5 1.1871E+02 6.3220E+03 5.1195E+01!  
ELEMENT TA BCC_A2 1.8095E+02 5.6819E+03 4.1472E+01!
```

```
$*****
```

```
$ The Gibbs energies of the elements  
$ in the stable and metastable forms from SGTE  
$-----  
$-----
```

* TA *

```
$-----  
$-----
```

FUNCTION GHSERTA

```
298.15 -7285.889+119.139857*T-23.7592624*T*LN(T)  
.002623033*T**2+1.70109E-07*T**3-3293*T**(-1); 1300 Y  
-22389.955+243.88676*T-41.137088*T*LN(T)+.006167572*T**2  
-6.55136E-07*T**3+2429586*T**(-1); 2500 Y  
+229382.886-722.59722*T+78.5244752*T*LN(T)-.017983376*T**2
```

+1.95033E-07*T**3-93813648*T**(-1); 3290 Y
-1042384.01+2985.49125*T-362.159132*T*LN(T)+.043117795*T**2
-1.055148E-06*T**3+5.54714342E+08*T**(-1); 6000 N REF20 !

FUNCTION GFCCTA

298.15 +8714.111+120.839857*T-23.7592624*T*LN(T)
.002623033*T**2+1.70109E-07*T**3-3293*T**(-1); 1300 Y
-6389.955+245.58676*T-41.137088*T*LN(T)+.006167572*T**2
-6.55136E-07*T**3+2429586*T**(-1); 2500 Y
+245382.886-720.89722*T+78.5244752*T*LN(T)-.017983376*T**2
+1.95033E-07*T**3-93813648*T**(-1); 3290 Y
-1026384.01+2987.19125*T-362.159132*T*LN(T)+.043117795*T**2
-1.055148E-06*T**3+5.54714342E+08*T**(-1); 6000 N REF20 !

FUNCTION GHCPTA

298.15 +4714.111+121.539857*T-23.7592624*T*LN(T)
.002623033*T**2+1.70109E-07*T**3-3293*T**(-1); 1300 Y
-10389.955+246.28676*T-41.137088*T*LN(T)+.006167572*T**2
-6.55136E-07*T**3+2429586*T**(-1); 2500 Y
+241382.886-720.19722*T+78.5244752*T*LN(T)-.017983376*T**2
+1.95033E-07*T**3-93813648*T**(-1); 3290 Y
-1030384.01+2987.89125*T-362.159132*T*LN(T)+.043117795*T**2
-1.055148E-06*T**3+5.54714342E+08*T**(-1); 6000 N REF20 !

FUNCTION GLIQTA

298.15 +21875.086+111.561128*T-23.7592624*T*LN(T)
.002623033*T**2+1.70109E-07*T**3-3293*T**(-1); 1000 Y
+43884.339-61.981795*T+.0279523*T*LN(T)-.012330066*T**2
+6.14599E-07*T**3-3523338*T**(-1); 3290 Y
-6314.543+258.110873*T-41.84*T*LN(T); 6000 N REF20 !

\$_____

\$_____

* SN *

\$_____

\$_____

FUNCTION GHSERSN

100 -7958.517+122.765451*T-25.858*T*LN(T)
+5.1185E-04*T**2-3.192767E-06*T**3+18440*T**(-1); 250 Y
-5855.135+65.443315*T-15.961*T*LN(T)-.0188702*T**2+3.121167E-06*T**3
-61960*T**(-1); 505.08 Y
+2524.724+4.005269*T-8.2590486*T*LN(T)-.016814429*T**2
+2.623131E-06*T**3-1081244*T**(-1)-1.2307E+25*T**(-9); 800 Y
-8256.959+138.99688*T-28.4512*T*LN(T)-1.2307E+25*T**(-9); 3000 N REF20 !

FUNCTION GBCCSN

100 -3558.517+116.765451*T-25.858*T*LN(T)
+5.1185E-04*T**2-3.192767E-06*T**3+18440*T**(-1); 250 Y
-1455.135+59.443315*T-15.961*T*LN(T)-.0188702*T**2+3.121167E-06*T**3
-61960*T**(-1); 505.08 Y
+6924.724-1.994731*T-8.2590486*T*LN(T)-.016814429*T**2
+2.623131E-06*T**3-1081244*T**(-1)-1.2307E+25*T**(-9); 800 Y
-3856.959+132.99688*T-28.4512*T*LN(T)-1.2307E+25*T**(-9); 3000 N REF20 !

FUNCTION GA12SN

100 -5958.517+122.765451*T-25.858*T*LN(T)
+5.1185E-04*T**2-3.192767E-06*T**3+18440*T**(-1); 250 Y
-3855.135+65.443315*T-15.961*T*LN(T)-.0188702*T**2+3.121167E-06*T**3
-61960*T**(-1); 505.08 Y+4524.724+4.005269*T-8.2590486*T*LN(T)
-.016814429*T**2+2.623131E-06*T**3-1081244*T**(-1)-1.2307E+25*T**(-9); 800 Y
-6256.959+138.99688*T-28.4512*T*LN(T)-1.2307E+25*T**(-9); 3000 N REF20 !

FUNCTION GA13SN

100 -5958.517+122.765451*T-25.858*T*LN(T)
+5.1185E-04*T**2-3.192767E-06*T**3+18440*T**(-1); 250 Y
-3855.135+65.443315*T-15.961*T*LN(T)-.0188702*T**2+3.121167E-06*T**3
-61960*T**(-1); 505.08 Y
+4524.724+4.005269*T-8.2590486*T*LN(T)-.016814429*T**2
+2.623131E-06*T**3-1081244*T**(-1)-1.2307E+25*T**(-9); 800 Y
-6256.959+138.99688*T-28.4512*T*LN(T)-1.2307E+25*T**(-9); 3000 N REF20 !

FUNCTION GDIAMOND

100 -9579.608+114.007785*T-22.972*T*LN(T)-.00813975*T**2
+2.7288E-06*T**3+25615*T**(-1); 298.15 Y

$-9063.001 + 104.84654T - 21.5750771T\ln(T) - .008575282T^{**2}$
 $+ 1.784447E-06T^{**3} - 2544T^{**(-1)}; 800 Y$
 $-10909.351 + 147.396535T - 28.4512T\ln(T); 3000 N \text{ REF20 !}$
FUNCTION GFCCSN
 $298.15 - 345.135 + 56.983315T - 15.961T\ln(T) - .0188702T^{**2}$
 $+ 3.121167E-06T^{**3} - 61960T^{**(-1)}; 505.08 Y$
 $+ 8034.724 - 4.454731T - 8.2590486T\ln(T) - .016814429T^{**2}$
 $+ 2.623131E-06T^{**3} - 1081244T^{**(-1)} - 1.2307E + 25T^{**(-9)}; 800 Y$
 $-2746.959 + 130.53688T - 28.4512T\ln(T) - 1.2307E + 25T^{**(-9)}; 3000 N \text{ REF20 !}$
FUNCTION GHCPSN
 $298.15 - 1955.135 + 57.797315T - 15.961T\ln(T)$
 $- .0188702T^{**2} + 3.121167E-06T^{**3} - 61960T^{**(-1)}; 505.08 Y$
 $+ 6424.724 - 3.640731T - 8.2590486T\ln(T) - .016814429T^{**2}$
 $+ 2.623131E-06T^{**3} - 1081244T^{**(-1)} - 1.2307E + 25T^{**(-9)}; 800 Y$
 $-4356.959 + 131.35088T - 28.4512T\ln(T) - 1.2307E + 25T^{**(-9)}; 3000 N \text{ REF20 !}$
FUNCTION GHCPZN_S
 $298.15 - 1950.135 + 57.797315T - 15.961T\ln(T)$
 $- .0188702T^{**2} + 3.121167E-06T^{**3} - 61960T^{**(-1)}; 505.08 Y$
 $+ 6429.724 - 3.640731T - 8.2590486T\ln(T) - .016814429T^{**2}$
 $+ 2.623131E-06T^{**3} - 1081244T^{**(-1)} - 1.2307E + 25T^{**(-9)}; 800 Y$
 $-4351.959 + 131.35088T - 28.4512T\ln(T) - 1.2307E + 25T^{**(-9)}; 3000 N \text{ REF20 !}$
FUNCTION GLIQSN
 $100 - 855.425 + 108.677684T - 25.858T\ln(T) + 5.1185E-04T^{**2}$
 $- 3.192767E-06T^{**3} + 18440T^{**(-1)} + 1.47031E-18T^{**7}; 250 Y$
 $+ 1247.957 + 51.355548T - 15.961T\ln(T) - .0188702T^{**2} + 3.121167E-06T^{**3}$
 $- 61960T^{**(-1)} + 1.47031E-18T^{**7}; 505.08 Y$
 $+ 9496.31 - 9.809114T - 8.2590486T\ln(T) - .016814429T^{**2}$
 $+ 2.623131E-06T^{**3} - 1081244T^{**(-1)}; 800 Y$
 $-1285.372 + 125.182498T - 28.4512T\ln(T); 3000 N \text{ REF20 !}$
FUNCTION GA7SN
 $100 - 5923.517 + 122.765451T - 25.858T\ln(T)$
 $+ 5.1185E-04T^{**2} - 3.192767E-06T^{**3} + 18440T^{**(-1)}; 250 Y$
 $- 3820.135 + 65.443315T - 15.961T\ln(T) - .0188702T^{**2} + 3.121167E-06T^{**3}$

$-61960*T^{**}(-1); 505.08 Y$
 $+4559.724+4.005269*T-8.2590486*T*LN(T)-.016814429*T^{**}2$
 $+2.623131E-06*T^{**}3-1081244*T^{**}(-1)-1.2307E+25*T^{**}(-9); 800 Y$
 $-6221.959+138.99688*T-28.4512*T*LN(T)-1.2307E+25*T^{**}(-9); 3000 N$ REF20 !
 FUNCTION GA6SN
 $298.15 -468.135+57.181195*T-15.961*T*LN(T)-.0188702*T^{**}2$
 $+3.121167E-06*T^{**}3-61960*T^{**}(-1); 505.08 Y$
 $+7911.724-4.256851*T-8.2590486*T*LN(T)-.016814429*T^{**}2$
 $+2.623131E-06*T^{**}3-1081244*T^{**}(-1)-1.2307E+25*T^{**}(-9); 800 Y$
 $-2869.959+130.73476*T-28.4512*T*LN(T)-1.2307E+25*T^{**}(-9); 3000 N$ REF20 !
 \$

FUNCTION UN_ASS 298.15 +0.0; 300 N !

\$

TYPE_DEFINITION % SEQ *!

DEFINE_SYSTEM_DEFAULT ELEMENT 2 !

DEFAULT_COMMAND DEF_SYS_ELEMENT VA /- !

\$

\$

TYPE_DEFINITION & GES A_P_D BCC_A2 MAGNETIC -1.0 4.00000E-01 !

PHASE BCC_A2 %& 2 1 3 !

CONSTITUENT BCC_A2 :SN,TA : VA : !

PARAMETER G(BCC_A2,SN:VA;0)

100 +GBCCSN; 3000 N REF20 !

PARAMETER G(BCC_A2,TA:VA;0)

298.15 +GHSERTA; 6000 N REF20 !

PARAMETER G(BCC_A2,SN,TA:VA;0)

298.15 7.0451375E+04; 6000 N !

PARAMETER G(BCC_A2,SN,TA:VA;1)

298.15 1.1223739E+05; 6000 N !

\$

PHASE BCT_A5 % 1 1.0 !

CONSTITUENT BCT_A5 :SN : !

PARAMETER G(BCT_A5,SN;0)

100 +GHSERSN; 3000 N REF20 !

\$

TYPE_DEFINITION ' GES A_P_D CBCC_A12 MAGNETIC -3.0 2.80000E-01 !
PHASE CBCC_A12 %' 2 1 1 !
CONSTITUENT CBCC_A12 :SN : VA : !

PARAMETER G(CBCC_A12,SN:VA;0) 100 +GA12SN; 3000 N REF20 !

\$

PHASE CUB_A13 % 2 1 1 !
CONSTITUENT CUB_A13 :SN : VA : !

PARAMETER G(CUB_A13,SN:VA;0) 100 +GA13SN; 3000 N REF20 !

\$

PHASE DIAMOND_A4 % 1 1.0 !
CONSTITUENT DIAMOND_A4 :SN : !

PARAMETER G(DIAMOND_A4,SN;0) 100 +GDIAMOND; 3000 N REF20 !

\$

TYPE_DEFINITION (GES A_P_D FCC_A1 MAGNETIC -3.0 2.80000E-01 !
PHASE FCC_A1 %(2 1 1 !
CONSTITUENT FCC_A1 :SN,TA : VA : !

PARAMETER G(FCC_A1,SN:VA;0) 298.15 +GFCCSN; 3000 N REF20 !
PARAMETER G(FCC_A1,TA:VA;0) 298.15 +GFCCTA; 6000 N REF20 !

\$

TYPE_DEFINITION) GES A_P_D HCP_A3 MAGNETIC -3.0 2.80000E-01 !
PHASE HCP_A3 %) 2 1 .5 !
CONSTITUENT HCP_A3 :SN,TA : VA : !

PARAMETER G(HCP_A3,SN:VA;0) 298.15 +GHCPSEN; 3000 N REF20 !
PARAMETER G(HCP_A3,TA:VA;0) 298.15 +GHCPATA; 6000 N REF20 !

\$

PHASE HCP_ZN % 2 1 .5 !
CONSTITUENT HCP_ZN :SN : VA : !

PARAMETER G(HCP_ZN,SN:VA;0) 298.15 +GHCPZN_S; 3000 N REF20 !
\$-----

PHASE LIQUID % 1 1.0 !
CONSTITUENT LIQUID :SN,TA : !

PARAMETER G(LIQUID,SN;0) 100 +GLIQSN; 3000 N REF20 !
PARAMETER G(LIQUID,TA;0) 298.15 +GLIQT; 6000 N REF20 !
PARAMETER G(LIQUID,SN,TA;0) 298.15 -1.7117919E+04; 6000 N !
\$-----

PHASE RHOMBOHEDRAL_A7 % 1 1.0 !
CONSTITUENT RHOMBOHEDRAL_A7 :SN : !

PARAMETER G(RHOMBOHEDRAL_A7,SN;0) 100 +GA7SN; 3000 N REF20 !
\$-----

PHASE TA3SN % 2 3 1 !
CONSTITUENT TA3SN :TA : SN : !

PARAMETER G(TA3SN,TA:SN;0)
298.15 -68843.951-6.00E+00*T+3*GHSERTA+GHSERSN; 3000 N !
\$-----

PHASE TASN2 % 2 1 2 !
CONSTITUENT TASN2 :TA : SN : !

PARAMETER G(TASN2,TA:SN;0)
298.15 -29678.180-4.202*T+GHSERTA+2*GHSERSN; 3000 N !
\$-----

PHASE TETRAGONAL_A6 % 1 1.0 !
CONSTITUENT TETRAGONAL_A6 :SN : !

PARAMETER G(TETRAGONAL_A6,SN;0) 298.15 +GA6SN; 3000 N REF20 !
\$-----

\$*****

LIST_OF_REFERENCES

NUMBER SOURCE

20 'A.T. Dinsdale, SGTE Data for Pure Elements,
CALPHAD.15 (1991) 317-425. '

!

Appendix C | Calculation and Fitting Details

Calculation Details for Chapter 3, 5, and 6

As discussed in each chapter the Monkhorst-Pack scheme is used for Brillouin zone sampling [61, 90]. The k-points grid used for each calculation done in chapter 3, 5 and 6 are listed in the table. The k-points grids are listed as AxAxA. In some cases, the automated k-point mesh generator in VASP was used and the length of the subdivisions specified are specified as number such as 50.

Structure	Type of Calc	relaxation k-points
hcp-Ti	Elemental	30
bcc-Ti	Elemental	50
bcc-Mo	Elemental	50
bcc-Nb	Elemental	50
bcc-Ta	Elemental	50
hcp-Zr	Elemental	30
bcc-Zr	Elemental	4x4x4
bcc-Ti _{0.94} Mo _{0.06}	Dilute	5x5x5
bcc-Ti _{0.88} Mo _{0.12}	Dilute	4x4x4
bcc-Ti _{0.75} Mo _{0.25}	SQS	4x4x4
bcc-Ti _{0.50} Mo _{0.50}	SQS	4x4x4
bcc-Ti _{0.25} Mo _{0.75}	SQS	4x4x4
bcc-Ti _{0.06} Mo _{0.94}	Dilute	80
bcc-Ti _{0.02} Mo _{0.98}	Dilute	50
bcc-Ti _{0.98} Nb _{0.02}	Dilute	4x4x4

Structure	Type of Calc	relaxation k-points
bcc-Ti _{0.88} Nb _{0.12}	Dilute	4x4x4
bcc-Ti _{0.75} Nb _{0.25}	SQS	4x4x4
bcc-Ti _{0.50} Nb _{0.50}	SQS	4x4x4
bcc-Ti _{0.25} Nb _{0.75}	SQS	4x4x4
bcc-Ti _{0.06} Nb _{0.94}	Dilute	80
bcc-Ti _{0.02} Nb _{0.98}	Dilute	80
bcc-Ti _{0.94} Sn _{0.06}	Dilute	80
bcc-Ti _{0.75} Sn _{0.25}	SQS	4x4x4
bcc-Ti _{0.50} Sn _{0.50}	SQS	80
bcc-Ti _{0.25} Sn _{0.75}	SQS	4x4x4
bcc-Ti _{0.98} Ta _{0.02}	Dilute	50
bcc-Ti _{0.94} Ta _{0.06}	Dilute	80
bcc-Ti _{0.88} Ta _{0.12}	Dilute	80
bcc-Ti _{0.75} Ta _{0.25}	SQS	80
bcc-Ti _{0.50} Ta _{0.50}	SQS	80
bcc-Ti _{0.25} Ta _{0.75}	SQS	4x4x4
bcc-Ti _{0.12} Ta _{0.88}	Dilute	80
bcc-Ti _{0.02} Ta _{0.98}	Dilute	80
bcc-Ti _{0.98} Zr _{0.02}	Dilute	3x3x3
bcc-Ti _{0.75} Zr _{0.25}	SQS	4x4x4
bcc-Ti _{0.50} Zr _{0.50}	SQS	4x4x4
bcc-Ti _{0.25} Zr _{0.75}	SQS	4x4x4
bcc-Ti _{0.06} Zr _{0.94}	Dilute	80
bcc-Mo _{0.50} Nb _{0.50}	SQS	3x3x3
bcc-Mo _{0.50} Sn _{0.50}	SQS	80
bcc-Mo _{0.50} Ta _{0.50}	SQS	80
bcc-Mo _{0.50} Zr _{0.50}	SQS	80
bcc-Nb _{0.50} Sn _{0.50}	SQS	80
bcc-Nb _{0.50} Ta _{0.50}	SQS	80
bcc-Nb _{0.50} Zr _{0.50}	SQS	80
bcc-Sn _{0.50} Ta _{0.50}	SQS	80
bcc-Sn _{0.50} Zr _{0.50}	SQS	80
bcc-Ta _{0.50} Zr _{0.50}	SQS	80

Structure	Type of Calc	relaxation k-points
bcc-Ti _{0.33} Mo _{0.33} Nb _{0.33}	SQS	4x4x4
bcc-Ti _{0.50} Mo _{0.25} Nb _{0.25}	SQS	4x4x4
bcc-Ti _{0.74} Mo _{0.13} Nb _{0.13}	SQS	4x4x4
bcc-Ti _{0.33} Mo _{0.33} Sn _{0.33}	SQS	4x4x4
bcc-Ti _{0.50} Mo _{0.25} Sn _{0.25}	SQS	4x4x4
bcc-Ti _{0.74} Mo _{0.13} Sn _{0.13}	SQS	4x4x4
bcc-Ti _{0.33} Mo _{0.33} Ta _{0.33}	SQS	4x4x4
bcc-Ti _{0.50} Mo _{0.25} Ta _{0.25}	SQS	4x4x4
bcc-Ti _{0.74} Mo _{0.13} Ta _{0.13}	SQS	4x4x4
bcc-Ti _{0.33} Mo _{0.33} Zr _{0.33}	SQS	4x4x4
bcc-Ti _{0.50} Mo _{0.25} Zr _{0.25}	SQS	4x4x4
bcc-Ti _{0.74} Mo _{0.13} Zr _{0.13}	SQS	4x4x4
bcc-Ti _{0.33} Nb _{0.33} Sn _{0.33}	SQS	4x4x4
bcc-Ti _{0.50} Nb _{0.25} Sn _{0.25}	SQS	4x4x4
bcc-Ti _{0.74} Nb _{0.13} Sn _{0.13}	SQS	4x4x4
bcc-Ti _{0.33} Nb _{0.33} Ta _{0.33}	SQS	4x4x4
bcc-Ti _{0.50} Nb _{0.25} Ta _{0.25}	SQS	4x4x4
bcc-Ti _{0.74} Nb _{0.13} Ta _{0.13}	SQS	4x4x4
bcc-Ti _{0.33} Nb _{0.33} Zr _{0.33}	SQS	4x4x4
bcc-Ti _{0.50} Nb _{0.25} Zr _{0.25}	SQS	4x4x4
bcc-Ti _{0.74} Nb _{0.13} Zr _{0.13}	SQS	4x4x4
bcc-Ti _{0.33} Sn _{0.33} Ta _{0.33}	SQS	4x4x4
bcc-Ti _{0.50} Sn _{0.25} Ta _{0.25}	SQS	4x4x4
bcc-Ti _{0.74} Sn _{0.13} Ta _{0.13}	SQS	4x4x4
bcc-Ti _{0.33} Sn _{0.33} Zr _{0.33}	SQS	4x4x4
bcc-Ti _{0.50} Sn _{0.25} Zr _{0.25}	SQS	4x4x4
bcc-Ti _{0.74} Sn _{0.13} Zr _{0.13}	SQS	4x4x4
bcc-Ti _{0.33} Ta _{0.33} Zr _{0.33}	SQS	4x4x4
bcc-Ti _{0.50} Ta _{0.25} Zr _{0.25}	SQS	4x4x4
bcc-Ti _{0.74} Ta _{0.13} Zr _{0.13}	SQS	4x4x4

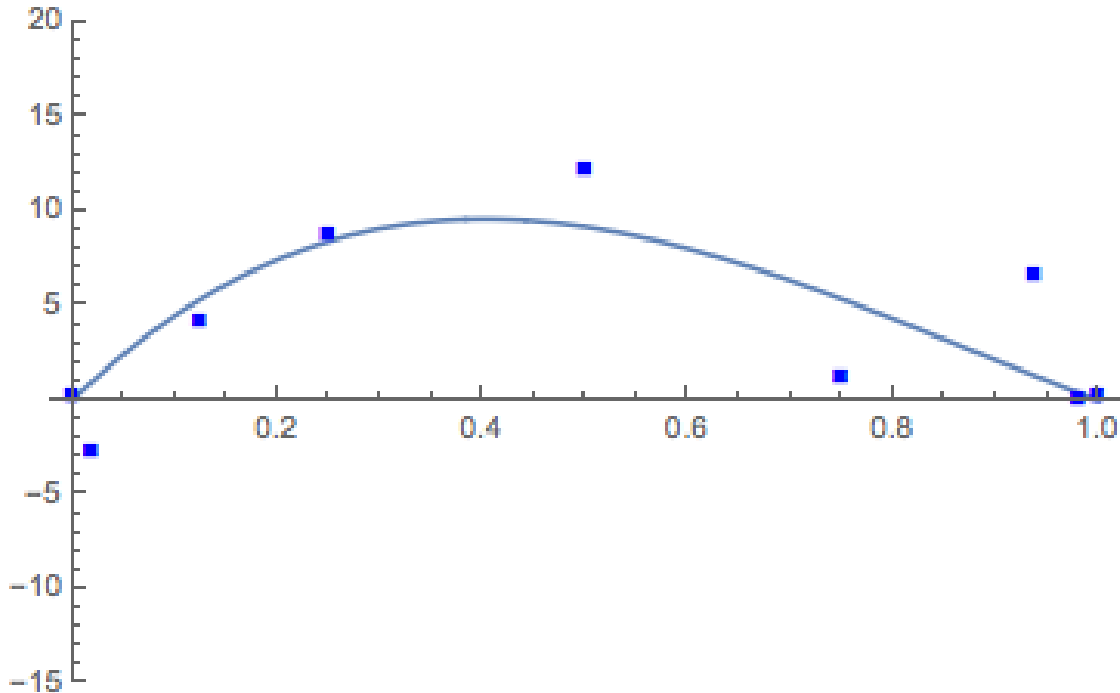
Fitting Code for Chapter 5 and 6

The code used in Mathematica to fit the binary and ternary interaction parameters is listed below.

```
input: n = 0, 0, 0.019, -2.81, 0.019, -2.81, 0.019, -2.81, 0.019, -2.81, 0.019, -2.81, 0.125, 4.00, 0.125, 4.00, 0.125, 4.00, 0.125, 4.00, 0.125, 4.00, 0.125, 4.00, 0.25, 8.67, 0.25, 8.67, 0.25, 8.67, 0.25, 8.67, 0.25, 8.67, 0.50, 12.00, 0.75, 1.00, 0.938, 6.42, 0.981, -0.11, 1, 0
```

```
output: 0, 0, 0.019, -2.81, 0.019, -2.81, 0.019, -2.81, 0.019, -2.81, 0.019, -2.81, 0.125, 4., 0.125, 4., 0.125, 4., 0.125, 4., 0.125, 4., 0.25, 8.67, 0.25, 8.67, 0.25, 8.67, 0.25, 8.67, 0.5, 12., 0.75, 1., 0.938, 6.42, 0.981, -0.11, 1, 0
```

```
input: gp = ListPlot[n, PlotMarkers -> □, 10, PlotStyle -> Blue] input: Fit[n, (x*(1 - x)), ((x*(1 - x))^(x - (1 - x))), x] (For a two parameter fit) input: Fit[n, (x*(1 - x)), x] (For a one parameter fit) input: Plot[%, x, 0, 1, PlotRange -> -100, 100] input: Show[%, gp]
```



Appendix D | Ti Elastic Database

```
$*****  
$ The definition of the pure elements, vacancy and species  
$-----  
TEMPERATURE_LIMIT 0 6000.00 !  
ELEMENT /- ELECTRON_GAS 0.0000E+00 0.0000E+00 0.0000E+00!  
ELEMENT VA VACUUM 0.0 0.0 0.0 !  
ELEMENT TI BCC_A2 !  
ELEMENT MO BCT_A5 !  
ELEMENT NB BCC_A2 !  
ELEMENT SN BCT_A5 !  
ELEMENT TA BCC_A2 !  
ELEMENT ZR BCT_A5 !
```

```
$*****  
$-----  
FUNCTION C11BCCTI 298.15 +93; 6000 N !  
FUNCTION C12BCCTI 298.15 +115; 6000 N !  
FUNCTION C44BCCTI 298.15 +41; 6000 N !  
FUNCTION C11BCCMO 298.15 +475; 6000 N !  
FUNCTION C12BCCMO 298.15 +164; 6000 N !  
FUNCTION C44BCCMO 298.15 +108; 6000 N !
```

FUNCTION C11BCCNB	298.15 +245;	6000 N !
FUNCTION C12BCCNB	298.15 +144;	6000 N !
FUNCTION C44BCCNB	298.15 +27;	6000 N !
FUNCTION C11BCCSN	298.15 +50;	6000 N !
FUNCTION C12BCCSN	298.15 +52;	6000 N !
FUNCTION C44BCCSN	298.15 +29;	6000 N !
FUNCTION C11BCCTA	298.15 +278;	6000 N !
FUNCTION C12BCCTA	298.15 +164;	6000 N !
FUNCTION C44BCCTA	298.15 +81;	6000 N !
FUNCTION C11BCCZR	298.15 +86;	6000 N !
FUNCTION C12BCCZR	298.15 +91;	6000 N !
FUNCTION C44BCCZR	298.15 +32;	6000 N !
FUNCTION UN_ASS	298.15 +0;	300 N !
\$		
FUNCTION UN_ASS	298.15 0;	300 N !
\$		
\$*****		
TYPE_DEFINITION % SEQ *		!
TYPE_DEFINITION G SEQ *		!
DEFINE_SYSTEM_DEFAULT SPECIE 5		!
DEFAULT_COMMAND DEF_SYS_ELEMENT VA		!
\$		
\$*****		
\$*****		
\$		
TYPE_DEFINITION & GES A_P_D BCC_A2 MAGNETIC -1.0 4.00000E-01		!
PHASE BCC_A2 %& 2 1 3		!
CONSTITUENT BCC_A2 :TI,MO,NB,SN,TA,ZR : VA :		!
PARAMETER C11(BCC_A2, TI:VA;0)		
298.15 +C11BCCTI;	6000 N !	
PARAMETER C11(BCC_A2, MO:VA;0)		
298.15 +C11BCCMO;	6000 N !	

PARAMETER C11(BCC_A2,NB:VA;0)
298.15 +C11BCCNB; 6000 N !

PARAMETER C11(BCC_A2,SN:VA;0)
298.15 +C11BCCSN; 6000 N !

PARAMETER C11(BCC_A2,TA:VA;0)
298.15 +C11BCCTA; 6000 N !

PARAMETER C11(BCC_A2,ZR:VA;0)
298.15 +C11BCCZR; 6000 N !

PARAMETER C11(BCC_A2,TI,MO:VA;0)
298.15 -22.16; 6000 N !

PARAMETER C11(BCC_A2,TI,NB:VA;0)
298.15 +40.46; 6000 N !

PARAMETER C11(BCC_A2,TI,SN:VA;0)
298.15 +119.46; 6000 N !

PARAMETER C11(BCC_A2,TI,TA:VA;0)
298.15 +83.65; 6000 N !

PARAMETER C11(BCC_A2,TI,TA:VA;1)
298.15 -67.76; 6000 N !

PARAMETER C11(BCC_A2,TI,ZR:VA;0)
298.15 +246.97; 6000 N !

PARAMETER C11(BCC_A2,TI,ZR:VA;1)
298.15 -135.95; 6000 N !

PARAMETER C11(BCC_A2,TI,MO,NB:VA;0)
298.15 -29.97; 6000 N !

PARAMETER C11(BCC_A2,TI,MO,SN:VA;0)
298.15 -83.85; 6000 N !

PARAMETER C11(BCC_A2,TI,MO,TA:VA;0)
298.15 -106.53; 6000 N !

PARAMETER C11(BCC_A2,TI,MO,ZR:VA;0)
298.15 -245.27; 6000 N !

PARAMETER C11(BCC_A2,TI,NB,SN:VA;0)
298.15 -41.52; 6000 N !

PARAMETER C11(BCC_A2,TI,NB,TA:VA;0)

298.15 -93.77; 6000 N !
PARAMETER C11(BCC_A2, TI, NB, ZR:VA;0)
298.15 -220.35; 6000 N !
PARAMETER C11(BCC_A2, TI, SN, TA:VA;0)
298.15 -95.39; 6000 N !
PARAMETER C11(BCC_A2, TI, SN, ZR:VA;0)
298.15 -155.34; 6000 N !
PARAMETER C11(BCC_A2, TI, TA, ZR:VA;0)
298.15 -149.67; 6000 N !
\$—————
PARAMETER C12(BCC_A2, TI:VA;0)
298.15 +C12BCCTI; 6000 N !
PARAMETER C12(BCC_A2, MO:VA;0)
298.15 +C12BCCMO; 6000 N !
PARAMETER C12(BCC_A2, NB:VA;0)
298.15 +C12BCCNB; 6000 N !
PARAMETER C12(BCC_A2, SN:VA;0)
298.15 +C12BCCSN; 6000 N !
PARAMETER C12(BCC_A2, TA:VA;0)
298.15 +C12BCCTA; 6000 N !
PARAMETER C12(BCC_A2, ZR:VA;0)
298.15 +C12BCCZR; 6000 N !
PARAMETER C12(BCC_A2, TI, MO:VA;0)
298.15 -36.40; 6000 N !
PARAMETER C12(BCC_A2, TI, NB:VA;0)
298.15 -32.39; 6000 N !
PARAMETER C12(BCC_A2, TI, SN:VA;0)
298.15 +15.90; 6000 N !
PARAMETER C12(BCC_A2, TI, SN:VA;1)
298.15 -146.80; 6000 N !
PARAMETER C12(BCC_A2, TI, TA:VA;0)
298.15 +38.05; 6000 N !
PARAMETER C12(BCC_A2, TI, ZR:VA;0)

298.15 -110.53; 6000 N !
PARAMETER C12(BCC_A2, TI, ZR:VA;1)
298.15 +78.00; 6000 N !
PARAMETER C12(BCC_A2, TI, MO, NB:VA;0)
298.15 +13.97; 6000 N !
PARAMETER C12(BCC_A2, TI, MO, SN:VA;0)
298.15 +31.80; 6000 N !
PARAMETER C12(BCC_A2, TI, MO, TA:VA;0)
298.15 -12.35; 6000 N !
PARAMETER C12(BCC_A2, TI, MO, ZR:VA;0)
298.15 +50.43; 6000 N !
PARAMETER C12(BCC_A2, TI, NB, SN:VA;0)
298.15 +25.52; 6000 N !
PARAMETER C12(BCC_A2, TI, NB, TA:VA;0)
298.15 -15.80; 6000 N !
PARAMETER C12(BCC_A2, TI, NB, ZR:VA;0)
298.15 +72.10; 6000 N !
PARAMETER C12(BCC_A2, TI, SN, TA:VA;0)
298.15 -10.94; 6000 N !
PARAMETER C12(BCC_A2, TI, SN, ZR:VA;0)
298.15 +68.86; 6000 N !
PARAMETER C12(BCC_A2, TI, TA, ZR:VA;0)
298.15 -8.91; 6000 N !
\$

PARAMETER C44(BCC_A2, TI:VA;0)
298.15 +C44BCCTI; 6000 N !
PARAMETER C44(BCC_A2, MO:VA;0)
298.15 +C44BCCMO; 6000 N !
PARAMETER C44(BCC_A2, NB:VA;0)
298.15 +C44BCCNB; 6000 N !
PARAMETER C44(BCC_A2, SN:VA;0)
298.15 +C44BCCSN; 6000 N !
PARAMETER C44(BCC_A2, TA:VA;0)

298.15 +C44BCCTA; 6000 N !
PARAMETER C44(BCC_A2,ZR:VA;0)
298.15 +C44BCCZR; 6000 N !
PARAMETER C44(BCC_A2,TI,MO:VA;0)
298.15 -142.90; 6000 N !
PARAMETER C44(BCC_A2,TI,NB:VA;0)
298.15 -41.54; 6000 N !
PARAMETER C44(BCC_A2,TI,NB:VA;1)
298.15 -41.95; 6000 N !
PARAMETER C44(BCC_A2,TI,SN:VA;0)
298.15 +59.75; 6000 N !
PARAMETER C44(BCC_A2,TI,SN:VA;1)
298.15 -94.38; 6000 N !
PARAMETER C44(BCC_A2,TI,TA:VA;0)
298.15 -51.96; 6000 N !
PARAMETER C44(BCC_A2,TI,ZR:VA;0)
298.15 +70.06; 6000 N !
PARAMETER C44(BCC_A2,TI,MO,NB:VA;0)
298.15 +9.72; 6000 N !
PARAMETER C44(BCC_A2,TI,MO,SN:VA;0)
298.15 +74.73; 6000 N !
PARAMETER C44(BCC_A2,TI,MO,TA:VA;0)
298.15 +5.27; 6000 N !
PARAMETER C44(BCC_A2,TI,MO,ZR:VA;0)
298.15 -44.96; 6000 N !
PARAMETER C44(BCC_A2,TI,NB,SN:VA;0)
298.15 +67.85; 6000 N !
PARAMETER C44(BCC_A2,TI,NB,TA:VA;0)
298.15 +4.25; 6000 N !
PARAMETER C44(BCC_A2,TI,NB,ZR:VA;0)
298.15 -55.29; 6000 N !
PARAMETER C44(BCC_A2,TI,SN,TA:VA;0)
298.15 +67.85; 6000 N !

```
PARAMETER C44(BCC_A2, TI, SN, ZR:VA;0)
298.15 +3.85; 6000 N !
PARAMETER C44(BCC_A2, TI, TA, ZR:VA;0)
298.15 -23.70; 6000 N !
$*****
*****LIST_OF_REFERENCES
NUMBER SOURCE
!
```

Appendix E | Pycalphad script

This code is used in pycalphad to plot the elastic moduli and elastic properites as a function of composition. A tdb file must be loaded into the script. In the present work the tdb file in appendix D is used.

```
import matplotlib
from matplotlib.axes import Axes
from matplotlib.patches import Polygon
from matplotlib.path import Path
from matplotlib.ticker import NullLocator, Formatter, FixedLocator
from matplotlib.transforms import Affine2D, BboxTransformTo, IdentityTransform
from matplotlib.projections import register_projection
import matplotlib.spines as mspines
import matplotlib.axis as maxis
import matplotlib.pyplot as plt

import numpy as np

class TriangularAxes(Axes):
    """
    A custom class for triangular projections.
    """

    name = 'triangular'

    def __init__(self, *args, **kwargs):
        Axes.__init__(self, *args, **kwargs)
        self.set_aspect(1, adjustable='box', anchor='SW')
        self.cla()
```

```

def __init__(self):
    self.xaxis = maxis.XAxis(self)
    self.yaxis = maxis.YAxis(self)
    self._update_transScale()

def cla(self):
    """
    Override to set up some reasonable defaults.
    """
    # Don't forget to call the base class
    Axes.cla(self)

    x_min = 0
    y_min = 0
    x_max = 1
    y_max = 1
    x_spacing = 0.1
    y_spacing = 0.1
    self.xaxis.set_minor_locator(NullLocator())
    self.yaxis.set_minor_locator(NullLocator())
    self.xaxis.set_ticks_position('bottom')
    self.yaxis.set_ticks_position('left')
    Axes.set_xlim(self, x_min, x_max)
    Axes.set_ylim(self, y_min, y_max)
    self.xaxis.set_ticks(np.arange(x_min, x_max+x_spacing, x_spacing))
    self.yaxis.set_ticks(np.arange(y_min, y_max+y_spacing, y_spacing))

def __set__lim_and__transforms(self):
    """
    This is called once when the plot is created to set up all the
    transforms for the data, text and grids.
    """
    # There are three important coordinate spaces going on here:
    #
    # 1. Data space: The space of the data itself
    #
    # 2. Axes space: The unit rectangle (0, 0) to (1, 1)
    # covering the entire plot area.
    #
    # 3. Display space: The coordinates of the resulting image,
    # often in pixels or dpi/inch.

```

```

# This function makes heavy use of the Transform classes in
# ``lib/matplotlib/transforms.py``. For more information, see
# the inline documentation there.

# The goal of the first two transformations is to get from the
# data space (in this case longitude and latitude) to axes
# space. It is separated into a non-affine and affine part so
# that the non-affine part does not have to be recomputed when
# a simple affine change to the figure has been made (such as
# resizing the window or changing the dpi).

# 1) The core transformation from data space into
# rectilinear space defined in the HammerTransform class.
self.transProjection = IdentityTransform()
# 2) The above has an output range that is not in the unit
# rectangle, so scale and translate it so it fits correctly
# within the axes. The peculiar calculations of xscale and
#yscale are specific to a Aitoff-Hammer projection, so don't
# worry about them too much.
self.transAffine = Affine2D.from_values(
    1., 0, 0.5, np.sqrt(3)/2., 0, 0)
self.transAffinedep = Affine2D.from_values(
    1., 0, -0.5, np.sqrt(3)/2., 0, 0)
#self.transAffine = IdentityTransform()

# 3) This is the transformation from axes space to display
# space.
self.transAxes = BboxTransformTo(self.bbox)

# Now put these 3 transforms together -- from data all the way
# to display coordinates. Using the '+' operator, these
# transforms will be applied "in order". The transforms are
# automatically simplified, if possible, by the underlying
# transformation framework.
self.transData = \
    self.transProjection + \
    self.transAffine + \
    self.transAxes

# The main data transformation is set up. Now deal with

```

```

# gridlines and tick labels.

# Longitude gridlines and ticklabels. The input to these
# transforms are in display space in x and axes space in y.
# Therefore, the input values will be in range (-xmin, 0),
# (xmax, 1). The goal of these transforms is to go from that
# space to display space. The tick labels will be offset 4
# pixels from the equator.

self._xaxis._pretransform = IdentityTransform()
self._xaxis._transform = \
    self._xaxis._pretransform + \
    self.transData
self._xaxis._text1._transform = \
    Affine2D().scale(1.0, 0.0) + \
    self.transData + \
    Affine2D().translate(0.0, -20.0)
self._xaxis._text2._transform = \
    Affine2D().scale(1.0, 0.0) + \
    self.transData + \
    Affine2D().translate(0.0, -4.0)

# Now set up the transforms for the latitude ticks. The input to
# these transforms are in axes space in x and display space in
# y. Therefore, the input values will be in range (0, -ymin),
# (1, ymax). The goal of these transforms is to go from that
# space to display space. The tick labels will be offset 4
# pixels from the edge of the axes ellipse.

self._yaxis._transform = self.transData
yaxis_text_base = \
    self.transProjection + \
    (self.transAffine + \
    self.transAxes)
self._yaxis._text1._transform = \
    yaxis_text_base + \
    Affine2D().translate(-8.0, 0.0)
self._yaxis._text2._transform = \
    yaxis_text_base + \
    Affine2D().translate(8.0, 0.0)

```

```

def get_xaxis_transform(self, which='grid'):
    assert which in ['tick1', 'tick2', 'grid']
    return self._xaxis_transform

def get_xaxis_text1_transform(self, pad):
    return self._xaxis_text1_transform, 'bottom', 'center'

def get_xaxis_text2_transform(self, pad):
    return self._xaxis_text2_transform, 'top', 'center'

def get_yaxis_transform(self, which='grid'):
    assert which in ['tick1', 'tick2', 'grid']
    return self._yaxis_transform

def get_yaxis_text1_transform(self, pad):
    return self._yaxis_text1_transform, 'center', 'right'

def get_yaxis_text2_transform(self, pad):
    return self._yaxis_text2_transform, 'center', 'left'

def _gen_axes_spines(self):
    dep_spine = mspines.Spine.linear_spine(self,
                                             'right')
    # Fix dependent axis to be transformed the correct way
    dep_spine.set_transform(self.transAffinedep + self.transAxes)
    return {'left': mspines.Spine.linear_spine(self,
                                                'left'),
            'bottom': mspines.Spine.linear_spine(self,
                                                 'bottom'),
            'right': dep_spine}

def _gen_axes_patch(self):
    """
    Override this method to define the shape that is used for the
    background of the plot. It should be a subclass of Patch.
    Any data and gridlines will be clipped to this shape.
    """
    return Polygon([[0, 0], [0.5, np.sqrt(3)/2], [1, 0]], closed=True)

# Interactive panning and zooming is not supported with this projection,

```

```

# so we override all of the following methods to disable it.
def can_zoom(self):
    """
    Return True if this axes support the zoom box
    """
    return False

def start_pan(self, x, y, button):
    pass

def end_pan(self):
    pass

def drag_pan(self, button, key, x, y):
    pass

# Now register the projection with matplotlib so the user can select
# it.
register_projection(TriangularAxes)

import pycalphad.io.tdb_keywords
pycalphad.io.tdb_keywords.TDB_PARAM_TYPES.extend\
([ 'EM', 'BULK', 'SHEAR', 'C11', 'C12', 'C44' ])
from pycalphad import Database, Model, equilibrium, calculate
import numpy as np
import pycalphad.variables as v
import sympy
from tinydb import where

class ElasticModel(Model):
    def build_phase(self, dbe):
        phase = dbe.phases[self.phase_name]
        param_search = dbe.search
        # EM, BULK, SHEAR, C11, C12, C44
        for prop in [ 'EM', 'BULK', 'SHEAR', 'C11', 'C12', 'C44' ]:
            prop_param_query = (
                (where('phase_name') == phase.name) & \
                (where('parameter_type') == prop) & \
                (where('constituent_array').test(self._array_validity)))

```

```

)
prop_val = self.redlich_kister_sum \
(phase, param_search, prop_param_query).subs(dbe.symbols)
setattr(self, prop, prop_val)

dbf = Database('ElasticTi.tdb')
mod = ElasticModel(dbf, ['TI', 'SN', 'ZR', 'VA'], 'BCC_A2')
symbols = dict([(sympy.Symbol(s), val) for s, val in dbf.symbols.items()])
mod.C11 = mod.C11.xreplace(symbols)
mod.C12 = mod.C12.xreplace(symbols)
mod.C44 = mod.C44.xreplace(symbols)
x1 = np.linspace(0, 1, num=100)
x2 = np.linspace(0, 1, num=100)
mesh = np.meshgrid(x1, x2)
X = mesh[0]
Y = mesh[1]
mesh_arr = np.array(mesh)
mesh_arr = np.moveaxis(mesh_arr, 0, 2)
dep_col = 1 - np.sum(mesh_arr, axis=-1, keepdims=True)
mesh_arr = np.concatenate((mesh_arr, dep_col), axis=-1)
mesh_arr = np.concatenate((mesh_arr, np.ones(mesh_arr.shape[:-1] + (1,))), axis=-1)
orig_shape = tuple(mesh_arr.shape[:-1])
mesh_arr = mesh_arr.reshape(-1, mesh_arr.shape[-1])
mesh_arr[np.any(mesh_arr < 0, axis=-1), :] = np.nan
res_c11 = calculate(dbf, ['TI', 'SN', 'TA', 'VA'], 'BCC_A2', T=300, P=101325,
    model=mod, output='C11', points=mesh_arr)
res_c11 = res_c11.C11.values.reshape(orig_shape)
res_c12 = calculate(dbf, ['TI', 'SN', 'TA', 'VA'], 'BCC_A2', T=300, P=101325,
    model=mod, output='C12', points=mesh_arr)
res_c12 = res_c12.C12.values.reshape(orig_shape)
res_c44 = calculate(dbf, ['TI', 'SN', 'TA', 'VA'], 'BCC_A2', T=300, P=101325,
    model=mod, output='C44', points=mesh_arr)
res_c44 = res_c44.C44.values.reshape(orig_shape)

```

```

import numpy as np
def compute_moduli(c11, c12, c44):
    """Consume elastic stiffness constants and, under symmetry assumptions, compute
    bulk modulus, shear modulus, and Young's modulus.

```

Parameters

c11: float64 array-like
c12: float64 array-like
c44: float64 array-like

Returns

```

B, G, Y : tuple of float64 array-likes """
# Ported from a matlab code
c11 = np.array(c11)
c12 = np.array(c12)
c44 = np.array(c44)
cij = np.zeros(c11.shape + (6,6))
cij [..., 0, 0] = cij [..., 1, 1] = cij [..., 2, 2] = c11
cij [..., 0, 1] = cij [..., 1, 0] = cij [..., 0, 2] = \
cij [..., 2, 0] = cij [..., 1, 2] = cij [..., 2, 1] = c12
cij [..., 3, 3] = cij [..., 4, 4] = cij [..., 5, 5] = c44
sij = np.linalg.inv(cij)
A_c = (cij [..., 0, 0] + cij [..., 1, 1] + cij [..., 2, 2]) / 3.
B_c = (cij [..., 0, 1] + cij [..., 0, 2] + cij [..., 1, 2]) / 3.
C_c = (cij [..., 3, 3] + cij [..., 4, 4] + cij [..., 5, 5]) / 3.
A_s = (sij [..., 0, 0] + sijs [..., 1, 1] + sijs [..., 2, 2]) / 3.
B_s = (sij [..., 0, 1] + sijs [..., 0, 2] + sijs [..., 1, 2]) / 3.
C_s = (sij [..., 3, 3] + sijs [..., 4, 4] + sijs [..., 5, 5]) / 3.
Bv = (A_c + 2*B_c) / 3.
Gv = (A_c - B_c + 3*C_c) / 5.
Br = 1. / (3*A_s + 6*B_s)
Gr = 5. / (4*A_s - 4*B_s + 3*C_s)
Bvrh = (Br + Bv) / 2.
Gvrh = (Gr + Gv) / 2.
Yvrh = (9*Bvrh*Gvrh) / (Gvrh + 3*Bvrh)
return Bvrh, Gvrh, Yvrh

```

bulk_modulus, shear_modulus, young_modulus = \

```

compute_moduli(res_c11, res_c12, res_c44)

%matplotlib inline
import matplotlib.pyplot as plt

fig = plt.figure(figsize=(12,12))
ax = fig.gca(projection='triangular')
CS = ax.contour(X, Y, bulk_modulus, linewidths=4, \
levels=list(range(100, 300, 10)), cmap='cool')
ax.clabel(CS, inline=1, fontsize=13, fmt='%1.0f')
#PCM=ax.get_children()[0] #get the mappable,
#the 1st and the 2nd are the x and y axes
#plt.colorbar(PCM, ax=ax)
ax.set_xlabel('x(Mo)', fontsize=18)
ax.set_ylabel('x(Nb)', fontsize=18, rotation=60, labelpad=-180)
ax.tick_params(axis='both', which='major', labelsize=18)
ax.tick_params(axis='both', which='minor', labelsize=18)
ax.set_title('Bulk modulus')
#fig.savefig('TiMoNb-Bulk.pdf')

%matplotlib inline
import matplotlib.pyplot as plt

fig = plt.figure(figsize=(12,12))
ax = fig.gca(projection='triangular')
CS = ax.contour(X, Y, shear_modulus, linewidths=4, \
levels=list(range(0, 150, 5)), cmap='cool')
ax.clabel(CS, inline=1, fontsize=13, fmt='%1.0f')
#PCM=ax.get_children()[0] #get the mappable,
#the 1st and the 2nd are the x and y axes
#plt.colorbar(PCM, ax=ax)
ax.set_xlabel('x(Mo)', fontsize=18)
ax.set_ylabel('x(Nb)', fontsize=18, rotation=60, labelpad=-180)

```

```

ax.tick_params(axis='both', which='major', labelsize=18)
ax.tick_params(axis='both', which='minor', labelsize=18)
ax.set_title('Shear_modulus')
#fig.savefig('TiMoNb-Shear.pdf')

%matplotlib inline
import matplotlib.pyplot as plt

fig = plt.figure(figsize=(12,12))
ax = fig.gca(projection='triangular')
CS = ax.contour(X, Y, young_modulus, linewidths=4, \
levels=list(range(0, 350, 10)), cmap='cool')
ax.clabel(CS, inline=1, fontsize=13, fmt='%1.0f')
#PCM=ax.get_children()[0] #get the mappable,
#the 1st and the 2nd are the x and y axes
#plt.colorbar(PCM, ax=ax)
ax.set_xlabel('x(Mo)', fontsize=18)
ax.set_ylabel('x(Nb)', fontsize=18, rotation=60, labelpad=-180)
ax.tick_params(axis='both', which='major', labelsize=18)
ax.tick_params(axis='both', which='minor', labelsize=18)
ax.set_title('Young\s_modulus')
#fig.savefig('TiMoNb-Young.pdf')

```

Appendix F | Ti-Nb Experimental Elastic Data

The experimentally determined E values for the Ti-Nb system reviewed and averaged for chapter 7 are listed here [6–9].

x(Nb)	x(Ti)	E (GPa)	Reference
0.00	1.00	117.16	[6]
0.00	1.00	132.00	[8]
0.00	1.00	115.77	[7]
0.00	1.00	108.30	[9]
0.01	0.99	112.30	[6]
0.01	0.99	112.74	[7]
0.02	0.98	109.05	[6]
0.02	0.98	107.61	[7]
0.05	0.95	79.46	[6]
0.05	0.95	78.69	[7]
0.05	0.95	80.27	[6]
0.08	0.92	66.49	[6]
0.08	0.92	66.33	[7]
0.09	0.91	66.89	[6]
0.09	0.91	70.58	[9]
0.10	0.90	66.49	[6]
0.10	0.90	115.00	[8]
0.10	0.90	91.00	[8]
0.10	0.90	66.09	[7]
0.11	0.89	77.99	[7]

x(Nb)	x(Ti)	E (GPa)	Reference
0.11	0.89	79.46	[6]
0.18	0.82	92.43	[6]
0.18	0.82	93.62	[7]
0.19	0.81	65.27	[6]
0.19	0.81	63.24	[6]
0.20	0.80	75.00	[8]
0.20	0.80	89.00	[8]
0.20	0.80	68.85	[9]
0.22	0.78	71.46	[7]
0.22	0.78	72.63	[9]
0.22	0.78	68.62	[9]
0.23	0.77	72.16	[6]
0.23	0.77	103.64	[7]
0.23	0.77	60.34	[9]
0.23	0.77	67.24	[9]
0.24	0.76	65.16	[9]
0.24	0.76	57.07	[9]
0.25	0.75	71.76	[6]
0.25	0.75	74.00	[8]
0.25	0.75	78.00	[8]
0.25	0.75	66.33	[7]
0.26	0.74	61.85	[9]
0.26	0.74	73.09	[9]
0.26	0.74	82.19	[7]
0.26	0.74	60.50	[7]
0.26	0.74	67.70	[6]
0.26	0.74	54.31	[9]
0.27	0.73	56.46	[9]
0.27	0.73	52.76	[9]
0.29	0.71	62.83	[7]
0.29	0.71	61.43	[7]
0.30	0.70	67.70	[6]
0.30	0.70	62.69	[9]

x(Nb)	x(Ti)	E (GPa)	Reference
0.30	0.70	72.00	[8]
0.30	0.70	69.00	[8]
0.30	0.70	69.31	[9]
0.30	0.70	67.96	[7]
0.34	0.66	76.21	[9]
0.34	0.66	86.02	[9]
0.34	0.66	74.26	[7]
0.34	0.66	75.84	[9]
0.34	0.66	75.00	[6]
0.36	0.64	73.78	[6]
0.39	0.61	76.62	[6]
0.43	0.57	84.00	[7]

This section introduces a theoretic framework to predict the formation of a solid with a mixture of multiple states. Our theoretic framework implies that the competition of stable and metastable states, results in an increase of entropy as a function of temperature. The increased entropy is what stabilizes the statistic existance of the metastable states similarly to how entropy stabilizes Ti in the bcc structure. The combined Helmholtz energy can be expressed by [134]:

$$F_c = -k_B T \left(\sum \frac{Z_i}{Z_c} \ln Z_i - \sum \frac{Z_i}{Z_c} \ln \frac{Z_i}{Z_c} \right) \quad (\text{F.1})$$

where Z_i represents the canonical partition function of a state:

$$Z_i = e^{-\frac{F_i}{k_B T}} = \sum_k e^{-\frac{E_{ik}}{k_B T}} \quad (\text{F.2})$$

where F_i is the Helmholtz energy of state i and E_{ik} is the energy eigenvalues of microstate k in the i state. Z_c represents the combined system expressed by [135]:

$$Z_c = e^{-\frac{F_c}{k_B T}} = \sum_j e^{-\frac{E_{cj}}{k_B T}} \quad (\text{F.3})$$

where F_c is the Helmholtz energy of the system and E_{cj} is the energy eigenvalues of microstate j in the combined state, c . Another way to write the combined Helmholtz energy, based on these equations, is:

$$F_c = \sum p_i F_i - TS_{SCE} \quad (\text{F.4})$$

where p_i is:

$$p_i = \frac{Z_i}{Z_c} \quad (\text{F.5})$$

and S_{SCE} is the state configurational entropy. The S_{SCE} is what stabilizes the phase formation and is predicted by:

$$S_{SCE} = -k_B \sum p_i \ln p_i \quad (\text{F.6})$$

This entropy takes into account the statistical competition between the states making the combined Helmholtz energy more accurate.

Bibliography

- [1] WU, C., Y. XIN, X. WANG, and J. LIN (2010) “Effects of Ta content on the phase stability and elastic properties of β Ti-Ta alloys from first-principles calculations,” *Solid State Sciences*, **12**(12), pp. 2120–2124.
- [2] IKEHATA, H., N. NAGASAKO, T. FURUTA, A. FUKUMOTO, K. MIWA, and T. SAITO (2004) “First-principles calculations for development of low elastic modulus Ti alloys,” *Physical Review B*, **70**(17), p. 174113.
- [3] ZHOU, Y. L., M. NIINOMI, and T. AKAHORI (2004) “Effects of Ta content on Young’s modulus and tensile properties of binary Ti-Ta alloys for biomedical applications,” *Materials Science and Engineering: A*, **371**(1-2), pp. 283–290.
- [4] ZHOU, Y.-L. and M. NIINOMI (2009) “Ti-25Ta alloy with the best mechanical compatibility in Ti-Ta alloys for biomedical applications,” *Materials Science and Engineering: C*, **29**(3), pp. 1061–1065.
- [5] FEDOTOV, S., T. CHELIDZE, Y. KOVNERISTYY, and V. SANADZE (1985) “Phase structure, critical points MS and AS of martensitic transformations and elastic properties of metastable alloys of the Ti-Ta system,” *Phys. Met. Metall.*, **60**(3), pp. 139–143.
- [6] TIMOSHEVSKII, A., S. YABLONOVSKII, and O. IVASHISHIN (2011) “First-principles calculations atomic structure and elastic properties of Ti-Nb alloys,” *arXiv preprint arXiv:1111.7182*.
- [7] OZAKI, T., H. MATSUMOTO, S. WATANABE, and S. HANADA (2004) “Beta Ti Alloys with Low Young’s Modulus,” *MATERIALS TRANSACTIONS*, **45**(8), pp. 2776–2779.
- [8] FRIÁK, M., W. COUNTS, D. MA, B. SANDER, D. HOLEC, D. RAABE, and J. NEUGEBAUER (2012) “Theory-guided materials design of multi-phase Ti-Nb alloys with bone-matching elastic properties,” *Materials*, **5**(10), pp. 1853–1872.

- [9] KARRE, R., M. NIRANJAN, and S. DEY (2015) “First principles theoretical investigations of low Young’s modulus beta Ti-Nb and Ti-Nb-Zr alloys compositions for biomedical applications,” *Materials Science and Engineering: C*, **50**, pp. 52–58.
- [10] MATSUMOTO, H., S. WATANABE, N. MASAHASHI, and S. HANADA (2006) “Composition dependence of Young’s modulus in Ti-V, Ti-Nb, and Ti-V-Sn alloys,” *Metallurgical and Materials Transactions A*, **37**(11), pp. 3239–3249.
- [11] XIONG, W., Y. DU, Y. LIU, B. HUANG, H. XU, H. CHEN, and Z. PAN (2004) “Thermodynamic assessment of the Mo-Nb-Ta system,” *Calphad-Computer Coupling of Phase Diagrams and Thermochemistry*, **28**(2), pp. 133–140.
- [12] PEREZ, R. and B. SUNDMAN (2003) “Thermodynamic assessment of the Mo-Zr binary phase diagram,” *Calphad-Computer Coupling of Phase Diagrams and Thermochemistry*, **27**(3), pp. 253–262.
- [13] GUILLERMET, A. (1991) “Thermodynamic analysis of the stable phases in the Zr-Nb system and calculation of the phase-diagram,” *Zeitschrift Fur Metallkunde*, **82**(6), pp. 478–487.
- [14] ABRIATA, J. P. and J. C. BOLCICH (1982) “The Nb-Zr (Niobium-Zirconium) system,” *Bulletin of alloy phase diagrams*, **3**(1), pp. 34–44.
- [15] GUILLERMET, A. (1995) “Phase-diagram and thermochemical properties of the Zr-Ta system - an assessment based on Gibbs energy modeling,” *Journal of Alloys and Compounds*, **226**(1-2), pp. 174–184.
- [16] ANSARA, I., A. DINSDALE, and M. RAND (1998) *COST 507: thermochemical database for light metal alloys*, vol. 2, European Communities, Brussels and Luxembourg.
- [17] MURRAY, J. (1981) “The Mo-Ti (Molybdenum-Titanium) system,” *Bulletin of Alloy Phase Diagrams*, **2**(2), pp. 185–192.
- [18] UESUGI, T., S. MIYAMAE, and K. HIGASHI (2013) “Enthalpies of Solution in Ti-X (X= Mo, Nb, V and W) Alloys from First-Principles Calculations,” *Materials Transactions*, **54**(4), pp. 484–492.
- [19] ZHANG, Y., H. LIU, and Z. JIN (2001) “Thermodynamic assessment of the Nb-Ti system,” *Calphad-Computer Coupling of Phase Diagrams and Thermochemistry*, **25**(2), pp. 305–317.
- [20] KUMAR, K., P. WOLLANTS, and L. DELAEY (1994) “Thermodynamic calculation of Nb-Ti-V phase diagram,” *CALPHAD*, **18**(1), pp. 71–79.

- [21] ——— (1994) “Thermodynamic assessment of the Ti-Zr system and calculation of the Nb-Ti-Zr phase-diagram,” *Journal of Alloys and Compounds*, **206**(1), pp. 121–127.
- [22] MURRAY, J. L. (1987) “Phase diagrams of binary titanium alloys,” *ASM International*, p. 354.
- [23] NIKITIN, P. and V. MIKHEYEV (1971) “Examination of titanium corner of Ti-Ta-Mo equilibrium diagram,” *Russian Metallurgy-Metally-USSR*, (1), pp. 144–147.
- [24] KAR, S. and D. LIPKIN (2008) “A CALPHAD-based phase equilibrium model of Mo-Ti-Zr-C,” in *TMS 2008 Annual Meeting Supplemental Proceedings, Vol 2: Materials Characterization, Computation and Modeling*, Minerals, Metals & Materials Soc, Warrendale, pp. 237–243.
- [25] PROKOSHKIN, D. A. and M. I. ZAKHAROVA (1967) “Phase equilibrium in the molybdenum-titanium-zirconium system(Ternary phase diagram of Mo-Ti-Zr system from eleven isothermal cross sections),” in *AKADEMIA NAUK SSSR, DOKLADY*, vol. 172, pp. 1382–1384.
- [26] NA, L. and W. WARNE (2001) “Estimation of the Nb-Ti-Ta phase diagram,” *Ieee Transactions on Applied Superconductivity*, **11**(1), pp. 3800–3803.
- [27] TOKUNAGA, T., S. MATSUMOTO, H. OHTANI, and M. HASEBE (2007) “Thermodynamic calculation of phase equilibria in the Nb-Ni-Ti-Zr quaternary system,” *Materials transactions*, **48**(2), pp. 89–96.
- [28] LIN, L., L. DELAEY, O. VANDERBIEST, and P. WOLLANTS (1996) “Calculation of isothermal sections of three ternary Ti-Zr-X systems,” *Scripta Materialia*, **34**(9), pp. 1411–1416.
- [29] HOCH, M. and D. BUTRYMOW (1964) “System tantalum-titanium-zirconium-oxygen at 1500 degrees C,” *Transactions of the Metallurgical Society of AIME*, **230**(1), pp. 186–192.
- [30] TAIOLI, S., C. CAZORLA, M. J. GILLAN, and D. ALFÈ (2007) “Melting curve of tantalum from first principles,” *Physical Review B*, **75**(21), p. 214103.
- [31] OLIJNYK, H. (1992) “Pressure dependence of Raman phonons of metallic β -Sn,” *Physical Review B*, **46**(10).
- [32] DINSDALE, A. (1991) “SGTE Data for Pure Elements,” *CALPHAD*, **15**(4), pp. 317–425.

- [33] TOFFOLON, C., C. SERVANT, and B. SUNDMAN (1998) “Thermodynamic assessment of the Nb-Sn system,” *Journal of Phase Equilibria*, **19**(5), pp. 479–485.
- [34] ZHANG, W.-D., Y. LIU, H. WU, M. SONG, T.-Y. ZHANG, X.-D. LAN, and T.-H. YAO (2015) “Elastic modulus of phases in Ti-Mo alloys,” *Materials Characterization*, **106**, pp. 302–307.
- [35] BOYER, R., G. WELSCH, and E. COLLINGS (1994) “Materials Properties Handbook: Titanium Alloys,” *ASM International, Materials Park, OH*.
- [36] SUNG, B.-S., T.-E. PARK, and Y.-H. YUN (2015) “Microstructures and electrochemical behavior of Ti-Mo alloys for biomaterials,” *Advances in Materials Science and Engineering*, **2015**(Article ID 872730), pp. 1–7.
- [37] TANE, M., S. AKITA, T. NAKANO, K. HAGIHARA, Y. UMAKOSHI, M. NIINOMI, H. MORI, and H. NAKAJIMA (2010) “Low Young’s modulus of Ti-Nb-Ta-Zr alloys caused by softening in shear moduli c' and c_{44} near lower limit of body-centered cubic phase stability,” *Acta Materialia*, **58**(20), pp. 6790–6798.
- [38] GEETHA, M., A. SINGH, R. ASOKAMANI, and A. GOGIA (2009) “Ti based biomaterials, the ultimate choice for orthopaedic implants - A review,” *Progress in Materials Science*, **54**(3), pp. 397–425.
- [39] MOHAMMED, M., Z. KHAN, and A. SIDDIQUEE (2014) “Beta titanium alloys: the lowest elastic modulus for biomedical applications: a review,” *International Journal of Chemical, Molecular, Nuclear, Materials and Metallurgical Engineering*, **8**(8), pp. 788–793.
- [40] NIINOMI, M., M. NAKAI, and J. HIEDA (2012) “Development of new metallic alloys for biomedical applications,” *Acta Biomaterialia*, **8**(11), pp. 3888–3903.
- [41] NOZOE, F., H. MATSUMOTO, T. K. JUNG, S. WATANABE, T. SABURI, and S. HANADA (2007) “Effect of low temperature aging on superelastic behavior in biocompatible beta TiNbSn Alloy,” *Materials transactions*, **48**(11), pp. 3007–3013.
- [42] OTIS, R. and Z.-K. LIU (2017) “pycalphad: CALPHAD-based computational thermodynamics in Python,” *Journal of Open Research Software*, **5**(1), pp. 1–11.
- [43] LONG, M. and H. RACK (1998) “Titanium alloys in total joint replacement-a materials science perspective,” *Biomaterials*, **19**(18), pp. 1621–1639.

- [44] KURTZ, S. (2007) “Projections of primary and revision hip and knee arthroplasty in the United States from 2005 to 2030,” *The Journal of Bone and Joint Surgery (American)*, **89**(4), pp. 780–785.
- [45] KRISHNA, B., S. BOSE, and A. BANDYOPADHYAY (2007) “Low stiffness porous Ti structures for load-bearing implants,” *Acta biomaterialia*, **3**(6), pp. 997–1006.
- [46] NIINOMI, M. (2003) “Recent research and development in titanium alloys for biomedical applications and healthcare goods,” *Science and Technology of Advanced Materials*, **4**(5), pp. 445–454.
- [47] ITO, A., Y. OKAZAKI, T. TATEISHI, and Y. ITO (1995) “In vitro biocompatibility, mechanical properties, and corrosion resistance of Ti-Zr-Nb-Ta-Pd and Ti-Sn-Nb-Ta-Pd alloys,” *Journal of Biomedical Materials Research*, **29**(7), pp. 893–899.
- [48] JAIN, A., S. ONG, G. HAUTIER, W. CHEN, W. RICHARDS, S. DACEK, S. CHOLIA, D. GUNTER, D. SKINNER, and G. CEDER (2013) “The Materials Project: A materials genome approach to accelerating materials innovation,” *Apl Materials*, **1**(1), p. 11002.
- [49] ANTOLIN, N., O. RESTREPO, and W. WINDL (2012) “Fast free-energy calculations for unstable high-temperature phases,” *Physical Review B*, **86**(5), p. 54119.
- [50] MEI, Z. Z. G. (2011) *First-principles Thermodynamics of Phase Transition: from Metal to Oxide*, Ph.D. thesis.
- [51] BRAILOVSKI, V., S. PROKOSHKIN, M. GAUTHIER, K. INAEKYAN, S. DUBINSKIY, M. PETRZHIK, and M. FILONOV (2011) “Bulk and porous metastable beta Ti-Nb-Zr (Ta) alloys for biomedical applications,” *Materials Science and Engineering: C*, **31**(3), pp. 643–657.
- [52] TANE, M., S. AKITA, T. NAKANO, K. HAGIHARA, Y. UMAKOSHI, M. NIINOMI, and H. NAKAJIMA (2008) “Peculiar elastic behavior of Ti-Nb-Ta-Zr single crystals,” *Acta Materialia*, **56**(12), pp. 2856–2863.
- [53] KHACHATURYAN, A. (1985) “Theory of structural transformations in solids,” *Wiley, New York, Jacobs AE, Phys. Rev. B*, **31**, p. 5984.
- [54] SALJE, E. (1990) “Phase transitions in ferroelastic and co-elastic crystals,” *Ferroelectrics*, **104**(1), pp. 111–120.
- [55] HOHENBERG, P. and W. KOHN (1964) “Inhomogeneous Electron Gas,” *Physical Review*, **136**(3B), pp. B864–B871.

- [56] KOHN, W. and L. SHAM (1965) “Self-Consistent Equations Including Exchange and Correlation Effects,” *Phys. Rev.*, **140**, pp. 1133–1138.
- [57] PERDEW, J. and Y. WANG (1992) “Accurate and simple analytic representation of the electron-gas correlation energy,” *Physical Review B*, **45**(23), p. 13244.
- [58] PERDEW, J., K. BURKE, and M. ERNZERHOF (1996) “Generalized gradient approximation made simple,” *Physical Review Letters*, **77**(18), pp. 3865–3868.
- [59] CUPERLEY, D. M. and B. J. ALDER (1980) “Ground state of the electron gas by a stochastic method,” *Physical Review Letters*, **45**(7), p. 566.
- [60] SHANG, S., Y. WANG, D. KIM, and Z.-K. LIU (2010) “First-principles thermodynamics from phonon and Debye model: Application to Ni and Ni₃Al,” *Computational Materials Science*, **47**(4), pp. 1040–1048.
- [61] KRESSE, G. and J. FURTHMÜLLER (1996) “Efficiency of ab-initio total energy calculations for metals and semiconductors using a plane-wave basis set,” *Computational Materials Science*, **6**(1), pp. 15–50.
- [62] KRESSE, G. and D. JOUBERT (1999) “From ultrasoft pseudopotentials to the projector augmented-wave method,” *Physical Review B*, **59**(3), pp. 1758–1775.
- [63] WANG, A., S. SHANG, D. ZHAO, J. WANG, L. CHEN, Y. DU, Z.-K. LIU, T. XU, and S. WANG (2012) “Structural, phonon and thermodynamic properties of fcc-based metal nitrides from first-principles calculations,” *Calphad*, **37**, pp. 126–131.
- [64] MORUZZI, V. L., J. F. JANAK, and K. SCHWARZ (1988) “Calculated thermal properties of metals,” *Physical Review B*, **37**(2), pp. 790–799.
- [65] LIU, X. L., B. K. VANLEEUWEN, S. SHANG, Y. DU, and Z.-K. LIU (2015) “On the scaling factor in Debye-Grüneisen model: A case study of the Mg-Zn binary system,” *Computational Materials Science*, **98**, pp. 34–41.
- [66] WANG, Y., Z.-K. LIU, and L.-Q. CHEN (2004) “Thermodynamic properties of Al, Ni, NiAl, and Ni₃Al from first-principles calculations,” *Acta Materialia*, **52**(9), pp. 2665–2671.
- [67] SHANG, S., Y. WANG, and Z.-K. LIU (2007) “First-principles elastic constants of alpha- and theta-Al₂O₃,” *Applied Physics Letters*, **90**(10), pp. 101909–1–101909–3.
- [68] SIMMONS, G. and H. WANG (1971) *Single Crystal Elastic Constants and Calculated Aggregate Properties: A Handbook*, M.I.T. Press, Cambridge.

- [69] ZUO, Y. and Y. CHANG (1993) “Thermodynamic calculation of the Mg-Cu phase diagram,” *Zeit. Metall.*, **84**(10), pp. 662–667.
- [70] CHUNG, D. H. and W. R. BUESSEM (1967) “The Voigt-Reuss-Hill approximation and elastic moduli of Polycrystalline MgO, CaF₂, β -ZnS, ZnSe, and CdTe,” *Journal of Applied Physics*, **38**(6), pp. 2535–2540.
- [71] BORN, M. and K. HUANG (1998) *Dynamical Theory of Crystal Lattices*, Oxford University Press.
- [72] NYE, J. (1985) *Physical Properties of Crystals: Their Representation by Tensors and Matrices*, Oxford University Press.
- [73] JIANG, C., C. WOLVERTON, J. SOFO, L.-Q. CHEN, and Z.-K. LIU (2004) “First-principles study of binary bcc alloys using special quasirandom structures,” *Physical Review B*, **69**(21), pp. 214202–1–214202–10.
- [74] JIANG, C. (2009) “First-principles study of ternary bcc alloys using special quasi-random structures,” *Acta Materialia*, **57**(16), pp. 4716–4726.
- [75] TOGO, A., F. OBA, and I. TANAKA (2008) “First-principles calculations of the ferroelastic transition between rutile-type and CaCl₂-type SiO₂ at high pressures,” *Physical Review B*, **78**(13), p. 134106.
- [76] ANDERSSON, J.-O., T. HELANDER, L. HÖGLUND, P. SHI, and B. SUNDMAN (2002) “Thermo-Calc & DICTRA, computational tools for materials science,” *Calphad*, **26**(2), pp. 273–312.
- [77] REDLICH, O. and A. T. KISTER (1948) “Algebraic representation of thermodynamic properties and the classification of solutions,” *Industrial & Engineering Chemistry*, **40**(2), pp. 345–348.
- [78] ZACHERL, C., S. SHANG, A. SAENGDEEJING, and Z.-K. LIU (2012) “Phase stability and thermodynamic modeling of the Re-Ti system supplemented by first-principles calculations,” *Calphad*, **38**, pp. 71–80.
- [79] LIU, Z.-K. (2009) “First-principles calculations and CALPHAD modeling of thermodynamics,” *Journal of Phase Equilibria and Diffusion*, **30**(5), pp. 517–534.
- [80] LUKAS, H., S. FRIES, and B. SUNDMAN (2007) *Computational Thermodynamics: the CALPHAD Method*, vol. 131, Cambridge University Press, Cambridge.
- [81] LIU, Z.-K., H. ZHANG, S. GANESHAN, Y. WANG, and S. MATHAUDHU (2010) “Computational modeling of effects of alloying elements on elastic coefficients,” *Scripta Materialia*, **63**(7), pp. 686–691.

- [82] SAUNDERS, N. and A. MIODOWNIK (1998) *CALPHAD (Calculation of Phase Diagrams): A Comprehensive Guide: A Comprehensive Guide*, vol. 1, Elsevier.
- [83] YOUNG, R. and A. LARSON (1998) “Rietveld analysis of X-ray and neutron powder diffraction patterns,” *Atlanta (GA): School of*.
- [84] TORAYA, H. (1986) “Whole-Powder-Pattern Fitting Without Reference to a Structural Model: Application to X-ray Powder Diffractometer Data,” *J. Appl. Cryst.*, **19**, pp. 440–447.
- [85] FULTZ, B., T. KELLEY, M. MCKERN, J. LIN, J. LEE, O. DELAIRE, M. KRESCH, and M. AIVAZIS (2009), “Experimental inelastic neutron scattering,” .
- [86] SQUIRES, G. L. (2012) *Introduction to the theory of thermal neutron scattering*, Cambridge university press.
- [87] MANLEY, M. E. (2001) *From elementary excitations to microstructures: The thermodynamics of metals and alloys across length scales*.
- [88] MANLEY, M. E., R. J. MCQUEENEY, B. FULTZ, R. OSBORN, G. H. KWEI, and P. D. BOGDANOFF (2002) “Vibrational and electronic entropy of β -cerium and γ -cerium measured by inelastic neutron scattering,” *Physical Review B*, **65**(14), p. 144111.
- [89] BLÖCHL, P. (1994) “Projector augmented-wave method,” *Physical Review B*, **50**(24), p. 17953.
- [90] MONKHORST, H. and J. PACK (1976) “Special points for Brillouin-zone integrations,” *Physical Review B*, **13**(12), pp. 5188–5192.
- [91] PREDEL, B. (1997) “Mo-Ti (Molybdenum-Titanium),” in *Li-Mg-Nd-Zr* (O. Madelung, ed.), Springer Berlin Heidelberg, Berlin, Heidelberg, pp. 1–3.
- [92] HOFFMAN, J. R., E. RUDY, S. T. WINDISCH, and A. J. STOSICK (1967) “The constitution of binary molybdenum-carbon alloys(Binary molybdenum-carbon system investigated using X-ray, metallographic, thermoanalytical and melting-point techniques),” *AIME, TRANSACTIONS*, **239**, pp. 1247–1267.
- [93] ENGLISH, J. (1961) *Binary and Ternary Phase Diagrams of Columbium, Molybdenum, Tantalum, and Tungsten, Tech. rep.*
- [94] SCHMITZ-PRANGHE, N. and P. DUENNER (1968) “Gitterstruktur und thermische Ausdehnung der Uebergangsmetalle Scandium, Titan, Vanadin und Mangan,” *Zeitschrift fuer Metallkunde*, **59**, pp. 377–382.

- [95] “Materials Project,” .
URL <http://www.materialsproject.org>
- [96] LAME, M. J., N. ZARIFI, M. NOBAKHTI, A. JAHANDOOST, and MARYAM (2011) “Pseudopotential calculation of the bulk modulus and phonon dispersion of the bcc and hcp structures of titanium,” *Physica Scripta*, **83**(6), p. 65603.
- [97] DOBROMYSLOV, A. V. and N. I. TALUTS (1987) “Structure Investigation of Quenched and Tempered Alloys of the Zr-Ti System,” *Phys. Met. Metallogr.(USSR)*, **63**(1), pp. 114–120.
- [98] YI, C., S. JIANG, and C. NANXIAN (2009) “The effect of Mo atoms in ternary nitrides with eta-type structure,” *Solid State Communications*, **149**, pp. 121–125.
- [99] DICKINSON, J. and P. ARMSTRONG (1967) “Temperature dependence of the elastic constants of molybdenum,” *Journal of Applied Physics*, **38**(2), pp. 602–606.
- [100] TSAI, H. T. and A. MUAN (1992) “Activity-Composition Relations in Refractory Oxide Solid Solutions at High Temperatures: The System Cr₂O₃-Al₂O₃,” *Journal of the American Ceramic Society*, **75**(6), pp. 1412–1415.
- [101] NEUBURGER, M. C. (1936) “Praezisionsmessung der Gitterkonstante von sehr reinem Niob,” *Zeitschrift fuer Kristallographie, Kristallgeometrie, Kristallphysik, Kristallchemie (-144,1977)*, **93**, pp. 158–159.
- [102] BOLEF, D. (1961) “Elastic constants of single crystals of the bcc transition elements V, Nb, and Ta,” *Journal of Applied Physics*, **32**(1), pp. 100–105.
- [103] STEINBINDER, D., H. WIPF, A. MAGERL, D. RICHTER, A.-J. DIANOUE, and K. NEUMAIER (1988) “Nonadiabatic low-temperature quantum diffusion of hydrogen in Nb(OH)_x,” *EPL (Europhysics Letters)*, **6**(6), p. 535.
- [104] NEUBURGER, M. C. (1936) “Praezisionsmessung der Gitterkonstante von sehr reinem Tantal,” *Zeitschrift fuer Kristallographie, Kristallgeometrie, Kristallphysik, Kristallchemie (-144,1977)*, **93**, pp. 312–313.
- [105] VAVILOVA, V. V., L. N. GALKIN, and M. V. GLAZOV (1988) “Stabilization of a Phase with the δ-Mn Structure by Rapid Quenching in the Rhenium-Tantalum System,” in *Dokl. Akad. Nauk SSSR*, vol. 300, pp. 1157–1161.
- [106] TRECO, R. M. (1953) “Effect of small additions of oxygen on lattice constants and hardness of zirconium,” *Transactions of the American Institute of Mining, Metallurgical and Petroleum Engineers*, **197**, pp. 344–348.

- [107] BERGERHOFF, G., R. HUNDT, R. SIEVERS, and I. D. BROWN (1983) “The inorganic crystal structure data base,” *Journal of Chemical Information and Computer Sciences*, **23**(2), pp. 66–69.
- [108] KARLSRUHE, F. I. Z., “Inorganic Crystal Structure Database,” .
- [109] PENG, Q., W. JI, J. LIAN, X.-J. CHEN, H. HUANG, F. GAO, and S. DE (2014) “Pressure effect on stabilities of self-Interstitials in HCP-Zirconium,” *Scientific Reports*, **4**, p. 5735.
- [110] PRAGER, A. I. K., A. M. BALAGUROV, I. O. BASHKIN, A. V. BELUSHKIN, E. G. PONYATOVSKY, and M (1994) “Neutron scattering studies of ordered γ -ZrD,” *Journal of Physics: Condensed Matter*, **6**(43), p. 8977.
- [111] KURODA, D., M. NIINOMI, M. MORINAGA, Y. KATO, and T. YASHIRO (1998) “Design and mechanical properties of new β type titanium alloys for implant materials,” *Materials Science and Engineering: A*, **243**(1), pp. 244–249.
- [112] HE, G. and M. HAGIWARA (2004) “Ti-Cu-Ni (Fe, Cr, Co)-Sn-Ta (Nb) alloys with potential for biomedical applications,” *Materials Transactions*, **45**(4), pp. 1120–1123.
- [113] ——— (2006) “Ti alloy design strategy for biomedical applications,” *Materials Science and Engineering: C*, **26**(1), pp. 14–19.
- [114] OKAMOTO, H. (2003) “Sn-Ta (Tin-Tantalum),” *Journal of Phase Equilibria*, **24**(5), p. 484.
- [115] STUDNITZKY, T. and R. SCHMID-FETZER (2002) “Phase Formation and reaction Kinetics in M-Sn systems (M=Zr, Hf, Nb, Ta, Mo),” *Zeitschrift Fur Metallkunde*, **93**(9), pp. 894–903.
- [116] BASILE, F. (1971) “Cristallographic study and supraconductive properties of compounds V_3Sn and Ta_2Sn_3 ,” in *Annales de chimie*, vol. 6, pp. 241–244.
- [117] YUE, Q., Y. LIU, M. CHU, and J. SHEN (2009) “Thermodynamic modeling of the Sn-V binary system,” *Calphad*, **33**(3), pp. 539–544.
- [118] TOFFOLON, C., C. SERVANT, J. GACHON, and B. SUNDMAN (2002) “Re-assessment of the Nb-Sn system,” *Journal of Phase Equilibria*, **23**(2), pp. 134–139.
- [119] COURTNEY, T., G. PEARSALL, and J. WULFF (1965) “Effect of Processing History on the Superconducting Properties and Long-Range Order of Ta_3Sn ,” *Journal of Applied Physics*, **36**(10), pp. 3256–3260.

- [120] PREDMORE, R. and R. ARSENAULT (1970) “Short range order of Ta-Mo B.C.C. alloys,” *Scripta Metallurgica*, **4**(3), pp. 213–217.
- [121] SHANG, S., A. SAENGDEEJING, Z. MEI, D. KIM, H. ZHANG, S. GANESHAN, Y. WANG, and Z.-K. LIU (2010) “First-principles calculations of pure elements: Equations of state and elastic stiffness constants,” *Computational Materials Science*, **48**(4), pp. 813–826.
- [122] ALLEN, W. and J. PEREPEZKO (1991) “Solidification of undercooled Sn-Sb peritectic alloys: Part I. Microstructural evolution,” *Metallurgical Transactions A*, **22**(3), pp. 753–764.
- [123] ARROYAVE, R. and Z.-K. LIU (2006) “Intermetallics in the Mg-Ca-Sn ternary system: Structural, vibrational, and thermodynamic properties from first principles,” *Physical Review B*, **74**(17), p. 174118.
- [124] CALVERT, L. and P. VILLARS (1991) “Pearson’s Handbook of Crystallographic Data for Intermetallic Phases,” *ASM, Materials Park, OH*.
- [125] PELETZER Y BLANCÁ, E. L., A. SVANE, N. E. CHRISTENSEN, C. O. RODRÍGUEZ, O. M. CAPPANNINI, and M. S. MORENO (1993) “Calculated static and dynamic properties of β -Sn and Sn-O compounds,” *Physical Review B*, **48**(21), pp. 15712–15718.
- [126] JOUAULT, F. and P. LECOCQ (1967) “Etude comparee des trois diagrammes V-Sn, Nb-Sn, Ta-Sn,” *Colloques Internationaux du Centre National de la Recherche Scientifique*, **157**, pp. 229–235.
- [127] GELLER, S., B. T. MATTHIAS, and R. GOLDSTEIN (1955) “Some new intermetallic compounds with the beta.-wolfram structure,” *Journal of the American Chemical Society*, **77**, pp. 1502–1504.
- [128] WANG, Y., S. CURTAROLO, C. JIANG, R. ARROYAVE, T. WANG, G. CEDER, L.-Q. CHEN, and Z.-K. LIU (2004) “Ab initio lattice stability in comparison with CALPHAD lattice stability,” *Calphad*, **28**(1), pp. 79–90.
- [129] ARROYAVE, R. and Z.-K. LIU (2006) “Thermodynamic modelling of the Zn-Zr system,” *Calphad*, **30**(1), pp. 1–13.
- [130] VAN DE WALLE, A., M. ASTA, and G. CEDER (2002) “The alloy theoretic automated toolkit: A user guide,” *Calphad*, **26**(4), pp. 539–553.
- [131] DENTON, A. R. and N. W. ASHCROFT (1991) “Vegard’s law,” *Physical Review A*, **43**(6), pp. 3161–3164.

- [132] KIM, H., Y. IKEHARA, J. KIM, H. HOSODA, and S. MIYAZAKI (2006) “Martensitic transformation, shape memory effect and superelasticity of Ti-Nb binary alloys,” *Acta Materialia*, **54**(9), pp. 2419–2429.
- [133] BUDAI, J. D., J. HONG, M. E. MANLEY, E. D. SPECHT, C. W. LI, J. Z. TISCHLER, D. L. ABERNATHY, A. H. SAID, B. M. LEU, L. A. BOATNER, R. J. MCQUEENEY, and O. DELAIRE (2014) “Metallization of vanadium dioxide driven by large phonon entropy,” *Nature*, **515**(7528), pp. 535–539.
- [134] LIU, Z. K. and Y. WANG (2016) *Computational Thermodynamics of Materials*, Cambridge University Press.
- [135] LIU, Z.-K., S.-L. SHANG, and Y. WANG (2017) “Fundamentals of Thermal Expansion and Thermal Contraction,” *Materials*, **10**(4).

Vita

Cassie Marker

Cassie Marker was born in Lansing, Michigan and after graduating from Haslett High School in 2008, Cassie enrolled at Alma College where she studied Chemistry and Math. After graduation she worked as a research technician for the Dow Chemical Company. Cassie then joined Dr. Zi-Kui Liu's research group at the Pennsylvania State University in 2013. During her graduate studies, she has had the opportunity to work at ATI specialty materials and South Central University in China. She won the U.S. DOE Graduate Student Research Award. Cassie is a NSF National Research Trainee Fellow and obtained a graduate minor in Computational Sciences.

Listed below are her publications during her Ph.D. study:

1. C. Marker, A. Ross, and Z.-K. Liu, "Chapter 3 Design of Materials Processing Using Computational Thermodynamics" submitted to the book Computational Materials System Design by D. Shin and J. Saal to be published in 2017
2. C. Marker, S. Shang, X. L. Liu, G. Lindwall, and Z.-K. Liu, "First-principles calculations and thermodynamic modeling of the Sn-Ta system," *Calphad*, vol. 57, pp. 46-54, Jun. 2017.
3. Z. Liu, M. D. Biegalski, S. L. Hsu, S. L. Shang, C. Marker, J. Liu, L. Li, L. Fan, T. L. Meyer, A. T. Wong, J. A. Nichols, D. Chen, L. You, Z. Chen, K. Wang, K. Wang, T. Z. Ward, Z. Gai, H. N. Lee, A. S. Sefat, V. Lauter, Z. K. Liu, H. M. Christen, Epitaxial Growth of Intermetallic MnPt Films on Oxides and Large Exchange Bias. *Adv. Mater.*, vol. 28, no. 1, pp. 118-123, 2016.
4. C. Marker, S. L. Shang, J.-C. Zhao, Z. -K. Liu, "Effects of alloying elements on the elastic properties of bcc Ti-X alloys from first-principles calculations" submitted *Journal of Alloys and Compounds*.
5. C. Marker, S. L. Shang, J.-C. Zhao, Z. -K. Liu, "Effects of alloying elements on the elastic properties of bcc Ti-X-Y alloys from first-principles calculations" submitted *Journal of Computational Materials Science*
6. T. Frueh, C. Marker, E. R. Kupp, C. Compson, J. Atria, J. Gray, Z. -K. Liu, and G. L. Messing, "Effects of Powder Chemistry on the Sintering of MgO-doped Bayer Al₂O₃" submitted *Journal of American Ceramic Society*